Breast and Skin Cancer Detection and Depth Profiling by Tissue Stiffness Contrasting Using Piezoelectric Fingers (PEFs)

A Thesis

Submitted to the Faculty

of

Drexel University

by

Xin Xu

in partial fulfillment of the

requirements for the degree

of

Doctor of Philosophy

August 2016

DEDICATIONS

This thesis is dedicated to my family with love.

ACKNOWLEDGMENTS

First of all, I would like to express my sincere gratitude to my advisors, Dr. Wan Y. Shih and Dr. Wei-Heng Shih for their invaluable advises about my research on every phase of this entire journey. Without their constant support and guidance, this dissertation would have never been completed.

Secondly, I would like to thank our clinical collaborators – Dr. Ari B. Brooks. Mr. Richard Sensenig, and Ms. Cynthia Gifford-Hollingsworth for helping me conduct the *in vivo* test. Their supports and suggestions were invaluable during my entire study.

I would like to thank the support of the entire lab. They have been very helpful in every step of my research and without their discussions and help, my research would not be at this stage.

Lastly, I would also like to acknowledge my thesis committee – Dr. Amy Throckmorton, Dr. Alan C. W. Lau, Dr. Lin Han, Dr. Wan Y. Shih and Dr. Wei-Heng Shih for their valuable inputs and critical review of my thesis. I appreciate all the time and effort you have put into helping me.

TABLE OF CONTENTS

LIST OF TABLES

LIST OF FIGURES

ABSTRACT

Breast and Skin Cancer Detection and Depth Profiling by Tissue Stiffness Contrasting Using Piezoelectric Fingers (PEFs)

Xin Xu

Wan Y. Shih Ph.D.

Wei-Heng Shih Ph.D.

Most imaging techniques project a 3-dimensional (3D) tumor into a 2-dimensional (2D) image that lacks the depth information. The ability to provide not only the lateral dimensions of tumors but also the depth profile is important for accurately sizing the tumor and is crucial for preliminary staging of the tumor prior to surgery, improving biopsy accuracy, and minimizing incomplete surgical removal of the tumors. Although computer tomography (CT) and magnetic resonance imaging (MRI) can provide tumor 3D images CT scans exposes patients to additional radiation risks and MRI is expensive. In addition, these techniques may not be suitable for assessing certain tumors such as skin cancers.

Piezoelectric finger (PEF) is a tissue stiffness sensor developed at Shih and Shih's lab that can measure the elastic modulus of tissues both *in vitro* and *in vivo*. Because breast tumors are stiffer than surrounding tissues, it is possible to detect and image breast tumors by contrasting the higher-elastic modulus regions with the surrounding tissues. In addition, a PEF with a larger contact area can assess the stiffness of tissues at a larger depth. It is thus possible to use PEFs with different contact areas to probe for depth profiles of tumors.

The goal of this study is to develop the methodology to use array PEFs not only to detect breast tumors and skin tumors but also image their locations and sizes in 3D for various applications. In Aim 1, a handheld probe containing an array of four PEFs of the same contact area (6.5 mm) is developed together with a custom-built circuit board to detect breast tumors in 40 patients. The results show that PEF detected 96% of breast tumors, including 100% of palpable and 67% non-palpable malignant tumors. Among the 28 patients with mammography records, PEF detected 92% malignant tumors while mammography only detected 80%. Furthermore, PEF detection was not affected by mammography density, indicating that PEF is promising for detecting breast tumors in young women and women with dense breasts for whom mammography is ineffective.

In Aim 2, tumor depth profiles was determined using the stiffness measurements by a set of PEFs with contact sizes 4.1 - 9.8 mm on model breast tumors of clays embedded in gelatin coupled with a spring model. The locations of the top of bottom-supported model breast tumors were determined within 1.1 mm of the actual values. For suspended model breast tumors both the top and the bottom margins were determined within 2.1 mm of the actual values, indicating that it is a promising methodology for tumor depth profiling. In addition to the depth accuracy, the current spring model-based methodology has the advantage of being instant as compared to the inversion simulations (IS) using finite element analysis (FEA) which gives similar accuracy but is tedious and time-consuming.

In Aim 3, a mechanical model of skin was established as a two-layer structure with the stiffer layer representing the epidermis and dermis (skin) on top of the softer subcutaneous layer. The elastic modulus and thickness of skin were then simultaneously determined using the stiffness measurements obtained with PEFs of different contact sizes of <3 mm coupled with an empirical formula for a two-layer structure derived from Green's function calculations. Both the elastic modulus and the thickness of the skin layer were resolved within <10% of the actual values in skin phantoms, and porcine skins and validated by FEA.

In Aim 4, the lateral extent and the depth profile of model skin cancers of clay embedded in porcine skins were determined using the stiffness measurements with PEFs of various contact sizes of <3 mm coupled with a modified spring model taking into account of the two-layer nature of skin. The lateral sizes of model skin cancers determined by PEF were within an error of 1 mm and the estimated depth profiles showed good agreement with the actual thickness with <0.4 mm discrepancy.

In conclusion, PEF is capable of detecting breast cancer with sensitivity better than mammography and independent of mammography density. In addition, using a set of PEFs of different contact areas coupled with simple spring-model calculations the depth profiles of both breast cancer and skin cancer can be accurately determined to facilitate 3D breast cancer/skin cancer imaging.

1. BACKGROUND AND LITERATURE REVIEW

1.1 Breast Anatomy and Breast Tumors

1.1.1 Breast Anatomy

The breast is a mass of glandular, fatty, and fibrous tissues positioned over the pectoral muscles of the chest wall and attached to the chest wall by fibrous strands [1]. A woman's breast as shown in Figure 1.1 [2] has glands that produce milk. The milk-producing part of the breast is organized into 15 to 20 sections, called lobes [3]. Within each lobe are smaller structures called lobules, where milk is produced. The milk travels through a network of tiny tubes called ducts. The ducts connect and assemble into larger ducts, which eventually exit the skin in the nipple. The dark area of skin surrounding the nipple is called the areola.

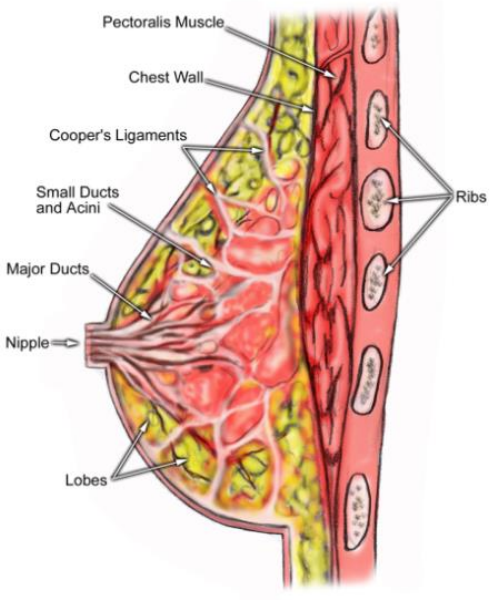

Figure 1.1 Breast anatomy [2]

Connective tissue and ligaments provide support to the breast and give it its shape. Nerves provide sensation to the breast. The breast also contains blood vessels, lymph vessels, and lymph nodes. Most of the lymph vessels that go through the breast carry the lymph to the lymph node underneath the arm pit, called axillary nodes. The other lymph vessels carry the lymph to the lymph nodes that are inside the chest, called the internal mammary nodes, or that are above or below the collarbone, called the supraclavicular or infraclavicular nodes. Lymph vessels can also carry possible diseases to lymph nodes and might increase the spread of the disease, for example breast cancer cells [4].

1.1.2 Breast Tumors

A breast tumor is a mass of abnormal tissue in the breast. It can occur in both men and women, although there is a very small probability for the disease to occur in men.

1.1.2.1 Statistics of Breast Cancer

Breast cancer is the most common type of cancer for women in the US, except for skin cancers. About 1 in 8 (12%) women in the US will develop invasive breast cancer during their lifetime. In the US, during 2016, it is estimated that there will be 843,820 cancer cases among women, and 246,660 of them will be invasive breast cancer cases which accounts for 29% of the total cancer cases [5].

In the US, Breast cancer is the second leading cause of cancer death in women, exceeded only by lung cancer. In 2016, 281,400 women are expected to die of cancer

and 40,450 of them will die from breast cancer which accounts for 15% of the total cancer death among women. [5, 6]. Worldwide, 500,000 women are estimated to die from breast cancer each year [7].

1.1.2.2 Types of Breast Conditions

Changes in the breast may be caused by either benign (non-cancerous) or malignant (cancerous) conditions. Benign tumors are very common and they are not generally aggressive toward surrounding tissue. But they still may continue to grow, pressing on organs and causing pain or other problems. Some of the benign tumors are linked with a higher risk of later development of malignant tumor [8-10]. A malignant tumor is a group of cancer cells that can grow into (invade) surrounding tissues or spread (metastasize) to distant areas of the body [11, 12]. Cancerous tumors can start in different areas of the breast, and are named according to the area they originate from. Biopsy is needed to understand if the irregularity in the breast is cancerous or not.

They are many types of non-cancerous and cancerous breast conditions. The most common types can be summarized as listed below.

1.1.2.2.1 Non-cancerous Breast Conditions

Fibrosis and Cysts: They are benign changes in breast tissue that happen in many women in their lives and are sometimes called fibrocystic changes. They can cause areas of lumpiness, thickening, or tenderness. Fibrosis is the formation of a large amount of fibrous tissue, the same material that ligaments and scar tissues are

made of. Areas of fibrosis feel firm. Cysts are fluid-filled, round or oval shaped fluid-filled sacs. It feels like a soft lump in the breast. A cyst cannot be diagnosed by physical exam or mammography. It can only be identified with ultrasound.

Fibroadenomas: They are the most common benign tumors found in the female breast. Fibroadenomas are benign tumors made up of both glandular breast tissue and connective tissue. They are solid, round, rubbery lumps that are distinct from the surrounding breast tissue. And they can move freely in the breast when pushed upon. Some fibroadenomas can be felt, but some are only found in an imaging test. Women with fibroadenomas have an increased risk of breast cancer – about 1.5 to 2 times the risk of women with no breast changes [4].

Hyperplasia: It is an overgrowth of the cells that line the ducts (ductal hyperplasia) or the lobules (lobular hyperplasia). It may cause a lump that can be felt. Based on the pattern of the cells, hyperplasia can be divided into two groups: usual and atypical. In usual hyperplasia, the pattern of cells is very close to normal, while in atypical hyperplasia the cells are more distorted and look abnormal. For women with atypical hyperplasia, the risk of breast cancer is about 3 to 5 times higher than that of a women with no breast abnormalities [8-10].

Fat necrosis: It happens when fatty breast tissue swells or becomes tender. It can occur spontaneously or as a result of an injury to the breast. It can also happen after surgery or radiation treatment. As the body repairs the damaged tissue, the affected area is replaced with firm scar tissue. As a result, it can form a lump that can be felt.

1.1.2.2.2 Cancerous Breast Conditions

Ductal Carcinoma in Situ (DCIS): DCIS is the most common type of non-invasive breast cancer. It is considered "non-invasive" because the cells have not invaded through the walls of the ducts into surrounding breast tissue. It is not life-threatening since it cannot spread (metastasize) outside the breast. However, DCIS could eventually develop into an invasive cancer if it is left in the body. Therefore, it is considered pre-cancerous. DCIS is usually found by mammography. As old cancer cells die off, calcifications or microcalcifications form within the broken down cells. The mammogram will show the cancer cells inside the ducts as cluster of these calcifications, which appear either as white specks or as a shadow.

Invasive (Infiltrating) Ductal Carcinoma (IDC): IDC is the most common type of invasive breast cancer, accounting for 80% of invasive breast cancers. It starts in a milk duct of the breast, breaks through the wall of the duct, and grows into the surrounding tissues. Since it has spread outside the duct walls, it is able to metastasize to other parts of the body.

Invasive (Infiltrating) Lobular Carcinoma (ILC): ILC accounts for 10% of the invasive breast cancers. It starts in the lobules of the breast where break milk is produced. Like IDC, it is invasive and can spread to other parts of the body. ILC may be harder to be detected by a mammogram than IDC.

Inflammatory Breast Cancer (IBC): IBC is a rare and aggressive form of breast cancer. It only accounts for 1-5% of breast cancer cases in the US. IBC is caused by cancers blocking lymph vessels in the skin. Usually it does not cause a

single lump or tumor. Instead, the skin on the breast looks red and has a pitted appearance. IBC has a higher risk of metastasis and a worse prognosis than typical IDC or ILC.

1.1.3 Early Detection of Breast Tumors

Early detection of diseases, especially cancers, can save thousands of lives each year. The five-year survival rate of Stage 0 & I breast cancers which are confined to a limited area is 100%. It decreases to 22% for stage IV in which case the cancer has spread beyond the breast to other areas of the body [13]. Therefore, patients will have better prognosis if breast cancers can be detect early.

Screening plays an important role in early detection of tumors. For breast tumor, screening can find breast cancers while they are still small in size and confined to the breast before they cause any symptoms. Breast cancers that cause discomfort to the patients and that are big enough to be easily felt tend to have already spread to other parts of the body [13].

Breast self-examination (BSE) is a step-by-step approach that a women can use to look at and feel her breasts. BSE seemed promising when it was first introduced. However, its effectiveness is being questioned [14-16]. Some studies have shown that it does not offer a beneficial effect whereas there is evidence for harms [15, 17].

Most national authorities in the US agree that women should begin mammography screening by age 50. The consensus is lower for screening those aged

40 to 50 years. The current guidelines from the American Cancer Society (ACS), the American Medical Association (AMA) and the American College of Radiology (ACR), and the National Cancer Institute recommend annual mammogram for every woman at ages 40 and up [13]. After a careful review of data in 2009, the United States Preventive Services Task Force (USPSTF) updated its previous recommendation to begin routine screening at age 50 years [18]. There is also remaining controversy about annual versus biennial mammography screening [19].

1.1.4 Determination of Breast Tumor Locations and Sizes in 3D

Accurate preoperative assessment of breast tumor locations and sizes in three dimensions (3D) are important for both biopsies and surgeries [20]. Underestimating pre-surgical tumor size may lead to incomplete margins in lumpectomy and hence, re-excision. The current re-excision rate of lumpectomy is 30-60% [21]. Tumor size is also a valuable indicator of stages, which are important in planning the appropriate treatment and estimating the prognosis [22]. Besides, precise measurements of tumor locations and sizes in 3D are required to monitor response of chemotherapy and radiotherapy for breast tumors.

1.1.5 Breast Tumor Imaging Modalities

1.1.5.1 Current Modalities

Clinical breast examination (CBE), ultrasound, mammography, and magnetic resonance imaging (MRI) are the main breast tumor detection and localization methodologies used currently. Each of them has their advantages and disadvantages as summarized below.

Clinical breast examination (CBE): CBE, or better known as palpation, is the physician's palpating the breast to detect any possible masses inside the breast. CBE is highly dependent on the physician's skills, expertise and experience [23, 24]. Some indications such as skin and nipple retraction are only detectable by CBE [25]. Although the techniques for CBE are well established, its effectiveness is still dependent on how good the physician is. CBE alone is sometimes not enough to detect breast cancer in its very early stages [26, 27]. It has difficulty detecting lesions with indistinct borders, lesions in large breasts, and non-palpable lesions [26, 28, 29]. Besides, CBE cannot provide quantitative value of the tumor size.

Ultrasound Imaging (Ultrasonography): Ultrasound is sound wave with a frequency greater than upper limit of the human hearing range, usually 20 kHz. Ultrasound can be directed as a beam and can be reflected by objects of small sizes. It obeys the theories of reflection, refraction, and scattering. Ultrasound is not radioactive, and therefore it is widely used in medical imaging. Typical ultrasound imaging operates in the frequency range of 1 to 18 MHz. The choice of frequency is a compromise between spatial resolution of the image and imaging depth: lower frequencies produce less resolution but image deeper into the body. High frequency sound waves have a smaller wavelength and thus are capable of reflecting or scattering from smaller structures.

Ultrasound examination is performed on patients in a supine position as shown in Figure 1.2. Ultrasound machine sends ultrasound to the tissue and monitors the echoes of ultrasound waves. The main part of the machine is the ultrasound probe

which consists of an array of piezoelectric transducers. When strong short electrical pulse voltages are applied to these transducers, they vibrate due to converse piezoelectric effect and generate ultrasound sent to the tissue. The sound wave is partially reflected from the layers between different tissues or scattered from smaller structures. If the breast tissue is uniform and there is no tumor inside, the ultrasound is echoed back from the muscles and bones underneath. If there is a tumor inside, the ultrasound is echoed when it hits the interface between the normal tissue and the tumor. When the echo comes back to the transducer, it vibrates the transducers and generates electricity due to direct piezoelectric effect. By measuring how long it takes the echo to be received and how strong the echo is, a 2D image of the scanned tissue can be formed. An approximate location of the tumor or any other abnormal in the tissue can be obtained by scanning the entire breast.

Figure 1.2 A picture showing how ultrasound examination is performed on breasts [30].

Ultrasound imaging is a useful technique for evaluating the suspicious lesions in the breast. It also confirms the presence of a lump that was detected by mammogram. One of the main reasons ultrasound is used in breast imaging is to differentiate between the cystic (fluid filled) lesions from solid lesions. Some microcalcifications in ductal carcinoma in situ may not be identified by ultrasound [31-33]. Besides, it underestimates the tumor size [34-36], which may lead to incomplete excision in lumpectomy [20]. It is hard to make sure that the image contains the whole breast. Because it is user dependent, ultrasound is not a good screening test for breast cancer [37-39].

Mammography: Mammography is a specific type of imaging technique which uses low-dose x-ray to create an image of the breast. During the procedure, the breast is compressed by parallel plates as shown in Figure 1.3, which can even out the thickness of breast tissue to increase image quality by reducing the thickness of tissue that x-rays must penetrate, to decrease the amount of scattered radiation, to reduce the required radiation does, and to hold the breast still.

It is an excellent tool for early detection of breast cancer in women, even if they experience no symptoms. Mammogram is the gold standards used in early detection of breast cancer because it can show changes in the breast up to two years before a patient or physician can feel them. Mammography is an FDA approved technique for breast cancer screenings. There is no proven screening test that has been shown to be better than mammography today. Early detection using mammography provides more opportunity to detect the tumors while they are small,

so offering more treatment options. The current guidelines from the American Cancer Society (ACS), the American Medical Association (AMA) and the American College of Radiology (ACR), and the National Cancer Institute recommend annual mammogram for every woman at ages 40 and up [13]. After a careful review of data in 2009, the United States Preventive Services Task Force (USPSTF) updated its previous recommendation to begin routine screening at age 50 years [18]. There are reports pointing out that in addition to unnecessary surgery and anxiety, the risks of more frequent mammograms include a small but significant increase in breast cancer induced by radiation [40, 41].

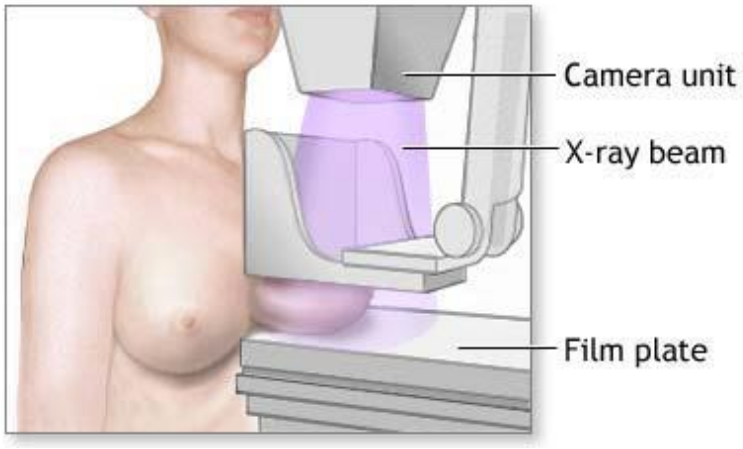

Figure 1.3 A schematic showing how mammogram is performed on breasts.

While mammography has a great potential for early detection of breast cancer, it has a high false positive rate. After 10 mammograms, the risk of a false-positive mammogram is over 40% [42-44]. Also the likelihood of having a biopsy after 10

mammograms is over 10%, but only a small percentage of those have a cancer. So most of the biopsies performed based on the results of the mammogram are unnecessary. Mammography is also not very sensitive for young women under 40 and women over 40 who have mammographically dense breasts [45-48]. According to the BI-RADS (Breast Imaging Reporting and Data System) reporting system, the density of breasts can be divided into four levels, which are almost entirely fatty (Grade 1), scattered fibroglandular density (Grade 2), heterogeneously dense (Grade 3) and extremely dense (Grade 4) as shown in Figure 1.4. The Table 1.1 below shows that the sensitivity of mammography is 87% for breasts with a density grade of 1 and the sensitivity is only 62.9% for grade 4 dense breasts [49]. The sensitivity of mammography decreases significantly with women with dense breasts [41, 48, 49].

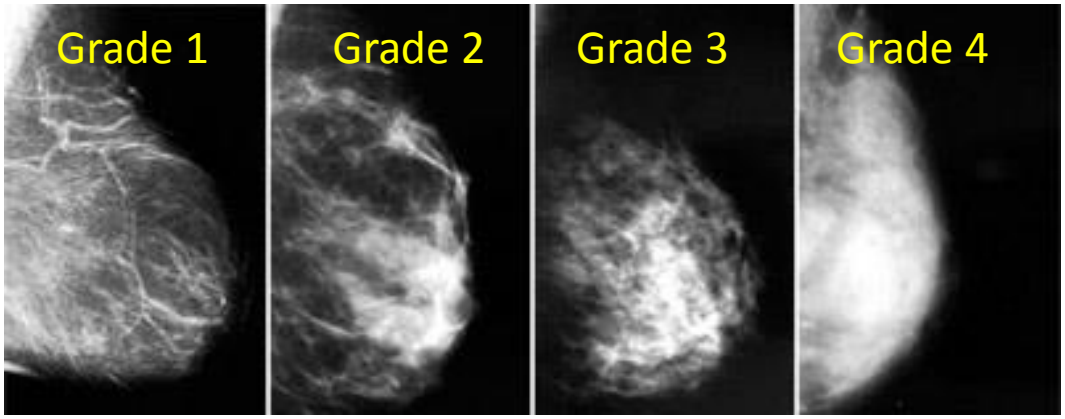

Figure 1.4 Mammogram images of breasts of different density grades. According to the BI-RADS reporting system, the levels are almost entirely fatty (Grade 1), scattered fibroglandular density (Grade 2), heterogeneously dense (Grade 3) and extremely dense (Grade 4) [50].

Table 1.1 Sensitivity of Mammography for Breasts with Different Densities [49]

Density grade	Ratio of fatty tissue to glandular tissue	Mammography sensitivity
Grade 1	Almost entirely fat (< 25% glandular)	87.0%
Grade 2	Scattered fibroglanular densities (25-50% glandular)	81.5%
Grade 3	Heterogeneously dense (51-75% glandular)	69.4%
Grade 4	Extremely dense (greater than 75% glandular)	62.9%

Although mammography takes two pictures: one viewed from top to bottom (craniocaudal, CC) and the other from a 45° angle (mediolateral oblique, MLO), it is still difficult to pinpoint the actual location and extent of the tumor. Compression of the breast can also lead to distortion of the location and extent of the tumor. Vague lesion boundaries can introduce error to the measurements [26]. Moreover, standard imaging projections do not always capture the maximum tumor extent [51]. In addition, patients are in a different position during regular mammography imaging from the supine position during surgery. Such differences can further distort the 3D localization of the tumor.

Magnetic Resonance Imaging (MRI): MRI produces high quality images of inside of the human body. It is based on the principles of nuclear magnetic resonance (NMR), a physical phenomenon in which nuclei in a magnetic field absorb and reemit electromagnetic radiation.

Human body is largely composed of water molecules, each of which contains two hydrogen nuclei, or protons. At the atomic level, when protons are placed in a

large external magnetic field, some protons align with the field and have a lower energy state and some align against the field and have a higher energy state. The protons are continually oscillating back and forth between the two states but any given instant and with a large enough sample, there will be a light majority aligned with the field. If an electromagnetic radio frequency (RF) pulse is applied at the resonance frequency, the protons can absorb that energy and jump to a high energy state. After the RF transmitter is turned off, the excited protons come back to the lower energy state and the absorbed RF energy is retransmitted, which yields a changing voltage in receiver coils to give the signal. By applying additional gradient magnetic fields that vary linearly over space, specific slices of the body can be imaged. The image is obtained by taking the 2D Fourier transform of the spatial frequencies of the signal. Tumors can be detected because the protons in different tissues return to their equilibrium state at different rates. By changing the parameters on the scanner this effect is used to create contrast between different types of body tissue.

In detecting and screening breast tumor, breast MRI is becoming an important tool nowadays. It can provide images with high contrast and high resolution and help detect breast cancer in its earliest stage. Besides, it does not have ionizing radiation. However, breast MRI may miss some cancers [52, 53]. It cannot visualize the calcium deposits [54, 55], known as calcifications or microcalcifications, which typically surround ductal carcinoma in situ (DICS) lesions. Moreover, a recent study indicated that MRI also underestimates the sizes of breast lesions especially those of ductal

carcinoma in situ (DCIS) [56]. The discordance between the tumor size on MRI and the pathological size may contribute to re-excisions in patients who undergo lumpectomy.

1.1.5.2 Emerging Modalities

Elastography: Elastography is a new medical imaging modality that maps the elastic properties of soft tissue. The main idea is that whether the tissue is hard or soft will give diagnostic information about the presence or status of disease. For example, breast tumors are usually stiffer than the surrounding normal tissues. Unlike palpation which is a qualitative method with low sensitivity, elastography is able to provide quantitative modulus results of breast to distinguish tumors from the normal tissue.

In elastography, external static compression (ultrasound elastography) or harmonic shear waves (magnetic resonance elastography) is applied to the tissue, and the resulting tissue displacements are then monitored using ultrasound (ultrasound elastography) or MRI (magnetic resonance elastography). These displacements are then used to reconstruct tissue stiffness using inversion technique based on tissue biomechanical model [57, 58].

Ultrasound elastography utilizes either strain or transient elastography. Strain elastography is also known as static or compression elastography. With this technique, compression is applied to tissue with an ultrasound probe. It results in tissue displacement (strain) which can be measured by tracking longitudinal movement of tissue before and after compression. Strain elastography provides strain ratios calculated by comparing the strain of a lesion to the surrounding normal tissue. Soft

tissue has higher strain values than stiff tissue. Transient elastography, also known as shear-wave elastography, utilizes a gentle compression force generated by the ultrasound probe and induces transversely oriented shear waves within tissue. The speed of the shear waves, which is directly proportional to Young's modulus, can be measured by the extremely fast ultrasound acquisition system. Therefore, transient elastography provides quantitative information about the Young's modulus of the tissue. Multiple studies have shown that ultrasound elastography may provide additional diagnostic information to further characterize breast lesions and has the potential to improve the specificity of low suspicion lesions evaluated with conventional ultrasound [59-62].

Using magnetic resonance elastography (MRE), shear modulus of the tissue can be measured. Acoustic shear waves are sent to the tissue, and an MRI based method is used to image the propagation of the waves inside the tissue. An algorithm is used to process the wave images and generate quantitative images that show the shear modulus values. McKnight et al. took the MRE of the breasts of six healthy women and six patients with known breast cancer and found that the shear stiffness of the tumors ranged from 18 to 94 kPa, while the shear stiffness of adipose breast tissue in the breast cancer patients ranged from 4 to 16 kPa [58]. MRE is being investigated as a complementary technique to conventional imaging methods to provide additional information about suspicious regions [63-65] and the combined technique has shown promise to increase diagnostic specificity [65-67].

Tactile imaging: Tactile imaging is a newly developed technique which emulates human tactile sensation. It measures the force or pressure on the breast surface and uses a mapping algorithm to form a composite tactile map of the tissue.

Egorov et al. developed a tactile imaging tool for breast tumor detection called Breast Mechanical Imager (BMI, trade name "SureTouch") [68-71] as shown in Figure 1.5. It is a compact device consisting of a hand held probe with a pressure sensor array, an electronic unit, and a touchscreen laptop computer. During measurement, the sensor array is pressed against the examined site. The changes in the surface stress patterns as a function of displacement, applied load and time provide information about the elastic composition and geometry of the underlying tissue structures. By using artificial neural network, an inversion technique, the 3D image of the mechanical properties of the breast can be constructed and the size, shape, stiffness, and mobility of detected lesions can be calculated. A clinical study with 179 cases has been done and demonstrated that the BMI can detect breast lesions and provide a reliable calculation of lesion features [70].

Yen et al. developed a stiffness measurement device that could be attached to a conventional ultrasound probe as shown in Figure 1.6 [72, 73]. When the device is slide across the lesion maintaining a constant compression depth, it measures the normal and lateral force on the tissue surface. The build-in inverse biomechanical model which is based on an artificial neural network can calculate the stiffness ratio of the lesion to its surrounding tissue. Simulations and experiments have been performed on phantoms with embedded inclusions, and they both show that the

stiffness ratio of the inclusion to its surrounding material can be accurately predicted. A preliminary test was performed on six patients and it showed that the stiffness ratios of fibroadenoma were in the range from 2.7 to 5.2, whereas the infiltrating ductal carcinoma were larger than 8.7 [73].

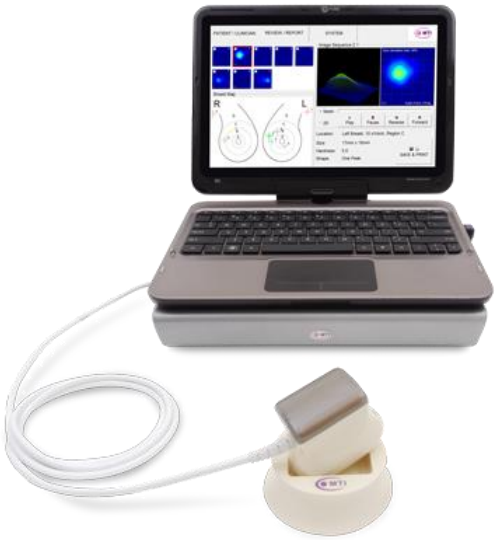

Figure 1.5 A picture of the Breast Mechanical Imager (BMI, trade name “SureTouch”) [70].

Lee et al. developed a tactile sensation imaging system (TSIS) based on an optical phenomenon known as the total internal reflection (TIR) [74-76]. In the system, a light is illuminated at the critical angle to be totally reflected within a multi-layer polydimethylsiloxane waveguide. When the waveguide is compressed by an external force dui to the stiff tissue inclusion, the contact area of the waveguide deforms and causes the light to scatter. The scattered light is captured by a high resolution camera and saved as an image. The size, depth and Young’s modulus can

be estimated based on a combination of a forward algorithm using 3D finite element method and an inversion algorithm using artificial neural network. A pilot clinical study with 3 patients was performed and it showed that the device could predict the sizes of breast tumors [76].

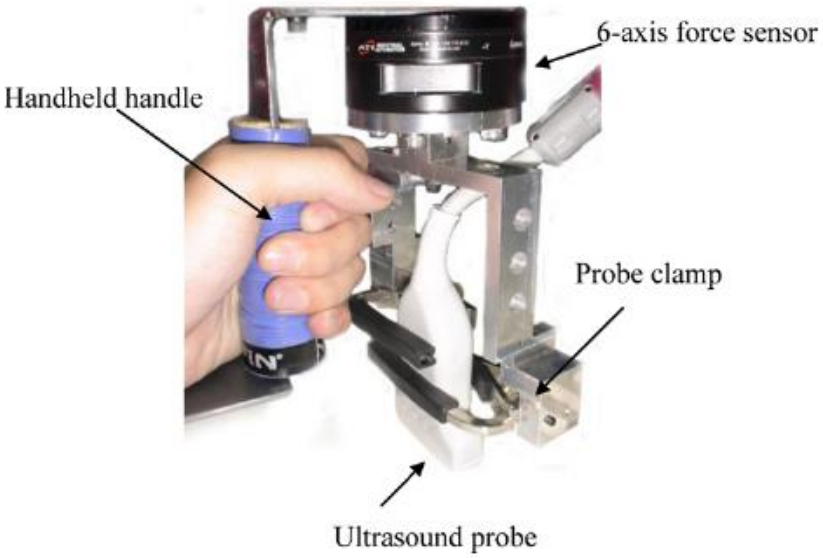

Figure 1.6 A stiffness measurement device which contains a handle, a 6-axis force sensor and a probe that can fix the ultrasound probe [73].

Uribe et al. developed a vibrating piezoelectric bimorph sensor (VPBS) which is composed by two piezoceramic plates attached to a common cantilever [77-79] as illustrated in Figure 1.7. One piezoceramic plate of the bimorph is used to generate the vibration of the beam by applying a sinusoidal voltage to its electrode and the common cantilever. The other plate is used to sense the vibration. The bimorph contacts with tissue surface by a spherical plastic tip. When the stiffness of the tissue

increases, there is a shift in the resonance frequency to higher values. The experiment was performed on gelatin phantoms with different concentrations and it showed that by monitoring the resonance frequency the device was able to tell the difference in stiffness [77-79].

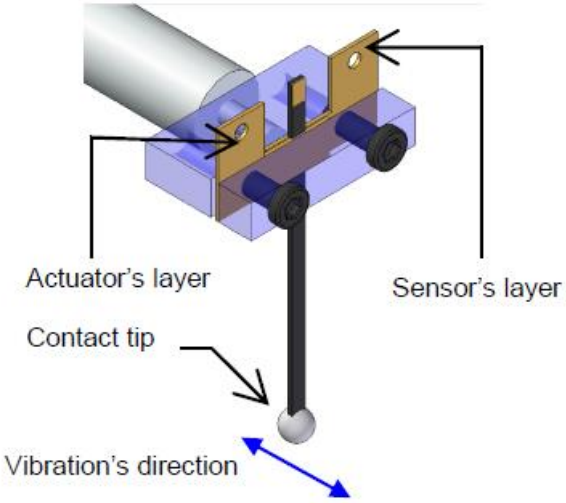

Figure 1.7 A schematic of the vibrating piezoelectric bimorph sensor (VPBS) [77].

Gwilliam et al. compared the performance of human finger and robotic tactile sensing on the same set of artificial tissue models [80]. They investigated the effects of various tissue parameters including lesion size, lesion depth, and surrounding tissue stiffness. They concluded that electronic palpation is more effective at detecting lumps than the human finger.

Most of the emerging methods including the elastography [57-59], BMI [69, 70], the ultrasound probe attachment [72, 73], the TSIS [74-76], and the VPBS [77, 78] do not measure tissue stiffness directly. Rather, they measure the stress or strain

distribution on the tissue surface and use an inversion technique such as artificial neural network technique and simulation to determine if there is a tumor and the diameter of the tumor if there is one.

1.1.6 Breast Tissue and Tumor Stiffness

There is a significant correlation between breast tissue histology and its stiffness. Many researchers have used the elasticity difference between the healthy and cancerous breast tissue to distinguish them [57, 58]. In addition to that, breast tumors can be imaged using the elastic modulus or stiffness contrast. The elastic modulus value of the breast tumor at a specific strain can also tell the histological properties of the tumor.

The stiffness of breast tumor has been reported in many studies [81-83]. The values vary depending on the tumor types and the measurement methods. It is assumed that different types of tissues (tumor, fat, gland, etc.) tested in the experiments were homogeneous and their behavior in compression were isotropic. Samani et al. characterized the mechanical response of 169 fresh *ex vivo* breast tumor specimens by the force-displacement slopes as they were undergoing indentation by a small flat-ended cylindrical indenter [81]. The elastic moduli of fat and fibroglandular tissue as well as benign and malignant breast tumors were calculated and compared. Wellman et al. measured the elastic modulus of different tissues and tumors of the breast immediately after they were removed from the body, using punch indentation method at different strains [82]. Krouskop et al. evaluated the viscoelastic properties of 112 excised breast tumors using an Instron testing machine with 5% pre-

compression strain [83]. They all reported that there is a significant difference between the healthy breast tissue and the tumor. A summary of the elastic modulus of normal breast tissues and tumors is shown in Table 1.2 below. As can be seen, the elastic modulus of normal breast tissues ranged from 3.24-33 kPa with an average of 13.5±2.6 kPa, while the elastic moduli of breast tumors ranged from 6.41-107 kPa with an average of 45.8±5.0 kPa. These results show that healthy breast tissue and tumors can be differentiated using the elastic modulus difference at low strain values.

Table 1.2 A summary of the elastic moduli of various breast tissues from Refs. [81, 83, 84]. The number in the parenthesis indicate the number of samples over which the elastic modulus was obtained. The average E in column 5 is the elastic modulus (E) averaged over different references.

	Tissue type	**E (kPa)**	**Reference**	**Average E (kPa)**
Normal tissue	Fat	4.8±2.5 (26)	[82]	9.0±2.5
		3.25±0.91 (71)	[81]	
		19±7 (8)	[83]	
	Gland	17.5±8.6 (7)	[82]	17.9±4.7
		3.24±0.61 (26)	[81]	
		33±11 (31)	[83]	
Tumor	Fibroadenoma	45.5±20.1 (5)	[82]	53.0±10.1
		6.41±2.86 (16)	[81]	
		107±31 (18)	[83]	
	Lobular Carcinoma	34.7 (1)	[82]	25.2±6.7
		15.62±2.64 (4)	[81]	
	Infiltrating Ductal Carcinoma	47.1±19.8 (25)	[82]	60.9±13.5
		42.52±12.47 (9)	[81]	
		93±12.47 (23)	[83]	
	Ductal Carcinoma in Situ	71.2 (1)	[82]	37.5±1.4
		16.38±1.55 (4)	[81]	
		25±4 (23)	[83]	

1.2 Skin Anatomy and Skin Cancers

1.2.1 Skin Anatomy

Skin is the largest organ of the body, with a total surface area of about 2 m^2. It works as a barrier and provides protection from mechanical impacts and pressures, variations in temperature, chemicals and pathogens. Besides, it regulates several aspects of physiology, including body temperature via sweat and air, and changes in peripheral circulation and fluid balance via sweat. Skin is also an organ of sensation. It contains an extensive network of nerve cells that permit the sensations of touch, heat, and cold.

Human skin is a complex organ with a layered structure that can vary in thickness depending on what part of the body it covers [85]. Skin has three layers as shown in Figure 1.8 [86].

Epidermis is the outermost layer of skin. It provides a waterproof barrier and creates the skin tone. It is the thinnest on the eyelids at 0.05 mm and the thickest on the palms and soles at 1.5 mm, and it is constantly renewing itself [87, 88]. The innermost layer of the epidermis consists of a single layer of basal cells standing on the basement membrane. These cells divide to form the predominant keratinocytes of the stratum spinosum. Keratinocytes make keratin to protect the body. Also contained in the basal layer (stratum basale) are the melanocytes which produce the pigment called melanin. They give the tan or brown color to skin and help protect the deeper layers of the skin from the ultraviolet light. As the keratinocytes are pushed towards the surface, they become flattened and the remnants of their nuclei cause the

cytoplasm to appear granular (stratum granulosum). Finally, the cells die and create the protective outermost layer, the stratum corneum, which provides the greatest barrier to water loss and invasion of foreign substances.

Dermis is the second layer of the skin and is beneath the epidermis. The dermis is much thicker than the epidermis and contains connective tissue, hair follicles, sweat glands, blood vessels, and nerves. The dermis ranges in thickness from 0.3 mm on the eyelids to 4 mm or more on the soles and palms [89]. The dermis is composed of two layers: the papillary layer and the reticular layer. The thin papillary layer lies directly beneath the stratum basale, and consists of slender and randomly ordered collagen fibers. The thicker reticular layer (4/5 of the dermis) is comprised by dense irregular connective tissue containing thick bundles of interlacing collagen fibers and some coarse elastic fivers that run in several directions.

Hypodermis, also known as subcutaneous tissue, is the innermost and thickest layer of the skin. The thickness is 3-100mm [90]. It invaginates into the dermis and is attached to the latter by collagen and elastin fibers. It is essentially composed of adipocytes, a type of cells specialized in accumulating and storing fats. It also protects the skin and allows for mobility of the skin over the underlying organs.

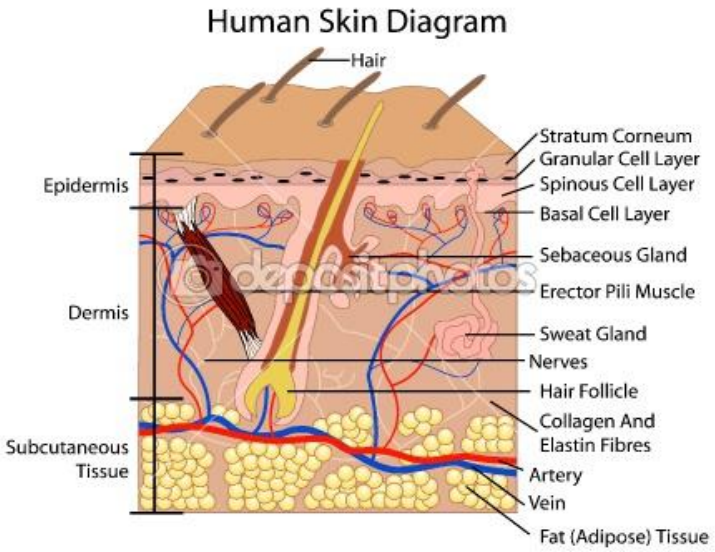

Figure 1.8 A schematic of human skin [91]

1.2.2 Skin Cancers

Within the skin and its many layers, there is a diverse range of cells and cell types. They are constantly renewing themselves. In principle, any cell that undergoes division has chance to become malignant due to genetic mutations during mitosis. Therefore, skin cancer, which is the uncontrolled growth of abnormal skin cells, is very common.

1.2.2.1 Statistics of Skin Cancers

Skin cancer is the most common form of cancer in the US. More than 3.5 million skin cancers are diagnosed annually, accounting for nearly 40% of all cancer cases. One in five Americans will develop skin cancer in the course of a lifetime [92]. Skin cancer can be divided into melanoma and non-melanoma skin cancers. The rates of melanoma have been rising for at least 30 years [93], according to National Cancer

Institute. In 1980, there were 10.5 new cases of melanoma per 100,000 people in the US. The number increases and in 2000, it increased to 19.0 new cases of melanoma per 100,000 people. In 2011, 22.7 new cases of melanoma were found per 100,000 people. It is estimated that 73,870 new melanomas will be diagnosed in the US in 2015 and 9,940 people are expected to die of melanoma [94]. Non-melanoma skin cancers refer to basal and squamous cell carcinomas. Each year in the US, nearly 5 million people are treated for non-melanoma skin cancers [95, 96]. And about 3,000 people die each year from non-melanoma skin cancers [97].

1.2.2.2 Types of Skin Cancers

There are three major types of skin cancers:

Basal Cell Carcinoma (BCC): BCC is abnormal, uncontrolled lesions that arise in the skin's basal cells in epidermis. It is the most frequently occurring form of skin cancers, accounting for 80% of skin cancer cases. Most of the lesions develop on sun-exposed areas, especially the head and neck. BCC typically grows slowly and generally spreads only locally. But if it is left untreated, it can grow into nearby areas, invade and destroy underlying structures and cause significant functional and cosmetic impairment. Besides, most of BCCs are non-pigmented [98].

Squamous Cell Carcinoma (SCC): SCC is an uncontrolled growth of abnormal squamous cells, which compose most of the skin's upper layer (epidermis). It is the second most common malignancy of the skin (after BCC), accounting for about 16% of skin cancer cases. Similar to BCC, SCC often appear on sun-exposed areas of the body such as the face, ears, neck, lips, and backs of the hands. But they

can also develop in scars or chronic skin scores elsewhere. It can become disfiguring and sometimes deadly if untreated. An estimated 700,000 cases of SCC are diagnosed each year in the US, resulting in approximately 2,500 deaths [99].

Melanoma: melanoma is a form of cancer that begins in melanocytes. It only accounts for less than 2% of skin cancer cases but causes a large majority of skin cancer deaths [94]. It can develop anywhere on the skin. It can be subdivided into 4 major pathologic subsets: lentigo maligna melanoma (LMM), superficial spreading melanoma (SSM), nodular melanoma (NM), and acral lentiginous melanoma (ALM). For all but NM, the growth pattern is biphasic. The initial growth occurs radially, sometimes persisting for years, but with little tendency to metastasize. Vertical growth then follows and develops much faster. NM growth pattern has only one phase, with growth in the vertical direction. It is during this vertical growth phase that the tumor can invade the underlying tissue and metastasize [100].

1.2.3 Diagnosis of Skin Cancers

Since most of the nonmelanoma skin cancers (BCC and SCC) are non-pigmented, it is difficult for the dermatologist to determine the lateral extent of the cancers by eye and remove them accordingly.

For melanomas, the Breslow thickness (as shown in Figure 1.9), which measures the distance between the upper layer of epidermis and the deepest point of tumor penetration [101], is one of the most important prognostic factors in melanoma [102]. If the thickness is smaller than 1mm (T1), the 5 year survival rate is 95-100%. If the thickness is larger than 4mm (T4), the 5 year survival rate is only 37-50% [103].

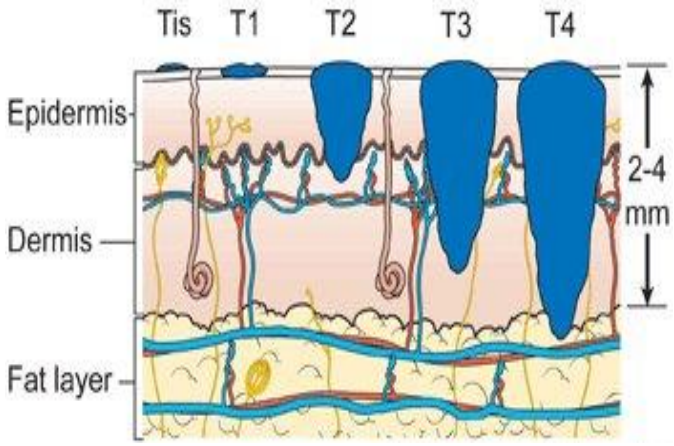

Figure 1.9 Breslow Thickness diagram for melanoma staging [104]. Malignant cells occupy surface layer only (Tis), <1mm (T1), 1-2mm (T2), 2-4mm (T3), and >4mm (T4).

1.2.3.1 Current Modalities

Physical exam is performed to detect skin cancers in clinics. The dermatologist uses a bright light and occasionally a magnifying lens to examine the skin and look for suspicious growths, moles, or lesions. The ABCDE guide which is a set of visual parameters is used to determine whether a skin lesion has a high probability of being a melanoma [105, 106]. A stands for asymmetry. Normal moles or freckles are completely symmetrical while melanomas are usually asymmetric. B stands for border, since the edges of melanomas are ragged, notched, or blurred. C means color. A lesion that has more than one color needs to be further evaluated. D is diameter. If the lesion is larger than 6 mm, further examinations are required. E stands for evolution. If the symmetry, border, color or diameter of a lesions changes over time, it is likely to be malignant. The ABCDE is an easy guide to the usual signs

of melanoma, but it cannot tell whether is lesion is indeed malignant or not. It does not provide any quantitative measurement results.

During the examination, a dermoscope may also be used, which is a noninvasive diagnostic tool that utilizes a handheld magnification device with a liquid at skin surface or a cross-polarized light source as shown in Figure 1.10. It allows detailed visualization of specific morphologic structures and colors from the epidermis to the superficial dermis which are invisible to the naked eye. However, it cannot be used to measure the lateral sizes or thickness of skin cancers.

Figure 1.10 A picture of the dermoscope [107].

The most important and widely used method for skin lesion characterization is pathological evaluation. Suspicious areas are selected by the dermatologist upon visual inspection, and the lesions are partially or wholly biopsied. A number of different biopsy techniques can be used including shave, punch, and excision. The

excised sample is then sectioned and stained for pathological investigation and diagnosis. The protocol for skin lesion diagnosis is the gold standard, but it is very time-consuming. Besides, the dermatologist does not always choose the correct area for biopsy. Partial biopsy cannot give the lateral sizes or thickness of the entire lesion, so the dermatologist do not know how much to cut during surgical removal of the lesion.

Currently, Mohs surgery is used to determine the border of the non-pigmented nonmelanoma skin cancers and to remove them at the same time. In the surgery, thin layers of skin tissues are removed progressively and examined under a microscope until all the margins of the sample are free of cancer. It can remove as much of the skin cancer as possible, while doing minimal damage to surrounding healthy tissue. Since most of the nonmelanoma skin cancers occur on head, neck and back of hands, patients would like to remove the cancer with as little healthy tissue as possible. Therefore, Mohs surgery is widely used in hospitals nowadays. The cure rate is more than 90% [108, 109]. However, it is very time consuming. After the tissue removal, the patient needs to wait for the pathological results. If the margin of the sample still has cancer cells, the patient has to have another surgery. Therefore, a fast method that can determine the lateral extent of nonmelanoma skin cancers is needed.

1.2.3.2 Emerging Modalities

There has been much interest in recent years to develop imaging methods for skin cancer diagnosis.

Laser-induced fluorescence spectroscopy (LIF): LIF is a non-invasive technique used for detection of cancer in a variety of organ systems. It can be applied to detect non-melanoma skin cancers [110-112]. LIF relies on the innate fluorescence of several common biological constituents such as elastin, collagen, and flavin when excited by a light source. By measuring the fluorescence of tissue it can be possible to learn about the biochemical state of the tissue. Studies have shown that in vivo LIF at 410 nm excitation and using the intensity of emission signal is effective for detection of BCC and SCC. However, the accuracy depends on the color of the skin. In patients with dark skins, the dark color and weaker fluorescence intensity for normal skin will cause more overlap of normal and cancer spectra which will lead to high rate of false positive [111, 113].

High-frequency ultrasound (HIUS): HFUS with frequencies between 20-100 MHz has been investigated for non-invasive evaluation of skin cancers [114-119]. Images are obtained in vertical sections with penetration and resolution varying with respective frequencies. Lower frequencies (20 MHz) depict flat and regular surfaces effectively and have a penetration depth of 3.8 mm with an axial resolution of 39 μm and a lateral resolution of 210 μm. Higher frequencies provide excellent study of superficial structures and irregular surfaces with a resolution of 9.9 μm and 84 μm, but have a decreased penetration of 1.1 mm [120, 121]. It has been investigated to determine the lateral size and thickness of melanoma as shown in Figure 1.11, but studies have shown that it tends to overestimate melanoma thickness [118, 122]. HFUS has not yet been established for nonmelanoma skin cancer diagnosis in clinics.

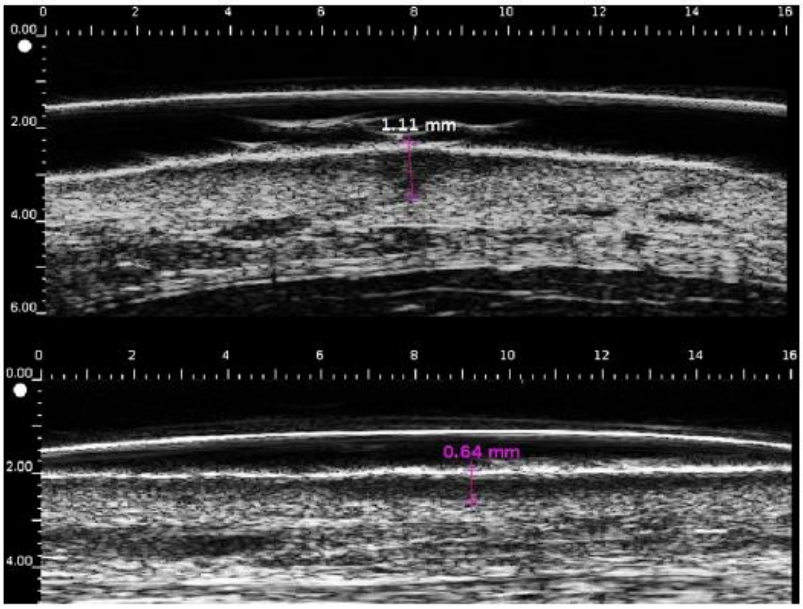

Figure 1.11 High frequency ultrasound imaging of two melanoma lesions [114]. Lesions were generally hypoechoic and well demarcated from the dermis.

Optical coherence tomography (OCT): OCT is a novel imaging technique based on interferometry. Comparing to HFUS, instead of sound wave, it uses infrared light. OCT has high depth resolutions (about 15 μm) and it has been shown that layers of skin and blood vessels can reliably be visualized using OCT. However, its penetration depth is only 1.0-2.0 mm [123-127]. It cannot be used to measure the thickness of melanoma deeper than 2 mm [128]. The basement membrane of skin cannot be distinguished, such that early tumor invasion cannot be determined by OCT. Preliminary studies have described the features of nonmelanoma skin cancers and suggested that this tool may aid in the diagnosis of nonmelanoma skin cancers [129]. An OCT image of a basal cell carcinoma and the corresponding histopathology of the same area (hematoxylin and eosin stain, magnification × 40) are shown in Figure 1.12 [130]. White arrow indicates a shadow in the OCT image. Black arrows point to

similar morphologies in the images. However, systematic studies evaluating the sensitivity and specificity of OCT for diagnosis are lacking [131].

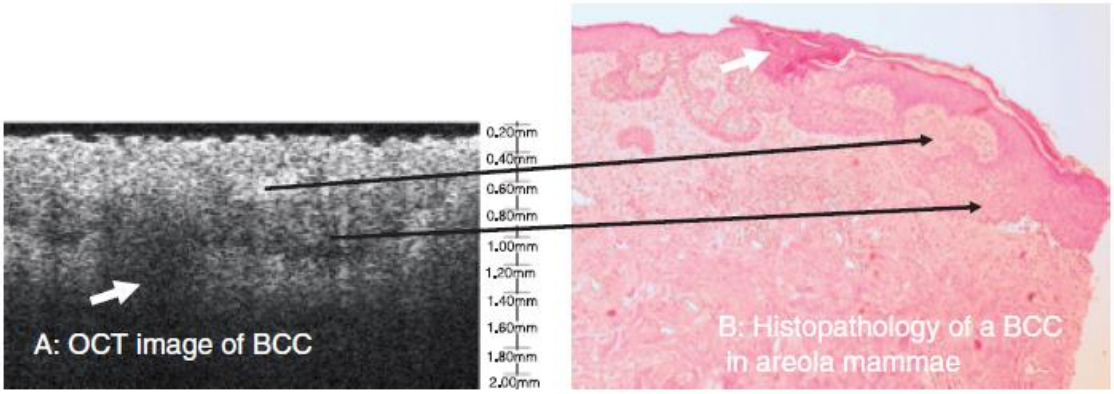

Figure 1.12 (A) An optical coherence tomography (OCT) image of a basal cell carcinoma; (B) Corresponding histopathology (hematoxylin and eosin stain, magnification × 40) from the same area [130].

In vivo confocal microscopy: *In vivo* confocal microscopy is an imaging modality for "optical sectioning" of tissue meaning the imaging of thin sections at high resolution and contrast without physically dissecting the tissue. It has two types: fluorescence confocal laser scanning microscopy (FLSM) and Reflectance mode confocal microscopy (RCM). In FLSM, exogenous fluorophores are injected and excited using a laser source. Emitted fluorescence is used to visualize the morphological details. RCM is based on the reflectance, scattering and absorption of monochromatic light by endogenous chromophores such as melanin, hemoglobin and other cellular microstructures. Both methods can visualize cellular and subcellular structures and can be comparable to routine histology. A RCM image of a basal cell

carcinoma and the corresponding histopathology of the same lesion are shown in Figure 1.13 [132]. It is clear that tumor nodules (TN) are separated from the dermal collagen by dark cleft-like spaces (red arrowheads). Dilated blood vessels (BV) are seen in the dermis. However, the penetration depth of *in vivo* confocal microscopy is only 0.2-0.25 mm [133]. Thus in vivo confocal microscopy is not able to visualize the depth invasion of skin tumors. Besides, this modality cannot evaluate lesions with significant hyperkeratosis (thickening of the stratum corneum).

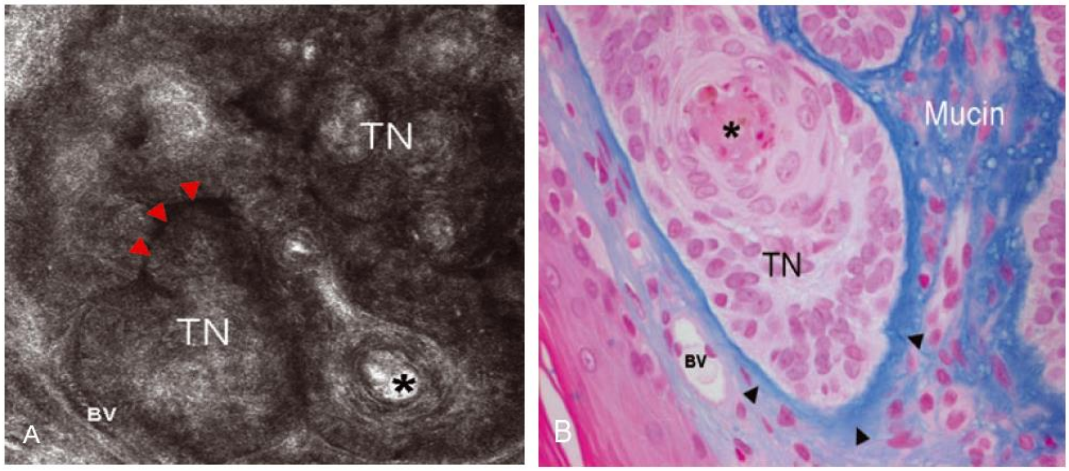

Figure 1.13 (A) A reflectance mode confocal microscopy (RCM) image of a basal cell carcinoma; (B) Corresponding histopathology of the same lesion [132].

1.2.4 Skin Tissue and Cancer Stiffness

To assess the mechanical properties of the skin, different noninvasive methods have been developed. The most commonly used methods are based on the measurement of suction [134], which requires applying a negative pressure to the skin, torsion and traction, by applying a linear displacement in the horizontal plane of the

skin. A tensile test, in which two tabs are glued to the skin and driven apart from each other, is also used to measure the mechanical behavior of skin. In the literature, the Young's modulus of the skin varies between 0.42 and 0.85 MPa for torsion tests [135], 4.6 and 20 MPa for the extension tests [136] and between 0.05 and 0.15 MPa for the suction tests [134, 137]. However, all these methods modify the natural state of stress on the skin during measurements and the values of mechanical properties might be affected.

The indentation and compression methods are also used to measure the stiffness of skin without prestressing the skin before the test. Geerligs et al. utilized a micro-indentation device with a spherical tip to measure the mechanical properties of the skin *in vivo*. Young's modulus of the skin was derived to be between 1 and 2 MPa using a numerical model [138]. Tilleman et al. investigated the elastic properties of cancerous skin tissues. It was reported that the average Young's modulus of 23 basal cell carcinoma tissue specimens was 52 kPa [139], while healthy skin has a stiffness of 100 to 2000 kPa [135, 137, 139]. Melanoma can be either softer or stiffer than normal skin [135, 140], depending on its malignancy. Therefore, there is a significant correlation between changes in tissue stiffness and abnormal pathological process. And thus, it is feasible to use stiffness contrast to differentiate cancerous tissues from normal skin.

1.3 Piezoelectric Finger (PEF)

Piezoelectric finger (PEF) is a piezoelectric cantilever, with two piezoelectric layers glued onto top and bottom of a stainless steel substrate, which can measure the

elastic modulus of a soft material or tissue using indentation method with the help of a cubic or cylindrical probe at the tip, all electrically.

PEF was invented in our laboratory at Drexel University. The initial work of PEF has been done by Markidou et al. [141], Szewzcyk et al. [142, 143], and Yegingil et al. [144-146].

Markidou et al. [141] developed a unimorph piezoelectric cantilever (as shown in Figure 1.14) to measure the elastic and shear moduli of samples that are equal to or smaller than cantilever contact area using compressive and shear tests. DC voltages were applied to the piezoelectric layer in the cantilever and the cantilever would bend due to inverse piezoelectric effect. The tip deflection of the cantilever was measured by a laser displacement meter. They found that at low DC voltages, the tip displacement of the cantilever was linear with the applied voltage, which made it possible to apply different DC voltages to the cantilever and obtain the deduced elastic and shear moduli of a sample from the stress vs. strain curve. They designed two kinds of tips: a straight tip to measure the elastic moduli via compression tests and an L-shape tip to measure the shear moduli via shear tests, as schematically shown in Figure 1.14 (a) and (b). Using gelatin and commercial rubber material as model soft tissues, they showed that the piezoelectric cantilever could measure the elastic and shear moduli of soft material samples in the small strain range (<1%).

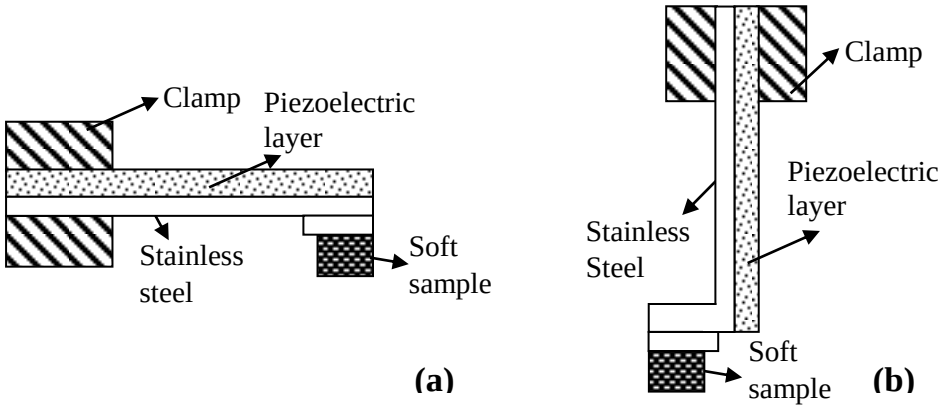

Figure 1.14 (a) A schematic of a piezoelectric unimorph cantilever for compression tests; (b) a schematic of a piezoelectric cantilever with an L-shape tip for shear tests.

Szewczyk et al. [142, 143] added another layer of piezoelectric material glued to the bottom of stainless steel. They named the initial top piezoelectric layer as "driving electrode" and the second piezoelectric layer as "sensing electrode" as shown in Figure 1.15. When a DC voltage were applied to the top driving electrode, the cantilever would bend and an induced voltage would be generated on the bottom sensing electrode due to direct piezoelectric effect. Szewczyk et al. investigated the relationship between the tip displacement of the cantilever and the induced voltage on the sensing electrode and found that they were linearly correlated. Using a straight tip the same with the one Markidou did, Szewczyk et al. did compression and flat punch indentation tests on soft samples. In the compression test, the surface area of the sample was equal to or smaller than the contact area of the tip as shown in Figure 1.15 (a), while in the indentation test the surface area of the sample was much larger than the contact area of the cantilever tip as shown in Figure 1.15 (b).

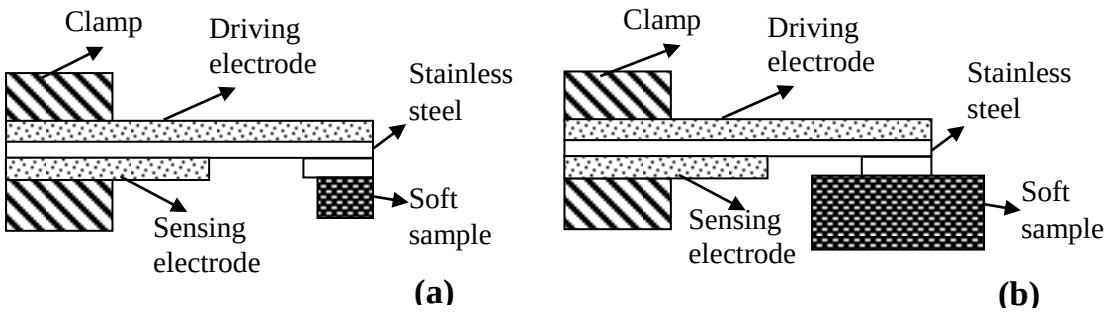

Figure 1.15 (a) A schematic of a piezoelectric bimorph cantilever in contact with a small sample in a compression test; (b) a schematic of a piezoelectric bimorph cantilever in contact with a large sample in an indentation test.

Yegingil et al. [144-146] combined the sensing electrode designed by Szewczyk et al. and the L shaped tip developed by Markidou et al. and developed a piezoelectric finger (PEF) which has two layers of piezoelectric material glued on the top and bottom of a stainless steel. It has a special designed square probe made with stainless steel so that the PEF can do both compression and shear tests within one sensor. As shown in Figure 1.16 (a) in compression tests, the PEF is held parallel to the sample, while in shear tests the PEF is held perpendicular to the sample as shown in Figure 1.16 (b).

Yegingil et al. carried out compression, shear, indentation and indentation shear tests on gelatin samples using PEF. In compression and shear tests, the surface area of the sample was equal to or smaller than the contact area of the tip, while in indentation and indentation shear tests, the surface area of the sample was much larger than the tip area. They showed that the elastic and shear moduli of the samples could be deduced either by the induced voltage measurements across the sensing piezoelectric layer. Later they constructed a model tissue consisting of modeling clay

imbedded in gelatin and performed PEF measurements on it. Two dimensional elastic and shear moduli maps were generated which could indicate the size and location of the clay inclusion accurately. Similar experiments were done on excised breast tissues and they found that PEF was capable of detecting tumors in them using the 2D modulus map, and that PEF could tell the malignancy of the tumor using the shear modulus (G) to elastic modulus (E) ratio, G/E [145]. Moreover, they investigated the depth sensitivity limit of a PEF and empirically determined that the depth sensitivity limit was twice the linear dimension of the indentation area (or probe width) [146].

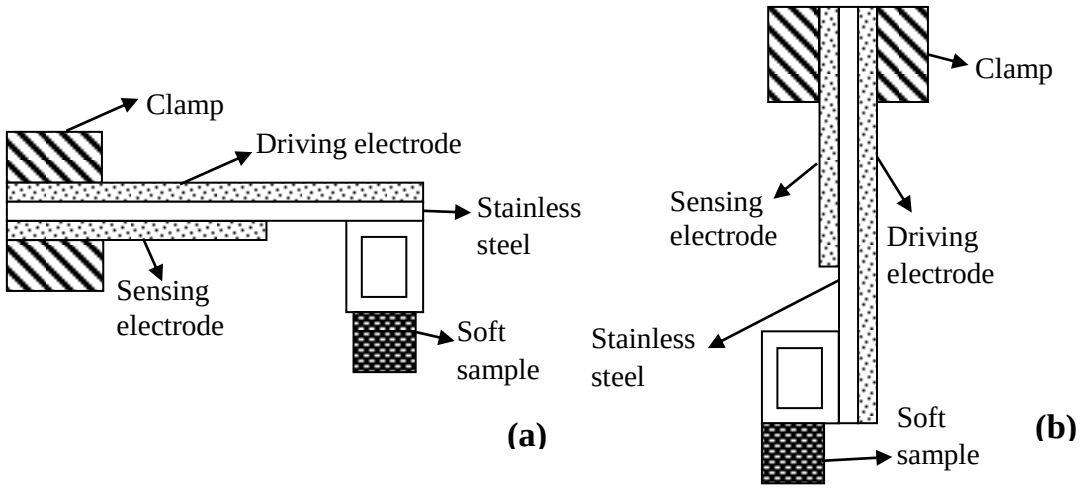

Figure 1.16 Schematics of a piezoelectric finger (PEF) with a special designed probe that can be used for both compression tests (a) and shear tests (b).

The PEF design uses 127 μm thick lead zirconate titanate (PZT) material (T105-H4E-602, Piezo Systems Inc., Cambridge, MA) for both piezoelectric layers and 50 μm thick stainless steel (Alfa Aesar, War Hill, MA) for the substrate the

square tip. The manufacturing, properties and characterization of the PEF will be explained in Chapter 3 in greater detail.

2. OBJECTIVES AND SPECIFIC AIMS

2.1 Motivations

Breast cancer is the most common type of cancer among women in the US. Early detection of breast cancer can result in better chances of effective treatment. Furthermore, accurate localization and sizing of breast cancer in three dimensions (3D) are important for biopsies, surgeries and monitoring response of chemotherapy and radiotherapy. Current breast tumor detection and localization methods include clinical breast examination (CBE, or palpation), ultrasound, mammography, and magnetic resonance imaging (MRI) but they all have limitations. For example, mammography, the FDA approved gold standard screening tool for breast cancer, has low sensitivity in tumor detection for dense breasts. The compression of breast during mammography testing may lead to distortions of the tumor locations and sizes. Ultrasound may underestimate the tumor size, leading to incomplete excision in lumpectomy. The emerging methods including the elastography [147-150], the BMI [69, 70], the ultrasound probe attachment [72], the TSIS [74, 75], and the VPBS [77, 78] do not measure tissue stiffness directly. Rather, they measure the stress or strain distribution on the surface and use an inversion technique or simulations to determine if there is a tumor and the location and size of the tumor, which requires much computation and time. In addition, all these methods have not been proven capable of detecting breast cancer in dense breasts. Therefore, a method that is capable of not only detecting breast tumors but also providing the locations and sizes without simulations is desired, especially for dense breasts.

Skin cancer, which is the uncontrolled growth of abnormal skin cells, is the most common form of cancer in the US. Most of nonmelanoma skin cancers, i.e. basal cell carcinoma (BCC) and squamous cell carcinoma (SCC) are non-pigmented, and thus it is difficult for dermatologists to determine the lateral extent of the cancers and remove them accordingly. The thickness of melanoma is one of the most important prognostic factors which will help the dermatologist decide the surgical margins. Currently, Pathological investigation is the current gold standard for skin cancer evaluation but it is tedious and time-consuming. A tool that can not only detect the skin cancer but also determine 3D profile is desired.

Meanwhile, it is well known that cancers have a different stiffness from normal tissue. Breast tumors are stiffer compared to the surrounding tissue and skin cancers can be either stiffer or softer than normal skin. Piezoelectric finger (PEF) is a tissue stiffness sensor that can measure the elastic modulus of tissues both *in vitro* and *in vivo*. Therefore, it is possible to detect and image tumors by contrasting the high (or low) elastic modulus regions with the surrounding tissues. Besides, a PEF with a larger contact area can assess the stiffness of tissues at a larger depth. It is thus possible to use PEFs with different contact sizes to deduce the depth profile of tumors.

There are many differences between breast cancers and skin cancers. Mechanically speaking, the normal breast tissue is quite uniform, while the normal skin has a layered structure with a stiff layer (epidermis and dermis) on top of a soft substrate (hypodermis). Breast tumors are stiffer than normal tissues and they are embedded in normal tissues. On the other hand, skin cancers can be either softer or

stiffer than normal skin and they start from the surface of skin and grow into deep tissue. The sizes of breast cancers and skin cancers are quite different. The breast cancer has a size of a few centimeters while the thickness of skin cancer is in millimeter and sub-millimeter scale. Thus, we may not apply the same method to deduce the depth profile of breast cancers and skin cancers.

2.2 Goal and Aims

2.2.1 Goal

The goal of the study is to not only detect breast tumors and skin tumors but also image their locations and sizes in 3D.

2.2.2 Objectives

The objectives of the study are (1) to use array piezoelectric fingers (PEFs) of the same contact area to provide a 2D tissue elastic modulus map to detect the breast tumor and the skin cancer by elastic modulus contrasts, and (2) to develop the methodology to determine the tissue depth profiles including cancer depth profiles by measuring the elastic modulus of tissue on the same spot using PEFs of various contact sizes.

2.2.3 Specific Aims

To achieve the goal and objectives, the study was organized into four specific aims as follows.

Aim 1: **Image breast tumors *in vivo* to generate a two dimensional (2D) elastic modulus map using an array of PEFs of the same contact sizes**.

- Develop a breast tumor detection system with a hand-held probe with 4×1 PEF array
- Validate the system on breast tumor models
- Perform *in vivo* breast tumor detection on 40 patients.
- Compare the detection sensitivity of PEF with mammography, especially for patients with dense breasts
- Determine the lateral size of breast tumor and compare with pathology

Aim 2: **Determine the depth profile of model breast tumors using the elastic modulus measurements from a set of PEFs of different contact sizes**

- Determine the depth sensitivity of a PEF empirically
- Use a 2-spring model to deduce the depth profile of bottom supported model breast tumors and compare with the actual values
- Compare spring model-based methodology with inversion simulations using finite element analysis (FEA)
- Extend the model to 3 springs and apply it to estimate the depth profile of suspended model breast tumors
- Image model breast tumors in 3D using the lateral and depth profile determined by PEF

Aim 3: **Simultaneous determination of the elastic modulus and thickness of skin (epidermis and dermis) using a set of PEFs of different contact sizes**

- Model the skin with a two-layer structure with a stiff layer representing the dermis on top of the soft hypodermis layer
- Couple PEF measurements with an empirical formula for a two-layer structure to determine the elastic modulus and thickness of dermis
- Validate the methodology using FEA with finite skin thickness
- Apply the methodology to skin phantoms and excised porcine skins

<u>Aim 4</u>: Determine both the lateral extent and depth profile of model skin cancers using a set of PEFs of different contact sizes

- Determine the lateral extent of model skin cancers using PEF with a small contact size
- Determine the depth profile of model skin cancers using PEFs with different contact sizes coupled with a modified 2-spring model
- Image skin cancers of clay embedded in porcine skins in 3D

3. IMAGE BREAST TUMORS *IN VIVO* USING PIEZOELECTRIC FINGER (PEF) ARRAY

In this chapter, a breast tumor detection system with a hand-held probe with an array of piezoelectric fingers (PEFs) of the same contact size is developed to image breast tumors in a two dimensional (2D) elastic modulus map. Breast tumor models consisting of modeling clays and gelatin matrix are constructed to validate the measurements by the PEF system. The system is then applied to perform *in vivo* breast tumor detection on 40 patients and the results are compared with mammography. The lateral sizes of detected breast tumors by PEF are compared with those provided by pathology.

3.1 Piezoelectric Finger (PEF)

3.1.1 Manufacturing of Piezoelectric Finger

Piezoelectric finger (PEF) has been briefly introduced in Section 1.3. The PEF has two piezoelectric layers, driving layer on the top and sensing layer on the bottom, as shown in Figure 3.1 (a). All the PEFs used are hand-built in our laboratory. The driving and sensing PZT layers used in the PEFs are lead zirconate titanate (PZT) 5H4E material (Piezo Systems Inc., Cambridge, MA), and both layers are 127μm thick. The stainless steel (Alfa Aesar, War Hill, MA), which is 50μm thick, is used as the substrate and the loop probe.

The PEF used in this chapter were all 6.5±0.5 mm wide. The lengths of driving and sensing PZT layers were 22±0.5 mm and 12±0.5 mm, respectively. The substrate stainless steel was 33±0.5 mm long. To make the PEF, the PZT layers were

bonded to the substrate stainless steel using a nonconductive epoxy (Henkel Loctite, Westlake, OH) at the edges and a small patch of conductive epoxy (ITW Chemtronics, Kennesaw, GA) at the center. The nonconductive epoxy was used so that there was no short circuit between the top and bottom electrodes of the PEF. After curing at room temperature overnight, a stainless steel strip was bent into a rectangular loop and glued to the free end of the cantilever using the same nonconductive epoxy. The stainless loops used in this chapter were 10 mm high, 6.5 mm wide and 6.5 mm deep. Wires were soldered on the top, bottom layers of the PZT and the stainless substrate. The PEF was then clamped to an acrylic fixture (as shown in Figure 3.1 (b)) made in the Drexel machine shop with 5 layers of scotch tapes (Scotch Magic tape, 3M, St. Paul, MN) as a spacer for further characterization.

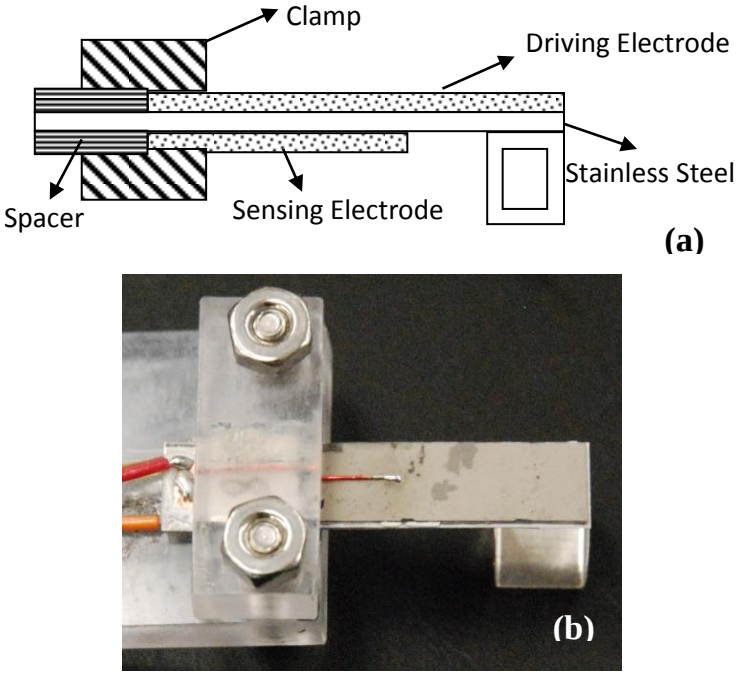

Figure 3.1 (a) A schematic of a piezoelectric finger (PEF); (b) A picture of the PEF.

3.1.2 Characterization of Piezoelectric Finger

3.1.2.1 Spring Constant Determination of PEFs

The effective spring constant (K) of a PEF is very important for its application in elastic modulus measurements since too low or too high value would not be suitable for tissue applications. Previous studies have indicated that the effective spring constant of the PEFs should be between 100 N/m to 400 N/m for soft material applications.

According to previous research results in our laboratory, the effective spring constant of a PEF can be theoretically calculated using the following formula [151]:

$$t_n = \frac{E_1 t_1^2 - E_2 t_2^2 - E_3 (t_3^2 + 2t_2 t_3)}{2(E_1 t_1 + E_2 t_2 + E_3 t_3)} \tag{3-1}$$

$$D = \frac{\begin{array}{l} 4E_1^2 t_1 + 4E_2^2 t_2 + 4E_3^2 t_3 + 2E_1 E_2 t_1 t_2 (2t_1^2 + 2t_2^2 + 3t_1 t_2) + \\ 2E_1 E_3 t_1 t_3 (2t_1^2 + 2t_3^2 + 3t_1 t_3) + 2E_2 E_3 t_2 t_3 (2t_2^2 + 2t_3^2 + 3t_2 t_3) + \\ 12E_1 E_3 t_1 t_2 t_3 (t_1 + t_2 + t_3) \end{array}}{12(E_1 t_1 + E_2 t_2 + E_3 t_3)} \tag{3-2}$$

$$K = \frac{3D^2 [w + (L_1 + L_2) L_1 L_2](3L_2 + w)}{3L_1} \tag{3-3}$$

where t_n is the neutral plane location, E_1, E_2 and E_3 are the elastic moduli of the top piezoelectric layer (i.e. driving electrode), middle stainless steel substrate, and the bottom piezoelectric layer (i.e. sensing electrode), respectively, t_1, t_2 and t_3 are the

thickness values of the top piezoelectric layer, middle stainless steel substrate, and the bottom piezoelectric layer respectively, D is the bending modulus, K is the effective spring constant of the PEF, w is the width of the PEF, and L_1, L_2 are the length of the section of the PEF with the bottom piezoelectric layer and the length of the section of the PEF with no sensing electrode, respectively. The elastic modulus E_1 and E_3 of the PZT and E_2 of the stainless steel are 62 GPa and 200 GPa, respectively.

By using the equations above, the theoretical effective spring constant of the PEF with the geometry described in Section 3.1.1 is 225.7 N/m. The effective spring constant of PEFs can also be measured experimentally. A set of weights were made to be hung on the tip of the cantilever. Using a laser displacement meter (LC-2450, Keyence Corporation, Osaka, Japan) mounted above the PEF we measured the tip displacement that resulted from hanging the weights on the free end of the cantilever. Since the effective spring constant K = F/d, where F is the force applied to the free end of the cantilever and d is the displacement of the cantilever tip, we determined K by calculating the slope of the linear curve that resulted from plotting the force applied by the weights versus the resulting displacement. As shown in Figure 3.2, the force is linear to the tip displacement (R^2 = 0.996) and the slope is 0.223. Therefore, the effective spring constant of that PEF is 223 N/m, which is very close to the theoretical value 225.7 N/m.

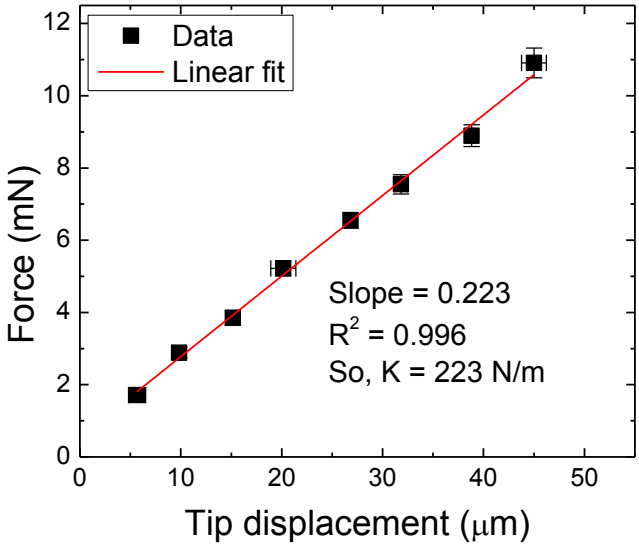

Figure 3.2 Force versus tip displacement of a PEF, whose driving electrode was 22 mm long, sensing electrode was 12 mm and width was 6.5 mm. The data was fit to linear function and the effective spring constant (K) is determined by the slope of the fit, which is 223 N/m, close to the theoretical calculation 225.7 N/m.

3.1.2.2 PEF Tip Displacement and Induced Voltage Measurements

The driving PZT bends when an electric field is applied to it, which in turn causes cantilever to bend and thus to generate an instantaneous induced voltage across the thickness of the sensing electrode. Since the PZT material is not absolutely insulated, the induced voltage peak decays to zero over time and can be monitored by an oscilloscope (Infiniium S4832D digital oscilloscope, Agilent, Palo Alto, CA). The magnitude of the induced voltage created is obtained by measuring the zero to peak value of the induced voltage.

The correlation between the PEF's tip deflection and the induced voltage production on the sensing electrode was investigated with the electric field (HP E3631A Triple Output Power Supply, Hewlett-Packard, Agilent, Palo Alto, CA)

applied to the driving electrode. The axial tip displacements and the corresponding induced voltages are plotted versus the direct current (DC) applied voltages of 6, 8, 10, 12, 14, 16, and 18 V for a 6.5±0.5 mm wide PEF in Figure 3.3. It demonstrates that as the magnitude of the applied voltage to the driving electrode of the PEF increases, the tip displacement and the induced voltage generated on the sensing electrode increases accordingly. It is also shown in the figure that both the PEF tip displacement and the induced voltage are proportional to the applied DC voltage. And thus, the induced voltage from the sensing electrode can be used to represent the tip displacement. A PEF can both apply a force and detect the corresponding displacement in one device using electrical means, offering the potential to palpate electrically on soft samples like a finger.

In Figure 3.4, the induced voltage from sensing electrode is plotted versus the corresponding axial tip displacement when DC voltages applied to the driving electrode were 4, 6, 8, 10, and 12 V with and without a soft sample. It shows that the induced voltage created on the sensing electrode is indeed linear to the tip displacement of the PEF (R^2 = 0.993). Besides, no matter whether there was a soft sample placed underneath the PEF or not, the slope of the induced voltage versus tip displacement remained the same, indicating the induced voltage can indeed be used to represent the tip displacement.

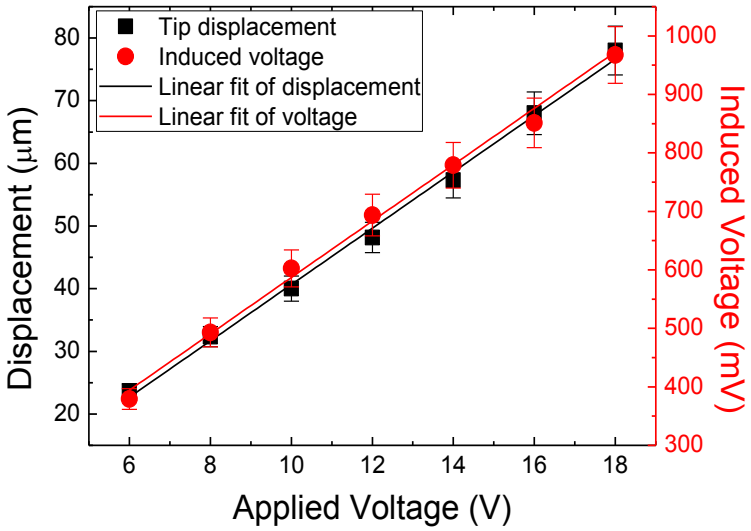

Figure 3.3 Tip displacement of the PEF and induced voltage from the sensing electrode versus direct current (DC) voltages applied to the driving electrode.

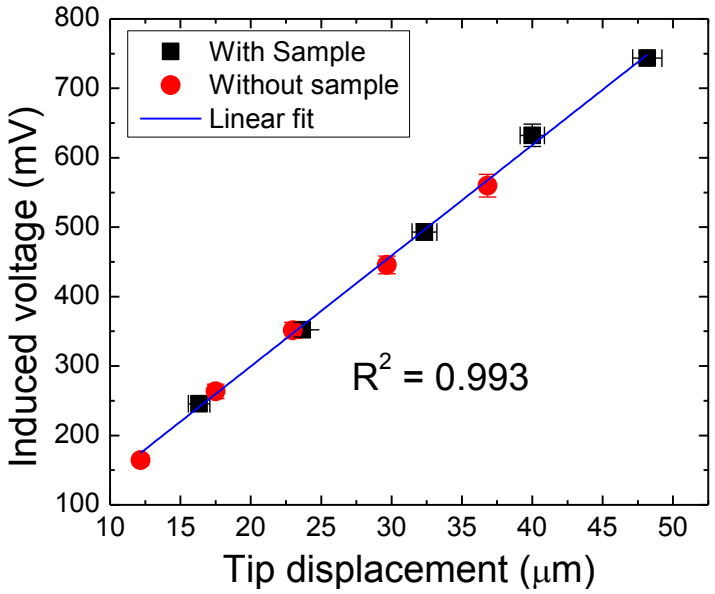

Figure 3.4 PEF induced voltage from the sensing electrode versus tip displacement with and without gelatin sample when direct current (DC) voltages were applied to the driving electrode.

3.1.3 PEF Indentation Elastic Modulus Measurements

A PEF measures the tissue stiffness as follows. Applying a direct current (DC) voltage to the top driving electrode of a PEF causes the PEF to bend due to the converse piezoelectric effect. Furthermore, the bending of the PEF generates an induced piezoelectric voltage in the sensing PZT layer. It has been shown in section 3.1.2.2 that the induced voltage is proportional to the PEF tip displacement, *d*. Therefore, the induced voltage can be used to represent the *d* [142, 144]. As a result, the elastic modulus, *E*, of the tissue is deduced as

$$E = \frac{1}{2}\left(\frac{\pi}{A}\right)^{1/2}\left(1-\nu^2\right)\frac{K(V_{in,0}-V_{in})}{V_{in}} \tag{3-4}$$

where $V_{in,0}$ and V_{in} are the induced voltages without and with the tissue, respectively, v is the Poisson's Ratio of the tissue, A is the contact area defined by the stainless steel square at the tip of the PEF, and K is the effective spring constant of the PEF.

To use Eq. (1) to deduce the elastic modulus at a particular location of the sample, a series of DC voltages, V_{ap}'s, were applied to a free PEF to obtain the corresponding induced voltages without the tissue, $V_{in,0}$'s. The PEF probe was then brought in contact with the sample. The same series of V_{ap}'s were applied to the PEF, and the corresponding set of induced voltages, V_{in}'s which were different from the $V_{in,0}$ were recorded. An example of d_0 and d measured by an LC-2450 laser displacement meter (Keyence, Itasca, IL) and induced voltages $V_{in,0}$ and V_{in} versus V_{ap} is shown in Figure 3.5 (a). To deduce the elastic modulus of the sample $(1/2)(\pi/A)^{1/2}\left(1-\nu^2\right)K(V_{in,0}-V_{in})$ was then plotted versus V_{in} as shown in Figure 3.5 (b).

The elastic modulus of the sample (gelatin in this case) was 8.4 kPa as determined by the slope of the curve. LabVIEW (National Instruments, Austin, TX) programming was used to conduct the measurement, record and plot the data, and deduce the E values, which will be explained in Section 3.2.2.

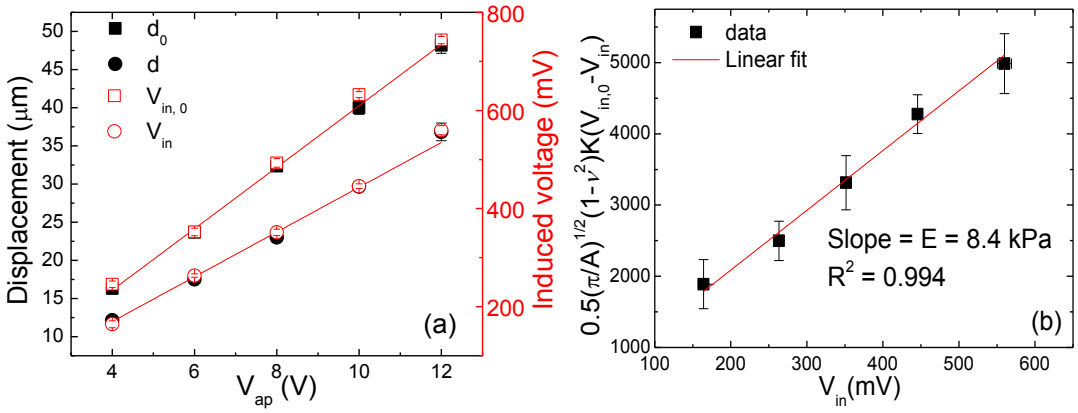

Figure 3.5 (a) The tip displacement and induced voltages from the sensing electrode without and with gelatin sample when the voltages applied to the driving electrode of PEF were 4, 6, 8, 10, and 12 V; (b) $0.5(\pi/A)^{1/2}(1-\nu^2)K(V_{in,0}-V_{in})$ versus V_{in}. The slope of the linear fitting is 8.4 kPa which is taken as elastic modulus of the gelatin.

3.2 PEF Array Breast Tumor Detection System

The capabilities of a single piezoelectric finger have been investigated in previous studies [144, 146, 151]. PEF has been tested on 77 cases of excised breast tissues [151] and demonstrated capable of detecting most types of breast tumors including invasive carcinoma (IC), hyperplasia, fibrocystic, ductal carcinoma in situ (DCIS), micro-calcifications and even a 3-mm satellite IC missed by mammography and by physician's palpation. To apply the PEF technique for breast tumor detection

in vivo, a system including a PEF array is developed. PEF array has the advantage of using more than one PEF to measure the elastic modulus of the soft sample or tissue at different locations simultaneously, which will provides faster measurements. Besides, it is a portable device that can be used in both laboratory and hospitals.

3.2.1 PEF Array Probe Design

A PEF compression array which consists of four 6.5±0.5 mm wide PEFs was developed. An acrylic box that is 51 mm in length, 51 mm in width, and 30 mm in height was designed to hold and protect the PEF array. As the PEF casing was hand-held by an operator who then pushed the bottom of the PEF casing against the breast to facilitate the PEF elastic modulus measurements, we positioned the probe surface to be slightly recessed from the bottom of the PEF casing (as shown in Figure 3.6) such that the pressure from the operator's pushing was exerted on the bottom of the casing but not the PEF probe surface. This allowed the probe surface of a PEF which is at the free end of the cantilever to be free from the pressure. Therefore, the elastic modulus measurement of a PEF would be insensitive to the pressure the operator applies to the housing of the device.

During tests, the wires soldered on the driving and sensing electrodes should not be pulled, otherwise the moving wires may bring noise to the measured induced voltages. To solve this problem, two copper foil squares with a length of 4 mm and a width of 3 mm were glued on the top and bottom of stainless steel substrate at the end of the PEF using nonconductive epoxy as illustrated in Figure 3.6. Wires with one end soldered on the driving and sensing electrodes were soldered on the two copper

foils on the top and bottom of stainless steel, respectively. The copper foil acts as a connector and another wire soldered on the copper foil connected it to the DB-25 connector at the rear of the housing box. During measurements, the DB-25 connector would be connected to the electrical controller and the electrodes of the PEF would not be moving.

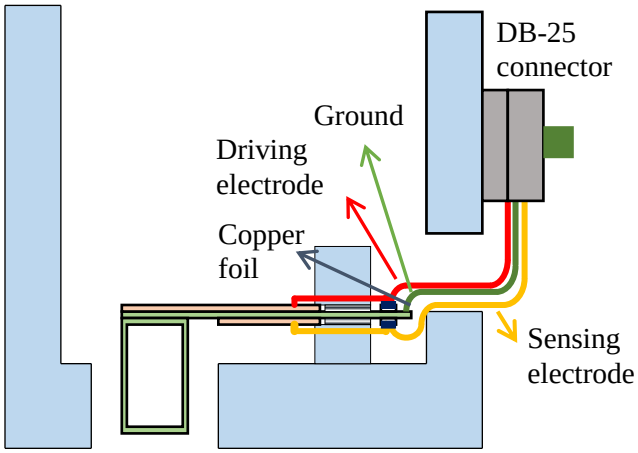

Figure 3.6 A schematic of the cross section of the PEF array and its housing box

3.2.2 Instantaneous Modulus Measurement by LabVIEW Program

In previous studies of PEF, applying DC voltages to the driving electrode of PEF using DC power source, measuring induced voltages from the sensing electrode of PEF using oscilloscope, and calculating the elastic moduli were all done manually. Controlling the equipment to acquire data (applied voltages and induced voltages) manually is very tedious and time consuming, and also involves post analysis of data to obtain the measured moduli. However, *in vivo* experiment requires faster

controlling, data acquisition and calculation because of the limited time during the experiments in the hospital.

To speed up the measurements, a circuit board was designed by M Squared Electronics. The circuit board could output a stimulus pulse that can range from 0 – 30 V DC to apply voltages to PEFs. It is also able to measure the induced voltages from the sensing electrode of a single PEF. It communicates with computer using RS-232 serial port and responds to a set of ASCII commands.

A software program was developed to control the circuit board, record the data, and do further calculation and analysis. LabVIEW (National Instrument) was chosen because the built-in user interface components (such as buttons, graphs, etc.) and the large library of drivers for data acquisition require less programming. The front panel of the written LabVIEW code is shown in Figure 3.7. The DC voltages that will be applied to the sensor, the Poisson' ratio, ν, of the sample, the effective spring constant, K, of the PEF are required as the input of the LabVIEW code.

The flow chart of part of the program to control the circuit board to apply a voltage to the driving electrode and read the response from the sensing electrode is illustrated in Figure 3.8. The magnitude of the applied voltage is input by the user and sent to the circuit board. Then the program takes a short break (380 ms) to wait for the board to be ready. After applying the previous set voltage to the driving electrode, the board will measure the induced voltage and return the value to the program using a range of 0000 to 1023 counts. The actual sensor voltage can be calculated using the

returned counts. After calculation, the buffers will be cleared for future inputs and outputs.

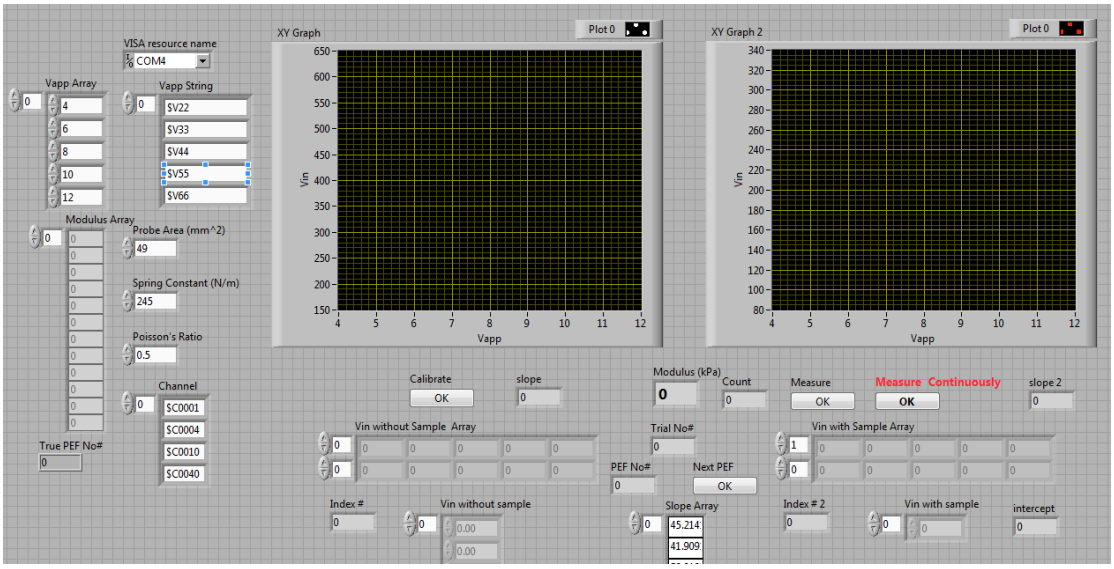

Figure 3.7 The front panel of the LabVIEW program for elastic modulus measurement.

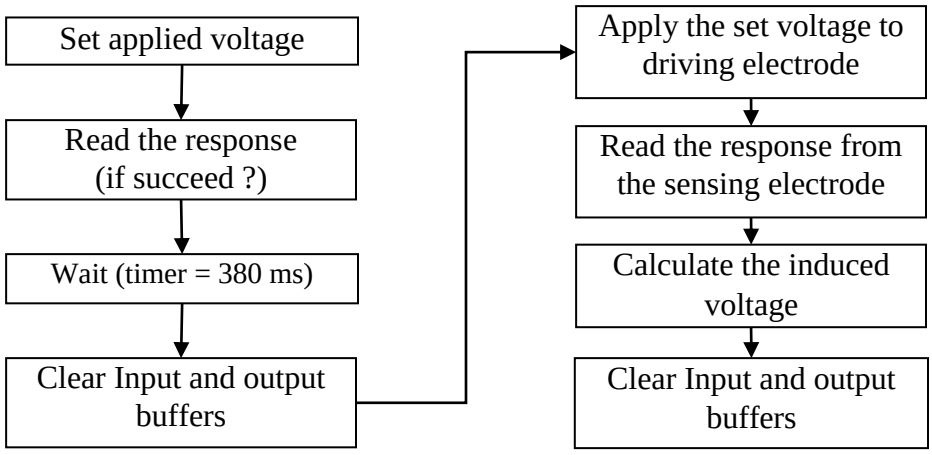

Figure 3.8 The flow chart of the program to control the circuit board for applying a voltage to the driving electrode of PEF and measuring the induced voltage from the sensing electrode.

The software program is able to calibrate the PEF by obtaining the induced voltage without any sample underneath the hand-held probe with the applied DC voltages which are the input by the user. After placing the hand-held probe on the sample and click the ‘measure’ button on the panel of the software, the program will send the command to the circuit board to apply voltages to the driving electrode of each PEF in the array and read the induced voltage from the sensing electrode of the same PEF sequentially, and calculate the modulus and record the data in the excel datasheet. Each PEF will do three repeated measurements and an average of the elastic moduli is calculated and recorded as well. The flow chart of the measurement part of the software is shown in Figure 3.9.

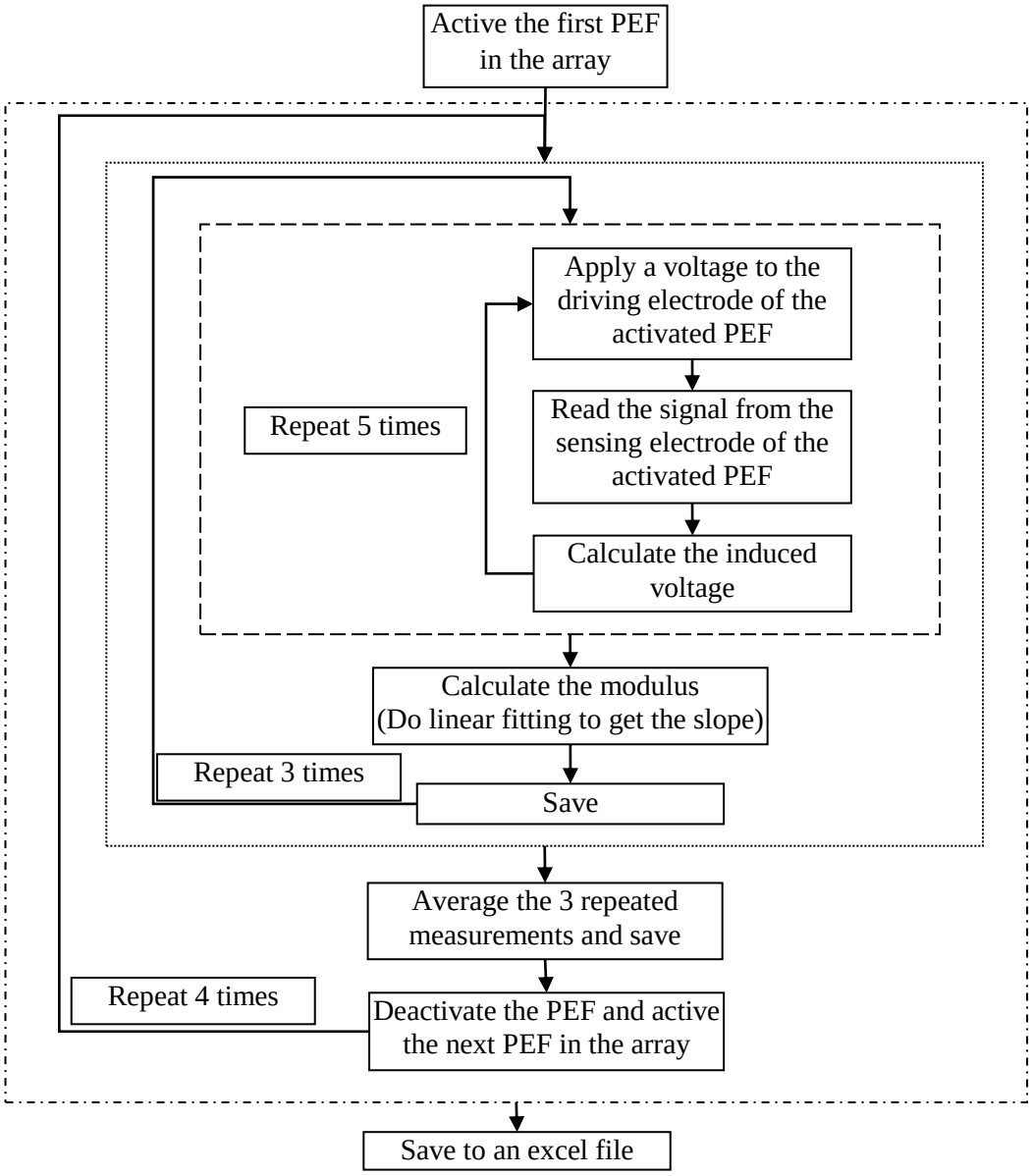

Figure 3.9 The flow chart of the measurement part of the program

3.2.3 Breast Tumor Detection System

The PEF breast tumor detection system consists of a hand-held 4×1 PEF array probe, a custom-build electronic board, and a laptop computer as shown in Figure 3.10. The electronic board, designed and fabricated by M Squared Electronics, worked to generate the applied voltages on the driving PZT of a selected PEF and to read the induced voltages from the sensing PZT of the PEF. It communicates with the laptop through a RS232-USB port. Figure 3.11 (a) and (b) shows a top and bottom view of the PEF array unit. As can be seen from Figure 3.11 (b), the bottom surface of the handheld unit was mostly flat to flatten out tissues surrounding the area under testing and make sure that the contact area of each of the four PEF was fully in contact with the tissue. Note that because the PEFs were in a cantilever geometry they had only one end fixed to the housing, which is different from sensors in "SureTouch" [68-70] that have all edges fixed to the housing of the device. This allowed the probe surface of a PEF at the free end of the cantilever to be free from the pressure exerted on the housing as long as the PEF was "recessed" from the bottom surface of the housing. Such an arrangement allows (1) protection of the PEFs from unintentional touching of the PEF tip which can damage the PZT layer and (2) desensitization of the PEFs from the pressure exerted by the hand on the housing against the breast (see Section 3.3.4). Figure 3.12 shows that the PEF array breast tumor detection system is performed on patients in a supine position. We define the maximum depth over which the elastic modulus of the tissue could be measured by the PEF as the depth sensitivity of the PEF. It has been shown in an earlier study [146]

that the depth sensitivity of a single PEF was all about twice the width of the contact area and independent of the inclusion elastic modulus values. Therefore, the current PEF with a 6.5 mm wide contact area had depth sensitivity about 13-15 mm. By further pushing the probe housing 6 mm (see Section 3.3.4) on the skin, the measurement can reach a depth of 2 cm, which was sufficient for detecting tumors in a normal-size breast as indicated by the results from the *in vivo* study below. For larger breasts and deeper tumors, PEFs with a larger contact width can be used, which was not within the scope of the present study.

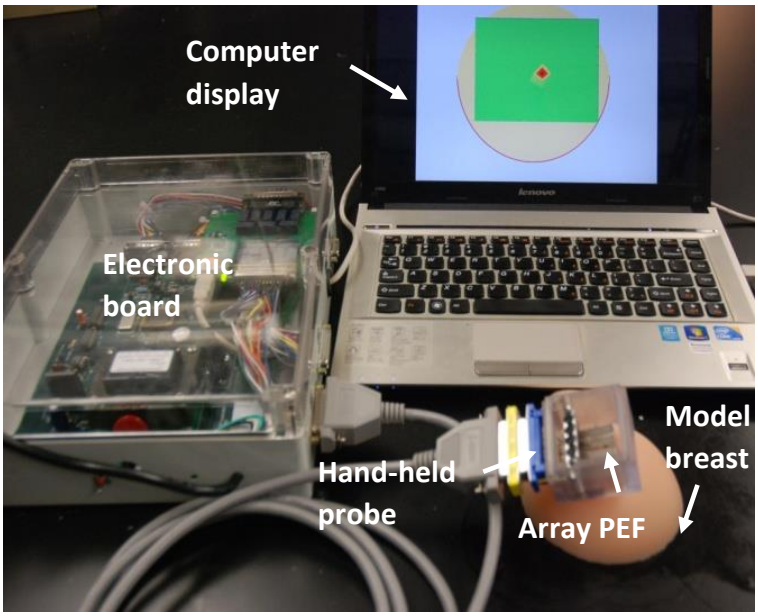

Figure 3.10 A photograph of PEF array breast tumor detection system which consists of PEF probe, electronic board, and a laptop for control and display.

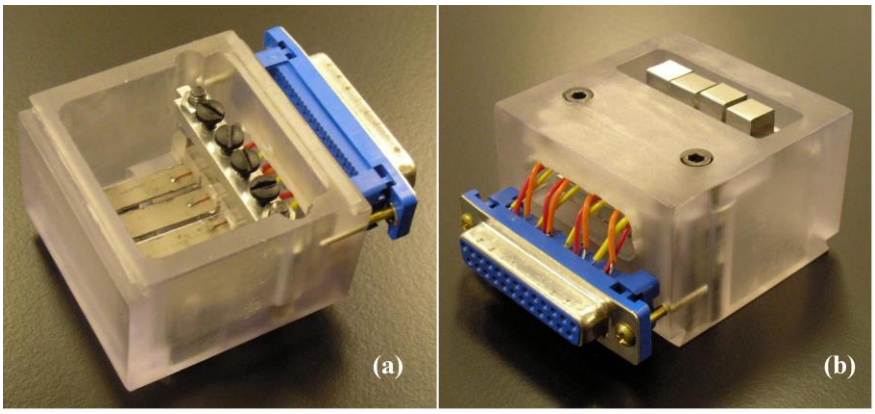

Figure 3.11 (a) The top view of the PEF probe; (b) the bottom view of the PEF probe

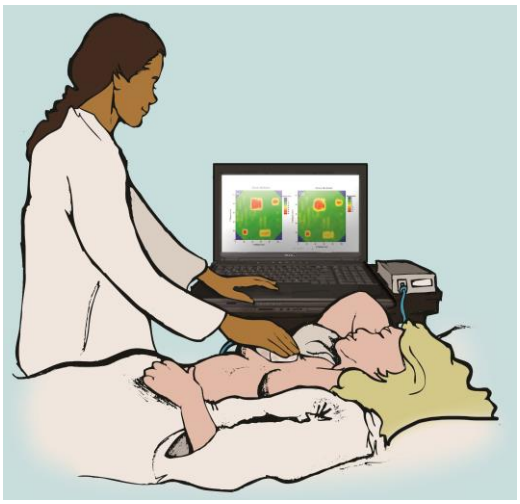

Figure 3.12 A schematic showing how the PEF breast cancer detection system was performed on patients

3.3 Measurements on Model Breast Tumor Samples

Breast tissue models with varying sizes and geometries of tumors were made and the PEF array breast tumor detection system was utilized to measure the elastic moduli of samples to investigate the accuracy of PEF measurements and validate the technique.

3.3.1 Model Breast Tumor Samples

Model breast tissue samples consisting of a gelatin (Now Foods, Bloomingdale, IL) matrix with model tumors of modeling clays (Crayola, Easton, PA) were prepared. The concentration of the gelatin matrix was 0.10 g/ml and its elastic modulus was similar to that of normal breast tissues, about 10 kPa [151-154]. The model clay was chosen because its elastic modulus of 60 kPa was similar to those of breast tumors measured *ex vivo* using PEF reported in Ref. [151]. In addition, these choices were consistent with the elastic modulus values of normal breast tissues and those of breast tumors reported in the literature, which were 3-33 kPa and 6-107 kPa, respectively [81, 83, 155-158] as shown in Table 2.2.

The gelatin matrix was prepared by mixing the gelatin powder in water with the concentration of 0.10 g/ml at 80 °C on the hot plate and stirring for 10 minutes. Then a part of the gelatin was slowly poured into the mold to avoid any bubbles which might introduce modulus variation inside the gelatin matrix. After pouring gelatin into the mold, it was cooled in 4 °C refrigerator for 10 minutes to solidify. Models clays were made into desired sizes and geometries to mimic the tumors and placed on the solidified gelatin in the mold. Afterwards, the rest of the gelatin was slowly poured into the mold and then cooled in 4 °C refrigerator for 10 minutes to solidify. The sample was taken out of the refrigerator and allowed to equilibrate at room temperature for 1 hour prior to the measurements. The gelatin was discarded after it was used for the day and a fresh gelatin sample was made every time.

An example of the model breast sample with four suspended model tumors of green modeling clay (seen in Figure 3.13 (a)) was prepared and shown in Figure 3.13 (b). The diameters of model tumors were 11.5±0.3mm, 10.3±0.3mm, 7.8±0.2mm, and 6.2±0.2mm, respectively. The depths of model tumors—which measure how far the top of the model tumors were under the gelatin surface—were 6.8±0.4mm, 9.3±0.3mm, 8.0±0.3mm, 5.5±0.2mm, respectively.

3.3.2 Scanning Model Breast Tumor Sample

Before the scanning using the PEF array breast tumor detection system, a grid was drawn on the model surface for location tracking. The PEF probe was then placed on the first location and the elastic modulus measurements were performed by activating the four PEFs sequentially. Each elastic modulus measurement required five applied voltages to the driving PZT of a PEF and deducing the elastic modulus as the slope of $(1/2)(\pi/A)^{1/2}(1-\nu^2)K(V_{in,0}-V_{in})$ versus V_{in} as described in Section 3.1.3. Three repeated elastic modulus measurements were made for each location to obtain an average elastic modulus and standard deviation.

Using the average elastic modulus, E obtained at each location, a color-coded E map was then created to visualize where and how big the tumor was. As an example, Figure 3.14 shows a color-coded elastic modulus map of the model tissue shown in in Figure 3.13 where the green color represents the elastic of the gelatin matrix while the red color represents the elevated elastic modulus of the modeling clay. The actual locations of the tumors are marked by the black circles. As can be seen, the higher modulus regions in the map were consistent the sizes and locations of

the model clay inclusions. PEF array system indeed detected all the model tumors. The locations of model tumors determined by the PEF array system also agreed with their actual locations. Therefore, the PEF array breast tumor detection system is capable of locating and sizing a hard inclusion embedded in a soft material.

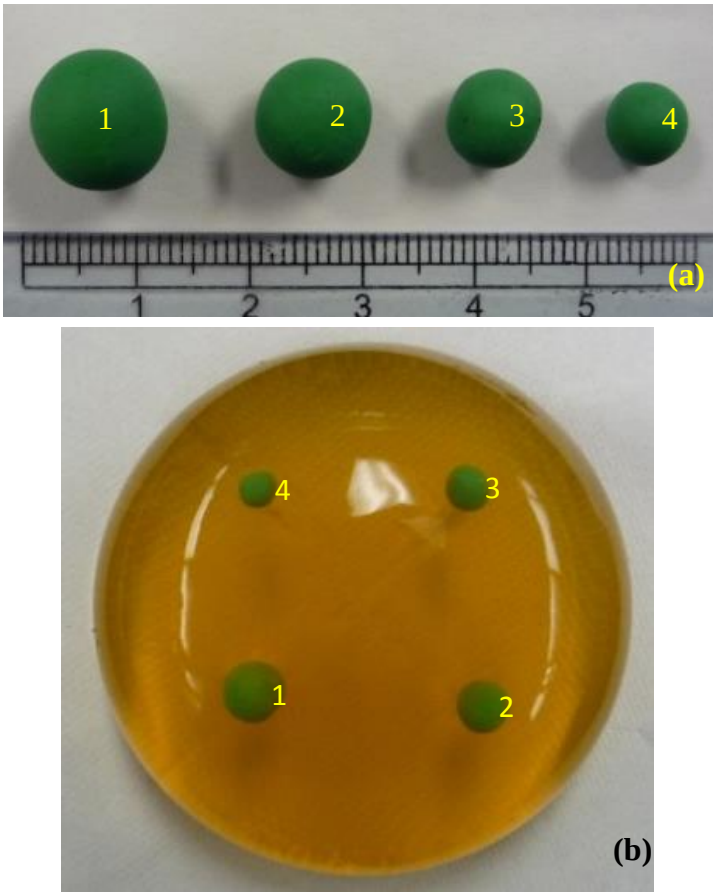

Figure 3.13 (a) Model tumors 1, 2, 3, and 4 made of green modeling clay. The diameters of the model tumors were 11.5±0.3 mm, 10.3±0.3 mm, 7.8±0.2 mm, 6.2±0.2 mm, respectively; (b) a photograph of the model breast made of gelatin with the four model tumors suspended in it. The distances from the top of the model tumors to the gelatin surface were 6.8±0.4 mm, 9.3±0.3 mm, 8.0±0.3 mm, 5.5±0.2 mm, respectively.

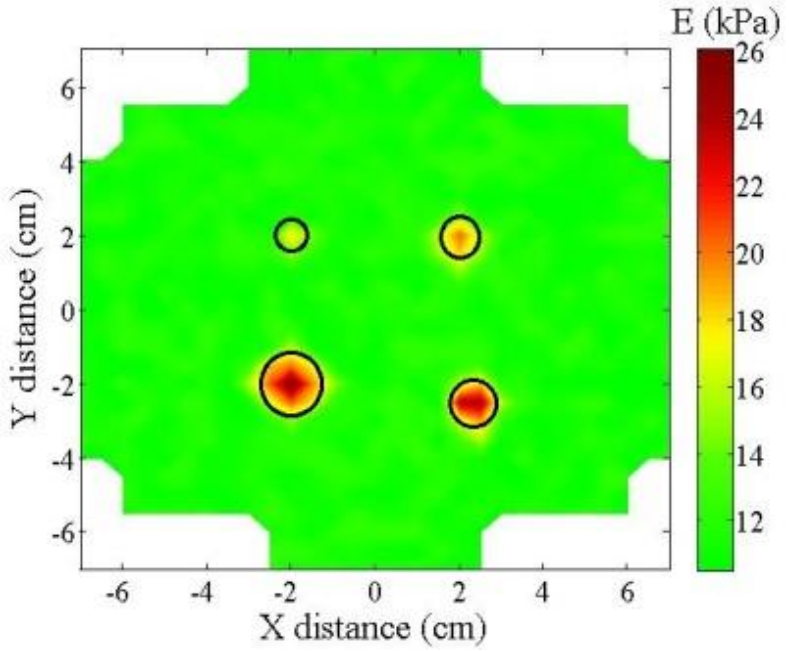

Figure 3.14 Elastic modulus map of the model breast of gelatin with clay model tumors shown in Figure 3.13 scanned by the PEF breast tumor detection system. The actual locations of the tumors are marked with black circles.

3.3.3 Lateral Tumor Size Determination

To determine the size of the tumor at a certain x distance, the elastic modulus at that x distance was plotted versus y distance. As an example the elastic modulus of Tumor 1 in the model breast sample shown in Figure 3.13 at x = -2 cm is plotted versus y distance in Figure 3.15. The model tumor had a diameter of 11.5±0.3 mm and a depth of 6.8±0.4 mm inside the gelatin. The data was then fitted to a Gaussian distribution (red line in the figure). The size of the tumor at x = -2 cm was determined to be the width at the half peak height of the Gaussian fit, 13.1 mm. The half peak height method takes the elastic moduli of the surrounding matrix and those over the inclusion into the consideration. In this example, the half peak is 18.4 kPa which is

calculated by averaging the elastic modulus of the gelatin matrix (baseline of the Gaussian fit, 11.6 kPa) and the elastic modulus of the peak position in the Gaussian fit, 25.2 kPa. The width of the bell shaped curve at the half peak provides the size of the tumor at x = 2 cm. It is understandable since the half peak of the modulus is obtained when the PEF is scanning over the edge of the tumor where half of the PEF is over the tumor and the other half of the PEF is over the gelatin matrix. That is way we use the width of the half peaks of the Gaussian fit to determine the tumor size.

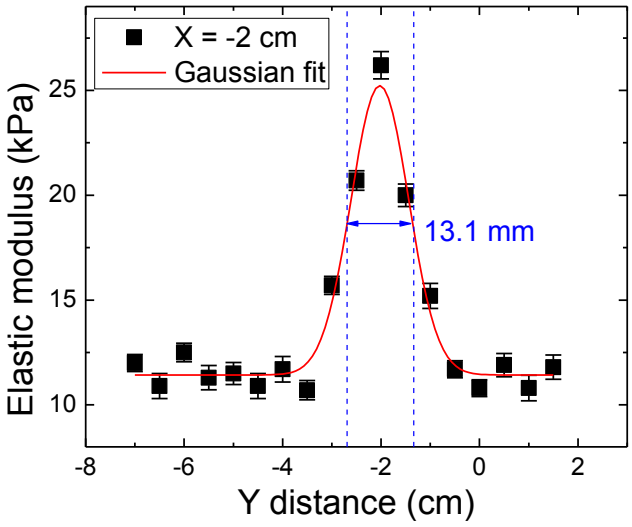

Figure 3.15 The measured elastic modulus versus Y distance at X = -2 cm extracted from the 2D elastic modulus map shown in Figure 3.14. The size of the tumor taken as the width at the half peak height of the Gaussian fit was 13.1 mm.

The lateral sizes of the model tumors as determined by the widths of the half peak heights are listed in Table 3.1. Also shown were the actual sizes measured with a caliper. The sizes estimated by PEF were larger than the actual ones by about 1-2 mm in the direction parallel to the PEFs and by about 1.5-3 mm in the direction

perpendicular to the PEFs. The larger errors in the direction perpendicular to the PEFs were presumably due to the larger interval perpendicular to the PEF array— 1 cm as opposed to the 7.5 mm in the parallel direction— between two adjacent measurements.

Table 3.1 (a): The sizes of model tumors in Figure 3.13 measured in the direction parallel to the PEF array.

Model Tumor	Size in the direction parallel to the PEF array		
	Measured	Actual	Error
1	13.1±0.6 mm	11.5±0.3 mm	1.6 mm
2	12.2±0.5 mm	10.3±0.3 mm	1.9 mm
3	9.1±0.7 mm	7.8±0.2 mm	1.3 mm
4	7.0±0.5 mm	6.2±0.2 mm	0.8 mm

Table 3.1 (b): The sizes of model tumors in Figure 3.13 measured in the direction perpendicular to the PEF array.

Model Tumor	Size in the direction perpendicular to the PEF array		
	Measured	Actual	Error
1	13.0±0.5 mm	11.5±0.3 mm	1.5 mm
2	13.0±0.6 mm	10.3±0.3 mm	2.7 mm
3	10.7±0.5 mm	7.8±0.2 mm	2.9 mm
4	8.1±0.6 mm	6.2±0.2 mm	1.9 mm

3.3.4 Depression Depth

As the PEF casing was hand-held by an operator who then pushed the bottom of the PEF casing against the sample to facilitate the PEF elastic modulus measurements, different operators would not use the exact the same force. And

therefore, they would have different depression depths in the samples during measurements as illustrated in Figure 3.16.

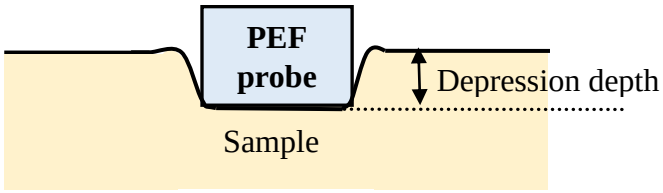

Figure 3.16 A schematic of the probe of PEF being pushed in with a depression depth during the measurement

The effect of the depression depth has been examined in model tissues, which showed the size of the tumor determined by the PEF was essentially the same when the depression depth was 4 mm or larger. As an example, we show the photograph of a model breast tumor consisting of a suspended model clay inclusion embedded in gelatin in Figure 3.17 (a). The measured elastic modulus maps in green (for the elastic modulus of the normal tissue) and red (for the elastic modulus of the tumor) obtained using the PEF array breast tumor detection system with a 2-mm, 4-mm, and 6-mm depression depth are shown in Figure 3.17 (b)-(d), respectively. The actual size of the model tumor was 2.0 cm in the x (horizontal) direction and 2.1 cm in the y (vertical) direction. The distance from the top of the tumor to the gelatin surface was 8.4±0.4 mm.

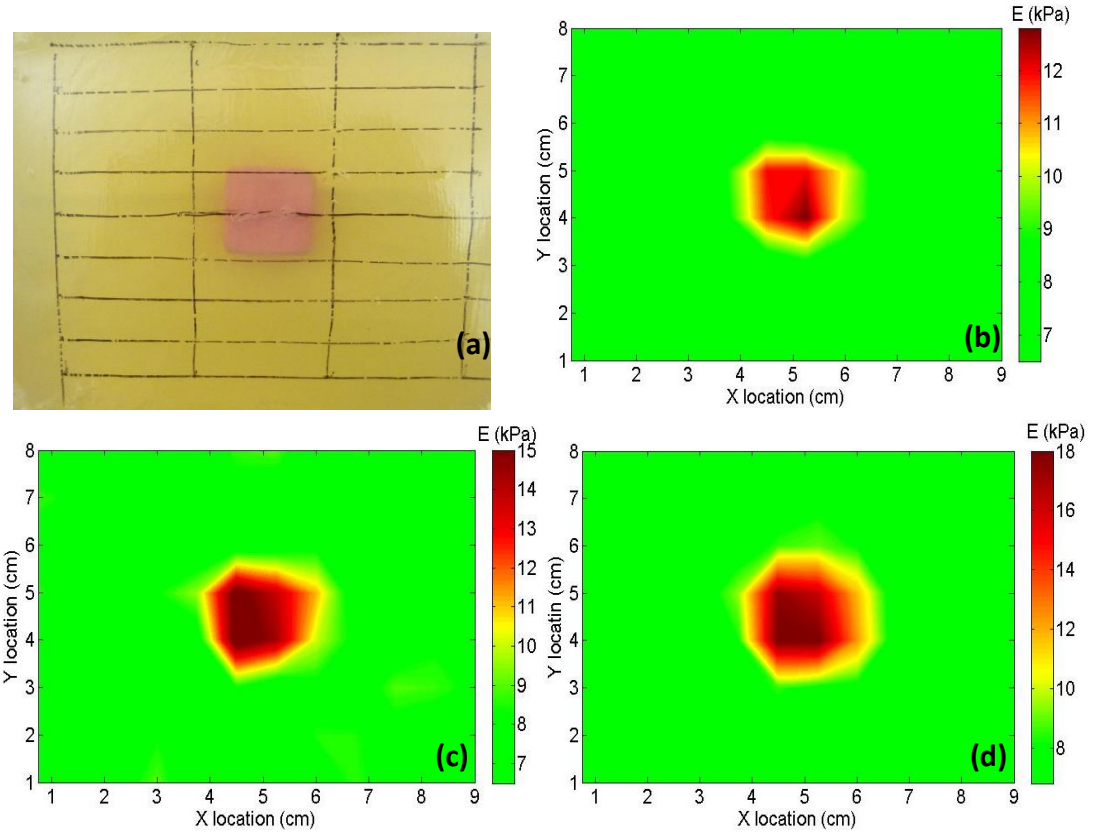

Figure 3.17 (a) A photography of the model tissue consisting of a suspended modeling clay in gelatin where the distance from the top of the tumor to the gelatin surface was 8.4±0.4 mm; elastic modulus map of the model tissue as measured by the PEF array with a (b) 2-mm, (c) 4-mm, and (d) 6-mm depression depth.

To determine the size of the tumor in the x and y directions we examined the x- and y-elastic modulus profile around the tumor as follows. As an example, the elastic modulus profile versus x distance at y = 4 cm with 2-mm, 4-mm, and 6-mm depression depths is shown in in Figure 3.18. The elastic modulus profiles were then fit to a Gaussian form as indicated by the solid lines in the figure. The size of the tumor was then taken as the width of the Gaussian function at half the peak height. Using this method, we found the tumor size at y = 4 cm was 1.7±0.1 cm, 1.9±0.2 cm,

and 1.9±0.1 cm with a 2-mm, 4-mm, and 6-mm depression depth, respectively. As can be seen, with an experimental uncertainty of 0.2 cm, the estimated tumor size was essentially the same for all depression depth, which was especially true when the depression depth was 4 mm or larger. Also note that the estimated tumor size was very close to the actual tumor size in the x direction, 2 cm, indicating the accuracy of the methodology. Moreover, the base of the Gaussian curves which represented the elastic modulus of the normal tissue remained the same regardless of the depression depths, indicating that the elastic modulus of the normal tissue was independent of the depression depth.

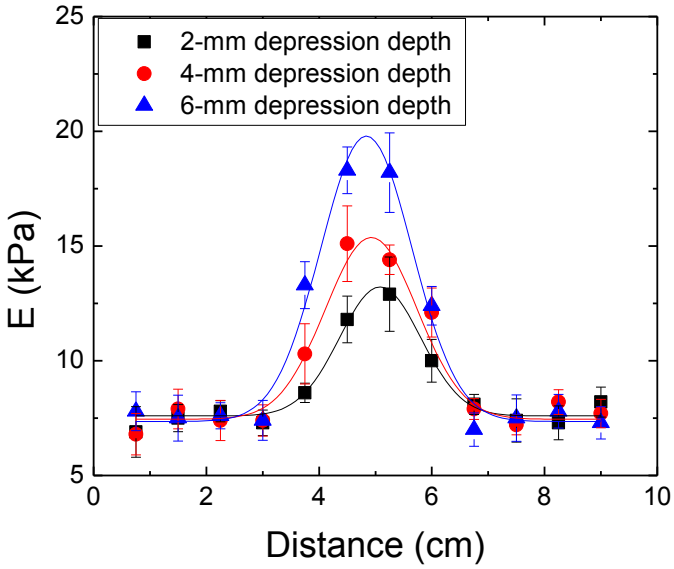

Figure 3.18 Elastic modulus versus x distance at y = 4 cm of the tumor shown in Figure 3.17 obtained with a 2-mm, 4-mm and 6-mm depression depth. The solid lines represent the Gaussian fits of the elastic modulus profiles. The sizes of the tumors were determined as the widths at half the peak height of the Gaussian fits as 1.7±0.1cm, 1.9±0.2cm, and 1.9±0.1cm for 2 –mm, 4-mm, and 6-mm depression depths, respectively.

The above conclusion for the model tumor shown in Figure 3.17 and for its x-elastic modulus at y = 4 cm have been applied to other model tumors and their x- and y-elastic modulus profiles as well. Therefore, it suffices to say that the tumor size estimated with half peak method was independent of the depression depth and close to the actual tumor size.

3.3.5 PEF simultaneous measurements

Although one advantage of using a PEF array is that all PEFs can carry out measurements simultaneously, during the measurements mentioned in Section 3.3.2 the PEFs in the array were activated sequentially to avoid the interference by the neighboring PEFs when more than one PEF were activated simultaneously. Studies have been done to investigate the interference of neighboring PEFs when they were doing the measurements at the same time.

A pure gelatin sample with a concentration of 0.08 g/ml was made in this study. The PEF array hand-held probe was placed on the sample. PEFs were activated sequentially to measure the elastic modulus of the pure gelatin: the first PEF (PEF#1) in the array was activated and did the measurement, after that PEF #1 was deactivated and the second PEF (PEF #2) was activated to the measure the modulus. It continued until the fourth PEF (PEF #4) finished measuring. The hand held probe was then moved to the next location and the same procedure was performed. The moduli read from each PEF were averaged and are shown as black bars in Figure 3.19.

When two PEFs were activated simultaneously, there were two options. One was that two adjacent PEFs were activated at the same time: voltages were applied to PEF #1 and #2 at the same time and induced voltages from these two PEFs were obtained. Afterwards, PEF #3 and #4 were activated at the same time and the same tests were done. The moduli measured from each PEF are shown as red bars in Figure 3.19. The other one was that two alternate PEFs were activated: voltages were applied to PEF #1 and #3 simultaneously and modulus measurements were done by them. Then PEF #2 and #4 were activated at the same time.

Four PEFs could also be activated at the same time. The measured elastic moduli from each PEF were averaged and plotted in Figure 3.19 as well. When a single PEF was activated each time, the measured elastic modulus of the gelatin sample was about 8 kPa. When two PEFs were activated at the same time, the measured elastic modulus was a little smaller, about 7 kPa. However, when four PEFs were doing the measurement simultaneously, the calculated elastic modulus was only about 4 kPa. Therefore, it can be conclude that when PEFs were activated simultaneously the measured elastic moduli were different from those measured when PEFs were activated sequentially. It is quite reasonable. When voltages were applied to multiple PEFs, they bent at the same time pressing the sample and thus created an extra stress and strain in the sample. Therefore, the PEF would generate a different modulus values. The elastic moduli measured by two alternate PEFs were slightly larger than those by two adjacent PEFs, because the neighbor PEF would cause a larger effect on the location of the sample that is being measured. Besides, the PEFs

in the center (PEF #2 and #3) would give smaller modulus values than the PEFs at the end (PEF #1 and #4). It is due to the fact that the PEFs at the end had only one neighbor PEF, while the PEFs in the center had two neighbor PEFs and would receive more interference from them.

Although using a PEF array has the potential to carry out measurements simultaneously, in the current study PEFs were activated sequentially. Studies using a PEF array that can mitigate the interference of neighboring PEFs and carry out simultaneous measurements can be a future study topic.

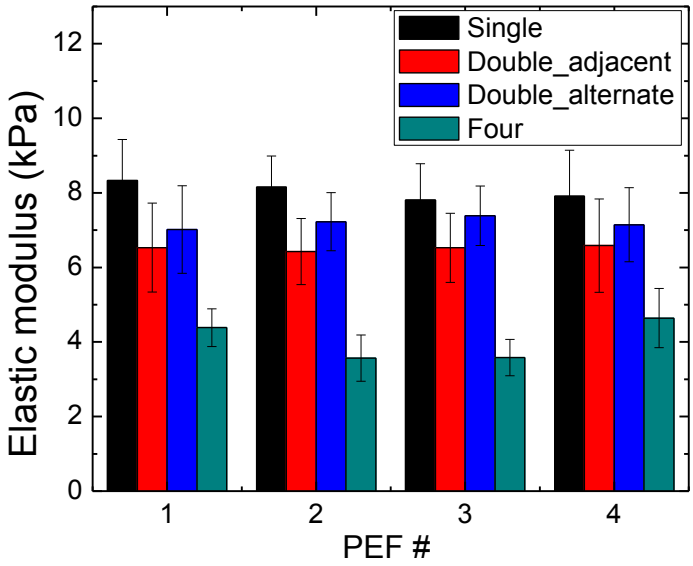

Figure 3.19 Elastic moduli measured by each PEF in the array when a single PEF, two adjacent PEFs, two alternate PEFs and four PEFs were activated.

3.4 *In Vivo* Breast Tumor Measurements

3.4.1 Scanning Breast Tumors *in vivo*

The *in vivo* testing was carried out on patients in a supine position as illustrated in Figure 3.12. It enrolled women 18 years of age and older seen in Dr. Ari Brooks' clinical practice at Drexel University College of Medicine who have been diagnosed with a palpable breast mass or who have had an abnormal result in a breast imaging study from May 2011 to April 2012. Forty subjects were enrolled under an IRB approved protocol. A summary of the age, race, and tumor type distributions of these subjects is given in Table 3.2. 39 of the patients had a breast abnormality identified by either palpation, mammography, or ultrasound and 1 patient had no breast abnormality. In all patients, the operator had no knowledge if there was a tumor within the tested area nor did she know the location or the extent of the tumor. The accuracy of the PEF measurement was assessed by comparing with the PEF results with the pathology reports. The PEF results were also compared to those of mammography and other imaging modalities when available.

Table 3.2 Summary of the 40 subjects in the in vivo study

Age (20-77)	20-40 41-50 51-60 61-80	15 10 8 7
Race	African American Asian Caucasian	24 2 14

Tumor Type	**Malignant**	**14**
	Ductal carcinoma in situ (DCIS)	2
	Invasive ductal carcinoma (IDC)	12
	Benign	**25**
	Cyst	5
	Fibroadenoma	7
	Adenosis stromal fibrosis	1
	Apocrine metaplasia	1
	Fat necrosis	3
	Stromal fibrosis	1
	Usual ductal hyperplasia	2
	Other	5
	No Tumor	**1**

As noted in Section 3.3.5, the PEFs in the current hand-held probe could not do measurements simultaneously. Due to the limited scanning time (30 minutes) of *in vivo* measurements, we carried out our study in four phases. In the beginning, a long duration time of 5 sec was used for each applied DC voltage to fulfill to the requirement of DC voltages. Under such conditions, only a quadrant of a breast could be completed in 30 min (Phase I, n=18). Because of this constraint, the surgeon would tell the operator which breast and which quadrant to test. Other than that, the operator had no knowledge if there was a tumor in that quadrant, or the size, or the location of the tumor. In Phase II (n=9) the duration of applied DC voltage was shortened to 3 sec. As a result, one half of a breast could be completed. Because of this, the surgeon would tell the operator which half of a breast to test. Other than that the operator did not know if there was a tumor in that half of a breast, or the location, or the size of the tumor. In phase III (n=7), we decreased the duration of the applied voltage to 2s so that a whole breast could be completed in 30 minutes. Because of this,

the surgeon would tell the operator which breast to scan. However, again the operator did not know if there was a tumor in that breast, or the location or the size of the tumor. In phase IV (n=6) we further reduce the duration of the applied DC voltage to 0.8s. As a result, both breasts could be completed in 30 min. In this final phase, the operator would scan both breasts while having no knowledge as to whether there was a tumor in either breast, or the location, or the size of the tumor. Note that all testing protocols such as shortening of the DC voltage duration time or the automated data acquisition were all well validated in model tissue studies before testing *in vivo*.

To create a coordinate system on a breast, a rectangular grid with a 1-cm increment was created on the breast with a washable marker. At each spot, the handheld unit was pressed against the breast with the same depression depth as marked on the outside of the housing. Three independent measurements were made to obtain an average and a standard deviation of the elastic modulus of the spot. The step size of the measurement was 7.5 mm in the x direction (which was parallel to the PEF array) and 1 cm in the y direction (which was perpendicular to the PEF array). The measurements were repeated until the entire assigned area was scanned. A 2-D elastic modulus map of the scanned area of the breast was then created with green representing the E values of the normal breast tissues and red representing the elevated E values of the tumors. This color-coded map allows the tumor to be easily identified and located.

3.4.2 Effect of Depression Depth

During measurements, the handheld unit was pressed against the breast with a depression depth as illustrated in Figure 3.16. To examine the effect of the depression depth on the detection of the tumors, we examined the effect of different depression depths: 2 m, 4 mm, and 6 mm on the tumor size determination in 15 patients.

As an example E versus x at y = 5 cm obtained with 2-mm, 4-mm, and 6-mm depression depths are shown as black full circles, red open squares, and blue full diamonds in Figure 3.20. The elastic modulus of the normal tissue did not change with depression depth. The larger measured modulus with a 6-mm depression depth than with a 2-mm depression depth at the center of the tumor was understandable since the PEF probe surface was now closer to the top surface of the tumor as a result of the larger depression depth. The data was then fitted to a Gaussian distribution (solid line). The size of the tumor with each depression depth was determined as the width at the half peak height of the Gaussian fit, which was 3.1 cm, 3.0 cm, and 3.2 cm, respectively as shown in Figure 3.20, indicating that the choice of the depression depth did not alter the measured tumor size. The reason is that increasing the depression depth did not alter the elastic moduli of the normal tissues at the bottom of the bell-shaped curves but only heightened the elastic moduli within the perimeter of the tumor as the depression pushed the PEFs closer to the tumor.

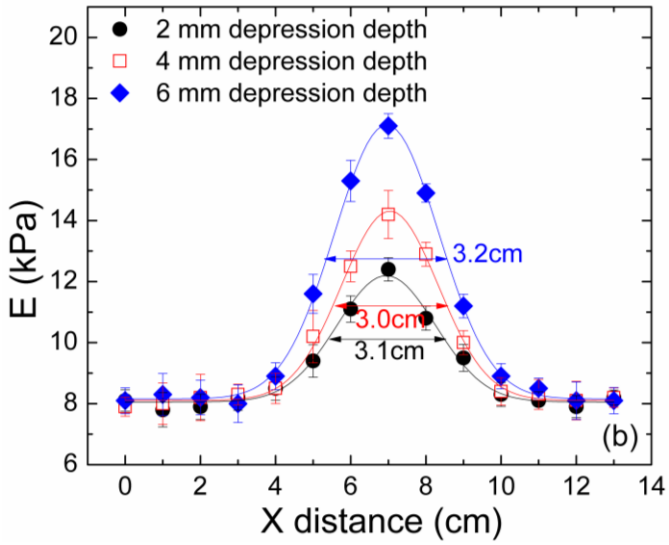

Figure 3.20 The measured elastic modulus at y = 5 cm versus distance around a tumor center at x = 7 mm with a 2-mm, 4-mm, and 6-mm depression depth.

For the 15 cases tested with three depression depths (2 mm, 4 mm, and 6 mm) during Phases I and II, PEF detected 16 out of 17 lesions with all three depths. The one lesion missed was due to the fact that the area with the lesion was not scanned. Furthermore, the sizes of the same tumor as determined by the three different depression depths were all within 10% of each other as similar to the results shown in Figure 3.20, indicating that for practical purpose, the measured tumor size was largely independent of the depression depth of 2 mm, 4 mm or 6 mm. Since the resultant tumor sizes were fairly insensitive to the choice of the depression depth, in the following, unless specified, all PEF measurements were carried out with a 4-mm depression depth.

3.4.3 Elastic Moduli of Breast Tumors and Normal Tissues *in vivo*

The result of the PEF scan on each subject was presented as a color-coded elastic modulus (E) map on a breast in polar coordinates in angle (in o'clock) and distance (in centimeter) with the nipple as the origin. As an example, the E maps of four subjects obtained in phase I- IV are shown in Figure 3.21 (a)-(h), respectively. These represent two of the partial scans obtained in Phase I and Phase II due to the time limitation as mentioned above. The green color represents the elastic modulus values of the normal breast tissues ranging 8-11 kPa, and the red color represents the elevated elastic modulus values of ≥ 15 kPa (which was at least 35% larger than the E of the normal tissues). Note that most of the patients had an E value of the normal breast tissues ranging 8-11 kPa. Within the same patient the E values of the normal breast tissues were quite uniform with a standard deviation less than 15%. The E map in Figure 3.21(a) obtained in Phase I shows that PEF detected a 2.4 cm × 2.5 cm lesion at 3 o'clock on the border of nipple of Subject 1, which was consistent with the mammography result shown in Figure 3.21(b). The E map shown in Figure 3.21(c) detected two lesions in Subject 2: a 1.5 cm × 2.1 cm lesion at 5 o'clock and 4 cm from the nipple, and a 2.4 cm × 2.0 cm lesion at 7 o'clock and 4 cm from the nipple. These lesions were missed by the mammogram shown in Figure 3.21(d) but were eventually confirmed as two DCIS by the pathology report. Furthermore, Subject 2's mammography report indicated that the breast was dense with a density score of 3-4. These results illustrate that PEF could detect tumors in dense breasts that were difficult to detect by mammography. It is of interest to note that the two lesions in

Subject 2 were also found by MRI (not shown).). Figure 3.21(e) represents an E map of a complete scan of the left breast of Subject 3 obtained in Phase III which indicates a 1.9 × 1.3 cm lesion at 3 o'clock and 5 cm from the nipple. The lesion was only shown in craniocaudal projection of the mammogram (see Figure 3.21(f)) and confirmed by biopsy as invasive carcinoma. The E map obtained in Phase IV shown in Figure 3.21(g) detected a 1.9 × 2.1 cm lesion at 10 o'clock 6 cm from nipple in right breast of Subject 4 which was confirmed as invasive carcinoma by pathology. The same PEF measurement was performed on the left breast as well and the E map did not show any lesions in the scanned area (see Figure 3.21(h)).

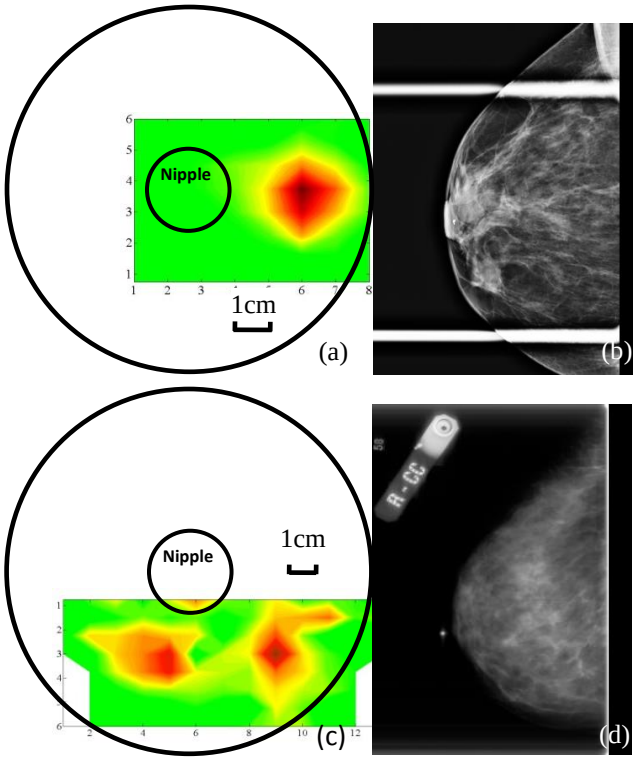

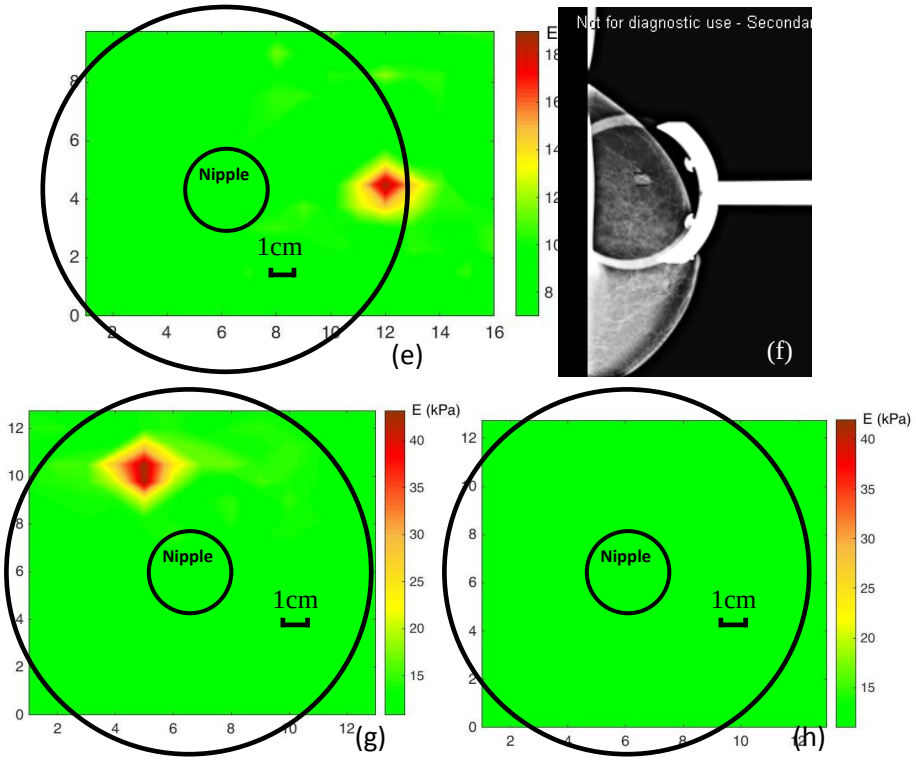

Figure 3.21 The E map of the right breast of Subject 1 in Phase I indicating a 2.4×2.5cm lesion at 3 o'clock on the border of nipple, consistent with an irregular mass with a spiculated margin in the subareolar region found in (b) the mammography of the same breast shown in (a); (c) the E map of the right breast of Subject 2 in Phase II, indicating a 1.5×2.1 cm lesion at 5 o'clock and 4 cm from nipple and a 2.4×2.0 cm lesion at 7 o'clock and 4 cm from nipple, both confirmed by pathology as DCIS but missed by (d) the mammography of the same breast shown in (c), which showed a dense breast with no visible sign of lesions; (e) the E map of the left breast of Subject 3 in Phase III, indicating a 1.9×1.3 cm lesion at 3 o'clock and 5 cm from nipple, which was confirmed by biopsy as invasive carcinoma and shown by (f) the mammogram of the same breast in (e) with an irregular mass 5 cm from the nipple; (g) the E map of the right breast and (h) that of the left breast of Subject 4 in Phase IV obtained within 30 min indicating a 1.9×2.1 cm lesion at 10 o'clock 6 cm from the nipple of the right breast which was confirmed as invasive carcinoma by pathology report while no lesions in the left breast.

Denoting the maximum elastic modulus (E) measured by PEF using Equation 3-4 within the region above the tumor as E_t, and the elastic modulus of the normal breast tissue away from the tumor as E_n, E_t (various colored symbols) and E_n (open

squares) of the 40 subjects versus subject age are plotted in Figure 3.22. Note that E_t was the effective elastic modulus of the tumor embedded/surrounded by normal breast tissues. The actual elastic modulus was not measurable in an *in vivo* study as the breast tumors were not removed from the patients. As can be seen from Figure 3.22, for all the 40 subjects, E_n hovered around 10 kPa while E_t for all tumors were much larger than E_n for all patients from Phase I to IV.

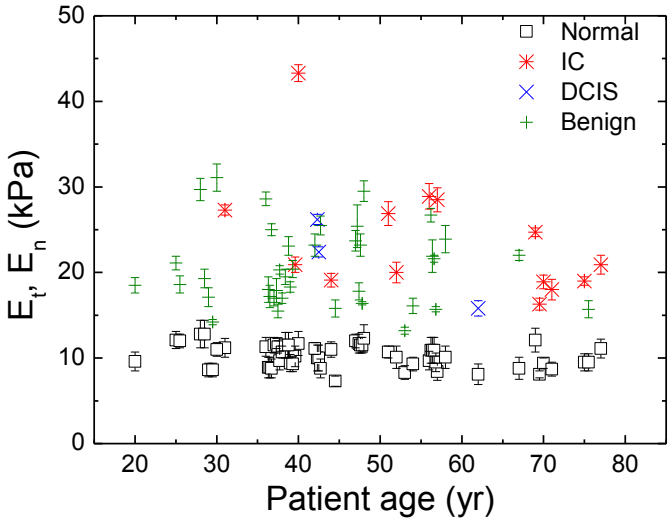

Figure 3.22 E_t, E_n versus age where E_n is the elastic modulus of the normal breast tissues and E_t is the maximum elastic modulus of the tumor region.

The distributions of E_t (red circles) and E_n (black squares) are further plotted in Figure 3.23. The solid and dashed lines are the fitted Gaussian distributions. Figure 3.22 and Figure 3.23 together indicate that the distribution of E_t and that of E_n barely overlapped. To further illustrate the separation of E_t and E_n, the ratio E_t/E_n of the same patient versus patient age is shown in Figure 3.24 where the E_n was normalized

as unity for each patient. Clearly, E_t/E_n was well separated from unity with a cutoff of about $E_t/E_n=1.35$, indicating that E_t was larger than E_n by at least 35%, which was 2.3 times larger than the standard deviation of E_n (not shown). Therefore, we used $E_t/E_n=1.35$ as a cutoff for tumors, i.e., the values of the E_t/E_n of all the tumors identified in this study were larger than or equal to 1.35. This cutoff worked well for all ages and the p value of the t test between E_t and E_n was much smaller than 0.001 indicating they are indeed different. Besides, Figure 3.24 shows that the malignant tumors (n=17), including both IC (n=14) and DCIS (n=3) appeared to have a higher E_t/E_n than benign tumors (n=39). It was reflected in a larger averaged E_t/E_n of malignant tumors which was 2.33±0.55 (open circles and triangles) than that of benign tumors which was 1.93±0.49 (crosses). Although the measured E_t could depend on both the E of the tumor and how close the tumor was to the breast surface, by averaging over a sufficient number of tumors, a larger averaged E_t/E_n for the malignant tumors than for the benign tumors may reflect that malignant tumors are stiffer than benign tumors, which was consistent with the finding in the earlier *ex vivo* studies [29].

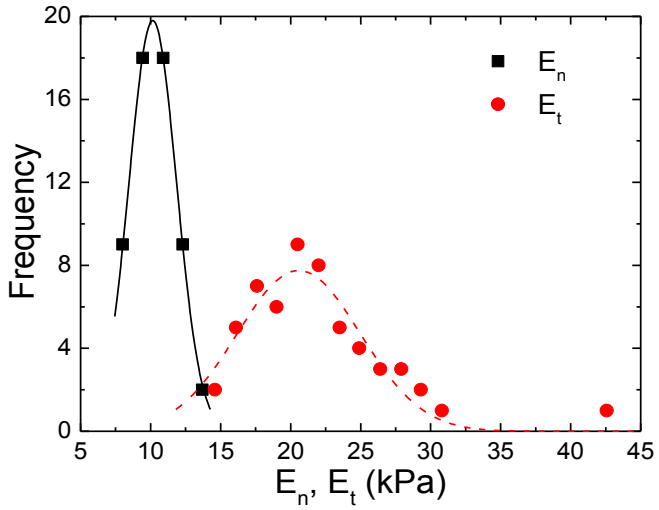

Figure 3.23 Distribution of E_n and E_t where E_n is the elastic modulus of the normal breast tissues and E_t is the maximum elastic modulus of the tumor region based on lesions of the 40 subjects. The solid line and dashed lines are the fitted Gaussian distributions for E_n and E_t, respectively.

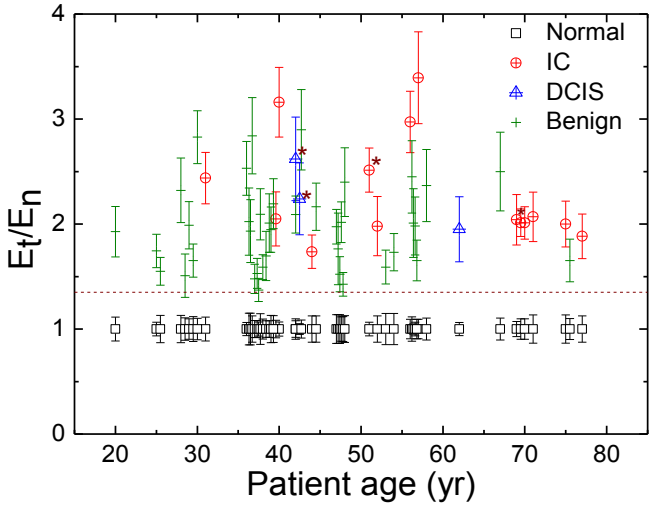

Figure 3.24 E_t/E_n versus patient age of 40 subjects where E_t is the maximum elastic modulus of the tumor region and E_n the elastic modulus of the normal breast tissues.

3.4.4 PEF Detection Sensitivity

In the 40 subjects enrolled in the study, a total of 48 lesions were confirmed by pathology or other imaging modalities such as mammography, ultrasound, and MRI. PEF detected 20 out of 20 lesions (20/20) in phase I, 10 of 11 lesions (10/11) in phase II, 7 out of 8 lesions (7/8) in phase III, and 9 of 9 lesions (9/9) in phase IV. As can be seen, PEF detected all the lesions in Phase I and Phase IV and missed only 1 lesion which was malignant in Phase II and 1 lesion which was benign in Phase III. The reason that PEF missed a malignant lesion in Phase II was because PEF scanned only half of the breast and did not scan the part containing the lesion while the missed benign tumor in Phase III was a nonpalpable lesion detected mammography. Clearly, as PEF progressed to faster scans with a shorter duration of each applied voltage, the detection accuracy remained consistent through the four phases, indicating that the shortened duration time of each applied DC voltage did not affect PEF's detection sensitivity. With all four phases, PEF detected 45 of the 47 lesions (45/47) including 15 malignant lesions (15/16) with only 1 missed malignant tumor in Phase II and 1 missed benign tumor in Phase III as explained above. A breakdown of the detection sensitivity in terms malignant or benign lesions in each of the phases is shown in Table 3.3.

Table 3.3 Detection sensitivity of PEF in different phases in terms of lesions and patients

	Detection sensitivity in terms of lesions		Detection sensitivity in terms of patients	
	Lesions detected by PEF	Malignant lesions detected by PEF	Patients detected by PEF	Malignant patients detected by PEF
Phase I	20/20 (100%)	7/7 (100%)	18/18 (100%)	6/6 (100%)
Phase III	10/11 (91%)	5/6 (83%)	8/9 (89%)	4/5 (80%)
Phase III	7/8 (88%)	2/2 (100%)	5/6 (83%)	2/2 (100%)
Phase IV	9/9 (100%)	1/1 (100%)	6/6 (100%)	1/1 (100%)
Total	46/48 (96%)	15/16 (94%)	37/39 (95%)	13/14 (93%)

3.4.5 Comparison of PEF Tumor Detection sensitivity with Mammography

We compared the tumor detection sensitivity of PEF with that of mammography among the 28 patients who had mammography records throughout each of the four phases. Because we had different number of patients in different phases, the PEF detected 17/17, 7/8, 4/5, and 3/3 lesions for phase I-IV, respectively and 31/33 overall while mammography detected 16/17, 6/8, 5/5, and 3/3 lesions for the corresponding phases and 30/33 overall. Overall, PEF detected about the same numbers of lesions as mammography for patients with mammography records, indicating that PEF do not generate more false positives than mammography. We also compare the detection sensitivity of malignant tumors between PEF and mammography in Table 3.4 for patients with mammography records as well. The PEF detected 7/7, 5/6, 1/1, and 1/1 malignant lesions for phase I-IV, respectively and14/15 (93%) overall while mammography detected 6/7, 4/6, 1/1, and 1/1 malignant lesions for phases I-IV, respectively and 12/15 (80%) overall. Note the one malignant tumor

missed by PEF in phase II was because PEF did not scan that half of the breast. That PEF had higher malignant tumor detection sensitivity (93%) than mammography (80%) while had similar all-tumor detection sensitivity with mammography indicates that PEF could detect malignant tumors not detectable by mammography without significantly increasing false positives.

Table 3.4 Detection sensitivity of PEF and Mammography based on 28 patients with mammography reports

	Detection sensitivity of PEF		Detection sensitivity of Mammography	
	Total lesions detected by PEF	Malignant lesions detected by PEF	Total lesions detected by mammography	Malignant lesions detected by mammography
Phase I	17/17 (100%)	7/7 (100%)	16/17 (94%)	6/7[a] (86%)
Phase II	7/8 (88%)	5/6 (83%)	6/8 (75%)	4/6[b] (67%)
Phase III	4/5 (90%)	1/1 (100%)	5/5 (100%)	1/1 (100%)
Phase IV	3/3 (100%)	1/1 (100%)	3/3 (100%)	1/1 (100%)
Total	31/33 (94%)	14/15 (93%)	30/33 (91%)	12/15 (80%)

[a] Mammography missed 1 invasive carcinoma

[b] Mammography missed 2 DCIS as shown in Figure 3.21 (d)

We also compared the locations of the lesions found in these 28 mammography reports as determined by PEF and by mammography. The position of a tumor determined by a different method may differ due to the fact that breasts are soft and movable and different methods may manipulate the breasts differently and thus produce somewhat different tumor locations. For example, PEF and US examined un-compressed breasts when the patients are supine while mammography and MRI require breasts to be compressed between two plates when the patients are

standing or on the stomach and pathology examined surgically excised breast tissues *ex vivo*. Because PEF does not require compressing a breast between two plates like mammography or MRI, the location, i.e., polar angle in o'clock determined by PEF may not be the same as that determined by mammography. For these reasons, we allowed some angular tolerance when comparing the tumor locations found by PEF to those found by mammography. With the 2 o'clock tolerance, we found that the locations determined by PEF agreed with those determined by mammography among tumors found by both PEF and mammography.

3.4.6 Comparison with Palpation

Compared to palpation, PEF detected 32/32 palpable tumors (11 malignant and 21 benign). More importantly, PEF detected 12 of the 14 non-palpable lesions (12/14) including 2 of 3 non-palpable cancers (2/3). As mentioned above, one non-palpable malignant lesion was not scanned by PEF in phase II because PEF did not scan the area containing the tumor. Not counting this one, the sensitivity for the non-palpable lesions would be 92% (12/13) instead of 86% (12/14).

3.4.7 Tumor Size Comparison with Pathology

To determine the size of the tumor at a certain y location, the elastic modulus at that y value was plotted versus x distance. The data was then fitted to a Gaussian. The size of the tumor at that y value was determined as the width at the half peak height of the Gaussian fit distribution. The size of the tumor in the y direction at a certain x was obtained in a similar fashion. As an example the elastic modulus versus x distance at y = 5 cm obtained with a 4-mm depression under the handheld probe on

patient is shown in Figure 3.20. The size of the tumor at y= 5 cm was determined as the width at the half peak height of the Gaussian fit, 3.0 cm. The reported tumor sizes in the x and y directions were the largest in those directions.

The tumor sizes determined by the PEF array system were compared with those reported in the pathological reports which were available only for malignant tumors. Since the orientation of the tumor during PEF measurement might not be exactly the same as that during pathological analysis, we defined the size of the tumor as the largest dimension by both the PEF and pathology. The size determined by PEF versus the size by pathology is plotted in Figure 3.25. The size of the smallest cancer PEF detected was 0.5 cm. For some of the cancers (6/11), the size obtained by PEF was the same as that determined by pathology, for others (4/11) PEF indicated a larger size than pathology. Since PEF was able to determine the model tumor sizes fairly accurately, the larger size obtained by PEF for some of the cancers might be the manifestation of the stroma surrounding the cancer as stroma was made of collagens which were also stiffer than normal breast tissues. Note that in one subject, the size determined by PEF was 5.9±0.5cm, which was much larger than the pathological size of 1.3 cm. This was because the patient had three cancerous lesions that were close to one another. The sizes of these three lesions were 1.3cm, 0.7cm, and 0.4 cm from pathology report. Because they were close together, PEF could not resolve them as separate tumors. As a result, the PEF size was much larger than the size determined by pathology.

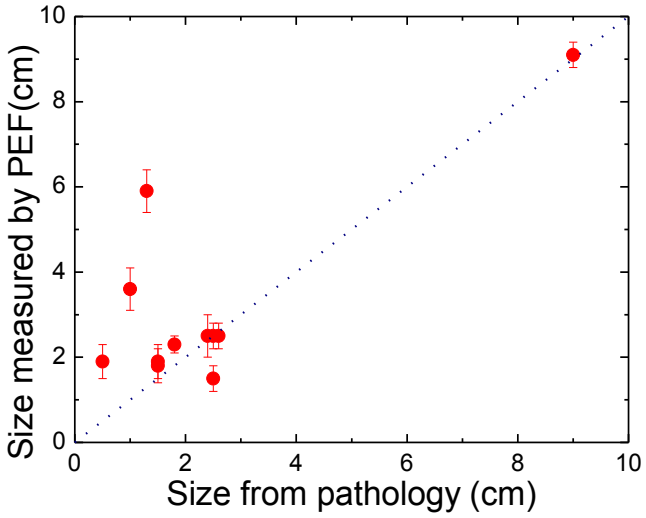

Figure 3.25 Tumor size determined by PEF versus tumor size measured by pathology.

3.4.8 Breast Density

PEF uses tissue elastic modulus contrast, i.e., E_t/E_n instead of density contrast to detect tumors. Therefore, the sensitivity of PEF does not depend on the mammography density of the breast. To illustrate this point, the patients were divided into two groups, low-density group (with density score 1 or 2) and high density group (density score 3 or 4) and E_n and E_t versus patient number were separate into these two groups in Figure 3.26. The breast density score is classified using BI-RADS (American College of Radiology Breast Imaging Reporting and Data System) scoring system. Density score 1 indicates that the breast is entirely fat and grade 4 means the breast is extremely dense. The result shows that denser breasts had a larger E_n. However, for all density scores, the E_t, were well separated from E_n, indicating that PEF was able to detect tumors in both dense breasts and non-dense breasts. Remarkably, PEF detected tumors with 100% sensitivity in women 40 years old or

younger who generally have dense breasts and for whom mammography is not very sensitive [159]. Combining this with the results PEF detected more malignant tumors than mammography (Section 3.4.5) without significantly increasing false positives indicates that PEF could be a potential tool for detection breast cancer in young women and women with dense breasts.

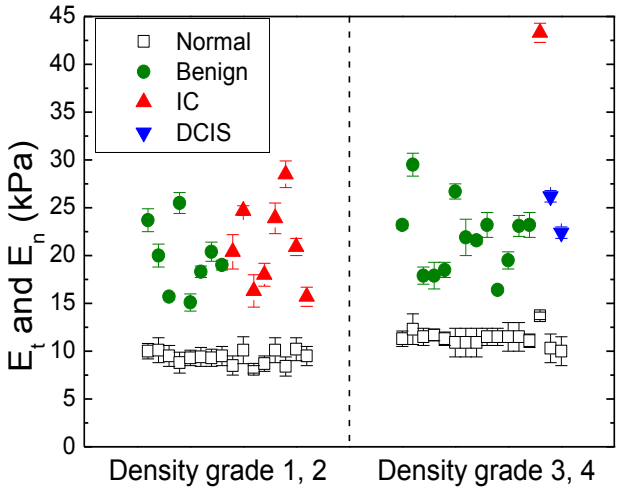

Figure 3.26 Maximum elastic modulus of tumor region, E_t, and elastic modulus of normal tissues, E_n, versus mammography density score.

3.5 Conclusions

Piezoelectric finger (PEF) is a piezoelectric cantilever, with two piezoelectric layers glued onto top and bottom of a stainless steel substrate, which can measure the elastic modulus of a soft material or tissue using indentation offering the potential to palpate electrically on samples like a finger. A portable PEF array breast tumor detection system which consists of a hand-held probe with 4×1 PEF array, an

electrical board and a laptop has been developed for *in vivo* breast tumor detection. Towards the goal, a hand-held acrylic box was designed to hold the PEF array and prevent overloading pressure on the PEFs from the operator's pushing. Custom software was developed in LabVIEW to acquire, analyze, display, and record the elastic moduli of tissue in real time. The effect of the duration of each applied DC voltage was examined and eventually shortened from 5 s to 0.8 s that towards the end of the study, both breasts could be scanned within 30 minutes.

The PEF breast tumor detection system was tested on model breast tumors consisting of a gelatin matrix with modeling clays inclusions. A two dimensional color coded elastic modulus map was created based on the measurement results. Green color represents the elastic of the gelatin matrix while red color represents the elevated elastic modulus of the modeling clay. It shows that PEF array system indeed detected all the model tumors and the locations of model tumors determined by the PEF array system also agreed with their actual locations. Moreover, the effect of the depression depth was examined in model tissues, which showed the size of the tumor determined by the PEF was essentially the same when the depression depth was 2 mm, 4mm, and 6 mm.

The *in vivo* investigation was carried out in the form of blind tests out on 40 subjects who were in a supine position. The tests were carried out in four phases: with DC voltage durations 5, 3, 2, to 0.8 sec corresponding to scanning a quadrant, a half, a whole breast, and both breasts within in 30 min, respectively. The detection results for all four phase were similar, indicating that faster measurements did not

affect the accuracy of the measurements. It is also shown that for the 15 cases tested for depression depths of 2-6 mm the detection results in terms of detection sensitivity and tumor size were unaffected by different depression depths.

Overall, PEF detected 46 of the 48 lesions (46/48) in 40 patients enrolled in the study. The smallest malignant tumor detected by PEF in this study was 5 mm. For the 28 patients with mammography reports, PEF detected 31/33 of all lesions and 14/15 of malignant lesions as compared with 30/33 of all lesions and 12/15 of malignant lesions by mammography, indicating that PEF could detect malignant tumors not detectable by mammography without significantly increasing false positives. In addition, PEF detected 100% of palpable and 67% non-palpable malignant tumors, suggesting PEF was capable of detecting both palpable and non-palpable lesions *in vivo*. The tumor sizes estimated by PEF were larger than those determined by pathology, likely a manifestation of the hard stroma surrounding the cancer. Furthermore, PEF detection was independent of breast density, suggesting that PEF could be a potential tool for detecting breast cancer in young women and women with dense breasts.

4. DETERMINE THE DEPTH PROFILE OF MODEL BREAST TUMORS

Accurate preoperative assessment of breast tumor locations and sizes in 3D are important for both biopsies and surgeries. Ideally, if there is a technique that can detect not only the presence but also the 3D location and size of the tumor, it will help with more accurate biopsies and surgeries. It is well known that breast tumors are stiffer compared with the surrounding normal tissue. The PEF array has shown to be able to detect breast tumors *in vivo* and determine the 2D locations and sizes of the tumors. Previous study has shown that the depth sensitivity of a PEF depends on the width of the contact. In other words, with a larger contact size a PEF can assess the elastic response of deeper tissues. Therefore, a set of PEFs of different contact sizes have the potential to provide the stiffness profile in depth direction and determine the tumor depth.

In this chapter, the depth profile of model breast tumors are determined based on the elastic modulus measurements from a set of PEFs of different contact sizes. Firstly, the depth sensitivity of a PEF which measures how deep a PEF can detect is determined empirically. Then a 2-spring model is used to deduce the depth profile of bottom supported model breast tumors from PEF measurements and compared with an inversion technique using finite element analysis (FEA). The model is further extended to 3 springs for suspended breast tumor depth profiling and the 3D image of the tumor is constructed.

4.1 Depth Sensitivity of a PEF

The depth sensitivity of a PEF is defined as the depth beneath the surface at which the elastic modulus of the tissue can be measurable by the PEF on the surface. In previous studies with a single PEF without a housing, the depth sensitivity of a PEF was shown to be about the twice of the contact width. However, it is unknown whether the depth sensitivity of a PEF will change if it is placed in the housing. Therefore, the depth sensitivity of PEFs with different contact sizes in the housing were determined. For this purpose different depths of modeling clay inclusions were embedded in gelatin matrix and PEFs of different contact sizes in the housing were used to measure the elastic moduli over the gelatin and inclusions. If the inclusion is within the depth sensitivity of a PEF, the PEF should be able to differentiate the effective modulus of the inclusion from the modulus of surrounding gelatin.

Four PEFs were used in the study. PEF A was 4.1±0.2 mm wide, PEF B was 6.5±0.2 mm wide, PEF C was 8.2±0.2mm wide, and PEF D was 9.8±0.3mm wide. All the four PEFs had two 127 µm thick lead zirconate titanate (PZT) layers (T105-H4E-602, Piezo Systems Inc., Cambridge) bonded to a 50 µm thick stainless steel (Alfa Aesar, War Hill, MA) layer using a nonconductive epoxy (Henkel Loctite, Westlake, OH) at the edges and a small patch of conductive epoxy (ITW Chemtronics, Kennesaw, GA) at the center. The PZT layer on the top of the stainless steel was used as driving electrode, and the PZT layer on the bottom of the stainless steel was sensing electrode as schematically shown in Figure 3.1 (a) and explained in great detail in Section 3.1. The driving PZT layers were 22.3±0.3 mm, 22.6±0.4 mm,

22.1±0.4 mm, and 22.4±0.4mm long and the sensing PZT layers were 10.1±0.3 mm, 10.5±0.3 mm, 10.3±0.4 mm, and 10.6±0.3 mm for PEFs A, B, C, and D, respectively, as shown in Table 4.1. Stainless strips were bent into rectangular loops and glued to the free end of the cantilever using the nonconductive epoxy. The width of the rectangular loop was equal to the width of the PEF.

During the measurement, the PEFs were clamped in the acrylic housing as shown in Figure 3.6 in Section 3.2.1. The contact area of the stainless loop to the sample was a square with each side equal to the width of the PEF. For PEFs A, B, C, and D, the contact areas of the stainless loops to the samples were 16±2 mm^2, 42±3 mm^2, 67±4 mm^2, and 96±6 mm^2, respectively. As the square stainless tip cross section was much smaller than the sample surface, the contact area of the square stainless loop was defined as the area of indentation.

Table 4.1 The dimensions of the PEFs used to determine the depth sensitivity

PEF cantilever	Contact width (mm)	Length of driving PZT (mm)	Length of sensing PZT (mm)	Contact area (mm^2)
A	4.1±0.2	22.3±0.3	10.1±0.3	17±2
B	6.5±0.2	22.6±0.4	10.5±0.3	42±3
C	8.2±0.2	22.1±0.4	10.3±0.4	67±3
D	9.8±0.3	22.4±0.4	10.6±0.3	96±6

To examine the depth sensitivity of PEFs in the housing, a model consisting of gelatin matrix (Now Foods, Bloomingdale, IL) and modeling clay (Crayola, Easton, PA) inclusions, with known elastic moduli (60 kPa) were built. The inclusions were

bottom supported and buried at various depths underneath the surface of the gelatin. PEF measurements were carried out on the gelatin surface above the center of each inclusion to determine the effective elastic modulus of the model tissue which included the gelatin on the top and the modeling clay inclusion at the bottom. As the bottom-supported inclusions became too deep below the surface and it was beyond the depth sensitivity of the PEF, the effective modulus would converge to the elastic modulus of the gelatin matrix. The depth sensitivity limit of a PEF was therefore determined as the depth of the modeling clay inclusion which was defined as the distance from the gelatin surface to the top surface of the inclusion. Beyond this depth, the effective elastic modulus measured by the PEF was indistinguishable from that of the gelatin matrix.

As an example, a schematic of the model A is shown in Figure 4.1. Ten cuboid inclusions, each with 16±0.5 mm by 16±0.5 mm in top surface but a different height, were put on the bottom of the container. The gelatin matrix was prepared by mixing the gelatin powder in water with a concentration of 0.06 g/ml at 80 °C on the hot plate and stirring for 10 minutes. The mixture was poured into the container and cooled in 4 °C refrigerator for 10 minutes to solidify. Before the measurement, the sample was left in room temperature for 1 hour to equilibrate. The total height of the model was 24±0.5 mm and the depths of the inclusions were 2.1±0.3 mm, 4.0±0.3 mm, 6.1±0.4 mm, 8.2±0.4 mm, 10.1±0.3 mm, 12.0±0.3 mm, 14.2±0.4 mm, 15.9±0.4 mm, 17.8±0.4 mm, and 20.1±0.5 mm.

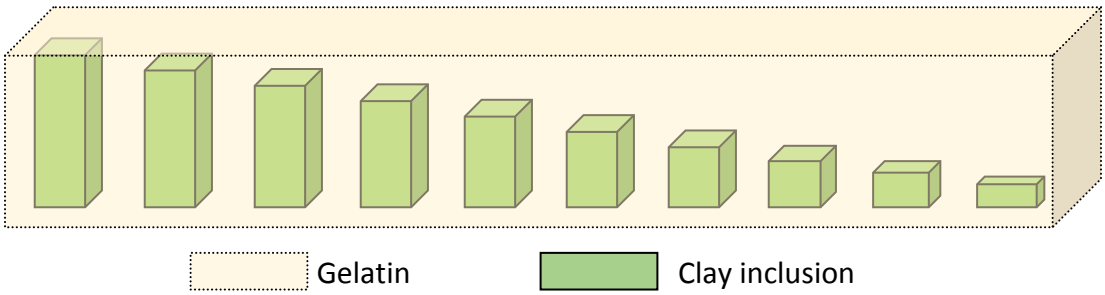

Figure 4.1 A schematic of the model A with bottom supported clay inclusions embedded at different depths in the gelatin

To experimentally determine the depth sensitivity of the PEFs, elastic modulus measurements were carried out at the gelatin surface above the centers of the bottom supported modeling clay inclusions using the breast tumor detection system and the LabVIEW as described in Chapter 3. The measured effective elastic moduli of the model tissue above the center of the modeling clay inclusions were plotted versus the known depths of the inclusions for PEFs A (green), B (blue), C (red), and D (black) in Figure 4.2. As can be seen from the figure, the measured effective elastic modulus decreased with an increase in tumor depth and saturated at about 5 kPa, which was the elastic modulus of the gelatin matrix as marked by two horizontal magenta dashed lines in Figure 4.2. The PEF's depth sensitivity was empirically defined as the largest depth at which the measured effective elastic modulus on the gelatin surface was larger than and distinguishable from the elastic modulus of gelatin matrix. Using this criterion, the depth sensitivity of PEFs A, B, C, and D were 8.3, 12.0, 14.2, and 17.8 mm, respectively. The uncertainty of the determined depth sensitivity was about 2 mm, since the difference between the depths of adjacent clay

inclusions was 2 mm. To reduce the uncertainty, the effective elastic modulus measured by the PEF was plotted versus the depths of the inclusions and fitted to an exponential function as shown in Figure 4.3. The elastic modulus of the gelatin matrix was about 5 kPa and marked as shaded area in the figure. The depth sensitivity of this PEF was determined as the depth at which the fitted curve encountered the range of elastic modulus of the gelatin matrix. Using this criterion, the depth sensitivity of PEF A was determined to be 8.3±0.3 mm. With the same method, the depth sensitivity of PEF B, C, and D were determined to be 13.4±0.4, 16.3±0.4, and 18.7±0.5 mm, respectively.

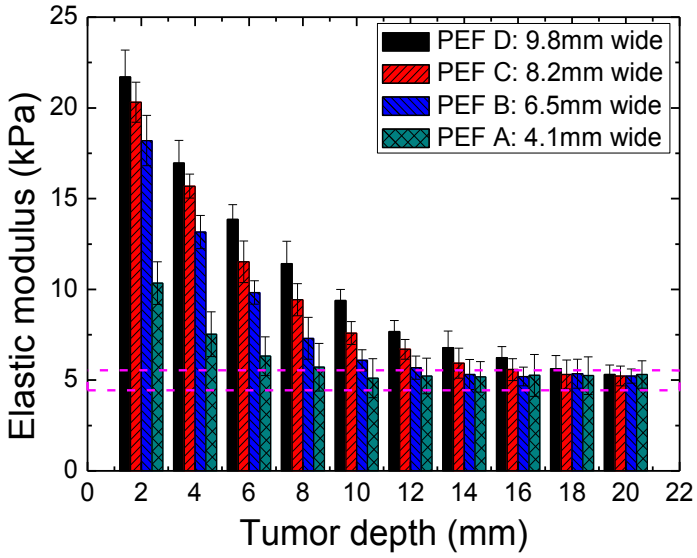

Figure 4.2 Effective elastic modulus of bottom-supported modeling clay inclusions (16 mm by 16 mm in top surface) embedded at various depths in a gelatin matrix using PEFs with different contact widths. The dashed area showed the range of the gelatin matrix (E_n = 5 kPa).

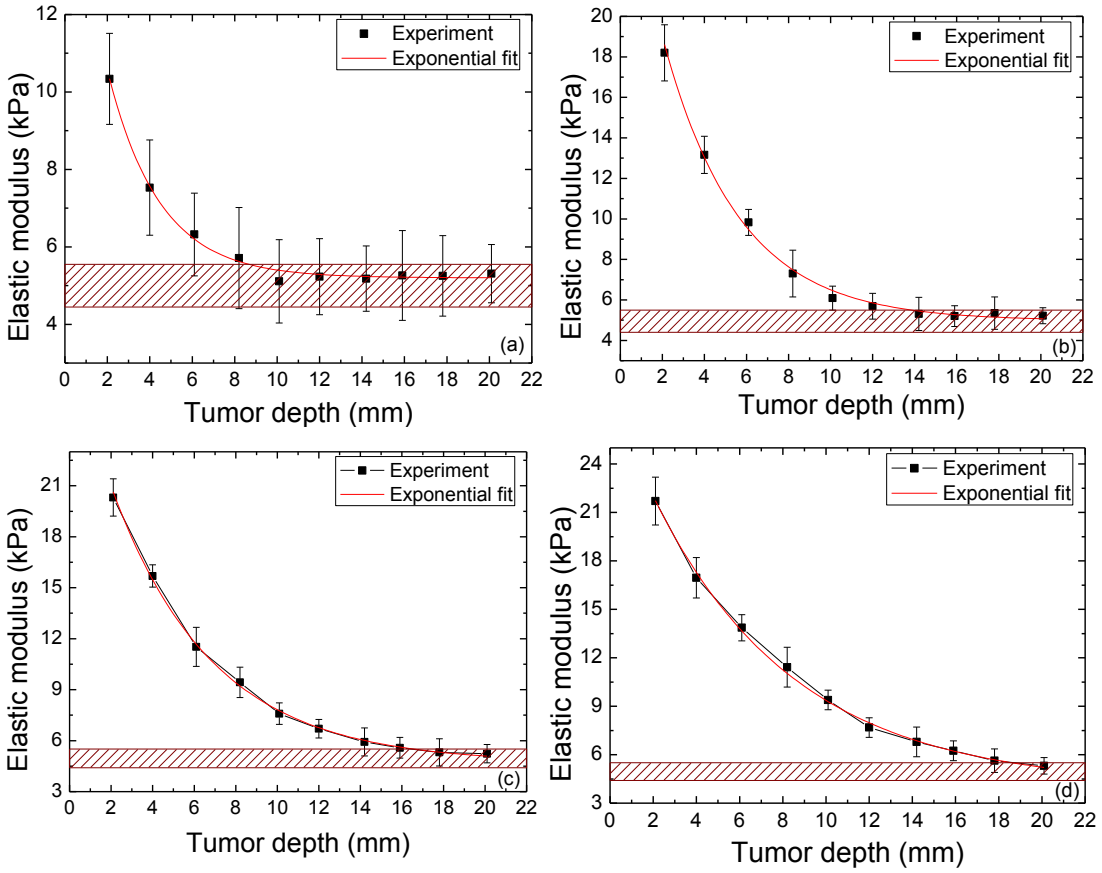

Figure 4.3 Effective elastic moduli of bottom-supported modeling clay inclusions embedded at various depths in a gelatin matrix measured by PEF A (a), PEF B (b), PEF C (c) and PEF D (d) and fitted to an exponential function.

The dependence of the depth sensitivity on the PEF width (the length or width of the contact) is summarized in Figure 4.4 where the depth sensitivity is plotted against PEF contact width. As can be seen, the depth sensitivity is linear with PEF contact width with a slope of about 2 (R^2=0.998), indicating that the depth sensitivity of a given PEF in the housing is about twice its contact width, consistent with previous studies with a single PEF.

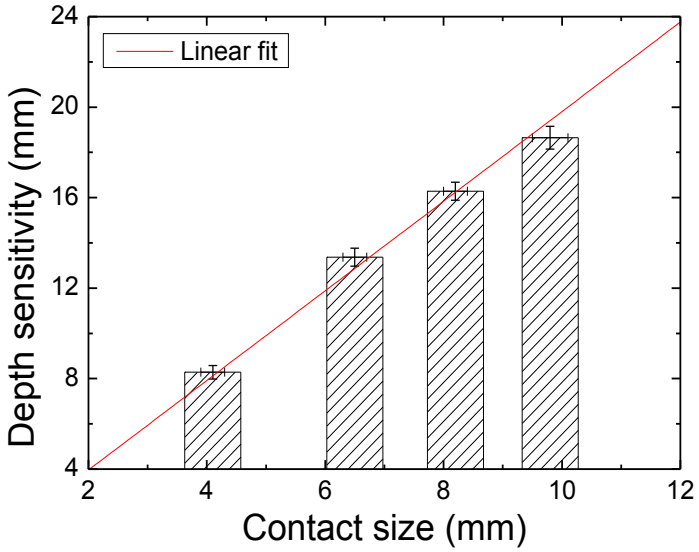

Figure 4.4 Depth sensitivity versus contact size of the PEF fitted to a linear function (red line)

4.1.1 Effect of Elastic Modulus of Normal Tissue

It is unknown that whether the elastic modulus of normal tissue would affect the depth sensitivity of the PEF or not. To answer it, different depths of modeling clay inclusions were embedded in a different concentration of gelatin matrix and PEFs of different contact sizes were used to measure the elastic moduli over the gelatin and inclusions. The depth sensitivity of PEFs were determined with the method described in Section 4.1 and compared with those shown in Figure 4.4.

The same four PEFs were used as shown in Table 4.1. Similar to Model A, Model B was built consisting of gelatin matrix (Now Foods, Bloomingdale, IL) and modeling clay (Crayola, Easton, PA) inclusions, with known elastic moduli (60 kPa). The ten inclusions had the same size with those in Model A and they were bottom supported and buried at various depths underneath the surface of the gelatin. The

gelatin matrix was prepared by mixing the gelatin powder in water with a concentration of 0.12 g/ml so the elastic modulus of the gelatin matrix in Model B after solidifying is about 10 kPa, about twice the elastic modulus of the gelatin matrix in Model A. These elastic moduli were consistent with the elastic modulus of normal breast tissues reported in literature and in Chapter 3. PEF measurements were carried out on the gelatin surface above the center of each inclusion. The effective elastic moduli of the model tissue were determined, plotted versus the depths of the inclusions (as shown in Figure 4.5), and fitted to an exponential function. The depth sensitivity of PEFs were defined as the depth at which the fitted curve come across the elastic modulus of the gelatin matrix. With this method, the depth sensitivity of PEFs A, B, C, and D were determined to be 8.5±0.3, 13.1±0.4, 16.6±0.4, and 18.9±0.4 mm, respective.

We further plot the depth sensitivity of PEFs when the elastic modulus of gelatin (E_n) was 10 kPa with those when E_n was 5 kPa in Figure 4.6. As can be seen, the depth sensitivity of PEFs when E_n was 10 kPa were about the same with those when E_n was 5 kPa, twice the contact width of the PEF. Therefore, we can conclude that the depth sensitivity of PEFs do not change with the elastic modulus of gelatin matrix (normal tissue).

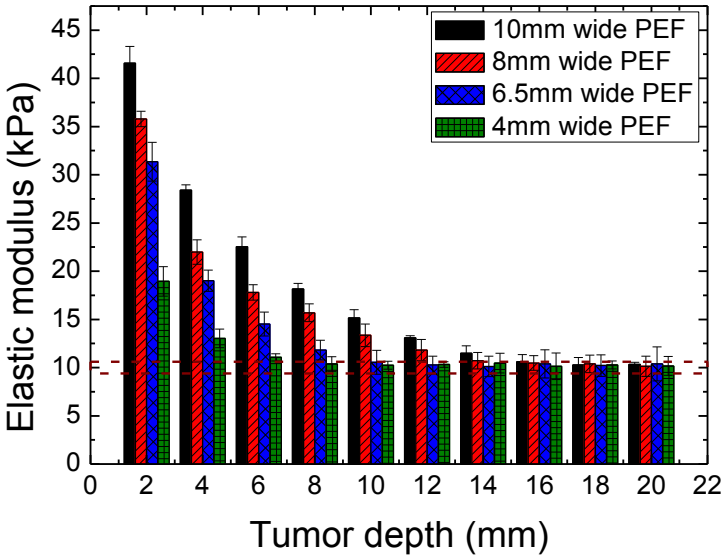

Figure 4.5 Effective elastic modulus of bottom-supported modeling clay inclusions (16 mm by 16 mm in top surface) embedded at various depths in a gelatin matrix using PEFs with different contact widths. The dashed area showed the range of the gelatin matrix (E_n = 10 kPa).

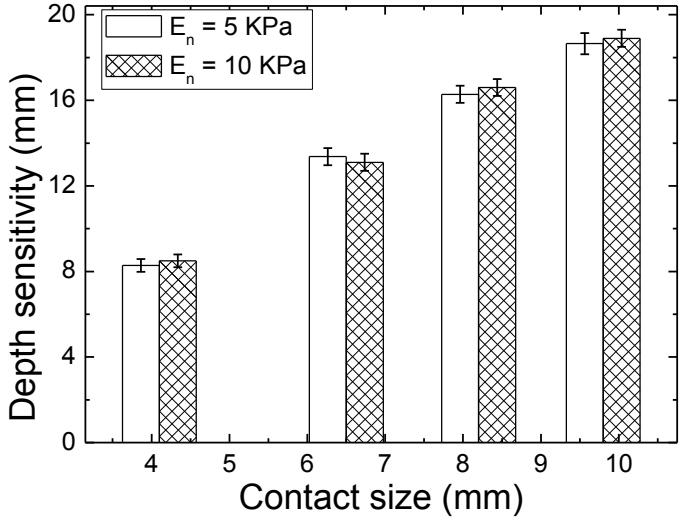

Figure 4.6 Depth sensitivity versus the contact size of the PEF when elastic modulus of gelatin (E_n) was 5 kPa (blank) and 10 kPa (shaded) respectively.

4.1.2 Effect of Elastic Modulus of Tumor

To illustrate the effect of the elastic modulus of tumor in determining the depth sensitivity of PEFs, different depths of modeling clay inclusions with various known elastic moduli were buried in a gelatin matrix and the effective elastic moduli over the gelatin and inclusions were measured using PEFs of different contact widths. The depth sensitivity of PEFs was determined based on the measurement results and compared.

The same four PEFs were used as shown in Table 4.1. Similar to Model A and B described in Section 4.1.1, the models used in this section were built consisting of gelatin matrix and modeling clay inclusions. The elastic moduli of the modeling clay inclusions were 38, 60 and 145 kPa, which were similar to those of breast tumors measured *ex vivo* using PEF reported in Ref. [151]. In addition, these choices were consistent with the elastic modulus of breast tumors reported in the literature, which were 3-33 kPa and 6-107 kPa, respectively [81, 83, 155-158] as shown in Table 1.2. The inclusions had the same size with those in Model A and they were bottom supported and embedded at different depths underneath the surface of the gelatin matrix, which was prepared by mixing the gelatin powder with water with a concentration of 0.06 g/ml. After the gelatin was solidified, the elastic modulus of the gelatin matrix was about 5 kPa, the same with that in Model A. The effective elastic modulus on the gelatin surface over the center of each inclusion was measured by the four PEFs, plotted versus the known depth of the inclusion and fitted to an exponential decay function. When the fitted curve met the range of the elastic

modulus of the gelatin matrix, the corresponding depth was defined as the depth sensitivity of the PEF. By this means, the depth sensitivity of the four PEFs were determined when the elastic moduli of the clay inclusions were 38, 60, and 145 kPa, respectively and plotted in Figure 4.7. The dashed line in the figure had a slope of 2. It can be seen clearly that no matter whether the elastic modulus of the clay inclusion (E_t) was 38, 60 or 145 kPa, the depth sensitivity of each PEF was about twice the width (contact width) of the PEF, indicating the depth sensitivity of PEFs is not affected by the elastic modulus of inclusions (tumors).

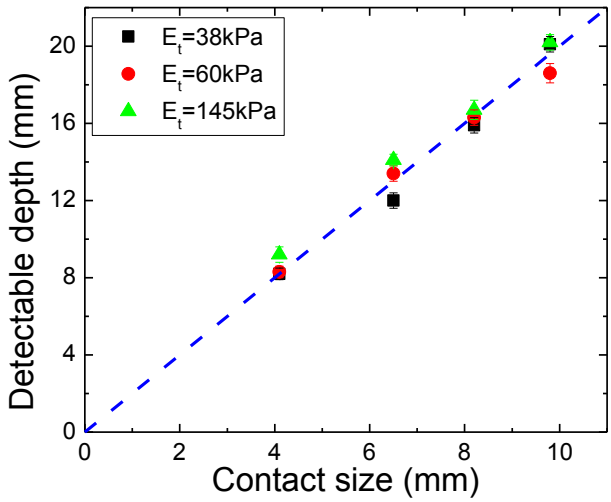

Figure 4.7 Depth sensitivity versus the contact width of the PEF when elastic modulus of clay inclusion (E_t) was 38 kPa (black square), 60 kPa (red circle) and 145 kPa (green triangle). The blue dashed line had a slope of 2.

4.1.3 Effect of Tumor Size

When we determine the depth sensitivity of the PEF, a larger size in top surface of the inclusion may introduce a larger effective elastic modulus measured by the PEF, which would make it more distinguishable from the gelatin matrix. In this case, the depth sensitivity of the PEF determined using the method describe in Section 4.1, which compares the fitted effective elastic modulus with the background elastic modulus of the gelatin matrix, would be larger. Therefore, the depth sensitivity of the PEF with this method may be affected by the size of the inclusions (tumors). To study this effect, models consisting of modeling clays with known elastic modulus (60 kPa) and various sizes in top surfaces and gelatin matrix were built. The effective elastic modulus measurements were done by PEFs of different contact widths on the gelatin surface with inclusions underneath and the depth sensitivity of these PEFs were determined based on the measurement results and compared.

Four PEFs were used in this section and the sizes are shown in Table 4.1. Similar to previous models in this chapter, the models used in this section were built consisting of gelatin matrix and modeling clay inclusions. The elastic modulus of the modeling clay inclusions was 60 kPa and the gelatin matrix had a concentration of 0.06 g/ml. After solidified, the elastic modulus of the gelatin matrix was about 5 kPa. The cuboid clay inclusions had a top surface of 16×16 mm^2, 5.5×5.5 mm^2, and 3.0×3.0 mm^2 and different heights. They were bottom supported and the depths of these inclusions, which were defined as the distance from the gelatin surface to the top of the inclusion, ranged from 2 mm to 20 mm with a 2-mm increment. The

effective elastic modulus which was measured by PEFs on the gelatin surface over the center of each inclusion was plotted versus the known depth of the inclusion as shown in Figure 4.3, Figure 4.8 and Figure 4.9 for inclusions with a top surface of 16×16 mm^2, 5.5×5.5 mm^2, and 3.0×3.0 mm^2, respectively. The data was then fitted to the exponential decay function. The depth sensitivity of the PEF was defined as the depth at which the fitted curve met the band of the elastic modulus of the gelatin matrix. In this way, the depth sensitivity of the four PEFs were obtained with different sizes in the top surface of the inclusions and plotted in Figure 4.10. Obviously, the depth sensitivity of the PEFs determined from small inclusions (3.0×3.0 mm^2, green triangle) were less than those determined from large inclusions (16×16 mm^2, black square). The depth sensitivity of the PEFs from 16×16 mm^2 inclusion was twice the contact widths of the PEFs indicated by the blue dashed line in the figure, while the those from 3.0×3.0 mm^2 was only about 1.65 times the contact widths of the PEFs, which was illustrated by the magenta dot line. The 5.5×5.5 mm^2 inclusion gave the depth sensitivity similar to the 16×16 mm^2 inclusion. As can be seen from Section 3.3.1, most of the breast tumors detected by PEFs in the *in vivo* study were larger than 10 mm. Therefore, it is safe to say that the depth sensitivity of the PEF is about twice the contact widths when we use the PEFs of different contact sizes to determine the depth profile of the breast tumors that have been detected by the PEFs.

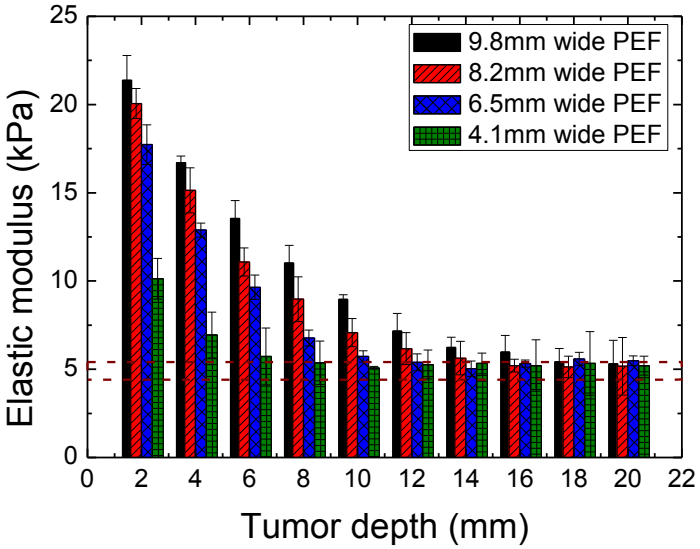

Figure 4.8 Effective elastic modulus of bottom-supported modeling clay inclusions (5.5 mm by 5.5 mm in top surface) embedded at various depths in a gelatin matrix using PEFs with different contact widths. The dashed area showed the range of the gelatin matrix (E_n = 5 kPa).

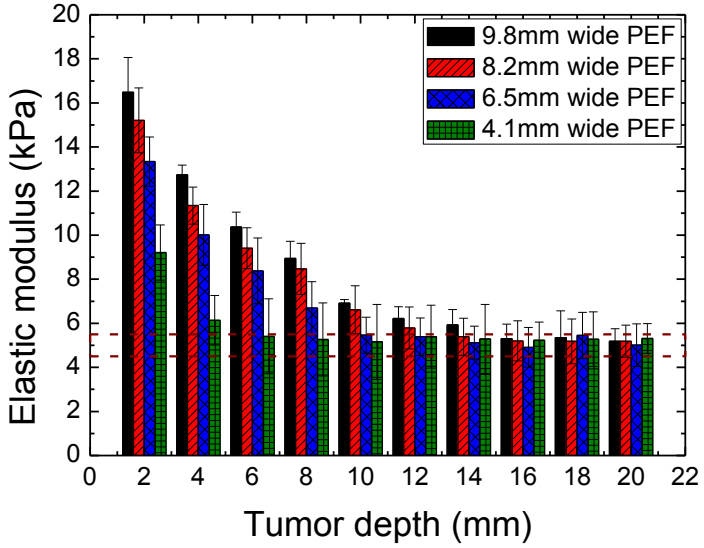

Figure 4.9 Effective elastic modulus of bottom-supported modeling clay inclusions (3.0 mm by 3.0 mm in top surface) embedded at various depths in a gelatin matrix using PEFs with different contact widths. The dashed area showed the range of the gelatin matrix (E_n = 5 kPa).

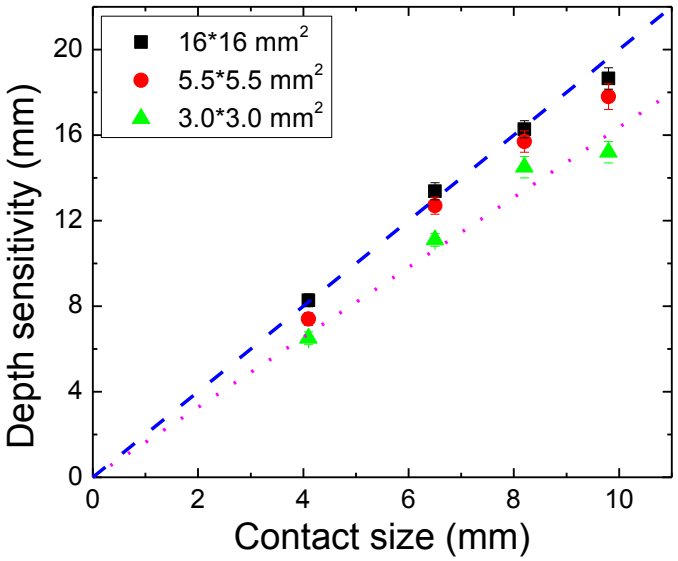

Figure 4.10 Depth sensitivity versus the contact size of the PEF when the top of the clay inclusions were 16×16 mm^2 (black square), 5.5×5.5 mm^2 (red circle), and 3.0×3.0 mm^2 (green triangle). The blue dashed line had a slope of 2 and the magenta dot line had a slope of 1.65

4.2 Determine the Depth Profile of Bottom Supported Model Breast Tumors

Since the depth sensitivity of a PEF in the housing is about twice the width of the contact, a PEF with a larger contact width can measure the elastic response from deeper tissues. Based on the effective elastic modulus measurement results on the same sample using a set of PEFs with different contact sizes, we should be able deduce the depth profile of breast tumors.

It is known that the effective elastic modulus measured by indentation on the surface of the breast depends on the elastic modulus of normal breast tissue (E_n), the elastic modulus of tumor underneath (E_t), and the size and depth of the tumor. And thus, deducing the depth profile of the tumor from the measured effective elastic modulus is an inverse process. Using PEFs with different contact sizes, the effective

elastic modulus can be directly obtained. The elastic modulus of normal breast tissue can be acquired by using PEFs on regions without tumors. The lateral size of the breast tumor is easily calculated based on the effective elastic modulus of the entire breast as explained in detail in Section 3.3.3. The elastic modulus of tumor is unknown because the tumor is embedded in the tissue and the depth profile of the tumor is what we want to know. A spring model in which the effective elastic modulus is calculated using an equation similar to the one for effective spring constant when two springs are connected in series is developed to deduce the depth profile in this section. It is applied to bottom supported model breast tumors and the results are compared with those obtained by an iterative technique that simulates the indentation experiment in each iteration until finding the depth profile of the tumor that has the same effective elastic moduli with the ones measured by PEFs. The spring model is then extended and applied to suspended model breast tumors.

4.2.1 Bottom Supported Model Breast Tumor Samples

Gelatin models with bottom supported clay inclusions as illustrated in Figure 4.11 were built to mimic the simplified breast tumors. The clays which have an elastic modulus of 60 kPa were made into cylindrical shapes with a radius of 15 mm and different heights. They were put in the center of petri dishes. Gelatin powders were mixed with water at 80 °C using a concentration of 0.08 g/ml, which was chosen so that the elastic modulus of gelatin was about 8 kPa. The gelatin solution was poured into the dishes and filled them. It was then cooled in 4 °C refrigerator for 10 minutes to solidify. Before each measurement, the sample was left in room temperature for 1

hour to equilibrate the temperature. The walls of the petri dishes were removed to eliminate the constraint to the boundaries of samples.

Four PEFs as listed in Table 4.1, whose contact widths are 4.1±0.2 mm, 6.5±0.2 mm, 8.2±0.2 mm, and 9.8±0.3 mm respectively, were used to measure the elastic moduli of the models on the surface, especially on pure gelatin area and on the center of inclusions. After the measurements, the depths of the bottom supported inclusions (t_1) were measured using a caliper and shown in Table 4.2.

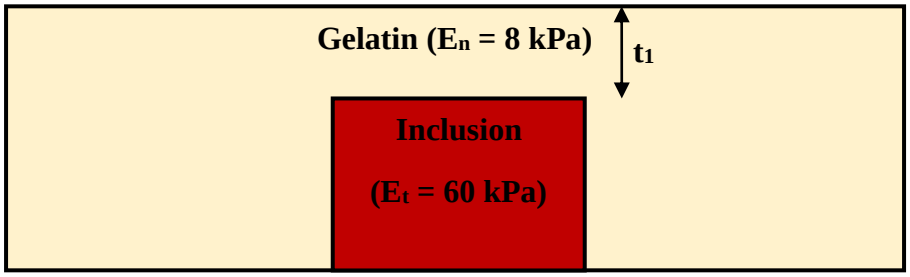

Figure 4.11 A schematic of the gelatin models with a bottom supported clay inclusion to mimic the breast tumors

Table 4.2 Depths of the inclusion in the bottom supported breast tumor models

Sample #	Inclusion depth (mm)
1	2.1±0.4
2	3.5±0.5
3	4.3±0.6
4	5.2±0.4
5	5.9±0.5
6	7.1±0.6
7	8.2±0.6
8	9.3±0.6
9	10.1±0.5
10	10.9±0.6
11	12.2±0.6

4.2.2 2-Spring Model to Deduce the Depth Profile

4.2.2.1 2-Spring Model

As we know, when two springs are connected in series as shown in **Error! Reference source not found.**(a), the overall spring constant k can be calculated using the following equation:

$$\frac{l_1 + l_2}{k} = \frac{l_1}{k_1} + \frac{l_2}{k_2} \tag{4-1}$$

where l_1 and l_2 are the length of the two springs, respectively; k_1 and k_2 are the spring constants of the two springs, respectively.

For bottom supported breast tumors, when the distance from the sample surface to the bottom of the tumor is larger than the depth sensitivity of a single PEF (d), the part of the tumor beyond the depth sensitivity could not be measured by the PEF and therefore the part is negligible. The normal tissue and the rest part of the tumor are like two elastic springs connected in series as can be seen in Figure 4.12 (b). Based on the Equation 4-1 the effective elastic modulus E measured by a single PEF, can be expressed as

$$\frac{d}{E} = \frac{t_1}{E_n} + \frac{d - t_1}{E_t} \tag{4-2}$$

where d is the depth sensitivity of a single PEF; t_1 is the distance from the surface of the normal tissue to the top of the tumor; E_n and E_t are the elastic moduli of the normal tissue and tumor, respectively.

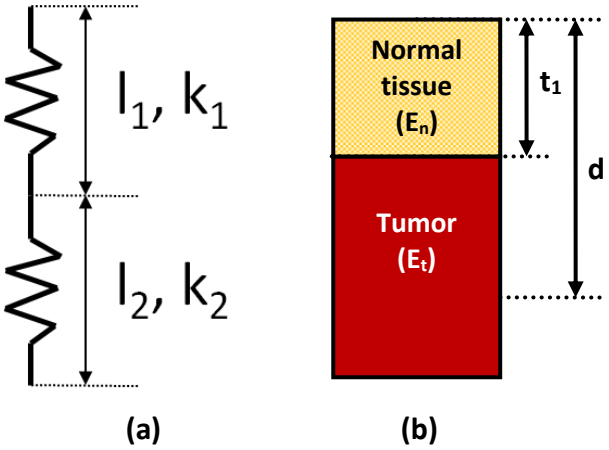

Figure 4.12 (a) A schematic illustrating two springs with a spring constant k_1, and k_2, respectively, were connected in series; (b) A schematic illustrating the bottom supported breast tumor with a depth of t_1. Its effective elastic modulus was measured with a PEF with a depth sensitivity of d.

The E_n was obtained by using the PEF on normal tissue area. E_t was unknown since the tumor was embedded in the normal tissue. In the paper published previously, the elastic moduli from two PEFs with different contact sizes were plugged into the equation to deduce the E_t and t_1 simultaneously. However, we may get negative t_1 sometimes. To solve this problem, we assume E_t values to be 40 and 60 kPa since our previous *ex vivo* breast tumor study has shown that the elastic moduli of excised breast tumors were in the range of 30 to 72kPa [151]. Because E_t is much larger than E_n, the term $(d-t_1)/E_t$ is small and a change in E_t will not have a large impact on the deduced t_1. Extreme E_t values (i.e. E_t = 100 and 200 kPa) were also used to see how the assumption of E_t affected the deduced depth profile.

4.2.2.2 Results using 2-Spring Model

The 2-spring model was applied to bottom supported breast tumor models to estimate the depth profile of the tumors. The deduced t_1 values of the tumors were plotted versus the true values as listed in Table 4.2 and were shown in Figure 4.13. Using large E_t values in the calculation gives large deduced t_1. However, no matter which E_t value was used in the equation, the deduced t_1 was within ±1.2 mm from the true t_1. It indicates that the t_1 values deduced from spring model theory were not sensitive to the assumed E_t values. The colored lines in the figure showed the linear fitting to the data. It could be found that the deduced t_1 using spring model theory had good linear correlation (R^2>0.995) with the true value. The slopes of the fitted curves were very close to 1. The slope, intercept, and R^2 of the linear fitting curve are listed in Table 4.3.

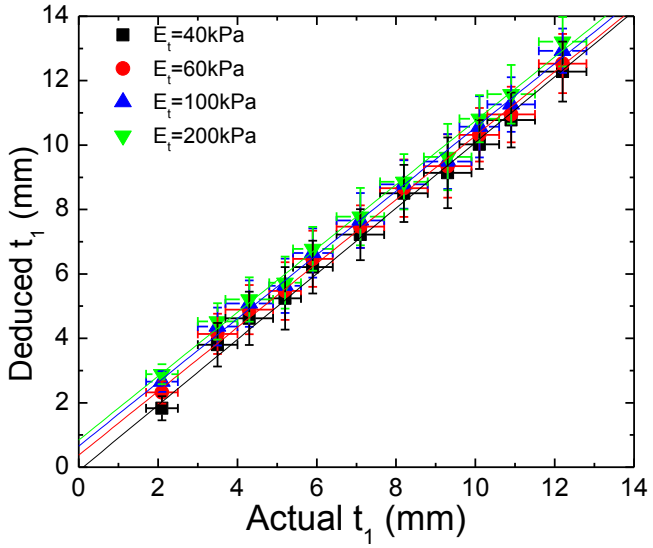

Figure 4.13 The estimated t_1 values using spring model theory with different E_t (40, 60, 100, and 200kPa) versus the actual values. The colored lines are the liner fitting.

Table 4.3 The linear fitting of the deduced tumor depth (t_1) of bottom supported tumors using spring model theory with different E_t versus the actual t_1

E_t (kPa)	Slope		Intercept		R^2
	Value	Standard Error	Value	Standard Error	
40	1.02	0.06	-0.11	0.42	0.99521
60	0.99	0.06	0.37	0.39	0.99676
100	0.99	0.06	0.66	0.36	0.99752
200	0.99	0.06	0.84	0.35	0.99764

The ratio of the deduced t_1 using spring model theory over actual t_1 is shown in Figure 4.14. The ratio was close to 1 with an error less than 40%. The error of the estimation of t_1 was larger when the tumor was closer to the sample surface. It was due to the reason that the ratio was calculated by dividing the deduced t_1 by actual t_1. It would be exaggerated when t_1 was small. When E_t was close to the true elastic modulus of the tumor (60 kPa), the ratio of deduced t_1 over actual t_1 was closer to 1, compared to the ratio when E_t was 100 or 200 kPa. Besides, when E_t was 100kPa (blue up triangles), the data was almost overlap with the ones when E_t was 200kPa (green down triangles). It proves that the assumed E_t values would not have much effect in the results of deduced t_1 and we can use the assumed values in the spring model theory to deduce the depth profile of bottom supported breast tumors.

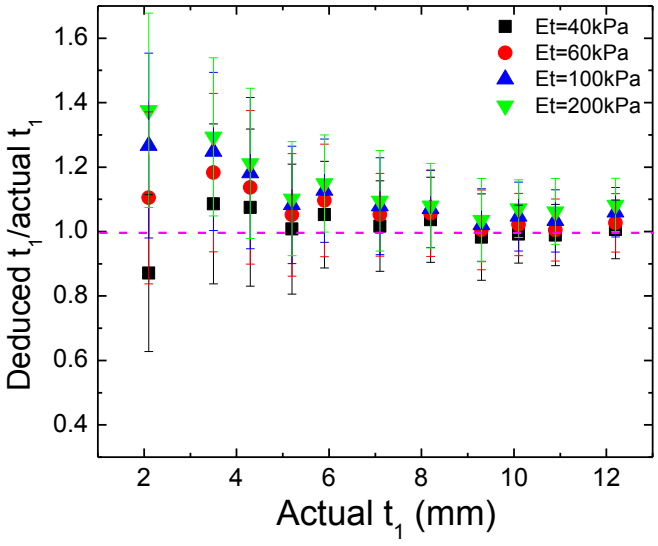

Figure 4.14 The ratio of deduced t_1 using sprint model theory to actual t_1. The dashed line shows where the ratio is 1.

4.2.3 Inversion Technique to Deduce the Depth Profile Using Finite Element Analysis (FEA)

An inversion technique based on Finite element analysis (FEA), a numerical method to find approximate solutions to boundary value problems for partial differential equations, has been developed to deduce the depth profile of bottom supported breast tumors. In FEA, an object is broken down into a large number of finite elements and simple mathematical equations are used to predict the behavior of each element. It then adds up all the individual behaviors of finite elements to approximate the behavior of the actual object. ABAQUS CAE 6.10 (SIMULIA, Dassault Systèmes) finite element software was used for the analysis.

4.2.3.1 FEA Model creation and validation

An axisymmetric model was used to minimize the computation time, since both the gelatin samples and the inclusions are cylinders. The model consisted of a clay inclusion embedded in a homogeneous gelatin matrix, the same with the bottom supported breast tumor model described in Section 4.2.1. The radius of the gelatin matrix (normal tissue) was 50 mm and the radius of the clay inclusions (tumor) was 15 mm. The height of the gelatin matrix (normal tissue) was 20 mm and the clay inclusion (tumor) varied during the simulation. A uniform displacement was applied to part of the surface of the gelatin (normal tissue) to simulate the indention with different-sized, rigid, flat-ended indenters performed by a PEF. The reaction force exerted on the gelatin surface could be simulated and summed, and the effective elastic modulus of the model could be deduced and compared with the experimental results from PEFs.

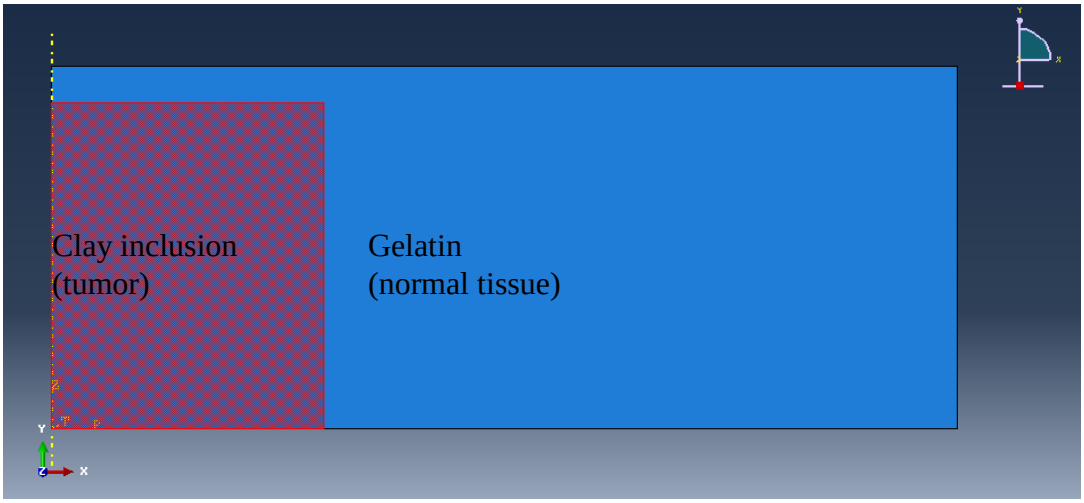

Figure 4.15 The breast tumor model created in ABAQUS which consisted of a gelatin matrix (normal tissue) and a bottom supported clay inclusion (tumor)

4.2.3.1.1 Material properties

The gelatin matrix (normal tissue) and clay inclusions (tumor) were defined as isotropic, linearly elastic materials. The mechanical properties were assigned as listed in Table 4.4. Young's moduli of gelatin (normal tissue) and clay inclusion (tumor) were taken from averages of PEF measurements. The density of the gelatin (normal tissue) was calculated to be 1080 kg/m^3 as the concentration of gelatin was 0.08 g/ml. The density of clay inclusion was deduced by measuring the weight and volume of a cubic clay. Poison' ratio values were 0.49999 since most of the soft tissues are nearly incompressible with Poisson's ratio ranging from 0.49000 to 0.49999 as reported in literatures [160, 161].

Table 4.4 Mechanical properties of the model breast tumors

	Density (kg/m^3)	Young's modulus (kPa)	Poisson's ratio
Gelatin (normal tissue)	1080	8	0.49999
Clay inclusion (tumor)	1500	60	0.49999

4.2.3.1.2 Contact interaction and boundary conditions

There are two parts in the simulation model: the gelatin (normal tissue) and the clay inclusion (tumor). The contact characteristics for the two parts must be carefully defined. In the bottom supported breast tumor model described in Section 4.2.1, the gelatin was crosslinked and had the clay embedded in it. They were bond together. Therefore, in the simulation model, the contact surfaces of gelatin and clay

inclusion were defined as “tie” in constraint. The contact surfaces in gelatin were set as “master surface” and the surfaces in clay inclusion were set as “slave surface”.

The boundary condition of the simulation was defined that the bottom of the model was “encastred” because the bottom of the gelatin (normal tissue) was fixed on the petri dish. The left edge of the model was the symmetry axis and it was set as “XSYMM” since it was an axisymmetric model. A uniform displacement (0.05 mm) was applied to the gelatin surface to simulate the indentation performed by PEF. The areas in the model where the displacement was applied were the same with the contact areas of the PEFs listed in Table 4.1. The radius of the area that the displacement applied to was 2.3 mm, 3.7 mm, 4.5 mm, and 5.6 mm for PEFs A, B, C, and D, respectively.

After simulation, the reaction forces exerted on the model surface were summed to calculate the effective elastic modulus. Based on Hayes’ solution [162], elastic modulus can be deduced using the following equation:

$$E = \frac{(1-\nu^2)F}{2a\kappa(a/h,\nu)w} \tag{4-3}$$

where E is elastic modulus; F is the indentation force, which can be calculated from the simulation results; ν is Poisson’s ratio, which is 0.49999 according to Table 4.4; w is the indentation depth, which is 0.05 mm as determined in the boundary condition; a is the radius of the indenter; h is the thickness of the tissue; κ is a scaling factor that depends on the aspect ratio a/h and Poisson’s ratio ν and it can be determined by another FEA simulation.

4.2.3.1.3 Mesh development

It is well known that the grid density plays a key role in the accuracy of finite element simulations. To validate the adequacy of mesh, the elastic modulus of the clay inclusion (tumor) was changed to 8 kPa which was the same with the elastic modulus of the surrounding gelatin (normal tissue). Although the model still had two parts, they had the same elastic moduli, and the effective elastic modulus of the entire model should be 8 kPa. To determine the appropriate mesh density, multiple trials of meshes with general element sizes of 2.0×2.0 mm^2, 1.0×1.0 mm^2, 0.75×0.75 mm^2, 0.5×0.5 mm^2, 0.25×0.25 mm^2, and 0.125×0.125 mm^2 were run. The size of the smallest mesh tested was partially determined by computer constraints. All the cases were examined with four PEFs with different contact sizes.

The effective elastic modulus of the model was calculated with different mesh sizes after simulations and it was compared to 8 kPa which was the elastic modulus of the model. Figure 4.16 plots the relationship between the effective elastic modulus calculated from simulations and the mesh density for the four PEFs. It is evident that coarser meshes over predicted the effective elastic modulus of the model. If the mesh size was 0.75×0.75 mm^2 or less, the prediction of effective elastic modulus was within 1% of the defined elastic modulus of the model (8 kPa) for all the four PEFs. Therefore, mesh size of the simulations in this chapter was 0.75×0.75 mm^2 or less. Sometimes the mesh at the contact area was made denser to achieve smoother stress/strain distributions. Figure 4.17 shows the deformed mesh with displacement

and reaction force distribution in the model during the indentation performed by PEF D, which had an indenter radius of 5.6 mm.

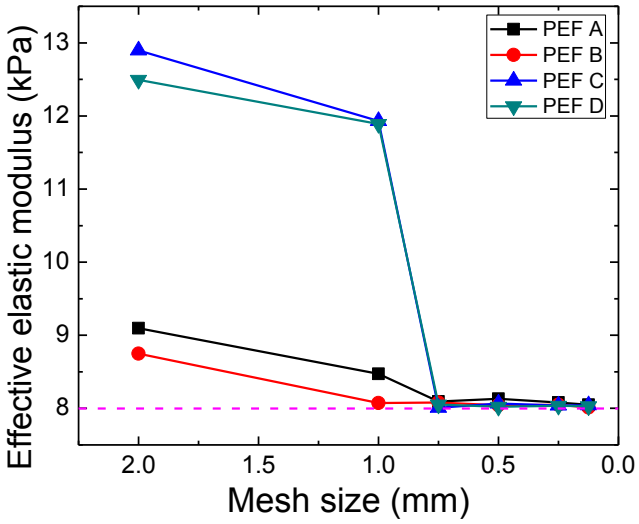

Figure 4.16 Change in effective elastic modulus calculated from simulations with different finite element mesh density. The dash line showed the defined elastic modulus of the model (8 kPa).

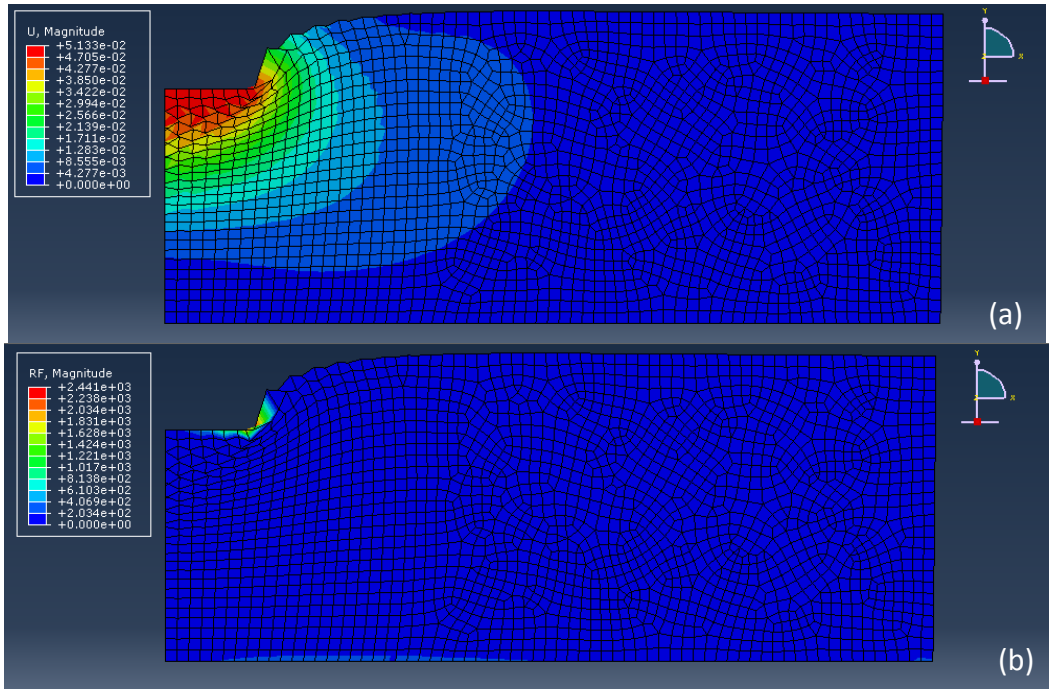

Figure 4.17 Deformed mesh (0.75×0.75 mm^2) of the model during indentation performed by PEF D, which had a indenter radius of 5.6 mm. (a) showed the displacement distribution and (b) showed the reaction force.

4.2.3.2 Inversion technique

To determine the depth profile of the breast tumors, an iterative inversion algorithm was developed. The algorithm is based on the fact that the measured elastic moduli by PEFs depend on the depth of the breast tumor t_1 which was defined as the distance from the model surface to the top surface of the tumor, if other parameters are fixed, including elastic moduli of the normal tissue (E_n), elastic modulus of the tumor (E_t), the size of the contact of the PEF, and the lateral size of the tumor. The smaller t_1 is, the closer the tumor to the surface, and the more portions of the tumor the PEF could detect, and therefore the larger the effective elastic modulus is from the PEFs.

In the algorithm, the elastic moduli measured by PEFs with different contact sizes on the center of the tumor (E) and on the normal tissue (E_n), and the lateral size of the inclusion deduced from PEF measurements as described in Section 3.3.3 were known and used as the input of iterations. Based on the experimental E values, we could have an initial guess of t_1. If the experimental elastic moduli measured on the center of the tumor were the same with E_n for certain PEFs, it indicated that these PEFs could not detect the inclusion. Therefore, the depth of the tumor (t_1) should be larger than the depth sensitivity of these PEFs. On the other hand, if the experimental elastic modulus was larger than the E_n, t_1 should be smaller than depth sensitivity of the PEF. Based on the lateral size of the tumor and the initial guess t_1, a breast tumor model was constructed in ABAQUS. In the simulation, both E_n and E_t are required. E_n was obtained by PEF measurements on normal tissue area, while E_t could not be measured directly, since the tumor was embedded in the normal tissue. Our previous *ex vivo* breast tumor study has shown that the elastic moduli of excised breast tumors were in the range of 30 to 72kPa [151]. Therefore, E_t was assumed to be 40 and 60 kPa in the simulation. Extreme E_t values (E_t = 100 and 200 kPa) were also used to see how the assumption of E_t affected the deduced depth profile.

After the simulation, the effective elastic moduli on the center of the tumor using different contact sizes could be deduced from the reaction forces using the Equation 4-3. The effective elastic moduli from simulations were compared with the experimental ones. If the elastic moduli from simulation were larger than the experimental ones, it indicated that the tumor in the simulation was too close to the

sample surface, and thus the t_1 was revised by take twice of the initial guessed value. On the other hand, if the elastic moduli from simulations were smaller than the experimental ones, t_1 was revised by taking half of the initial value. The revised t_1 was then used to construct a second model for simulation, and the simulation results were compared with the experimental results. It was repeated until the elastic moduli from simulations were within 10% of the experimental values which was the standard deviation of the PEF measurements. The t_1 used in the last simulation was the estimated depth of the tumor. The flow chart of the iteration algorithm is shown in Figure 4.18.

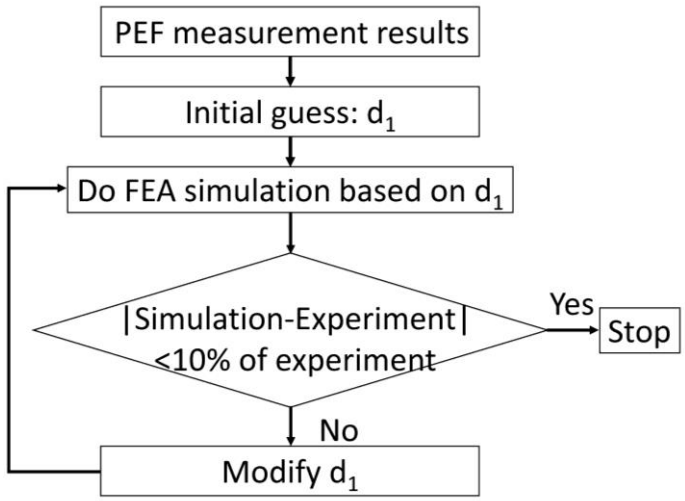

Figure 4.18 The flow chart of the inversion technique which used iterations to deduce the depth profile of inclusions

4.2.3.3 Results Using Inversion Technique

The inversion technique was applied to the bottom supported breast tumor models described in Section 4.2.1 to estimate the depths of the tumors. The elastic moduli of the models measured by PEFs with different contact sizes and the deduced lateral size of the tumor were input into the iterative algorithm along with an initial guess.

As an example, the elastic moduli of the sample #1 in which the tumor depth was 2.1±0.4 mm as listed in Table 4.2 were measured by PEFs and were shown in Figure 4.19. The elastic moduli measured on the center of the sample were 21.1±1.8, 25.7±2.2, 30.1±3.5, and 35.4±3.4 kPa from PEFs A, B, C, and D, respectively. The elastic modulus of normal tissue (E_n) was 8.1±0.9 kPa as indicated as green shaded area in the figure. It is obvious that the elastic modulus on the tumor area from the PEF with a 4.1 mm wide contact was larger than E_n. Therefore, the tumor supposed be within the depth sensitivity of that PEF. As discussed in Section 4.1, the depth sensitivity of a PEF is about twice of the contact width, so the tumor depth (t_1) should be less than 8.2 mm. Assuming the elastic modulus of the pure tumor was 40 kPa and the initial guess of t_1 was 8 mm, a bottom supported breast tumor model was built and simulated in ABAQUS. The elastic moduli of the center of the tumor area using different sizes of indenters were calculated based on the simulation results and compared with experimental results as shown in Figure 4.20. The elastic moduli from simulation were at least 57% smaller than those from experiment, indicating the tumor should be closer to the surface and the initial guess of t_1 was too large. In the

second iteration, t_1 was 4 mm, which was half of the initial value. The simulations and comparisons were repeated until t_1 was 1.5 mm, in which case the difference between $E_{simulation}$ and $E_{experiment}$ was within 10% of $E_{experiment}$. Therefore, based on the inversion technique, the depth of the tumor (t_1) in model sample #1 was estimated to be 1.5 mm, which was very close to 2.1±0.4 mm, the true depth measured by caliper.

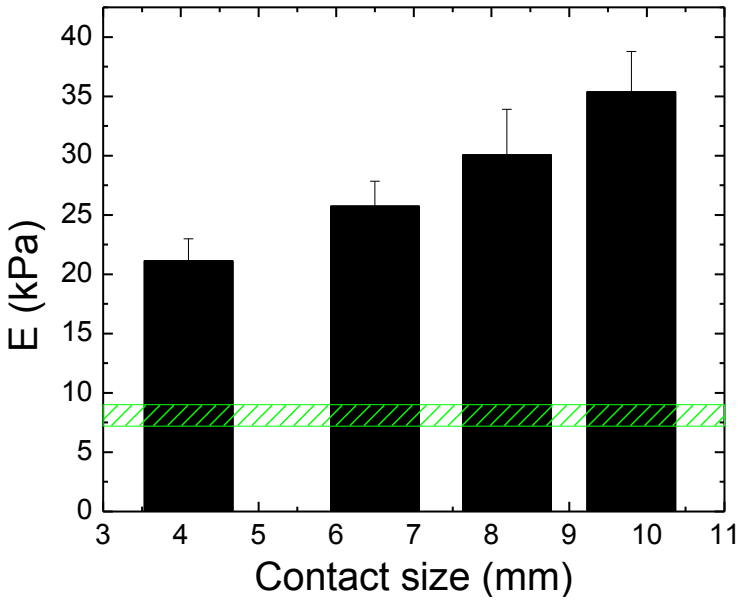

Figure 4.19 Elastic modulus (E) measured on the center of bottom supported breast tumor model sample #1 in which the tumor depth was 2.1±0.4 mm by PEFs with different contact sizes. The green bar showed the elastic modulus of the pure gelatin area (8.1±0.9 kPa).

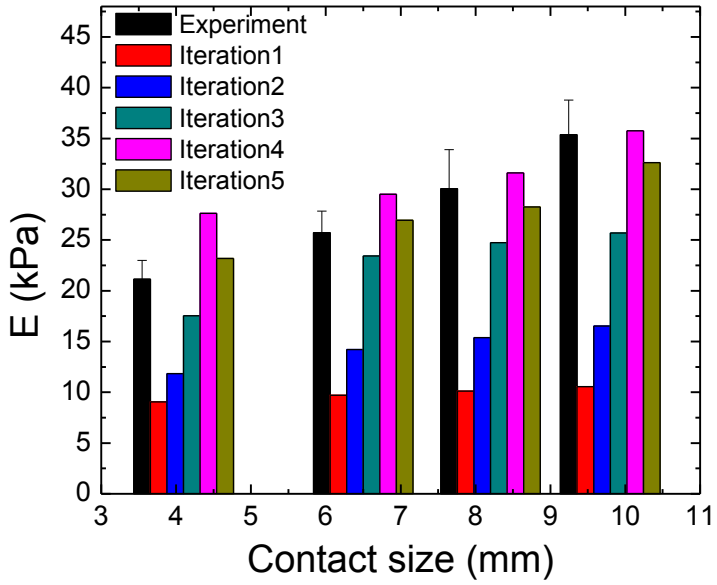

Figure 4.20 The elastic modulus (E) of the bottom supported tumor model sample #1 from PEFs (black) and ABAQUS simulations during inversion iterations with an initial guess of t_1=8 mm

Table 4.5 Tumor depth (t_1) used in iterations and the difference between $E_{simulation}$ and $E_{experiment}$ for tumor model sample #1 with an initial guess of t_1=8 mm

Iteration#	t_1 (mm)	Difference between $E_{simulation}$ and $E_{experiment}$			
		PEF A	PEF B	PEF C	PEF D
1	8.00	-57%	-62%	-66%	-70%
2	4.00	-44%	-45%	-49%	-53%
3	2.00	-17%	-9%	-18%	-27%
4	1.00	31%	15%	5%	1%
5	1.50	10%	5%	-6%	-8%

4.2.3.3.1 Effect of the Initial Guess

In the inversion technique, based on the elastic moduli from PEFs, we need to have an initial guess of the tumor depth (t_1). It is of interest to see whether the estimated tumor depth (t_1) depends on the initial guess or not. To address this

question, different initial guesses were tested in the inversion technique and the estimated t_1 were compared here.

Taking the tumor model sample #1 as we discussed before as an example. The PEF elastic modulus results have shown that the tumor depth (t_1) should be smaller than 8.2 mm. In the iterations listed in Table 4.5, the initial guess of t_1 was 8 mm and after 5 iterations it was obtained that t_1 was 1.5 mm. Different from that, we change the initial guess of t_1 to 1 mm. After the simulation, the deduced elastic moduli were larger than the experimental results as shown in Figure 4.21, indicating the initial guess was too small. Therefore, the tumor depth was within the range of 1 mm and 8.2 mm. The midpoint 4.5 mm was taken as the t_1 in the second iteration. After 7 iterations as listed in Table 4.1, the tumor depth of the sample #1 was determined to be 1.55 mm, which agreed with 1.5 mm, the t_1 determined with an initial guess of 8 mm. Therefore, it can be concluded that the results of the iterations does not depend on the initial guess of t_1. The iterations in both directions: t_1 from large to small and t_1 from small to large, could determine t_1 precisely.

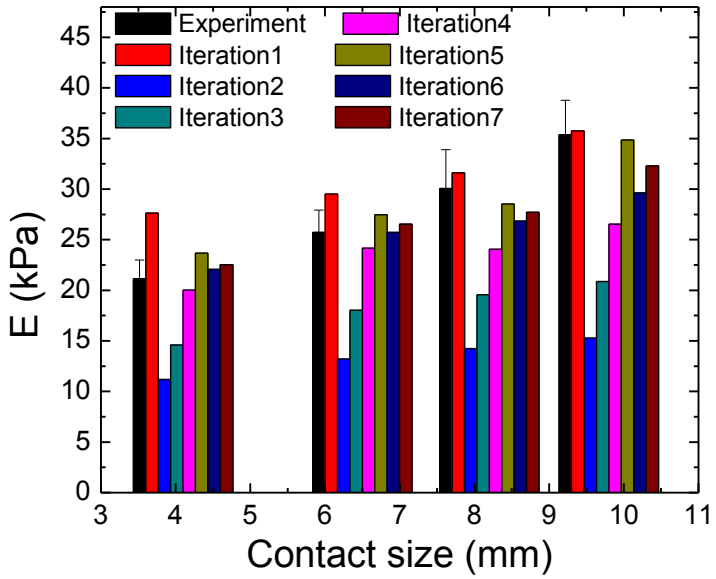

Figure 4.21 The elastic modulus (E) of the bottom supported tumor model sample #1 from PEFs (black) and ABAQUS simulations during inversion iterations with an initial guess of t_1=1 mm

Table 4.6 Tumor depth (t_1) used in iterations and the difference between $E_{simulation}$ and $E_{experiment}$ to determine t_1 of the tumor model sample #1 with an initial guess of t_1=1 mm

Iteration#	t_1 (mm)	Difference between $E_{simulation}$ and $E_{experiment}$			
		PEF A	PEF B	PEF C	PEF D
1	1.00	31%	15%	5%	1%
2	4.50	-47%	-49%	-53%	-57%
3	2.75	-31%	-30%	-35%	-41%
4	1.88	-5%	-6%	-20%	-25%
5	1.44	12%	7%	-5%	-1%
6	1.66	4%	0%	-11%	-16%
7	1.55	7%	3%	-8%	-9%

4.2.3.3.2 Effect of the Assumed E_t

In the inversion technique, both the elastic moduli of normal tissue (E_n) and that of tumor (E_t) are required. E_n could be obtained by PEF measurements on normal tissue area, while E_t could not be measured directly, since the tumor was embedded in the normal tissue. Same with the 2-spring model, in inversion technique E_t was assumed to be 40 and 60 kPa in the iterations. Extreme E_t values (i.e. E_t = 100 and 200 kPa) were also used to see how the assumption of E_t affected the deduced depth profile.

The deduced tumor depth (t_1) using the inversion technique with different E_t values (40, 60, 100, and 200 kPa) was plot versus the actual t_1 measured by caliper in Figure 4.22. When using a larger E_t (i.e. E_t = 200 kPa, green triangles), the estimated t_1 was larger, compared with using small E_t (i.e. E_t = 40 kPa, black square). However, the difference was less than 1mm which was negligible. The colored lines in the figure show the linear fitting of data with different E_t values and the fitted slopes and intercepts are listed in Table 4.7. It is obvious that there was very good correlation (R^2>0.998) between the t_1 deduced from the inversion technique and t_1 measured by caliper, no matter which E_t was used in the iterations. And the slopes from the linear fitting were close to 1 with an error smaller than 5%.

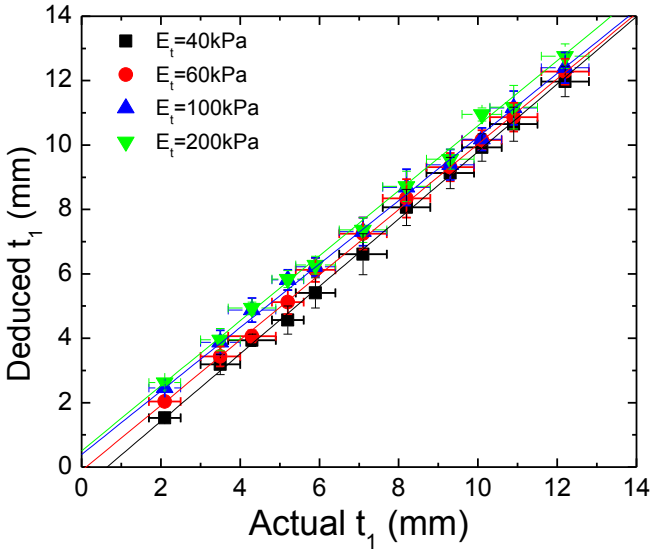

Figure 4.22 The deduced tumor depth (t_1) using the inversion technique with different E_t (40, 60, 100, and 200kPa) versus its actual value. The colored lines are the linear fitting.

Table 4.7 The linear fitting of the deduced tumor depth (t_1) of bottom supported tumors using the inversion technique with different E_t versus the actual t_1

E_t (kPa)	Slope		Intercept		R^2
	Value	Standard Error	Value	Standard Error	
40	1.05	0.02	-0.67	0.06	0.99926
60	1.01	0.02	-0.11	0.12	0.99896
100	0.99	0.02	0.39	0.05	0.99893
200	1.01	0.02	0.50	0.05	0.99865

The ratio of the deduced t_1 over actual t_1 was plotted in Figure 4.23. When the tumor depth was small (i.e. d=2.1±0.4mm), the error of the estimation of t_1 was larger. It was reasonable since we calculated the ratio by dividing the estimated t_1 by actual t_1. When t_1 was small, even a small difference between the estimation and actual values may lead to a large error. Besides, when measuring the t_1 with a caliper, the

smaller the t_1 was, the larger the uncertainty of measurements. Therefore, the deduced t_1 was more different from the actual values when dt_1 was small.

When E_t in the simulation was 60kPa (red circles) which was the exact elastic modulus of the inclusion, the ratios were 1 and on the dashed line. When E_t was 40kPa (black squares), the ratios were smaller than 1; while when E_t was 100kPa or 200kPa, the ratios were larger than 1, and the differences were less than 24%. Besides, when E_t was 100kPa (blue up triangles), the data were almost the same with the ones when E_t was 200kPa (green down triangles). It further proves that assuming E_t values in inversion technique would not have much impact on the deduced t_1 values. Therefore, we are able to use assumed E_t values, instead of actual E_t values, to run simulations and iterations to determine the depth profile of bottom supported breast tumors accurately.

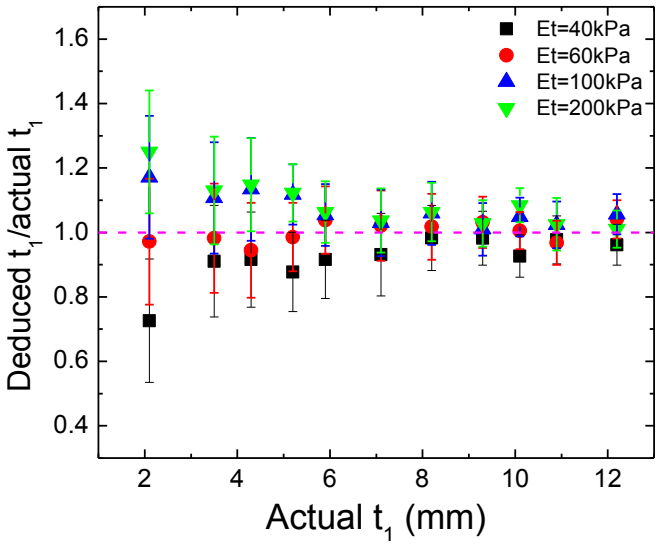

Figure 4.23 The ratio of deduced t_1 using inversion technique to actual t_1. The dashed line shows where the ratio is 1.

4.2.4 Comparison of the 2-Spring model and Inversion Technique

Since the deduced tumor depths are not affected by the assumed E_t values for both 2-spring model and inversion technique, the average of the depths deduced using E_t = 40 kPa and 60 kPa was used to represent the measured tumor depth for both methods. In Figure 4.24, the tumor depths determined by 2-Spring model and inversion technique were plotted versus the actual values. The blue dashed line has a slope of 1. It shows that both the 2-spring model and the inversion technique are able to determine the depth profile of bottom supported tumor accurately. The tumor depth (t_1) determined by 2-spring model was within 1.1 mm of the actual value and that estimated using inversion technique was within 0.6 mm. Although the inversion technique showed a slightly smaller error in deducing the tumor depth, its improvement over 2-spring model is very limited for breast tumors whose sizes are usually in centimeter scale. Besides, the inversion technique is very time consuming. After each iteration, the model in FEA needs to be rebuilt manually and it cannot be integrated into an automatic system. One the other hand, 2-spring model is based on simple calculations and could be done in seconds. Therefore, spring model is chosen for tumor depth profile determination.

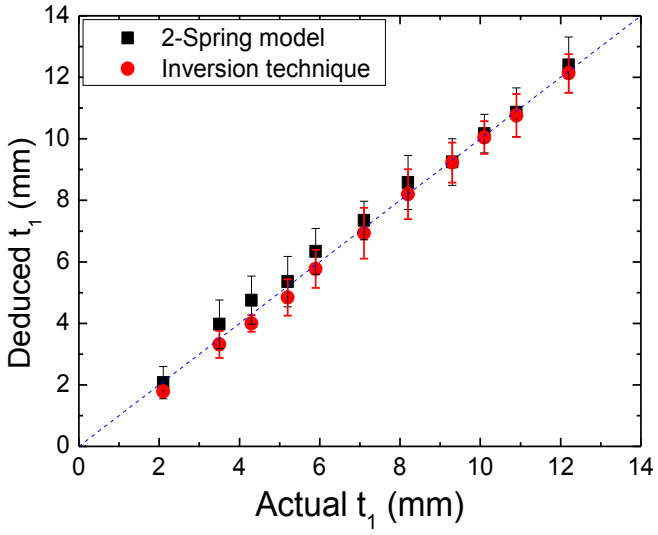

Figure 4.24 The deduced tumor depth (t_1) using the 2-spring model and the inversion technique versus its actual value. The blue dashed line has a slope of 1.

4.3 Determine the Depth Profile of Suspended Model Breast Tumors

4.3.1 Suspended Model Breast Tumor Samples

Gelatin models with suspended clay inclusions were built to mimic the breast with lumps. The clays (Modeling Clay, Crayola, Easton, PA) were made into cuboid shapes with 15mm in length, 15mm in width, and different heights (5-15mm) for suspended inclusions. The elastic modulus of the clay was 60 kPa, and it is within the range of the elastic modulus of excised breast tumors (30-72 kPa) measured by PEF in *ex vivo* breast tumor study [151]. Gelatin powders were mixed with water at 80 °C with a concentration of 0.12 g/ml, which was chosen so that the elastic modulus of gelatin is about 10 kPa. The choices were consistent with the elastic moduli of the normal breast tissues and those of breast tumors reported in the literature, which were 3-28 kPa and 11-106 kPa, respectively [81, 83, 155-158]. The gelatin solution was

poured into a 35 cm×23 cm×20 cm container and put into the 4°C refrigerator for 10 minutes to solidify. Subsequently the clay inclusions were placed on top of the gelatin layer. Afterward, another gelatin solution of the same concentration was poured into the container to enclose the clays as inclusions. When the gelatin was solidified, the clay inclusion would be suspended in the gelatin matrix. The total height of the gelatin matrix is 34 mm. A picture of the suspended breast tumor model is shown in Figure 4.25. The clay inclusions in the same row had identical dimensions, but they were embedded at different depths. The inclusions in the same column had different heights, but the distances from the gelatin surface to the tops of the inclusions were similar. The exact values of the inclusion dimensions and the depth profiles were measured by a caliper and listed in Table 4.8.

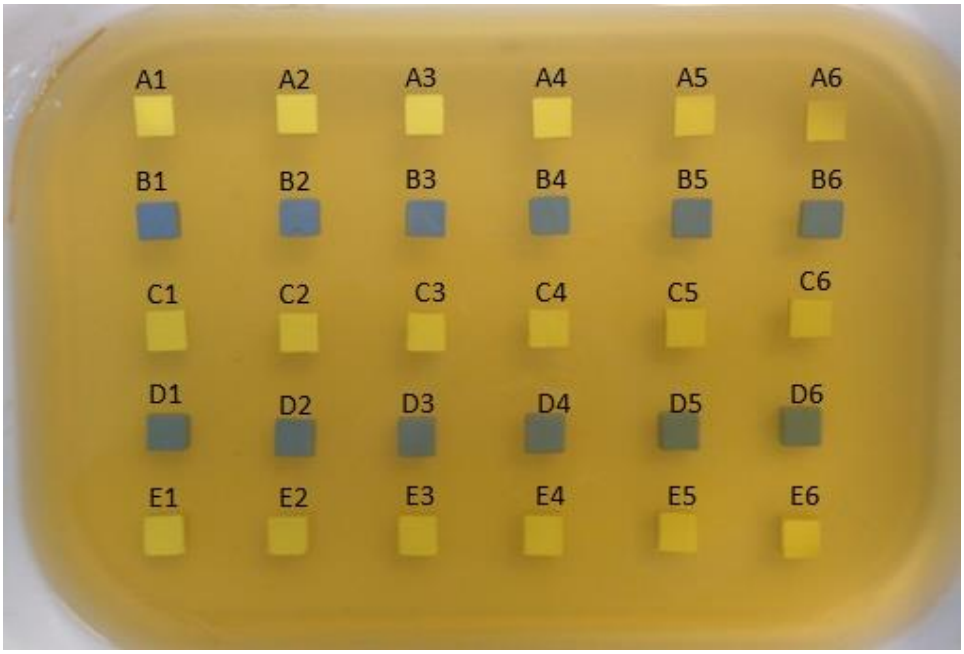

Figure 4.25 A picture of the suspended breast tumor model made of gelatin matrix with suspended clay inclusions.

Table 4.8 The dimensions and depths of the suspended inclusions in the model

Inclusion Number	Inclusion dimensions						Inclusion depths			
	Length (mm)		Width (mm)		Height (mm)		t_1 (mm)		t_2 (mm)	
	AVE	SD	AVE	SD	AVE	SD	AVE	SD	AVE	SD
A1	14.53	0.26	15.20	0.40	4.87	0.35	2.22	0.28	7.09	0.45
A2	15.24	0.38	15.26	0.20	4.98	0.29	4.09	0.33	9.07	0.44
A3	15.36	0.25	15.14	0.37	5.24	0.31	5.94	0.26	11.18	0.40
A4	15.90	0.35	15.17	0.23	4.97	0.42	7.21	0.32	12.18	0.53
A5	15.23	0.25	15.21	0.30	5.23	0.29	10.34	0.30	15.57	0.42
A6	15.36	0.26	15.55	0.24	5.30	0.28	11.92	0.21	17.22	0.35
B1	14.51	0.39	14.63	0.40	8.47	0.34	3.03	0.28	11.50	0.44
B2	15.19	0.20	15.18	0.35	7.97	0.32	4.07	0.39	12.04	0.50
B3	14.72	0.21	15.76	0.29	7.23	0.29	6.45	0.32	13.68	0.43
B4	15.40	0.31	15.69	0.37	7.45	0.35	9.55	0.38	17.00	0.52
B5	15.62	0.24	15.46	0.38	7.69	0.31	11.79	0.33	19.48	0.45
B6	15.62	0.39	15.27	0.20	7.71	0.31	11.95	0.41	19.66	0.51
C1	16.19	0.38	16.04	0.35	9.43	0.27	5.27	0.26	14.70	0.37
C2	16.15	0.27	15.32	0.24	9.66	0.30	7.00	0.33	16.66	0.45
C3	15.88	0.28	15.42	0.30	9.45	0.33	8.34	0.31	17.79	0.45
C4	15.67	0.21	16.07	0.30	9.29	0.33	11.21	0.48	20.50	0.58
C5	15.95	0.28	15.71	0.32	9.83	0.27	12.18	0.28	22.01	0.39
C6	15.85	0.39	16.18	0.26	9.73	0.34	13.67	0.40	23.40	0.52
D1	14.71	0.35	15.40	0.22	11.40	0.35	4.22	0.30	15.62	0.46
D2	14.66	0.29	14.89	0.33	11.58	0.29	6.66	0.28	18.24	0.40
D3	14.64	0.22	15.18	0.34	11.68	0.34	10.45	0.37	22.13	0.50
D4	14.85	0.28	14.95	0.36	11.57	0.31	12.13	0.28	23.70	0.42
D5	14.81	0.20	15.08	0.34	11.72	0.32	15.06	0.30	26.78	0.44
D6	15.20	0.40	14.83	0.37	11.68	0.36	16.24	0.31	27.92	0.48
E1	15.79	0.25	15.74	0.33	14.82	0.30	3.19	0.32	18.01	0.44
E2	15.77	0.38	15.75	0.31	15.04	0.27	6.44	0.29	21.48	0.40
E3	15.81	0.34	16.05	0.28	15.12	0.30	8.58	0.44	23.70	0.53
E4	15.40	0.35	15.71	0.38	15.11	0.32	10.30	0.29	25.41	0.43
E5	15.74	0.39	15.71	0.31	15.17	0.36	13.58	0.43	28.75	0.56
E6	15.66	0.30	15.64	0.35	14.78	0.35	15.59	0.39	30.37	0.52

4.3.2 Scanning Model Breast Tumor Sample with PEFs

Before the measurement, the sample was left in room temperature for 1 hour to equilibrate the temperature. Four PEFs with different contact sizes as listed in Table 4.1 were used to measure the elastic moduli of the entire gelatin model with inclusions. Five repeated measurements were taken on the same location by each PEF, and they were averaged. The result of the PEF scan on the model tissue was presented as a color coded elastic modulus map. As an example, the E maps generated by PEFs B and D, whose contact width were 6.5±0.2 mm and 9.8±0.3 mm, respectively, are shown in Figure 4.26. The green color represents the elastic moduli of the gelatin matrix (9-12 kPa), while the yellow (14-16 kPa) and red color (18-28 kPa) represents the elevated elastic moduli of areas containing the clay inclusions. Since the depth sensitivities of these PEFs were different, distinct elastic moduli were obtained using these PEFs on the same location. As can be seen, PEF B could only detect the left half part of the inclusions. It was because PEF B had a depth sensitivity of about 13 mm. When the inclusions were more than 13 mm deep from the gelatin surface, they were beyond the detectable depth of PEF B. Therefore, PEF B was unable to differentiate the gelatin and inclusions for the right part of the inclusions which were deeper embedded. Since PEF D had a depth sensitivity of 20 mm, it could detect most of the inclusions. However, the elastic modulus values of the inclusions in the first row (Inclusions A1-A6) measured by PEF D were smaller than those measured by PEF B. It was because those inclusions had a small height which was only about 5 mm and the entire inclusions were within the depth sensitivity of PEF D. The

proportion of inclusion to the entire volume that PEF D detected was smaller compared with that for PEF B. And thus the effective elastic modulus measured by PEF D was mostly from the elastic modulus of gelatin, resulting in a smaller value.

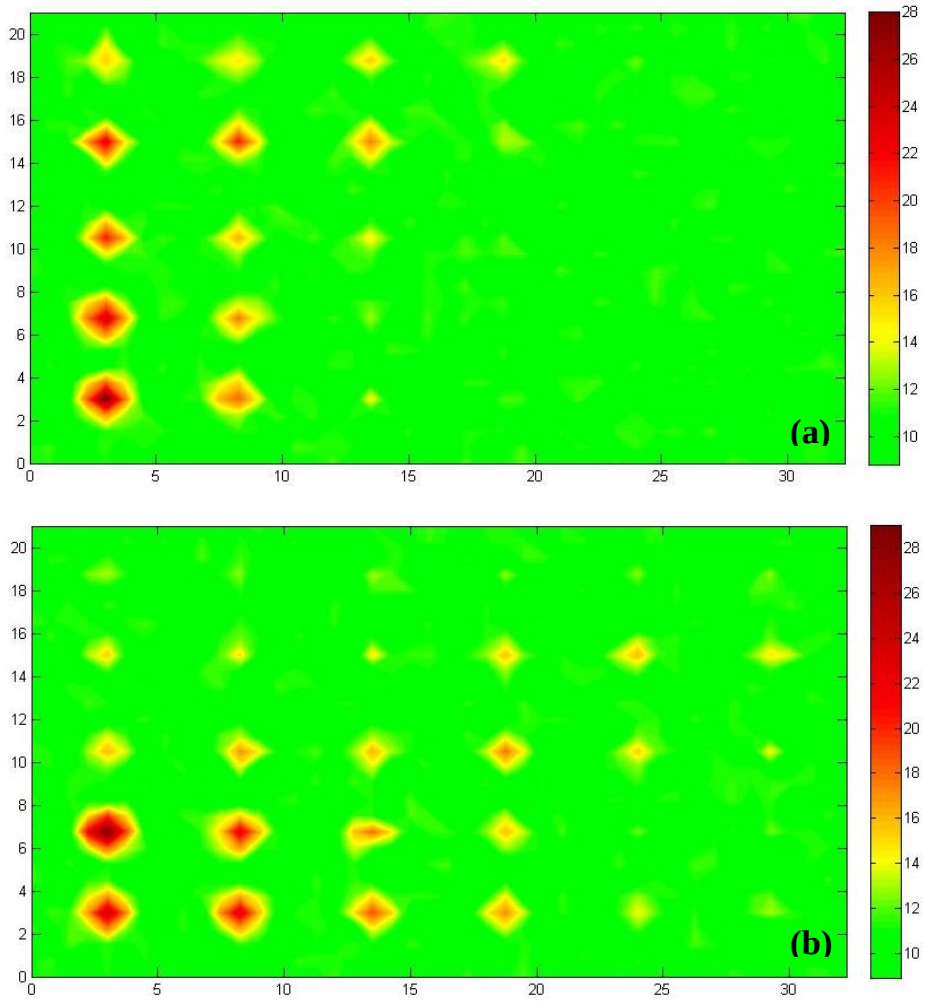

Figure 4.26 (a) The 2D elastic modulus map of the model generated by using the measurement results from PEF B, which had a contact width of 6.5±0.2 mm; (b) The 2D elastic modulus map of the model generated by using the measurement results from PEF D, which had a contact width of 9.8±0.3 mm.

After the PEF measurements, the depth profile of the tumor as illustrated in Figure 4.27, which is the distance from the gelatin surface to the top of the inclusion (t_1) and the distance from the gelatin surface to the bottom of the inclusion (t_2), were measured using a caliper and listed in Table 4.8.

4.3.3 3-Spring Model

For suspended breast tumors, if the distance from the surface to the bottom of the tumor (t_2) is larger than the depth sensitivity (d) of a single PEF as shown in Figure 4.27 (a), the normal tissue underneath the tumor and bottom part of the tumor beyond the depth sensitivity could not be measured by that PEF and thus they are negligible. The normal tissue on the top and the rest part of the tumor are like two elastic springs in series. Same with bottom supported breast tumors, the effective elastic modulus measured by that PEF can be calculated using the Equation 4-2. If the depth sensitivity of a single PEF is larger than t_2 as shown in Figure 4.27 (b), the normal tissue underneath the tumor should also be taken into account in deducing the effective elastic modulus. The system is similar to three springs connected in series. And therefore, the effective elastic modulus E measured by a single PEF, can be expressed as

$$\frac{d}{E} = \frac{t_1}{E_n} + \frac{t_2 - t_1}{E_t} + \frac{d - t_2}{E_n} = \frac{d - (t_2 - t_1)}{E_n} + \frac{t_2 - t_1}{E_t} \tag{4-4}$$

where d is the depth sensitivity of a single PEF; t_1 is the distance from the skin surface to the top of the tumor; t_2 is the distance from the skin surface to the bottom

of the tumor; t_2-t_1 is the height of the tumor; E_n and E_t are the elastic moduli of the gelatin and inclusion, respectively.

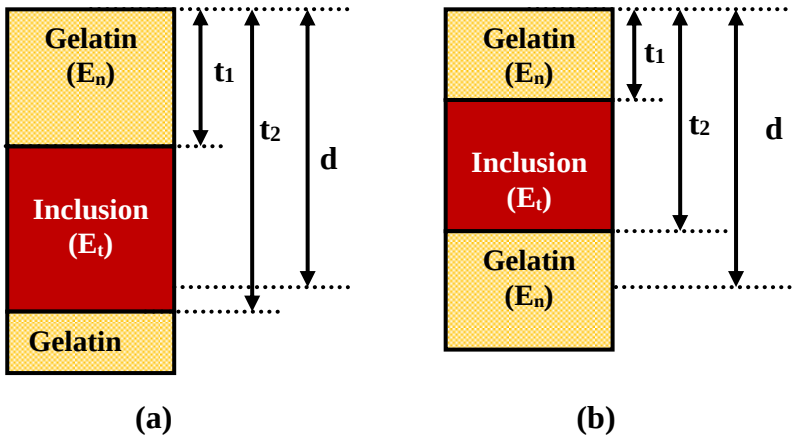

Figure 4.27 (a) A schematic illustrating the gelatin sample with suspended inclusion when $d<t_2$; (b) A schematic illustrating the gelatin sample with a suspended inclusion when $d<t_2$; d is the depth sensitivity of a single PEF.

4.3.4 Results Using 3-Spring Model

Equations 4-3 and 4-4 were used to deduce the depth profile of the tumors. The effective elastic modulus E was measured by PEFs with different contact widths. The elastic modulus of normal tissue (E_n) could be obtained by PEF measurements on normal tissue area, while the elastic modulus of inclusion (E_t) could not be measured directly, since the tumor was embedded in the sample. Similar to Section 4.2.2, E_t = 40 and 60 kPa were used to solve for t_1 and t_2. Extreme E_t values (E_t = 100 and 200 kPa) were also used to see how the assumption of E_t affected the deduced depth profile.

The deduced t_1 using the spring model theory was plotted versus the actual values in Figure 4.28. It is clear that all the data points are close to the dash line which has a slope of 1. It shows that all the estimated values agreed with the actual values very well. When E_t was 40 kPa or 60 kPa, which was within the range of the elastic modulus of breast tumors, the estimations of t_1 values were quite good. When E_t was 100 kPa or 200 kPa, which was much larger than the elastic modulus of the breast tumors, the estimations were not very different from the actual values. Therefore, we could draw the same conclusion with the inversion technique that the estimation of t_1 is not sensitive to the assumed E_t values. And thus it is feasible to use assumed E_t to deduce d_1 values.

The deduced t_1 versus actual t_1 was fit to linear curve and the fitting results are listed in Table 4.9. The slopes were very close to 1, no matter which E_t value was used for spring model theory. When E_t was smaller than 100 kPa, R^2 was larger than 0.977, indication there was good correlation between the deduced t_1 and the true t_1. When E_t was 200 kPa, R^2 was slightly smaller. It was understandable since the elastic modulus of the tumor in the model was 60 kPa. The linear fitting further prove that we were able to estimate t_1 accurately using spring model theory.

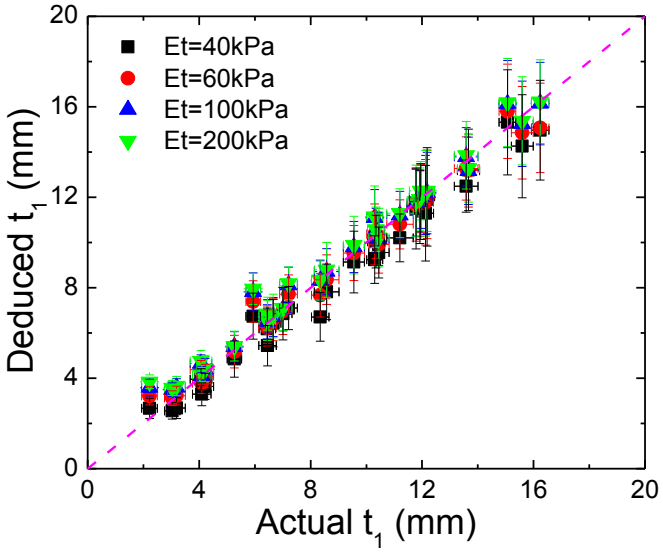

Figure 4.28 The estimated t_1 values using spring theory versus the actual values. The dashed line has a slope of 1.

Table 4.9 The linear fitting of the deduced t_1 of suspended breast tumors using spring model theory with different E_t versus the actual t_1

E_t (kPa)	Slope		Intercept		R^2
	Value	Standard deviation	Value	Standard deviation	
40	0.94	0.05	-0.08	0.29	0.9788
60	0.93	0.04	0.45	0.27	0.9790
100	0.93	0.04	0.80	0.25	0.9770
200	0.91	0.04	1.03	0.24	0.9596

The estimated t_2 values deduced by spring model versus the actual values are shown in Figure 4.29. Apparently the deduced t_2 had good correlation with actual values. Besides, it is consistent with t_1 that the estimation of t_2 was not sensitive to the assumed E_t values. The linear fitting results are listed in Table 4.10. The slopes were close to 1 and the R^2 were larger than 0.95, no matter which E_t was used in the

equations. The slopes of the linear fitting for t_2 were smaller than those for t_1 and the intercepts were larger, indicating the estimation of t_2 was not as accurate as t_1.

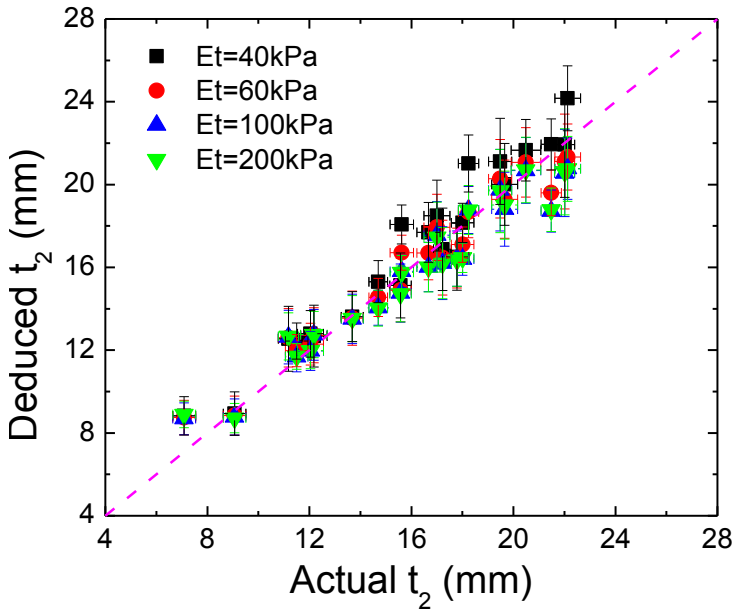

Figure 4.29 The estimated t_2 values using spring theory versus the actual values. The dashed line has a slope of 1.

Table 4.10 The linear fitting of the deduced t_2 of suspended breast tumors using spring model theory with different E_t versus the actual t_1

E_t (kPa)	Slope		Intercept		R^2
	Value	Standard deviation	Value	Standard deviation	
40	0.99	0.06	0.95	0.99	0.9595
60	0.86	0.06	2.13	0.90	0.9607
100	0.82	0.06	2.41	0.84	0.9544
200	0.81	0.05	2.51	0.74	0.9553

A schematic of the suspended breast tumor model with estimated depth profile is shown in Figure 4.30. The blue cuboids showed the exact locations of the inclusions, while the red cuboids represented the estimated sizes and locations of the inclusions. It should be noted that the estimated sizes and locations were averaged values, since we used multiple E_t values to do the calculations. As can be seen, the red cuboids overlapped with blue cuboids for most of the inclusions and they were shown as a purple color. Therefore, the deduced 3D profiles of the inclusions were quite accurate.

Besides, for the inclusions C6, D4-D6, and E4-E6, because their t_2 values were larger than the maximum depth sensitivity of PEFs, we could not assess t_2 using the four PEFs in the study. Only t_1 values were deduced for them. By using the four PEFs listed in Table 4.1, the depth profiles of the inclusions when they were less than 2 cm deep could be successfully determined, which was sufficient for tumors in a normal size breast but not for tumors whose bottom surfaces were more than 2 cm deep. For larger breasts and deeper tumors, PEFs with a larger contact width can be used.

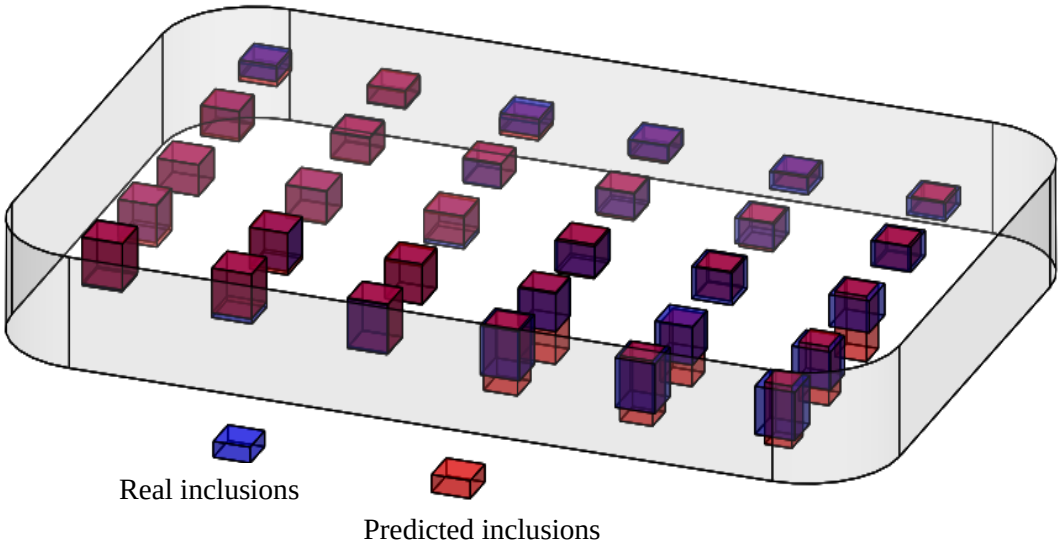

Figure 4.30 A schematic of the gelatin model with suspended inclusions. The blue cuboids showed the location of the inclusions. The red cuboids illustrated the estimated locations of the inclusions.

4.3.5 Deduce the Depth Profile of Spherical Suspended Tumors

To evaluate the performance of applying spring model theory to estimating depths profiles of breast tumors, gelatin models with spherical suspended clay inclusions were also built to mimic the breast with lumps. The procedures of making these models were similar to those described in Section 4.3.1. The clays were made into spheres with different diameters. The elastic modulus of the clay was 60 kPa, the same with the models in previous sections. Gelatin powders were mixed with water at 80°C with a concentration of 0.08 g/ml so that the elastic modulus of gelatin is about 8 kPa. The height of the gelatin matrix was 30 mm. A picture of the breast tumor model is shown in Figure 4.31 and the schematic of the cross section of the model is

shown in Figure 4.32. The inclusions in the same column had the same diameters but were embedded at different t_1. The inclusions in the same row had distinct sizes but their t_1 were similar. The exact values of the inclusion dimensions and the depth profiles were measured by a caliper and listed in Table 4.11.

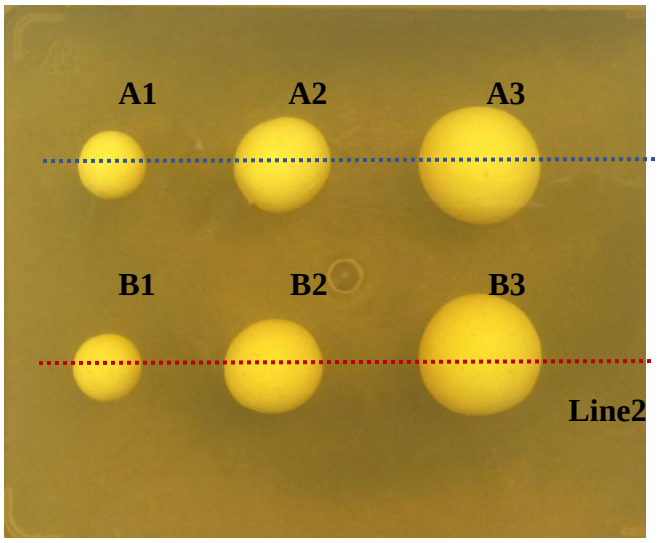

Figure 4.31 A picture of the suspended breast tumor model made of gelatin matrix with spherical clay inclusions.

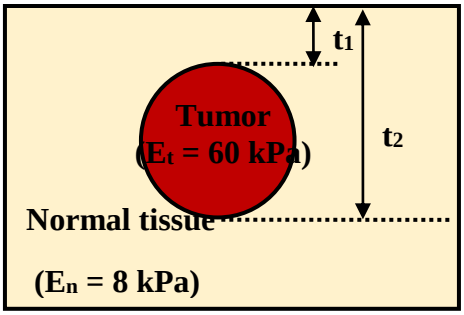

Figure 4.32 A schematic of the cross section of spherical suspended breast tumor model. t_1 is the distance from the model surface to the top of the tumor and t_2 is the distance to the bottom of the tumor. The elastic modulus of the normal tissue (E_n) and tumor (E_t) were 8 and 60 kPa, respectively.

Table 4.11 The dimensions and depths of the spherical suspended inclusions in the model

Inclusion #	Inclusion diameter (mm)		Inclusion depth t_1 (mm)	
	AVE	SD	AVE	SD
A1	10.5	0.3	3.5	0.3
A2	15.8	0.2	3.0	0.4
A3	20.1	0.3	2.8	0.2
B1	10.8	0.3	5.6	0.3
B2	16.8	0.4	5.3	0.3
B3	20.9	0.3	4.6	0.1

Five PEFs with different contact sizes, including four PEFs listed in Table 4.1 and another with a contact width of 12.1±0.3 mm, were used to measure the elastic moduli of the entire gelatin model with inclusions. Five repeated measurements were taken on the same location by each PEF, and were averaged. The depth profiles of the inclusions were deduced using the spring model theory as explained in Sections 4.3.3 and compared with the actual values in Figure 4.33. It clearly shows that the depth profiles of the tumors deduced with spring model theory were very close to the actual depths.

The averaged t_1 and t_2 deduced using spring theory were plot versus their actual values in Figure 4.34 (a) and (b), respectively. Linear regression was performed and the R^2 values were close to 1, indicating there was good correlation between the deduced and actual depths. The slopes of linear fitting were 0.983 and 1.012 for t_1 and t_2, further showing that using spring model theory could estimate the depth profile of suspended breast tumors very accurately.

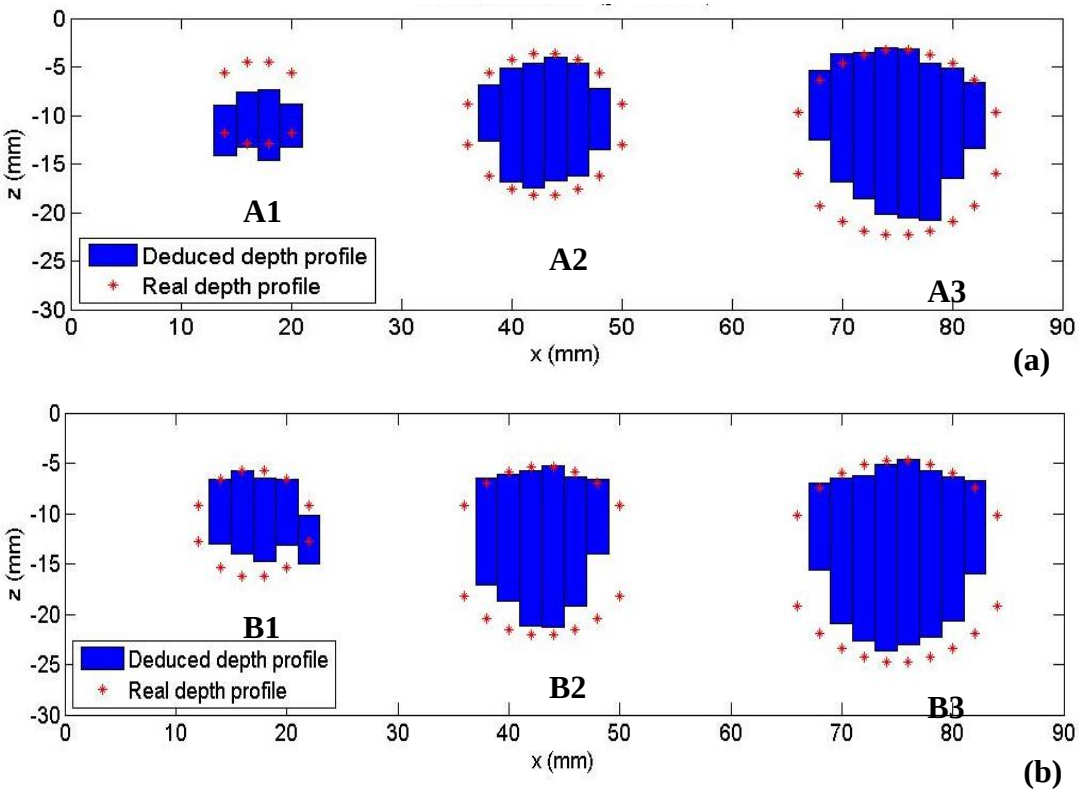

Figure 4.33 Comparison of the tumor depth profiles deduced with spring model theory and those measured using a caliper in cross section view

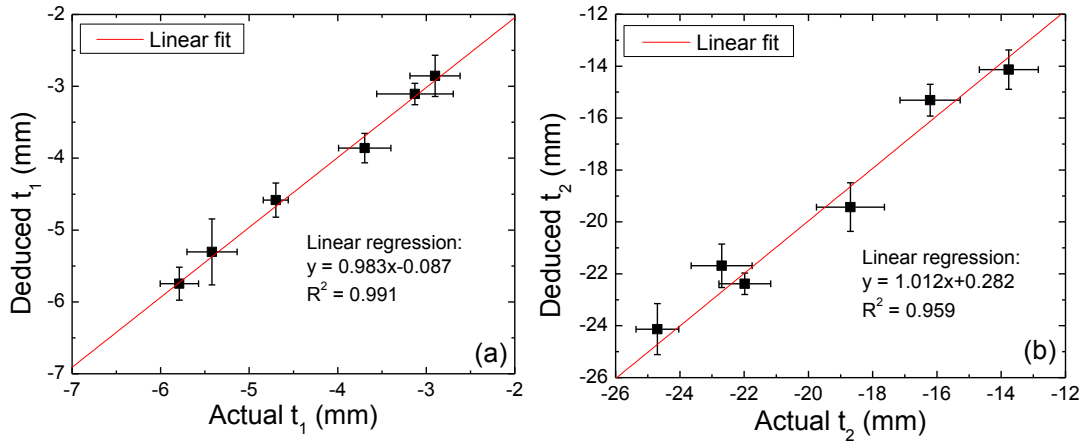

Figure 4.34 (a) the estimated t_1 values using spring model theory versus the actual values; (b) the deduced t_2 versus the actual values;

4.3.6 Deduce the Depth Profile of Suspended Tumors with Irregular Shapes

As is known to all, the shape of many breast tumors is irregular. To further validate the spring model theory for estimating depth profile of breast tumors, gelatin models with irregular shaped inclusions were made to simulate the breast tumors. One inclusion was like two tumors merged together, and the other inclusion was a spherical tumor with spiculated boundaries which was a sign of malignancy. Both shapes could be found in excised breast tumors in previous *ex vivo* study [151]. The procedures of making the models were the same with those described in Section 4.3.1. A picture of the model is shown in Figure 4.35. Five PEFs with different contact sizes were used to measure the effective elastic modulus of the entire model. The spring model theory was applied to deduce the depth profiles of the inclusions and a 3D image was created based on the deduced results as shown in Figure 4.36. Obviously, the inclusion on the left looked like two tumors merged together, very consistent with the shape in the picture of the model (Figure 4.35). The inclusion on the right in the 3D image had rough boundaries, similar to the shape in the picture. However, the spicules in the inclusion could not be fully speculated by the spring model theory. When two spicules were at the same lateral location but different depths, the deduced depth profile would show only one spicule with a larger size. It was due to the reason that in the 3-spring model theory, we assumed that the sample had a three-layer structure (normal tissue-tumor-normal tissue). If the assumption was not valid in the case of two spicules, the spring model theory could not accurately deduce the depth profile. For the inclusion on the right, although the spring model theory could not

speculate the spicules completely, the depth of major part of the tumor and rough boundary was estimated accurately enough for the diagnostics of breast tumors. Therefore, it can be concluded that the depth profiles of irregular shaped tumors could be estimated accurately using spring model theory.

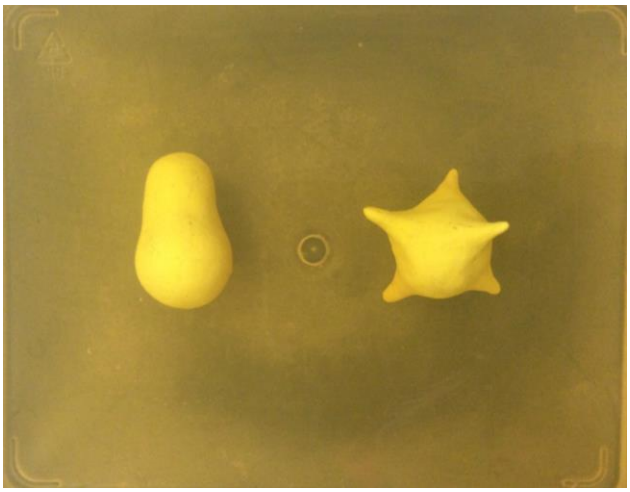

Figure 4.35 A picture of the suspended breast tumor model made of gelatin matrix with irregular shaped clay inclusions.

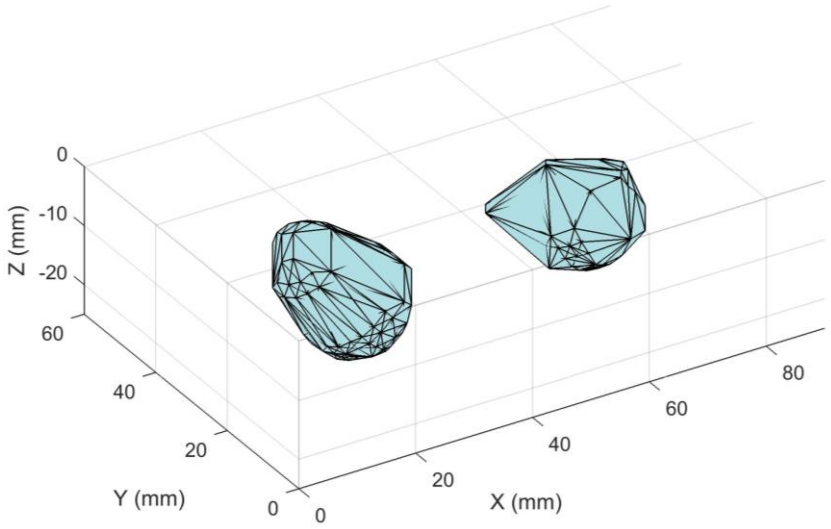

Figure 4.36 The 3D image of the irregular shaped suspended inclusions deduced from PEF measurement results

4.4 Conclusions

In this chapter, the depth sensitivity of a piezoelectric finger (PEF) in the housing was examined and the results showed that the depth sensitivity of a PEF is about the twice of the contact width. The depth sensitivity is independent on the elastic modulus of normal tissue (E_n) or that of tumor (E_t). It is not affected by the size of the tumors unless the tumor was less than 5 mm. Since most of the breast tumors in the *in vivo* study in Chapter 3 had a size larger than 10 mm, it is safe to say that the depth sensitivity of the PEF in the housing is twice the contact width the majority of breast tumors.

With a larger contact, a PEF can assess the elastic response of deeper tissues. To deduce the depth profile of breast tumor, a set of PEFs with different contact sizes were applied on the same sample. A 2-spring model theory was then developed to fast determine the depth profile of both bottom supported and suspended tumors. When applied to bottom supported breast tumor models, the 2-spring model theory can determine the depth t_1 of tumors accurately, with an error of less than 1.1 mm. We also found that the estimated depth values were insensitive to the assumed E_t in the spring model, consistent with the findings using inversion technique.

An inversion technique based on finite element analysis (FEA) was also developed to retrieve the depth information of the tumor from PEF's elastic modulus measurements. It calculated the elastic moduli from the model in FEA, compared with PEF results, and modified the model until the elastic moduli from FEA were the same with those from PEF. The inversion technique was applied to bottom supported

breast tumor models and it showed that the deduced tumor depth t_1 agreed with the actual value with an error less than 0.6 mm. Besides, the deduced depths were found not sensitive to the initial guess of depth t_1 and the E_t values assumed.

Both the 2-spring model and the inversion technique can determine the depth profile of bottom supported breast tumor models accurately and robustly. However, the inversion technique is time-consuming and requires heavy computations. The 2-spring model theory, on the other hand, can give the results in seconds.

A 3-spring model was then developed based on 2-spring model by adding an additional normal tissue layer under the tumor. It was applied to suspended breast tumor models, and the deduced depth profiles t_1 and t_2 correlated with the actual values very well, with an error smaller than 2.1 mm. When the tumors were irregular, the shapes could be restored well by the spring model theory, including some of the spicules at the tumor margin. Therefore, it is feasible to use spring model theory to estimate the tumor depth without knowing the exact E_t values and the 3D image of the tumor could be obtained.

5. DETERMINE THE ELASTIC MODULUS AND DEPTH PROFILE OF SKIN

Human skin is a complex material, composed of three heterogeneous layers: epidermis, dermis, and hypodermis. The elastic modulus and thickness of each skin layer vary as a function of age, body zone, hydration, and etc. Mechanical testing of skin contributes to detection of skin diseases and quantification of effectiveness of dermatologic products. Different noninvasive methods, such as suction test, torsion test, and tensile test, have been developed to characterize the mechanical properties of skin as described in detail in Chapter 1. However, during these tests, the natural state of stress on the skin was modified and the mechanical properties measured might be affected.

In this chapter, indentation by Piezoelectric Fingers (PEFs) was used to measure the effective elastic modulus of the skin. Since the depth sensitivity of a PEF depends on the contact size, a PEF with a larger contact size can measure the stiffness of a deeper tissue. Therefore, the elastic modulus and thickness of the skin is deduced simultaneously by coupling PEF measurements with an empirical formula for a two-layer structure. The methodology is validated using finite element analysis (FEA) with finite skin thickness. After that, the methodology is applied to skin phantoms and excised porcine skin samples to retrieve the elastic modulus and thickness of dermis simultaneously.

5.1 Skin Structure

Human skin is a complex organ with a layered structure that varies in thickness depending on what part of the body it covers [85]. Skin has three main layers, the epidermis, the dermis and the hypodermis layer as shown in Figure 5.1. The epidermis, the outermost layer of skin, is relatively thin, only 0.05 mm on the eyelids and 1.5 mm on the palms and soles [87, 88]. It has the highest elastic modulus (approximately 1 MPa [138]) compared with the other skin layers. The dermis, beneath the epidermis, is a thick layer of fibrous and elastic tissue that gives the skin its flexibility and strength. The thickness of dermis ranges from 0.3 mm on the eyelids to 4 mm or more on the soles and palms [89]. The elastic modulus of dermis layer is about 88 to 300 kPa [163-166]. The hypodermis layer is made up of fat and connective tissue and can be 3-100 mm thick [90]. It has the lowest stiffness among all skin layers, only a few kPa [167].

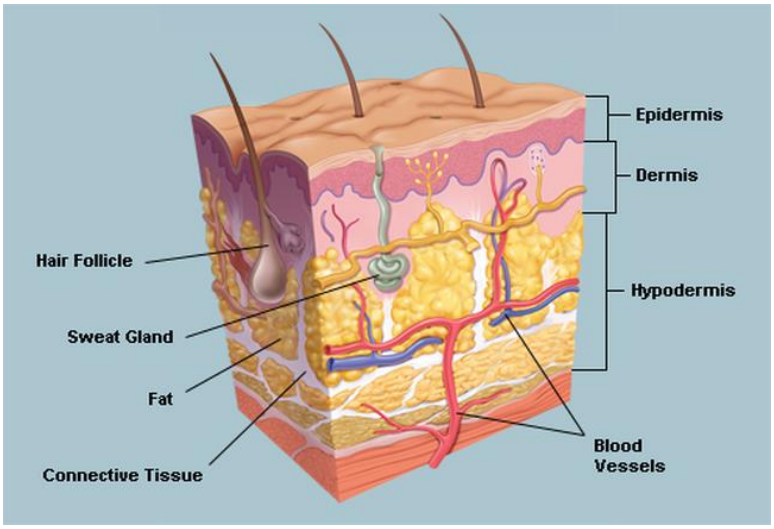

Figure 5.1 A schematic of human skin [168]

Since the epidermis layer of human skin is very thin compared to the other two layers of the skin, the effective elastic modulus measured by a PEF on the skin surface mostly depends on the elastic moduli of the dermis and the hypodermis layer. Therefore, we do not separate the epidermis from the dermis layer in the following chapters. For simplicity, we call the combination of the epidermis and dermis layer as dermis. The effective elastic modulus of the combination of the epidermis and dermis layer denoted as E_{dermis} is much larger than the elastic modulus of hypodermis layer (E_{fat}). Besides, both the epidermis and dermis layer are thin. Therefore, the skin can be modeled as a thin film of stiff material (dermis) on a soft substrate (hypodermis) as illustrated in Figure 5.2.

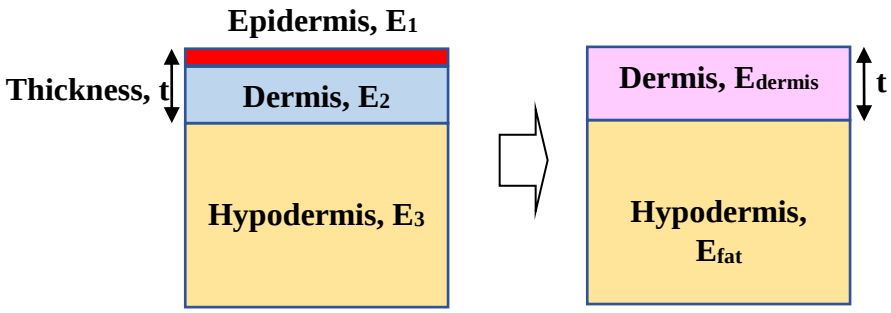

Figure 5.2 A schematic illustrating that the skin is modeled as a film-substrate system.

5.2 Skin Elastic Modulus Measured by Piezoelectric Fingers (PEFs)

5.2.1 Piezoelectric Fingers (PEFs) for Skin Measurements

The Piezoelectric Fingers (PEFs) for skin measurements consists of 3 layers: a lead zirconate titanate (PZT) layer on the top, a stainless steel layer in the middle, and another PZT layer on the bottom as shown in Figure 3.1 (a). The top and bottom PZT layers are 5H4E PZT sheet (Piezo Systems Inc., Cambridge, MA) with a thickness of 127 μm. The top layer serves as a driving layer and the bottom is the sensing layer. The stainless steel (Alfa Aesar, War Hill, MA) layer in the middle is 50-μm thick.

The PEFs used in this chapter were 3.5±0.5 mm wide. The lengths of driving and sensing PZT layers were 22±0.5 mm and 12±0.5 mm, respectively. The stainless steel was 33±0.5 mm long. To make the PEF, the driving and sensing PZT were bonded to the stainless steel using nonconductive epoxy (Henkel Loctite, Westlake, OH) along the edges, and a very small patch of conductive epoxy (ITW Chemtronics, Kennesaw, GA) at the center. After curing overnight, different sizes of cylindrical probes were bonded to the PEF using nonconductive epoxy. Since the human skin has a small thickness, the probes of the PEF were made from thin metal wires of different diameters. The wires were cut into 10 mm-long segments using precision wire saw (WS-22, Princeton Scientific, Easton, PA) so that the contacting surfaces of the probes were very smooth. The PEF was then clamped to an acrylic fixture (as shown in Figure 3.1 (b)) made in the machine shop with 5 layers of scotch tapes (Scotch Magic tape, 3M, St. Paul, MN) as a spacer. The radiuses of the probes are shown in Table 5.1.

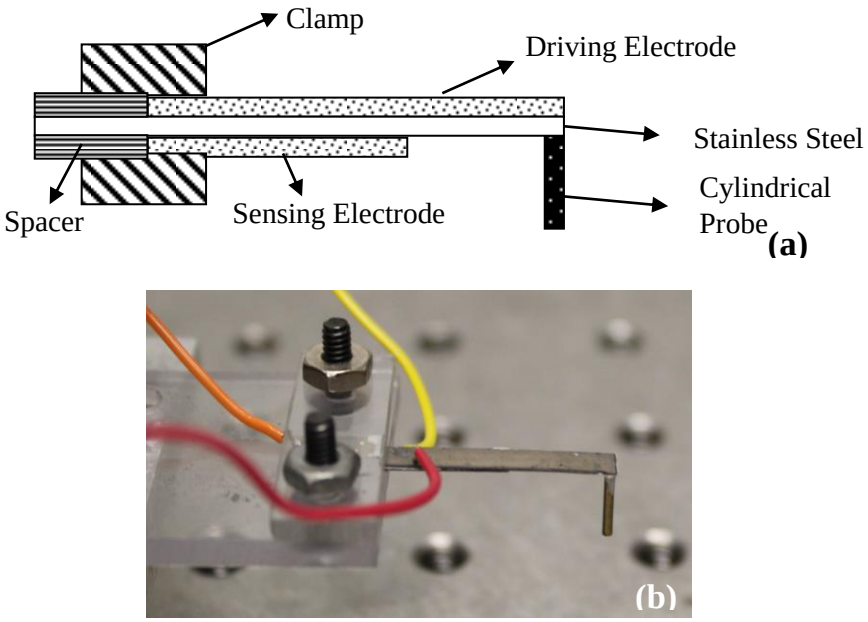

Figure 5.3 (a) A schematic of a piezoelectric finger (PEF) with cylindrical probe for skin and skin cancer measurements; (b) A picture of the PEF in acrylic clamp.

Table 5.1 The radiuses of the PEF probes

PEF#	Contact radius (mm)
1	0.23±0.01
2	0.38±0.01
3	0.42±0.01
4	0.52±0.01
5	0.66±0.01
6	0.83±0.01
7	0.98±0.01
8	1.05±0.11
9	1.38±0.05
10	1.68±0.02
11	2.00±0.01
12	3.80±0.11

The PEF measurement system for skin consists of a PEF, a custom-build electronic board, and a laptop computer as shown in Figure 5.4. The electronic board worked to generate the applied voltages on the driving PZT of the PEF and to read the induced voltages from the sensing PZT of the PEF. It communicates with the laptop through a RS232-USB port.

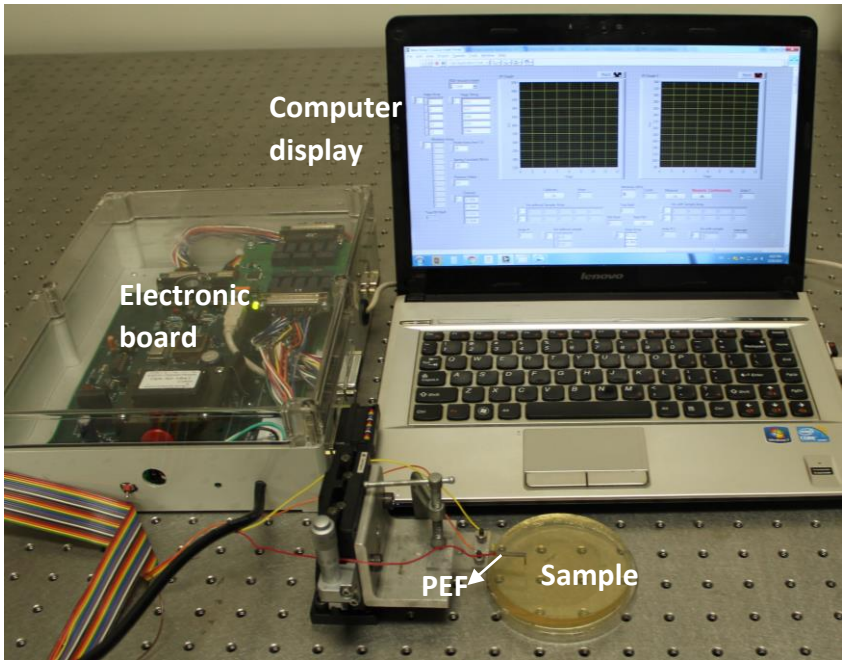

Figure 5.4 A photograph of PEF measurement system which consists of a PEF, an electronic board, and a laptop for control and display.

5.2.2 Elastic Modulus of Skin

As an example, the elastic modulus of a 40 mm × 40 mm × 7 mm porcine skin sample measured by 12 PEFs with different contact sizes is shown in Figure 5.5. The elastic modulus of the sample decreases with the contact size at the beginning due to

the reason that the depth sensitivity of a PEF is related to its contact size. A PEF with a larger contact can measure the stiffness from deeper tissues. As illustrated in Figure 5.2, the skin can be modeled as a stiff film (dermis) on a soft substrate (hypodermis). The elastic modulus measured by a large contact, i.e. 2 mm in radius, is mostly composed of the modulus of the hypodermis, and therefore is smaller than that measured by a small contact. However, the measured elastic modulus by 3.8-mm contact size increases due to a limited thickness in skin sample. When the depth sensitivity of a PEF is larger than the sample thickness, it may detect the stiff substrate underneath the sample, for example petri dish and table top, resulting in an increase in the measured elastic modulus. A methodology is then developed to retrieve the elastic modulus and thickness of dermis from PEF measurements.

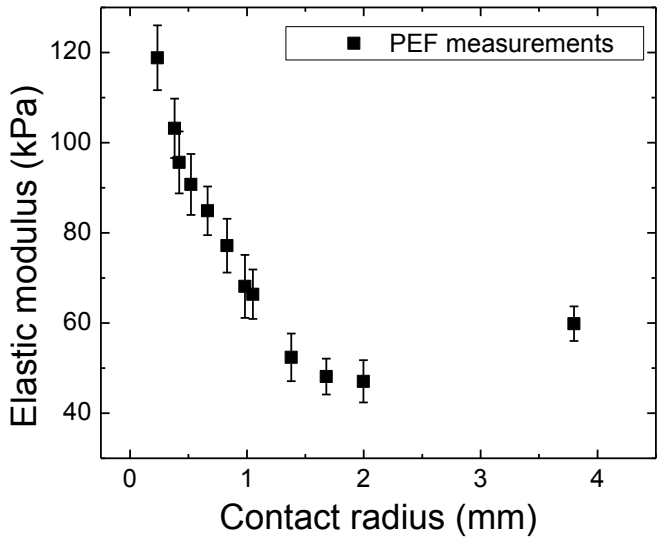

Figure 5.5 Elastic modulus measured by PEFs with different contact size on porcine skin sample

5.3 Determine the Elastic Modulus and Thickness of Dermis

5.3.1 Methods to Deduce the Modulus and Thickness in a Film-Substrate System

Indentation of an elastic thin film on a substrate has been extensively studied in the literature. Several models have been proposed to describe the relationship between the effective elastic modulus and the elastic properties of the film-substrate system, indenter geometry, and film thickness in order to allow film modulus and thickness to be extracted from data collected from indentation tests.

Doerner and Nix [169] developed an empirical model including exponential terms depending on the relative indentation depth, h/t, where h is the indentation depth and t is the film thickness, multiplied by an empirically determined weight factor α. The expression was valid only for Berkovich indenter discussed in their paper. King [170] modified the model using numerical analysis and extended it for different indenter geometries. Battacharya and Nix [171] demonstrated that results from finite element method were in good agreement with King's model for aluminum film on silicon substrate and vice versa. Saha and Nix [172] subsequently modified King's model for non-flat indenter geometries. They applied the model to aluminum films of various thickness on different substrates (sapphire, silicon and aluminum). The calculated film modulus value was in the order of magnitude of the actual value for indentation depths less than 50% of the film thickness, but with rather large variance. Another analytical model was developed by Bec et al. [173, 174] , based on the indentation by cylindrical flat punch on an homogeneous film deposited onto a

semi-infinite substrate. The system was modelled by two spring connected in series and the global stiffness was calculated from the reciprocal sum of the film stiffness and the substrate stiffness. Gao [175] developed an analytical expression with a perturbation method for the film and substrate modulus, from the analysis of the contact between a cylindrical flat punch and a coated material. The ratio of the film and substrate modulus has to be between 0.5 and 2, which gives the limit of use for this model. Rar [176] proposed an extension of Gao's model to become applicable to a larger range of film and substrate moduli mismatch, from 0.1 to 10. However, in Gao or Rar's models, the Poisson's ratios of the film and substrate have to be known, which brings difficulty in applying the models to skin and skin cancers.

Recently, Perriot and Barthel [177] proposed an empirical expression derived from Green's function to calculate the effective elastic modulus of a semi-infinite film-substrate system as illustrated in . It has been showed that the model of Perriot et al. had the best agreement with the results from finite element method compared with the models of Bec et al. and Rar et al., in the case of a rigid layer onto a compliant substrate [178].

In the model of Perriot et al., the effective elastic modulus (E) of the film-substrate system by indentation can be expressed as

$$E = E_s + \frac{E_f - E_s}{1 + (\frac{tx_0}{a})^n} \tag{5-1}$$

where E_f and E_s are the elastic moduli of film and substrate, respectively; t is the thickness of film; a is the radius of the indenter; n and x_0 are adjustable variables. x_0 depends on the moduli ratio of the two layers:

$$x_0 = -0.093 + 0.792\log(\frac{E_f}{E_s}) + 0.05[\log(\frac{E_f}{E_s})]^2 \tag{5-2}$$

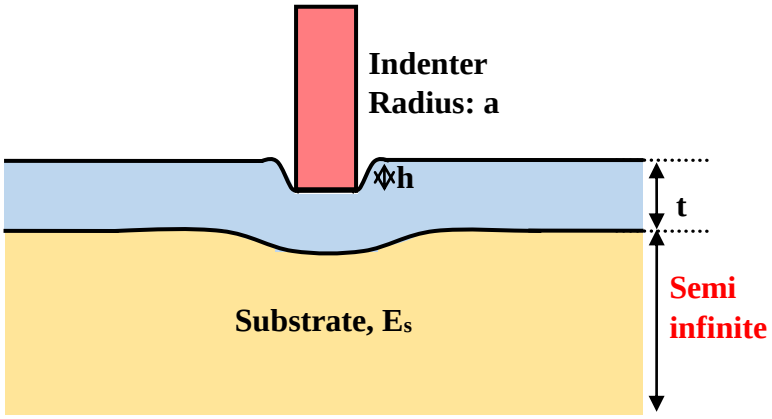

Figure 5.6 An illustration of the indentation on a semi-infinite film-substrate system

In the skin, the thin and stiff dermis layer is the film and the thick and soft hypodermis layer is the substrate. The effective elastic moduli measured by PEFs with different contact sizes on the skin surface are a combination of the respective moduli of the dermis and the hypodermis. The relative contribution of each individual layer to the effective elastic modulus is determined by the thickness of dermis and the

contact size of each PEF. Therefore, the effective elastic modulus E measured by PEF indentation can be expressed as

$$E = E_{fat} + \frac{E_{dermis} - E_{fat}}{1 + (\frac{tx_0}{a})^n} \tag{5-3}$$

where E_{dermis} is the elastic modulus of the dermis layer and E_{fat} is the elastic modulus of the hypodermis which is mostly fat; t is the thickness of dermis; a is the radius of the PEF contact; n and x_0 are adjustable variables. x_0 depends on the moduli ratio of the two layers:

$$x_0 = -0.093 + 0.792 \log(\frac{E_{dermis}}{E_{fat}}) + 0.05[\log(\frac{E_{dermis}}{E_{fat}})]^2 \tag{5-4}$$

The equation has been proved to be in good agreement with the results from finite element method when the modulus ratio between the two layers varies between 0.01 and 100. The elastic modulus of dermis is in the range of 40 to 2000 kPa [135, 137, 139] and the elastic modulus of hypodermis is about 10 kPa. Therefore, it is possible to use the model of Perriot et al. to extract the mechanical properties and thickness of human skins from PEF indentation results.

5.3.2 Evaluate the Method Using Finite Element Analysis (FEA)

The model developed by Perriot et al. was derived from semi-infinite samples, while human skins have finite thickness. It remains unclear whether the model could be applied to deduce the mechanical properties of skin. Finite element simulations were done to evaluate the performance of the model for skin applications.

5.3.2.1 FEA Model Creation

An axisymmetric model was used to minimize the computation time, since the indenter was a cylindrical. The model consisted of a stiff dermis layer and a soft hypodermis layer as illustrated in Figure 5.7. The radius of the skin model was 125 mm, large enough for the indentation test. The thickness of the dermis layer, t, changed from 1 mm to 3 mm, which was consistent with the thickness of human skin. The thickness of the skin model, D, changed from 10 mm to 150 mm, in order to include various hypodermis thickness.

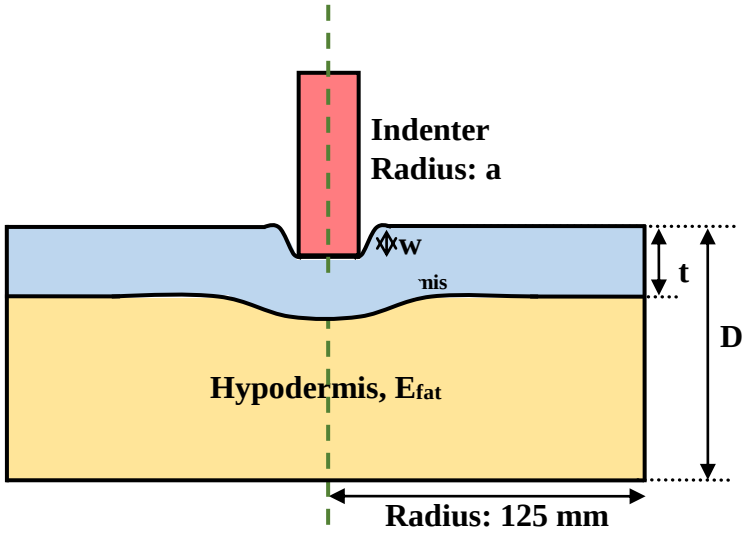

Figure 5.7 A schematic to illustrate the skin model created in finite element simulation

The dermis and hypodermis in the skin model were defined as isotropic, linearly elastic materials. The Young's modulus of dermis layer, E_{dermis}, was assumed to be 38, 68, 100, 130, and 170 kPa in the simulations. Since the hypodermis layer

was mostly fat tissue, the Young's modulus of hypodermis was defined as 8 kPa. Poisson's ratio of both the dermis and hypodermis was defined as 0.49999 since most soft tissues are nearly incompressible with Poisson's ratio ranging from 0.49000 to 0.49999 [160, 161]. The mesh of the skin model was set dense enough so that the convergence could be reached. Figure 5.8 shows a portion of the mesh in the skin model with a dermis thickness of 2.5 mm.

In human skins, the dermis and hypodermis layers are bond closely. Therefore, the contact surfaces of dermis and hypodermis were defined as "tie" in constraint with the contact surface in hypodermis as "master surface" and the surface in dermis as "slave surface". The boundary condition of the skin model was defined that the bottom of the model was "encastred". The left edge of the model was the symmetry axis and it was set as "XSYMM" since it was an axisymmetric model. A uniform displacement (0.01 mm) was applied to the skin surface to simulate the indentation with rigid and flat-ended cylindrical indenters. The radius of the indenter, a, varied from 0.01 mm to 5.00 mm in the simulation.

5.3.2.2 Elastic Modulus of Skin from FEA

As an example, the simulation result of indentation on the skin model with an indenter of 5 mm in radius is shown in Figure 5.8. The thickness of the dermis was 2.5 mm and the total thickness of the skin was 150 mm. The reaction forces exerted on the model surface were summed to calculate the effective elastic modulus. Based on Hayes' solution [162], elastic modulus can be deduced using the following equation:

$$E = \frac{(1-\nu^2)F}{2a\kappa(a/h,\nu)w} \tag{5-5}$$

where E is elastic modulus; F is the indentation force, which can be calculated from the simulation results; ν is Poisson's ratio, which is 0.49999 defined before simulations; w is the indentation depth, which is 0.01 mm as determined in the boundary condition; a is the radius of the indenter; h is the thickness of the tissue; κ is a scaling factor that depends on the aspect ratio a/h and Poisson's ratio ν.

FEA was performed for indenters ranging from 0.01 to 5 mm and the effective elastic modulus calculated from simulations was plotted versus the indenter radius in Figure 5.9. The total thickness of the skin model (D) was 150 mm, and the thickness of dermis layer (t) was 2.5 mm. Young's moduli of dermis and hypodermis were 38 kPa and 8 kPa, respectively. The data was fit to the Perriot's model using the Equations 5-3 and 5-4 shown as the red curve in the figure. Obviously, the data fit to the model very well, with R^2 larger than 0.999. From the fitting curve, the elastic moduli of the dermis and hypodermis were determined to be 37.6 kPa and 7.6 kPa, respectively, in good agreement with the values defined in the simulation. The deduced thickness of dermis was 2.56 mm, very close to the dermis thickness in the skin model. The result suggests that the model developed by Perriot et al. can be applied to determine the mechanical properties and thickness of human skins.

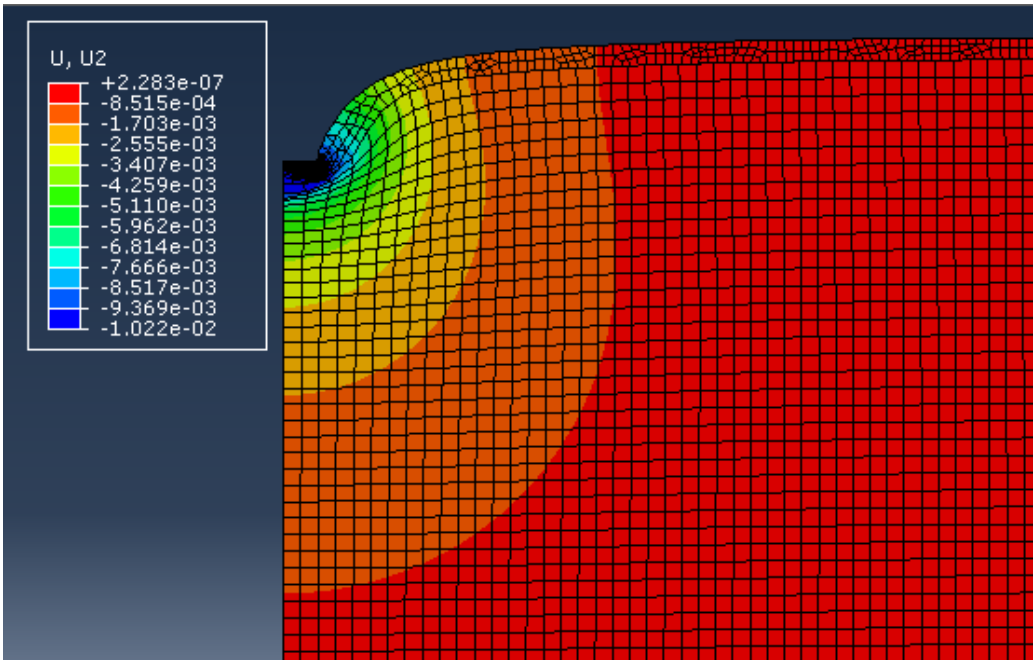

Figure 5.8 A portion of the skin with a 2.5-mm thick dermis layer simulated in ABAQUS. The radius of the model was 125 mm and the radius of the indenter was 5 mm.

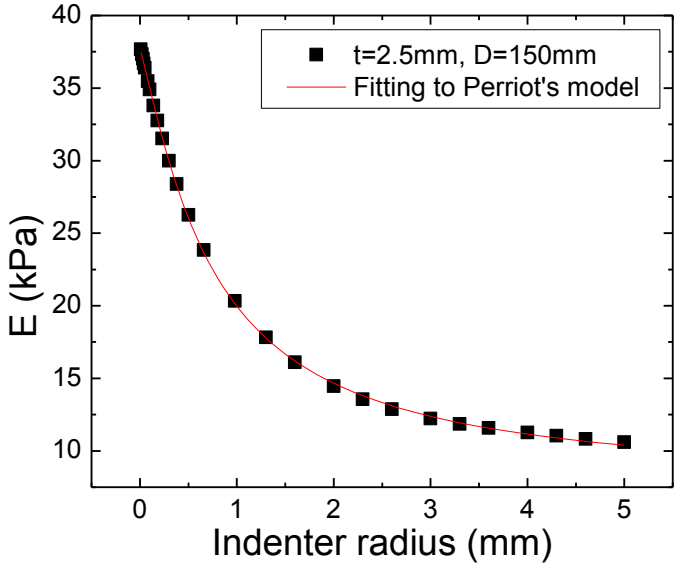

Figure 5.9 Effective elastic modulus (E) versus indenter radius from finite element analysis. The dermis thickness (t) was 2.5 mm and the total thickness of the model (D) was 150 mm.

5.3.2.3 Results with Finite Sample Thickness

Skin models with different hypodermis thickness were also simulated in FEA to evaluate the performance of using Perriot's Model for skins. The effective elastic modulus versus indenter radius when the dermis thickness was 1.0 mm is plotted in Figure 5.10. The elastic moduli of dermis and hypodermis were 38 kPa and 8 kPa, respectively. The total sample thickness (D) varied from 10 mm to 150 mm. It is clear that the effective elastic modulus decreases with the indenter radius, since a larger indenter is able the detect more of the soft hypodermis. However, when the total sample thickness is small, for example D = 10 mm, and indenters are large enough, the effective elastic moduli increase with the contact sizes. It is because in the simulation, the bottom of the skin was defined as fixed which was similar to the situation that the skin was on stiff muscles or bones *in vivo* or to the situation that excised skin tissues was placed in a petri dish on a very rigid desk. When the indenters were very large, the indentation test was measuring the skin as well as the stiff tissue or desk underneath, and thus the effective elastic modulus increased. The model developed by Perriot et al. was based on semi-infinite samples and did not take into account this effect. Therefore, it could not be directly applied to thin skin samples.

To overcome this problem, data affected by the stiff tissue underneath the skin was excluded in the fitting. The slope of effective elastic modulus (E) versus indenter radius (a), which was calculated by dividing the difference in E values (ΔE) by the difference in the indenter radius (Δa) between two adjacent data points as shown in

Figure 5.10, is used as a criterion. When the slope was larger than 0, the elastic modulus increased with the indenter size, which means the data was affected by the stiff tissue underneath the skin and should be excluded in the analysis. When the slope was smaller than 0, the E values were plotted versus the indenter sizes and fit to the model developed by Perriot et al. and the elastic modulus and thickness of dermis could be determined.

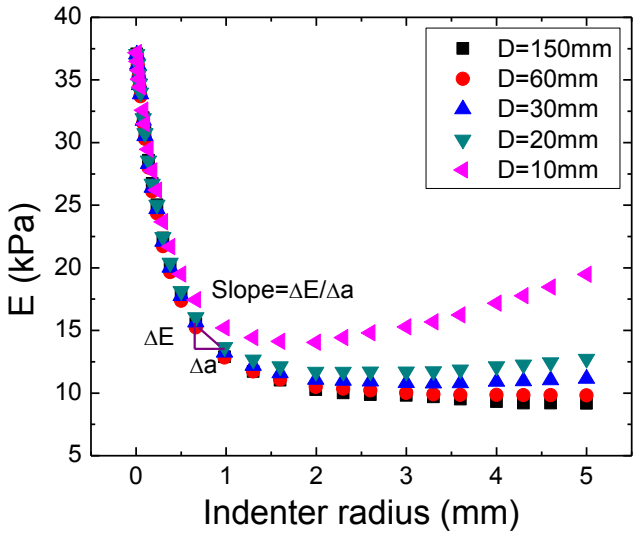

Figure 5.10 Simulated effective elastic modulus (E) versus indenter radius (a) with different skin sample thickness (D). Elastic moduli of dermis and hypodermis were set as 38 kPa and 8 kPa, respectively. The dermis thickness (t) was 1.0 mm.

Based on the criterion, proper data was selected for fitting and the elastic modulus and thickness of the dermis were determined for skin models with dermis thickness ranging from 1 mm to 3 mm. The deduced dermis elastic modulus was very close to the actual value which was 38 kPa as shown in Figure 5.11 (a). The deduced values were very accurate and were not affected by the dermis thickness (t) or total

sample thickness (D). The estimated dermis thickness was plotted versus its actual values in Figure 5.11 (b) and the data was all close to the dashed line which had a slope of 1. Linear fitting was performed and the fitted slopes and intercepts were listed in Table 5.2. It is obvious that there was very good correlation (R^2>0.98) between the t deduced from the Perriot's model and t defined in the simulation, no matter of the skin sample thickness. Besides, the slopes from the linear fitting were close to 1 with an error smaller than 11%. These results proves that we can determine the elastic modulus and thickness of dermis in skin samples very accurately using Perriot's model combined with the criterion to exclude data affected by substrate underneath the skin. When the skin sample is too thin, i.e. less than 6 mm, there is not enough data for the fitting and thus the elastic modulus and thickness of dermis cannot be determined accurately.

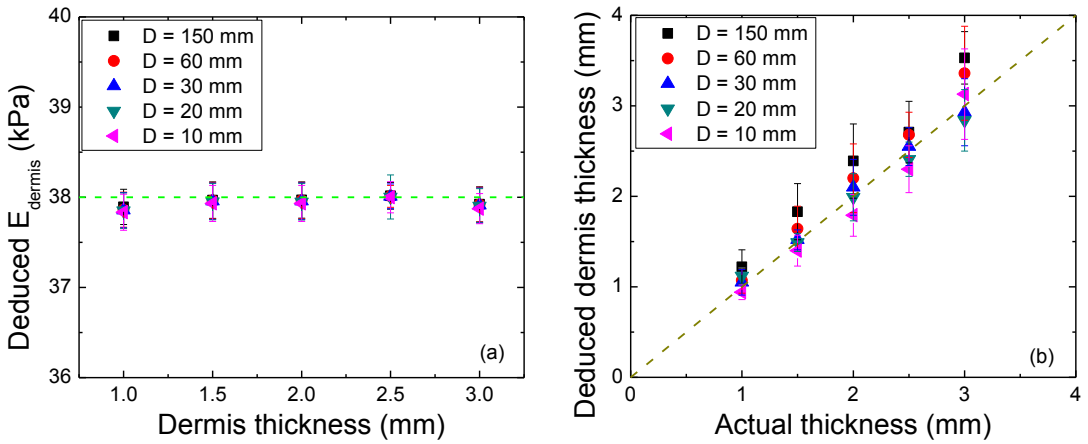

Figure 5.11 (a) The deduced elastic modulus of dermis versus dermis thickness. The actual dermis modulus was 38 kPa as shown in green dashed line. (b) The deduced dermis thickness versus the actual values. The dashed line has a slope of 1.

Table 5.2 The linear fitting of the deduced dermis thickness (t) of skin samples versus the actual t values

Total sample thickness D (mm)	Intercept		Slope		R^2
	Value	Error	Value	Error	
150	0.11	0.30	1.11	0.16	0.9891
60	-0.03	0.26	1.10	0.16	0.9981
30	0.06	0.23	0.98	0.14	0.9964
20	0.24	0.17	0.86	0.11	0.9947
10	-0.01	0.18	0.94	0.13	0.9853

5.3.2.4 Results with Different E_{dermis} and Dermis Thickness

Different Young's moduli of dermis, 38, 68, 100, 130, and 170 kPa, were also tried in FEA to evaluate the methodology. The thickness of the dermis varied from 1.0 mm to 3.0 mm with a 0.5 mm interval, within the range of human skin thickness. The skin sample was 10 mm thick. The elastic modulus of dermis (E_{dermis}) was deduced from stiffness measurements with indenters of different sizes using the Perriot's model and plotted versus the actual value in Figure 5.12 (a). It is obvious that E_{dermis} were determined very accurately using the method for various dermis thickness. The linear fitting of the data in Table 5.3 showed that the slope was very close to 1 with a R^2 larger than 0.9994, indicating the deduced values were very accurate and they were not affected by the dermis thickness. The dermis thickness was also determined using the model and plotted versus the actual value in Figure 5.12. The error of the thickness determination was less than 0.5 mm for various E_{dermis} values. The linear fitting results in Table 5.4 further demonstrate that the deduced dermis thickness was in good agreement with the actual value.

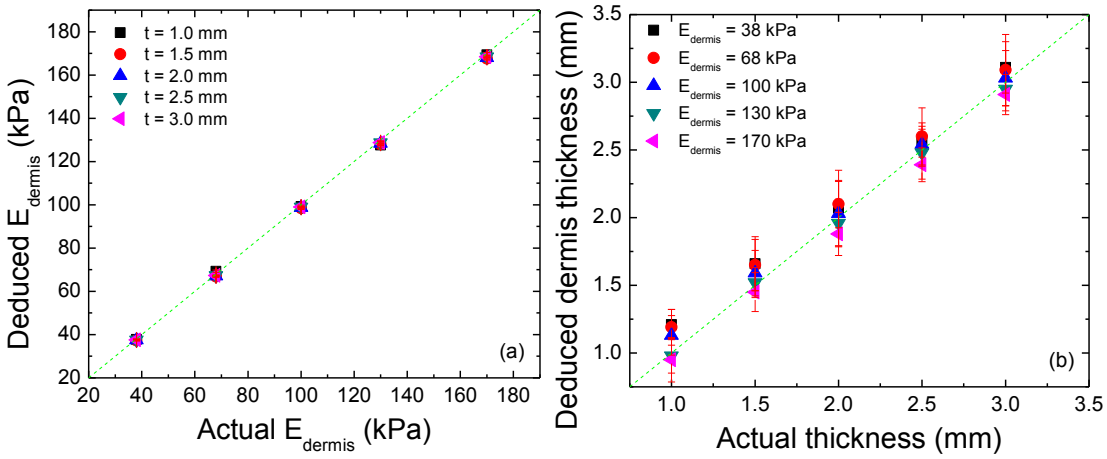

Figure 5.12 (a) The deduced elastic modulus of dermis (E_{dermis}) versus its actual value when the dermis thickness (t) changed from 1.0 to 2.5 mm. (b) The deduced dermis thickness versus the actual values when the elastic modulus of dermis ranging from 38 kPa to 170 kPa. The dashed green line in both figures has a slope of 1.

Table 5.3 The linear fitting results of the deduced elastic modulus of dermis versus the actual E_{dermis} for different dermis thickness (t)

t (mm)	Slope		Intercept		R^2
	Value	Standard deviation	Value	Standard deviation	
1.0	0.99	0.01	0.41	0.42	0.9994
1.5	0.99	0.00	-0.22	0.36	0.9999
2.0	0.99	0.00	-0.09	0.27	0.9999
2.5	0.99	0.00	-0.09	0.26	0.9999
3.0	0.99	0.00	-0.08	0.29	0.9999

Table 5.4 The linear fitting results of the deduced dermis thickness (t) versus the actual value for different E_{dermis}

Ef (kPa)	Slope		Intercept		R^2
	Value	Standard deviation	Value	Standard deviation	
38	0.92	0.09	0.28	0.18	0.9970
68	0.94	0.12	0.24	0.22	0.9993
100	0.95	0.11	0.17	0.22	0.9994
130	0.98	0.09	0.02	0.18	0.9986
170	0.97	0.10	-0.03	0.21	0.9987

Based on all the FEA results above, we can get to the conclusion that the elastic modulus and thickness of dermis could be determined accurately from stiffness measurements by indenters of different sizes using the model developed by Perriot et al. combined with the criterion for excluding data affected by stiff substrate underneath the skin sample.

5.3.3 Deduce the Elastic Modulus and Thickness of Dermis in Skin Phantoms

Skin phantoms as illustrated in Figure 5.13 were constructed to simulate normal human skins. They consisted of a thin film which was Versaflex (CL2003, CL2000, and CL30, GLS, McHenry, Illinois), a kind of elastic polymer, and a gelatin substrate. The elastic moduli of Versaflex CL2003, CL2000, and CL30 were determined to be 38.5±2.1 kPa, 68.2±3.6 kPa, and 130.4±3.8 kPa, respectively by PEF measurements on bulk material. They were made into thin films to mimic the dermis layer in human skin. Gelatin with an elastic modulus of 8.3±1.4 kPa was used to simulate the hypodermis/fat layer of the skin. The diameter of the skin phantom was 90 mm. The thin film of Versaflex was carefully placed on the gelatin surface so that there was no air bubbles between the two layers. The thickness of the Versaflex layer varied from 0.5 to 3 mm and the total thickness of the skin phantom ranged from 6 to 15 mm.

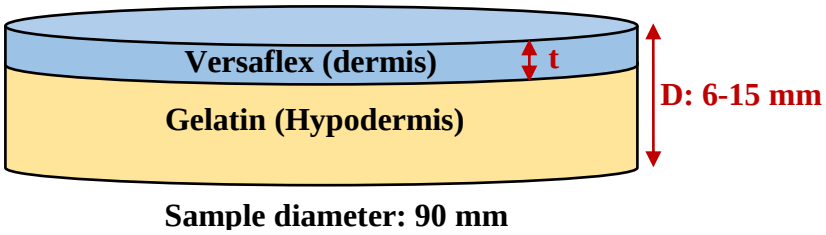

Figure 5.13 A schematic of the skin phantom

PEFs of different contact sizes ranging from 0.23 mm to 3.8 mm as listed in Table 5.1 were used to measure the effective elastic moduli of skin phantoms on the surface. As an example, the elastic modulus of the skin phantom (t = 1.19±0.13 mm and D = 6.1 mm) is plotted versus the PEF contact size in Figure 5.14. The data (black squares) which was not affected by the stiff substrate underneath the phantom was fitted to Perriot's model using the criterion that the slope of modulus E versus indenter radius was smaller or equal to 0. The deduced elastic modulus of dermis from the fitting results was 34.8±1.9 kPa, matching the actual modulus of Versaflex (38.5±2.1 kPa). The dermis thickness was determined to be 1.38±0.15 mm, showing good agreement with the actual value (1.19±0.13 mm) measured by caliper.

The elastic modulus and thickness of dermis deduced from the fitting results were compared with the actual values for all the 18 samples. Figure 5.15 shows the deduced elastic modulus for various dermis thickness. The shaded area in the figure indicates the actual elastic modulus of the dermis layer. As can be seen, most of the deduced E_{dermis} were in the shaded areas when the dermis thickness was between 0.5

mm and 3.5 mm, suggesting that the methodology could be used to determine the elastic modulus of dermis very accurately.

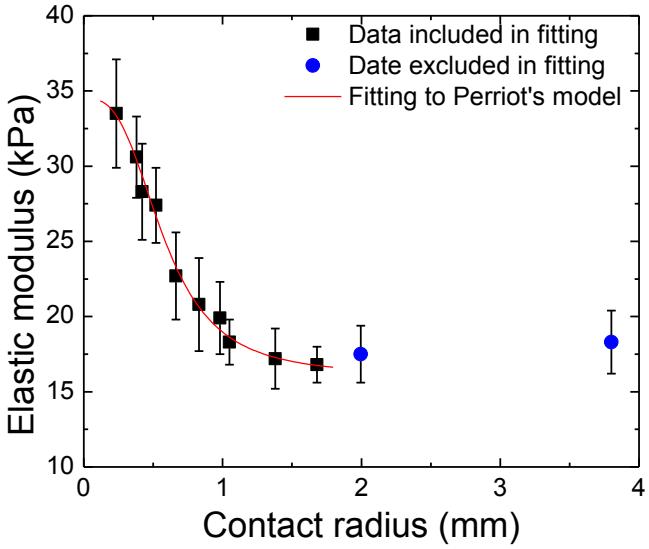

Figure 5.14 Elastic modulus versus PEF contact radius on skin phantoms. The dermis thickness (t) was 1.19±0.13 mm and the total thickness of the model (D) was 6.2 mm.

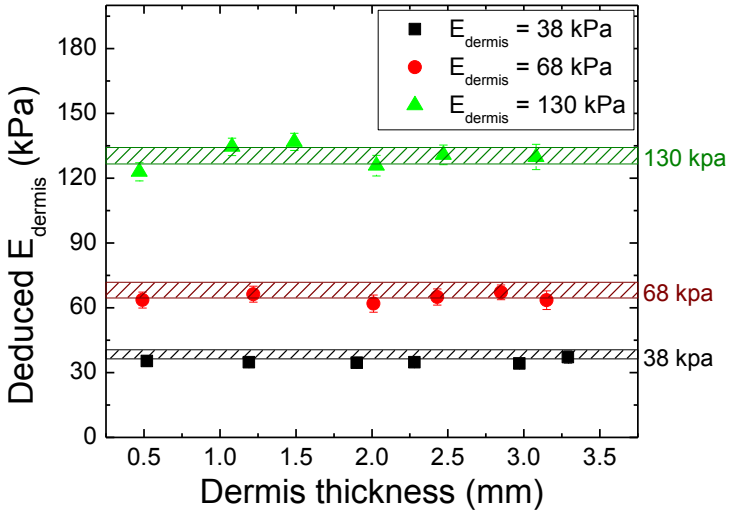

Figure 5.15 The deduced elastic modulus of dermis (E_{dermis}) versus dermis thickness. The expected values of the dermis modulus were 38.5±2.1 kPa, 68.2±3.6 kPa, and 130.4±3.8 kPa as shown in shaded areas.

The dermis thickness was also gathered and plotted versus its actual value, which was measured with a caliper, in Figure 5.16. It is apparent that all the data points were close the dashed line whose slope was 1. No matter how the E_{dermis} changed, the calculated dermis thickness agreed with the actual value well. Linear fitting was performed on the data and the fitting curve had a slope of 1.01 with an intercept of 0.02. R^2 was 0.9878, implying there was a good linear relationship between the deduced and actual values.

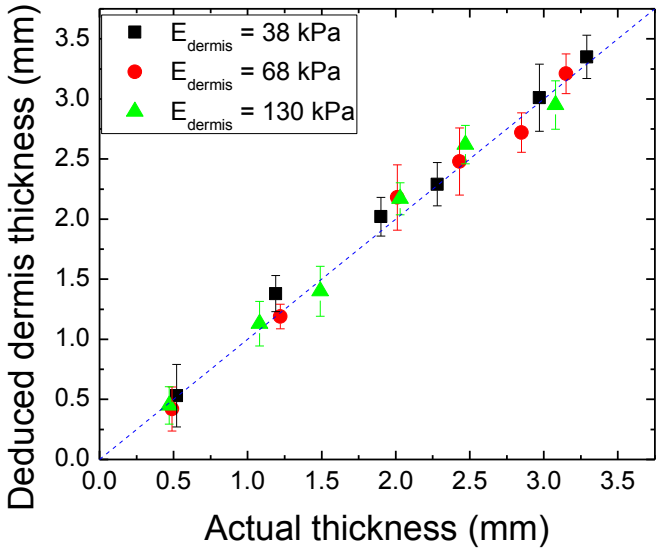

Figure 5.16 The deduced dermis thickness versus its actual value. The dashed line had a slope of 1.

From the results shown above, we can tell that the elastic modulus and thickness of dermis could be determined correctly by applying the Perriot's model to the stiffness measurement results from PEFs of different contact sizes. If the slope of modulus E versus indenter radius was larger than 0, the stiffness data was excluded in

the model fitting due to the reason that it contained the elastic information of the substrate underneath the skin phantom.

5.3.4 Deduce the Elastic Modulus and Thickness of Dermis in Porcine Skin

A number of morphologic, anatomic, dermatologic, and immunohisto-chemically studies have demonstrated that porcine skin has important similarities in morphology and cellular composition to human skin [179-182]. The epidermis of the pig is reported as varying in thickness from 30 to 100 μm [183] and 70 to 140 μm [184], thus being within a range similar to that in human, 50 to 150 μm [87, 88]. The dermis layer is also very similar to human skin. Collagen in the porcine dermis shows a remarkable similarity to human collagen [185], making the mechanical properties of porcine dermis very similar to that of human skin. In addition, the properties of porcine skin are not significantly affected by the lack of a physiological environment provided there is enough moisture [186]. Therefore, porcine skin was used in this section as an analogue of human skins.

Fresh porcine skin was harvested from the belly part from a local abattoir. Each sample was cut into 40 mm × 40 mm pieces as shown in Figure 5.17. The muscle layer was removed if found. Only the skin and fat tissue was left in the sample. The total thickness of the sample was 6-10 mm. Paper tissue was damped with saline solution and placed on the sample to keep it moist. Effective elastic moduli were measured by PEFs of different contact sizes as listed in Table 5.1 on the center of the sample. Afterward, a 10 mm × 10 mm square was marked on the center of the sample and the part outside the square was cut. The hypodermis layer was removed by a

razor blade. The thickness of the dermis (including the epidermis layer) was measured with a caliper. The stress/strain curve of the 10 mm × 10 mm porcine dermis was measured by Bose ElectroForce® 3100 (TA Instruments, New Castle, DE) as shown in Figure 5.18 using compression testing to deduce the elastic modulus of the dermis layer.

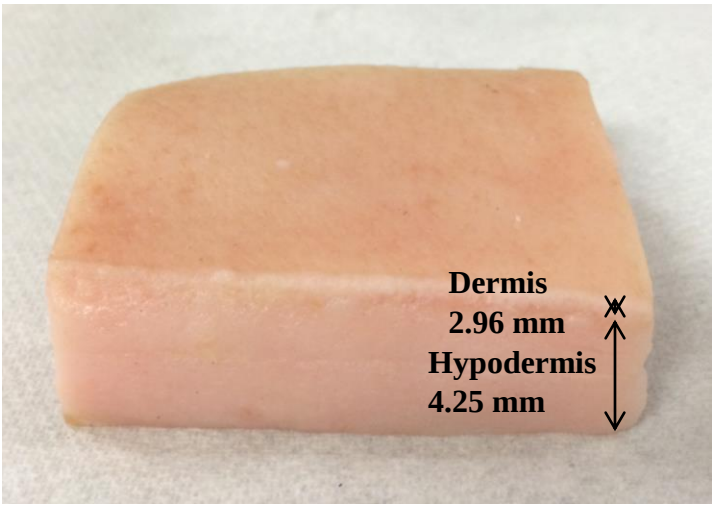

Figure 5.17 A picture of the porcine skin sample

Figure 5.18 The Bose ElectroForce® 3100 for compression test

As an example, the effective elastic moduli of the porcine skin sample shown in Figure 5.17 measured by PEFs were shown in Figure 5.19. The data with monotonic decrease was fit to Equations 5-3 and 5-4 in Perriot's model. From the fitting results, the elastic modulus of dermis was determined to be 127.8±9.8 kPa. The thickness of the dermis was calculated to be 2.87±0.38 mm, which agreed well with that measured by a caliper, 2.96±0.18 mm, after the hypodermis layer was removed by a razor blade. The stress/strain curve of the dermis layer of the same sample was measured by Bose system as shown in Figure 5.20. Linear fitting was performed on the relatively linear region of loading data where the strain was less than 2.5%. The slope of the fitting, which represented the elastic modulus of the dermis, was determined to be 118.9 kPa. Three independent compression tests were done for the same sample and the averaged value of the dermis modulus was 121.9±5.3 kPa. It suggests that the dermis modulus deduced from PEF measurements was very accurate.

Six porcine skin samples were tested in this study. The elastic modulus and thickness of the dermis determined by PEFs were compared with other methods in Table 5.5. The dermis moduli deduced from PEF measurement results were quite consistent with those calculated from the stress/strain curve for all the six samples, with an error less than 15 kPa, which was calculated by taking the difference between E_{demis} deduced by PEF and by Bose. The dermis thickness determined by PEF was also in good agreement with the value measured by caliper, with a maximum error of 0.39 mm.

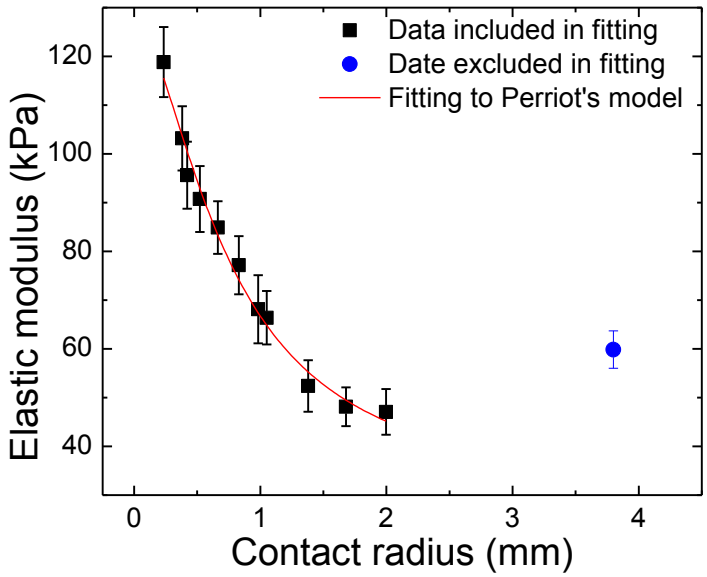

Figure 5.19 Elastic modulus of a porcine skin sample measured by PEFs of different contact size. The data was fit to Perriot's model to deduce the elastic modulus and thickness of dermis.

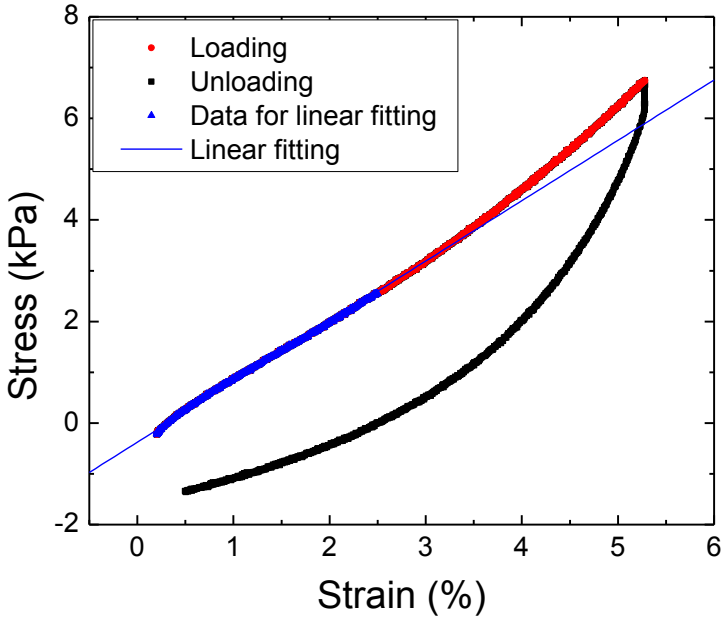

Figure 5.20 The stress versus strain curve of a porcine dermis in a compression test measured by Bose ElectroForce® 3100. The slope of the linear fitting curve is the elastic modulus of the dermis, 118.9 kPa.

Table 5.5 Elastic modulus and thickness of the dermis layer in porcine skin samples

Sample #	E_{dermis} (kPa)			Dermis thickness (mm)		
	By Bose	By PEF	PEF Error	By caliper	By PEF	PEF Error
1	125.4 ± 10.4	124.2 ± 4.1	-1.2	2.85 ± 0.18	3.04 ± 0.21	0.19
2	111.3 ± 14.4	125.6 ± 12.2	14.2	3.06 ± 0.17	3.31 ± 0.51	0.25
3	121.9 ± 3.3	127.8 ± 9.8	5.9	2.96 ± 0.18	2.87 ± 0.38	-0.09
4	127.1 ± 11.4	115.2 ± 4.2	-11.8	2.51 ± 0.21	2.30 ± 0.29	-0.21
5	126.9 ± 8.2	128.2 ± 5.5	1.3	2.77 ± 0.23	2.38 ± 0.37	-0.39
6	124.8 ± 12.7	139.5 ± 6.8	14.7	2.39 ± 0.19	2.19 ± 0.34	-0.20

In this section, excised porcine skin samples were used to mimic human skins. The results showed that the elastic modulus and thickness of dermis could be accurately deduced from effective elastic moduli measured by PEFs using the combination of Perriot's model and the criterion to exclude the data affected by stiff substrate for model fitting.

5.4 Conclusions

In this chapter, PEFs with different contact sizes were used to measure the elastic modulus of skin. The results show that the moduli decrease with an increase in PEF contact size, indicating that the effective elastic modulus measured by the PEF with a small contact size mainly depends on the stiff dermis layer while that measured by the PEF with a large contact size is more affected by the soft hypodermis layer. Besides, if the skin sample is not thick enough, the elastic moduli from the PEF with a large contact size, may be affected by the stiff substrate underneath the sample, i.e. petri dish and the table.

To resolve the elastic modulus and depth profile of skin, the effective elastic moduli (E) were plotted versus the PEF contact radiuses. If the slope between two

adjacent data points was larger than 0, it means the later data point was affected by the sample substrate and thus was excluded for depth profile determination. The model developed by Perriot et al., which showed good results in the case of a rigid layer on a compliant substrate [177], was chosen to fit the data and the elastic modulus and thickness of the dermis layer in skin could be deduced from the fitting results.

The methodology was first validated using finite element analysis (FEA) in which skin models with different dermis thickness (1-3 mm) and total thickness (10-150 mm) were constructed and the effective elastic moduli from indenters of 0.01-0.50 mm in radius were simulated. The deduced elastic moduli of dermis agreed with the defined values in FEA well with a maximum error of 2.4 kPa. The dermis thickness determined by the methodology was within 0.1 mm from the actual value. It suggests the elastic modulus and thickness of dermis can be resolved from PEF measurements with different contact sizes using Perriot's model.

Skin phantoms were built using Versaflex CL2003, CL2000, and CL30 with an elastic modulus of 38.5, 68.2, and 130.4 kPa, respectively, as dermis layer and gelatin matrix with an elastic modulus of 8.3 kPa as hypodermis layer. PEFs with contact sizes ranging from 0.23 to 3.80 mm were used to measure the effective elastic moduli of skin phantoms. Elastic modulus of dermis was deduced from the fitting of Perriot's model and showed good agreement with the actual values, with a discrepancy less than 7.5 kPa. The dermis thickness by PEF was within 0.2 mm of the actual values measured by caliper.

Six porcine skin samples with a size of 40 mm × 40 mm were measured by PEFs. The deduced elastic moduli of dermis layer from PEF were compared with those measured by Bose ElectroForce® 3100 using a compression test. It shows that PEF could determine the dermis modulus accurately, with an error less than 14.7 kPa. The dermis thickness estimated by PEF also matched the actual values measured by caliper, with an error less than 0.4 mm.

In conclusion, the elastic modulus and thickness of dermis in skin could be determined accurately from PEF measurements with different contact sizes combined with Perriot's model, making the PEF a good tool for skin characterization. It will help detect skin disease and quantify the effectiveness of dermatologic products.

6. DETERMINE THE 3D PROFILE OF SKIN TUMOR IN PHANTOMS

Most nonmelanoma skin cancers, i.e. basal cell carcinoma and squamous cell carcinoma, are non-pigmented. It is difficult for the dermatologist to decide where to cut by eye. Mohs surgery, in which skin tissues are removed progressively and examined by pathology until only cancer-free tissue remains, is widely used for nonmalenoma skin cancers. However, the procedure is tedious and time-consuming and it requires the patient to lie under local anesthesia as histology is performed. An inability to remove a tumor in one day may preclude immediate reconstruction after complete excision. A rapid technique to identify the borders of nonmelanoma skin cancers is desired to reduce the time spent in surgery.

For melanomas, the thickness of the cancer, which is the distance from the skin surface to the deepest point of cancer, is one of the most important prognostic factor. It also help the dermatologist decide the surgical margin [187, 188]. In removing an invasive melanoma that is 1 mm or less in thickness, the surgeon excises 1 cm of the normal skin surrounding the tumor. If the melanoma is 2 mm thick or greater, a margin of 2 cm is taken. Pathological investigation is the current gold standard for melanoma evaluation, but it is time-consuming and can only be done after surgery. A method that can quantify the thickness of melanoma before the surgery is needed.

It has been reported that the elastic modulus of basal cell carcinoma is much smaller than that of normal skin [139]. And melanoma can be either softer or stiffer

than normal skin [135, 140], depending on its malignancy. It is therefore feasible to use stiffness contrast measured to differentiate cancerous tissues from normal skin.

In this chapter, PEF with a contact radius of 0.23±0.01 mm is used to detect skin cancers in phantoms and determine the lateral sizes of cancers. Then the depth profile of skin is estimated by coupling the elastic modulus measurements by PEFs with different contact sizes and a modified 2-spring model. Combining the lateral and depth profile of model skin cancers in porcine skins, the 3D image of the cancers is constructed.

6.1 Determine the Lateral Extent of Skin Tumor in Phantoms

6.1.1 Skin Cancer Phantoms

Skin tumor phantoms were constructed using Versaflex CL2003, CL2000, and CL30 (GLS, McHenry, Illinois) and gelatin (Now Foods, Bloomingdale, IL) matrix. The Versaflex CL2003 and CL2000 were mixed with a ratio of 1:1 and melt at 100 °C on a hot plate to form a thin layer (about 1 mm thick) to mimic the skin cancer because its elastic modulus of 55.2±3.4 kPa was similar to that of basal cell carcinoma reported in the literature [139]. After cooling at room temperature, they were cut into 4×4, 6×6, 8×8, 10×10, and 12×12 mm^2 squares. The dermis layer of the skin tumor phantom was made of Versaflex CL2000 and CL30 with a ratio of 1:3 and its elastic modulus was 115.3±4.2 kPa, consistent with the elastic modulus of dermis measured by PEFs in porcine skins as described in Chapter 5 and that reported in References [163, 164, 166] which was approximately from 88 to 300 kPa. The dermis layer with a thickness of 1-3 mm and a diameter of 90 mm, was melt in a petri dish

with the same diameter at 100 °C. The skin tumor squares were then placed on the dermis and they gradually sank in the melt dermis until their surfaces had the same level. After cooling, the skin tumors were bond to the dermis tightly. They hypodermis/fat layer of the skin was made of gelatin with a concentration of 0.8 g/ml and has an elastic modulus of 8.5±1.2 kPa. The thickness of the hypodermis layer was 4-5 mm and the diameter was 90 mm. The dermis layer with skin tumor was placed on the gelatin matrix carefully so that there was no air bubbles between two layers.

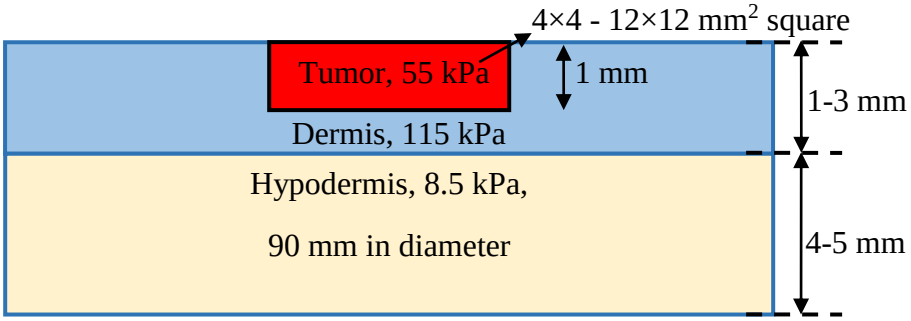

Figure 6.1 A schematic illustration the cross section of the skin tumor phantom

6.1.2 PEF Measurements on Skin Tumor Phantoms

Since skin cancer starts from the surface of skin, using the stiffness contrast on the outermost of the skin is better than using that of deep tissue in order to differentiate skin cancers from normal tissue. Therefore, the PEF with a smallest contact radius (0.23±0.01 mm) whose depth sensitivity was only about 0.46 mm was chosen to measure the elastic modulus of the phantom. Firstly, a grid was drawn on the phantom surface for location tracking. The PEF was then placed on the first

location and the elastic modulus measurements were performed. Five repeated measurements were made for each location to obtain an average elastic modulus and standard deviation. Then the PEF was placed on the second location. It was repeated until the entire phantom was scanned. A 2D color coded elastic modulus map of the scanned skin tumor phantom was created based on the average elastic modulus.

As an example, the 2D elastic modulus map of the skin phantom with a 4×4 mm^2 skin tumor is shown in Figure 6.2 . The green color stands for the normal tissue while the red color represents the decreased elastic modulus, indicating the skin tumor. The actual location of the cancer is marked by the black square in the figure. It is clear that the red region matches the location and size of the tumor very well. It suggests that the PEF is able to successfully detect the skin tumor and locate it in 2D accurately.

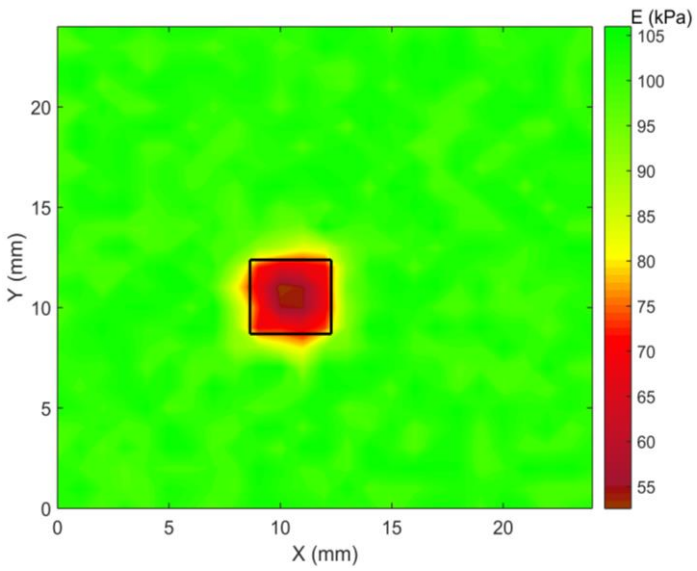

Figure 6.2 Elastic modulus map of the phantom with a 4×4 mm^2 skin cancer by PEF. The actual location of the cancer is marked with black squares

6.1.3 Lateral Tumor Size Determination

To determine the size of the cancer quantitatively, the elastic modulus at certain x distance was plotted versus y distance. As an example the elastic modulus of the skin cancer shown in Figure 6.2 at x = 10 mm is plotted versus y in Figure 6.3. The data was then fitted to a Gaussian function and the half peak width was taken as the size of the cancer. In this example, the half peak was 76.9 kPa which wass calculated by averaging the baseline of the Gaussian fit (101.6 kPa) and the peak (52.2 kPa). The width of the bell shaped curve at the half peak provides the size of the cancer, 3.9 mm. It is consistent with the actual size of the cancer which is 4.1±0.2 mm. It is reasonable since the half peak of the modulus is obtained when the PEF is scanning over the edge of the cancer where half of the PEF is over the cancer and the other half of the PEF is over the normal skin.

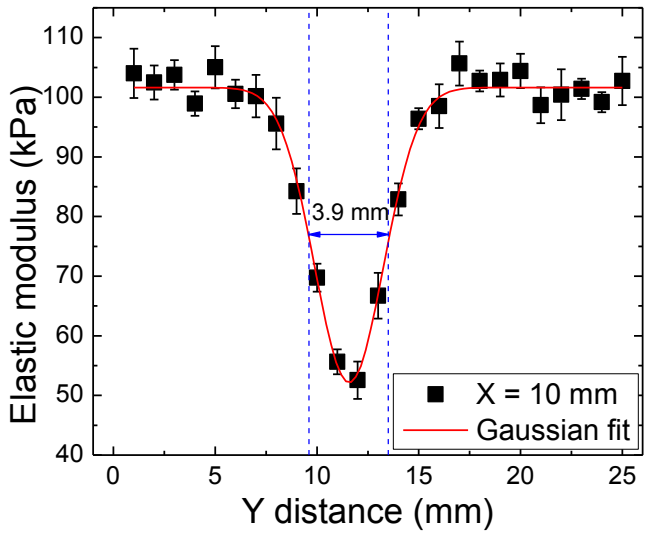

Figure 6.3 The measured elastic modulus versus y distance at x = 10 mm for the skin cancer phantom shown in Figure 6.2. The size of the cancer taken as the width at the half peak height of the Gaussian fit was 3.9 mm.

The lateral extent of the skin tumors in phantoms determined by PEF is listed in Table 6.1. The actual sizes measured with a caliper are also included. The sizes estimated by PEF had good agreement with the actual ones, with an error less than ±1mm. Therefore, it can be concluded that the PEF could not only detect skin cancers but also determine the locations and lateral sizes of the skin cancers accurately.

Table 6.1 Comparison of the lateral sizes of skin cancers in phantoms measured by PEF and their actual values by caliper

Model #	Size in X direction (mm)			Size in Y direction (mm)		
	Actual value by caliper	Measured by PEF	PEF Error	Actual value by caliper	Measured by PEF	PEF Error
1	4.1±0.2	3.9±0.4	-0.2	4.3±0.4	4.0±0.5	-0.3
2	6.2±0.4	5.8±0.5	-0.4	6.1±0.5	6.5±0.6	0.4
3	7.9±0.5	8.6±0.4	0.7	8.3±0.6	9.2±0.4	0.9
4	9.8±0.4	10.6±0.6	0.8	9.7±0.5	8.9±0.7	-0.8
5	12.2±0.5	11.3±0.8	-0.9	11.8±0.5	12.5±0.8	0.7

6.2 Determine the Depth Profile of Skin Tumors in Phantoms Using Spring Model

6.2.1 Skin Cancer Phantoms

Skin cancer phantoms consisting of Versaflex CL2003, CL2000, and CL30 and gelatin matrix were built to mimic skin cancers with different depth profile. Same with the phantoms mentioned in Section 6.1.1, the elastic moduli of skin cancer, dermis and hypodermis are 55.2±3.4 kPa, 115.3±4.2 kPa, and 8.5±1.2 kPa, respectively. The size of the model tumors was 8×8 mm^2 and the thickness of the tumors varied from 0.6 mm to 4.4 mm. The thickness of dermis ranged from 1.9 mm to 3.2 mm so that some tumors are within the dermis layer as illustrated in Figure 6.4 (a-c) and some have invaded into hypodermis layer as shown in Figure 6.4 (d-e). The phantoms were all about 10 mm in total thickness.

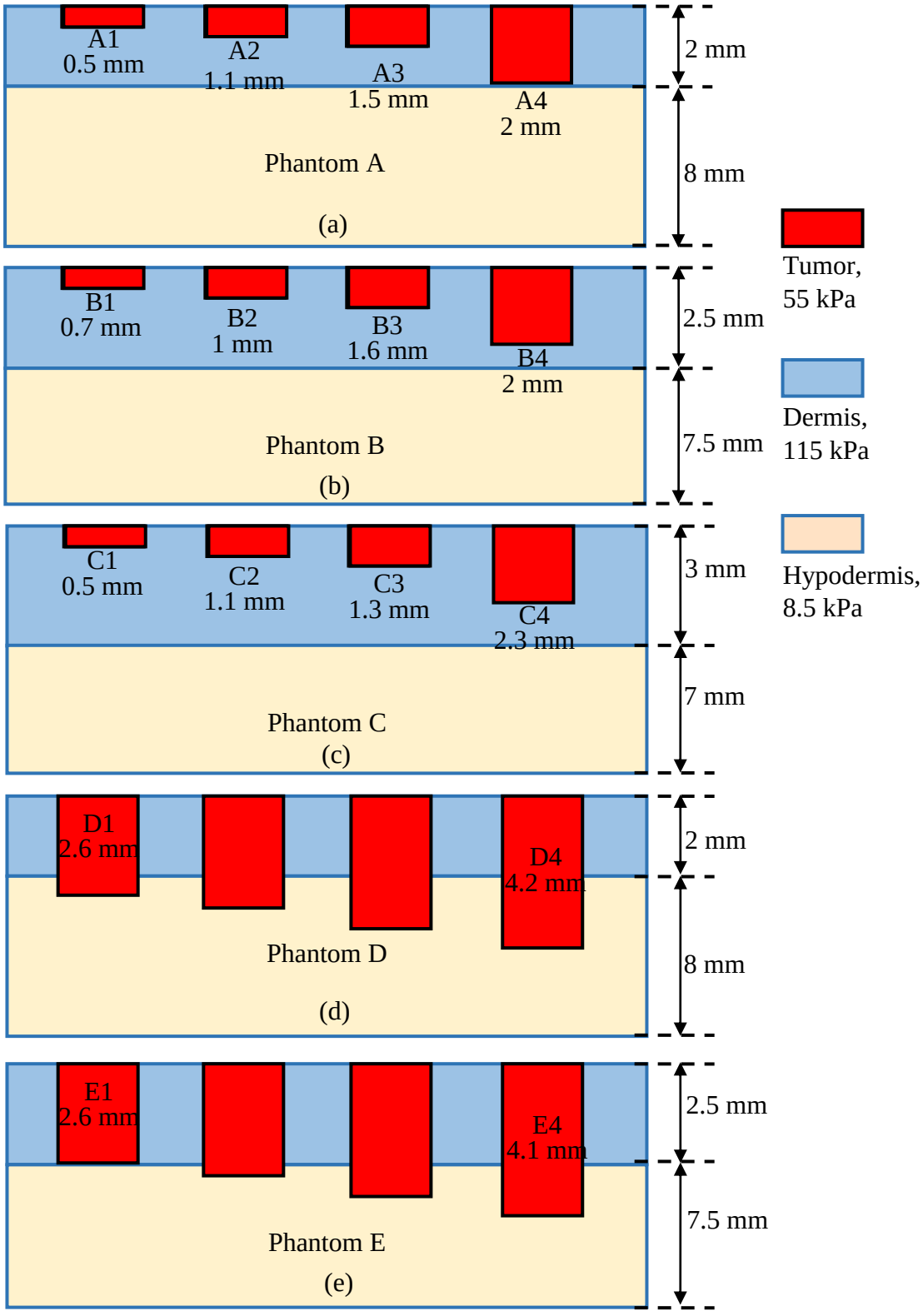

Figure 6.4 A schematic illustrating the depth profile of skin cancers in phantoms A-E

6.2.2 Determine the Elastic Modulus and Thickness of Dermis in Phantoms

PEFs of different contact sizes ranging from 0.23 mm to 3.8 mm as listed in Table 5.1 were used to measure the elastic moduli of normal tissue in phantoms. The data was fitted to Perriot's model using the criterion that the slope of modulus E versus indenter radius was smaller or equal to 0. As an example, the elastic modulus of normal tissue in Phantom A versus the PEF contact size is plotted in Figure 6.5. The elastic modulus and thickness of dermis could be deduced from the fitting results and they were compared with the actual values in Table 6.2. As can be seen, the E_{dermis} deduced from PEF stiffness measurements agreed with the actual value very well, with an error smaller than 3%. Besides, PEF could estimate the thickness of the dermis accurately, with an error less than 0.2 mm. It further validates that the elastic modulus and thickness of dermis could be estimated accurately by combining PEF measurement and the Perriot's model. Moreover, the thickness of dermis will be compared with the thickness of cancer in the phantom in next sections to determine whether the cancer has invaded into the hypodermis layer or not, which is important for cancer staging.

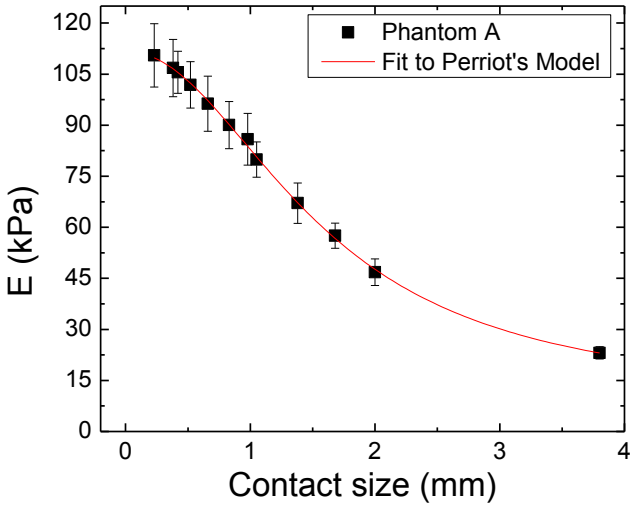

Figure 6.5 Elastic modulus measured by PEFs with different contact sizes on normal region of Phantom A

Table 6.2 The comparison of elastic modulus (E_{dermis}) and thickness of dermis determined by PEF and the actual values in skin tumor phantoms

Phantom #	E_{dermis} (kPa)					Dermis thickness (mm)				
	Actual		Measured by PEF		PEF Error	Actual		Measured by PEF		PEF Error
	AVE	SD	AVE	SD		AVE	SD	AVE	SD	
A	115.3	4.2	112.9	4.9	-2.4	2.1	0.2	2.3	0.3	0.2
B	115.3	4.2	114.1	3.8	-1.2	2.5	0.3	2.6	0.3	0.1
C	115.3	4.2	112.8	4.6	-2.5	3.2	0.3	3.1	0.4	-0.1
D	115.3	4.2	116.2	5.1	0.9	1.9	0.2	2.1	0.2	0.2
E	115.3	4.2	118.3	4.2	3.0	2.4	0.2	2.6	0.3	0.2

6.2.3 Modified 2-Spring Model to Deduce the Depth Profile of Skin Cancers

It is known that human skin has a layered structure with a stiff dermis layer (including the epidermis) on a soft hypodermis substrate as illustrated in Figure 6.6 (a). The elastic modulus measured by PEF on the normal region is the effective elastic modulus of the dermis and hypodermis (E_{eff}) as shown in Figure 6.6 (b). Since

the skin cancer origins from the surface and grow into the skin, it can be modeled as an extra layer on top of the dermis as shown in Figure 6.6 (c). The system is then further simplified to a two-layer structure by combining the dermis and hypodermis together with an effective elastic modulus (E_{eff}) which can be measured by PEF on normal region. When the thickness of the tumor (t_1), which is the distance from the sample surface to the bottom of the tumor, is smaller than the depth sensitivity (d) of a PEF as shown in Figure 6.6 (d), the tumor and part of the skin within d behave like two elastic springs connected in series. The effective elastic modulus E measured by PEF on the skin cancer surface can be expressed as

$$\frac{d}{E} = \frac{t_1}{E_t} + \frac{d - t_1}{E_{eff}} \tag{6-1}$$

where E_t is the elastic modulus of skin tumor which can be measured by a PEF with a small contact, i.e. 0.23±0.01 mm in radius; E_{eff} is the effective elastic modulus of normal skin which can be measured by PEF on normal regions in the sample; d is the depth sensitivity of a PEF which is about twice the contact size; and t_1 is the thickness of skin tumor.

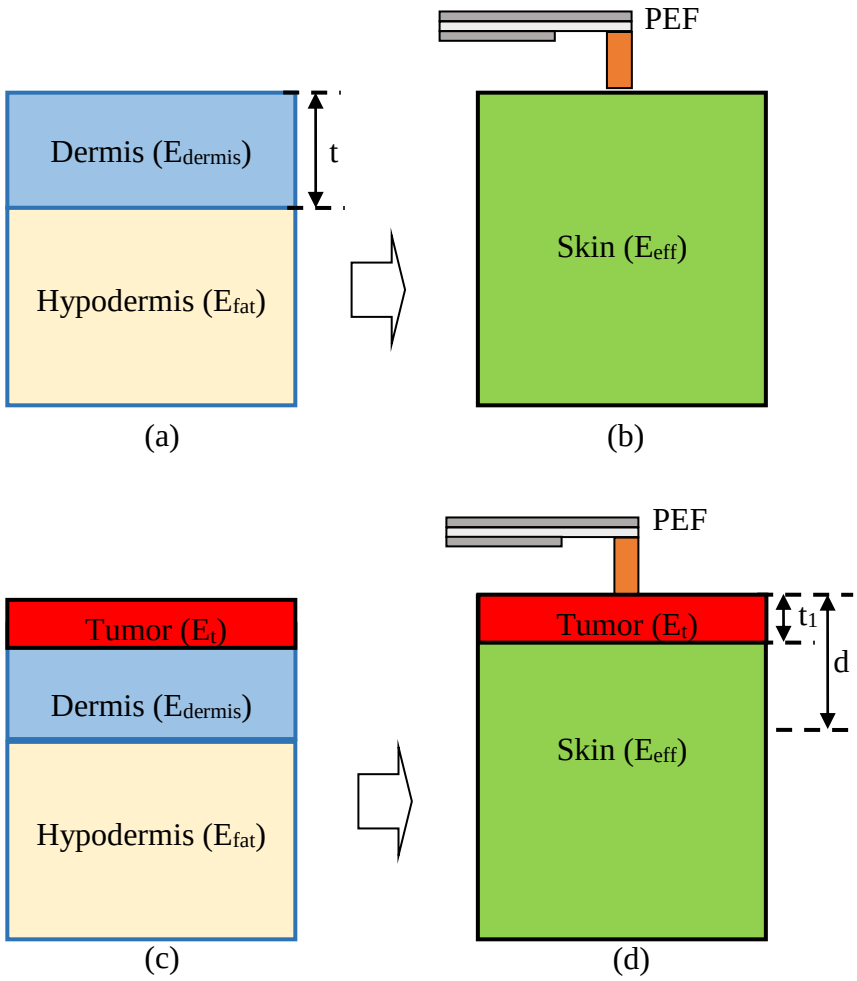

Figure 6.6 (a) A schematic illustrating the skin with a 2-layer structure; (b) Effective elastic modulus of skin (E_{eff}) measured by PEF; (c) A schematic illustrating the 3-layer structure of skin cancer; (d) The skin cancer is modeled as a 2-layer structure by combining the dermis and hypodermis together.

As an example, the elastic moduli of skin and skin tumors A1 and A4 (shown in Figure 6.4) measured by PEFs with different contact sizes on the phantom surface are plotted in Figure 6.7 (a). The elastic modulus of cancer A1 measured by the PEF with smallest contact (0.23±0.01 mm in radius) is 53.5±6.3 kPa, the same with the known modulus of the phantom, 55.2±3.4 kPa. It is because the depth sensitivity of

that PEF is smaller than the tumor thickness and the PEF can only detect the tumor layer. As shown in Figure 6.7 (a), when the PEF contact size is less than 1mm, the measured elastic moduli of cancer increase with the contact radius due to the reason that the skin cancer (55.2±3.4 kPa) in the phantom is softer than the dermis layer (115.3±4.2 kPa). PEF with a larger contact, which has a larger depth sensitivity, can detect more dermis, resulting an increase in modulus. When contact radius is larger than 1 mm, the PEF starts to detect the soft hypodermis layer (8.5±1.2 kPa) and therefore the measured elastic moduli decreases with the contact radius. When the contact radius is larger than 1.5 mm, due to large depth sensitivity, the measured elastic moduli of cancer are about the same with those of skin.

For the skin cancer A4 which has the same thickness with the dermis layer (about 2 mm), the measured elastic modulus is constant when the contact size is less than 1 mm. Then the modulus increases a little as the PEF detects the stiff dermis layer. When the contact size further increases, the PEF detects the soft hypodermis resulting in a decrease in the measured modulus. The elastic modulus of skin cancer A4 measured by the PEF with a contact size of 3.8 mm is larger than that of normal skin.

If the skin cancer has penetrated the dermis layer and invaded into hypodermis as the skin cancer D3 illustrated in Figure 6.4, the elastic modulus measured by the PEF was constant when the contact size is small as shown in Figure 6.7 (b). Then the modulus decreases with the contact size as the PEF detects the hypodermis layer.

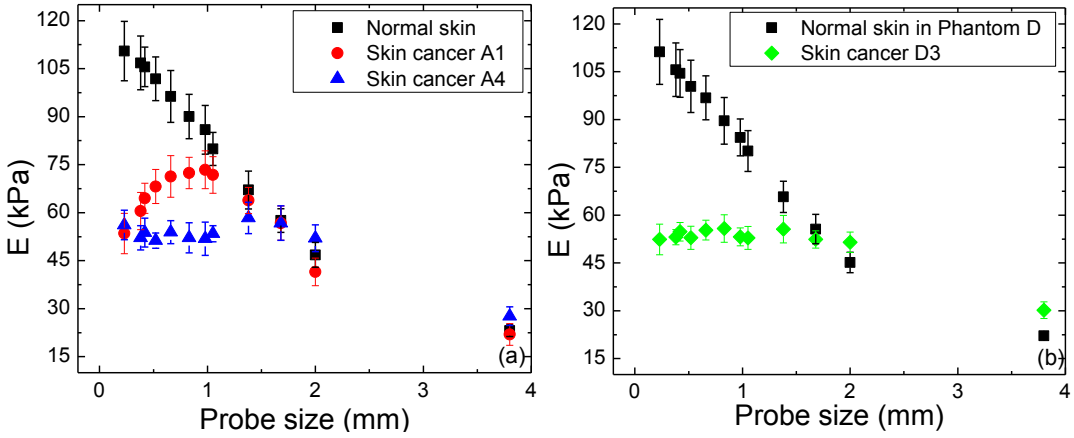

Figure 6.7 (a) Elastic moduli of skin and skin cancers A1 and A4 (illustrated in Figure 6.4) measured by PEFs with different contact sizes; (b) Elastic moduli of skin and skin cancer D3. The thickness of dermis was about 2 mm and the thickness of skin cancers A1, A4, and D3 was 0.5±0.1 mm, 2.2±0.1 mm, and 3.6±0.2 mm, respectively.

Assuming the modulus measured by the PEF with smallest contact on skin cancer was the elastic modulus of tumor (E_t), the stiffness of cancer and normal skin measured by PEFs was used to deduce the thickness of skin cancer using the Equation 6-1. Note that when the contact size is large, the measured elastic moduli of cancer may be the same with those of skin and therefore those data cannot be used for calculation. The deduced thickness of each tumor is averaged and compared with the actual value measured by caliper in Table 6.3. The skin tumors in phantoms A, B, and C are within the dermis layer. The estimated tumor thickness correlated with the actual value well, with an error less than 0.2 mm. In phantoms D and E, the tumor thickness was larger than the dermis thickness, simulating the situation that the skin tumors have penetrated the dermis layer and invaded into hypodermis layer. The thickness of tumor determined by PEF was still very accurate and the error was smaller than 0.4 mm. It suggests that PEF is able to determine the thickness of the

tumor accurately no matter whether the tumor has invaded into hypodermis layer or not.

Table 6.3 The comparison of tumor thickness determined by PEF and the actual value in skin tumor phantoms

Skin tumor #	Dermis thickness (mm)	Tumor thickness (mm)		
		Actual	Measured by PEF	Error
A1	2.1±0.2	0.5±0.1	0.6±0.2	0.01
A2		1.1±0.1	1.0±0.3	-0.12
A3		1.5±0.1	1.5±0.4	-0.06
A4		2.2±0.1	2.2±0.4	-0.01
B1	2.5±0.3	0.7±0.2	0.7±0.2	0.03
B2		1.0±0.2	1.0±0.3	0.07
B3		1.6±0.1	1.6±0.3	0.07
B4		2.0±0.1	2.0±0.4	-0.06
C1	3.2±0.3	0.5±0.1	0.7±0.2	0.16
C2		1.1±0.1	1.1±0.3	0.01
C3		1.3±0.1	1.5±0.3	0.17
C4		2.3±0.2	2.1±0.3	-0.19
D1	1.9±0.2	2.6±0.1	2.5±0.3	-0.11
D2		3.1±0.1	2.9±0.4	-0.22
D3		3.6±0.2	3.5±0.4	-0.06
D4		4.2±0.1	4.1±0.5	-0.02
E1	2.4±0.2	2.6±0.1	2.4±0.3	-0.16
E2		3.1±0.2	3.3±0.4	0.19
E3		3.7±0.2	3.9±0.5	0.26
E4		4.1±0.2	4.4±0.7	0.36

By combining the results in Table 6.2 and Table 6.3, we can find that the thickness of dermis and skin tumor can be accurately deduced from the measurements by a set of PEFs with different contact sizes. Given this information, whether the skin tumor has invaded into the hypodermis layer can be easily judged. Among the 20 skin

cancers in the phantoms, 7 of them have invaded into the deep tissue. PEF is able to identify 6 of them. The only cancer not identified by PEF is the cancer D1 which is a little thicker than the dermis layer. It will help the dermatologist decide how deep they should remove the tissue during surgery, so that the skin cancer can be removed completely while normal tissue is retained as much as possible.

6.3 Determine the 3D Profile of Skin Tumors in Porcine Skin Sample

Porcine skin sample with model tumors were constructed to validate the methodology. A 5 cm × 5 cm porcine skin was harvested from the belly part from a local abattoir. Two rectangular areas with a size about 10 cm in the dermis were removed with a razor blade. A pre-cut modeling clay was placed in the area where the dermis was removed in porcine skin to simulate the skin tumor as shown in Figure 6.8. Modeling clay was chosen because its elastic modulus of 60.3±1.6 kPa was similar to that of basal cell carcinoma reported in literature [139]. Another benefit of using modeling clay is that its shape can be adjusted so that it can fill all the gaps after the dermis removal. The clay was bonded to the surrounding tissue and the sample surface was made flat.

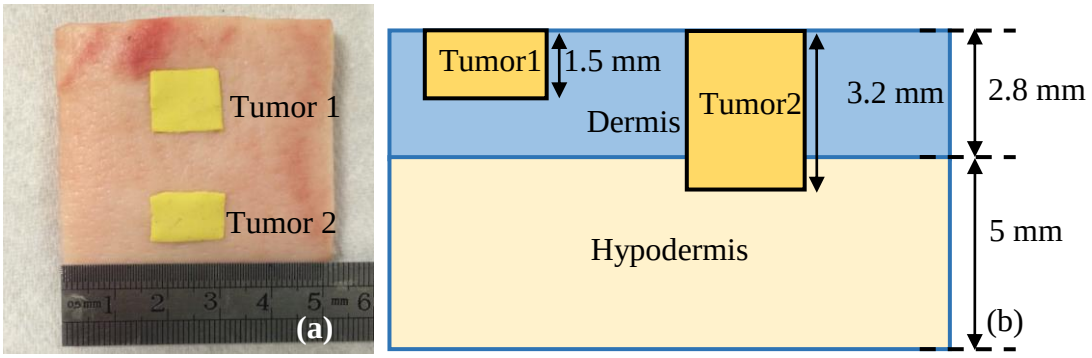

Figure 6.8 (a) A photograph of the model skin tumor embedded in porcine skin. (b) A schematic showing the cross section of the sample.

A grid was first drawn on the sample surface for location tracking. The PEF with a contact radius of 0.23±0.01 mm was placed on the first location and the effective elastic modulus was measured five times on the surface. An average of elastic modulus and standard deviation was calculated for that location. Then the PEF was moved to the next location and the measurement was performed. It was repeated until the entire sample was scanned. After that elastic moduli of the tumor and normal tissue areas were measured using a set of PEFs with contact radius ranging from 0.23±0.01 mm to 3.80±0.11 mm as listed in Table 5.1. The lateral size and thickness of the model skin tumors were measured with a caliper after PEF measurements. The dermis layer of the porcine skin was cut into 1 cm × 1 cm squares and the stress-strain curve was measured by Bose ElectroForce® 3100 using compression test 3 times. The average of the slopes of stress versus strain curves was the determined elastic modulus of dermis. The thickness of dermis was measured by caliper for comparison.

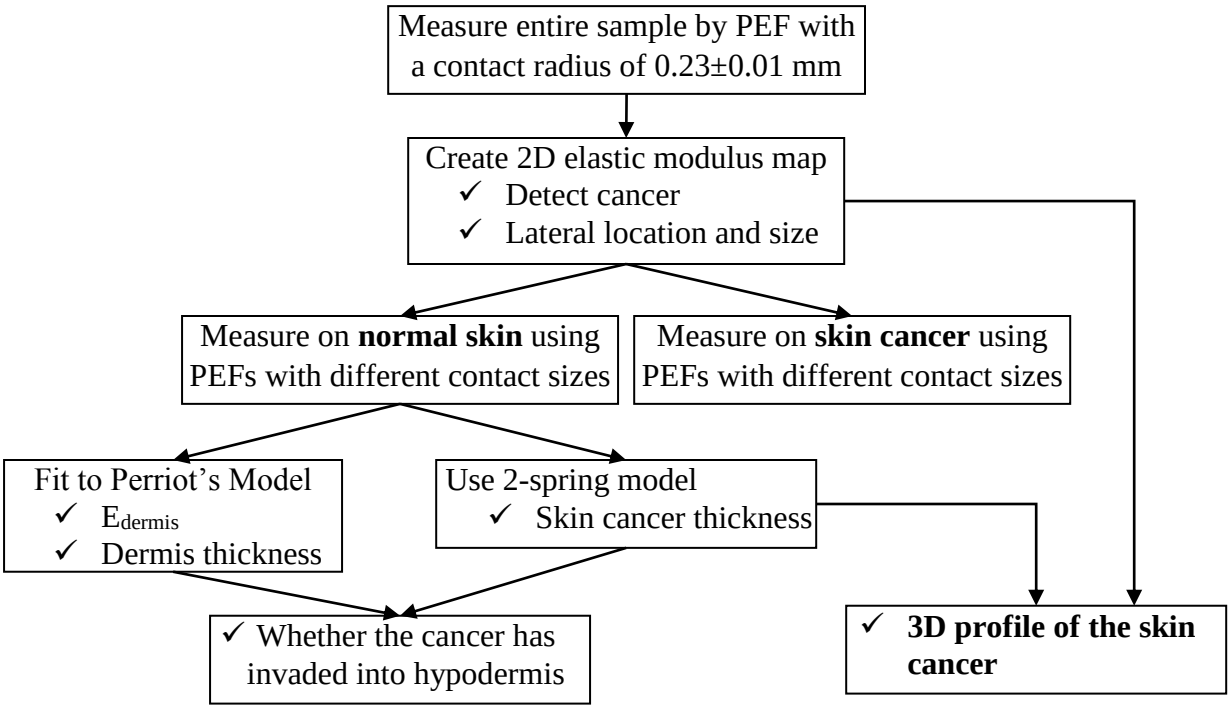

Figure 6.9 A flow chart showing how to determine the 3D profile of skin cancers based on PEF measurements.

A 2D color-coded elastic modulus map was created as shown in Figure 6.10 based on the results from the PEF with a contact radius of 0.23±0.01 mm. The green color represents the elastic modulus of normal tissue while the red color shows the decreased elastic modulus, indicating the location of the tumor. The actual locations of the tumors are marked by the black square. It is clear that PEF detected both tumors in the sample and the lower modulus regions in the map were consistent with the locations of the tumors. The lateral size of the tumors was deduced using the half peak width method as explained in Section 6.1. The comparison of the sizes determined by PEF and those measured by caliper is listed in Table 6.4. As can be seen, the sizes of model tumors estimated by PEF agreed with their actual sizes, with

an error less than 1 mm. It suggests that the PEF can not only detect the skin tumors but also determine the lateral extend of the tumors accurately.

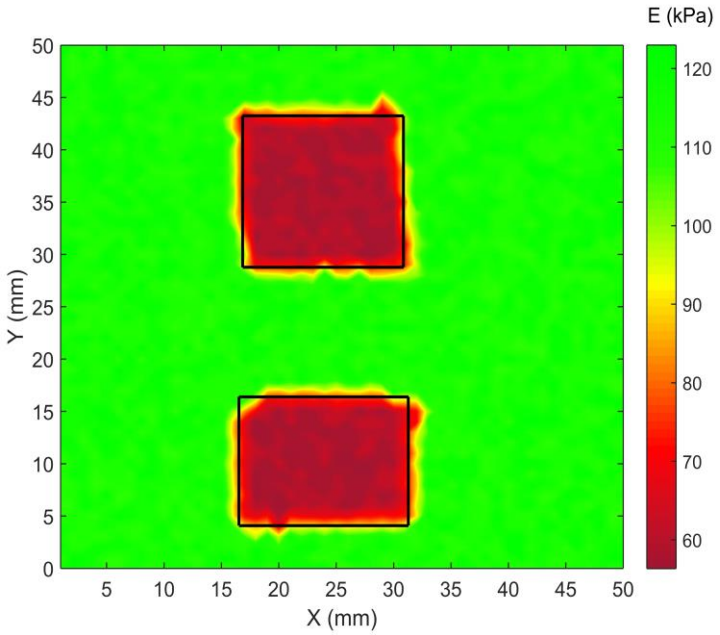

Figure 6.10 Elastic modulus map of the model skin tumors shown in Figure 6.8 scanned by PEF with a contact radius of 0.23±0.01 mm. The actual locations of the tumors are marked with black squares.

Table 6.4 Comparison of the lateral size of the skin tumors in Figure 6.8 measured by caliper and PEF

tumor #	Size in x direction (mm)			Size in y direction (mm)		
	Measured by caliper	Measured by PEF	PEF error	Measured by caliper	Measured by PEF	PEF error
1	13.53±0.53	12.91±0.72	-0.62	14.15±0.54	14.26±0.64	0.11
2	14.25±0.78	13.26±0.46	-0.99	11.63±0.82	11.13±0.51	-0.50

The effective elastic moduli measured by a set of PEF with different contact sizes on normal regions were fit to Perriot's model if the modulus E versus indenter radius was not greater than 0 as shown in Figure 6.11. The elastic modulus of dermis was estimated to be 134.7±9.0 kPa from the PEF fitting results, very close to the averaged value of the slopes of stress-strain curves from 3 repeated compression tests, 143.6±7.5 kPa. As an example, the stress-strain curve of one compression test is plotted in Figure 6.12. The slope of the curve, 145.4 kPa, is the determined elastic modulus of dermis from that test. The thickness of the dermis determined by PEF was 2.59±0.26 mm. It is within the range of the actual dermis thickness, 2.76±0.17 mm, measured by caliper.

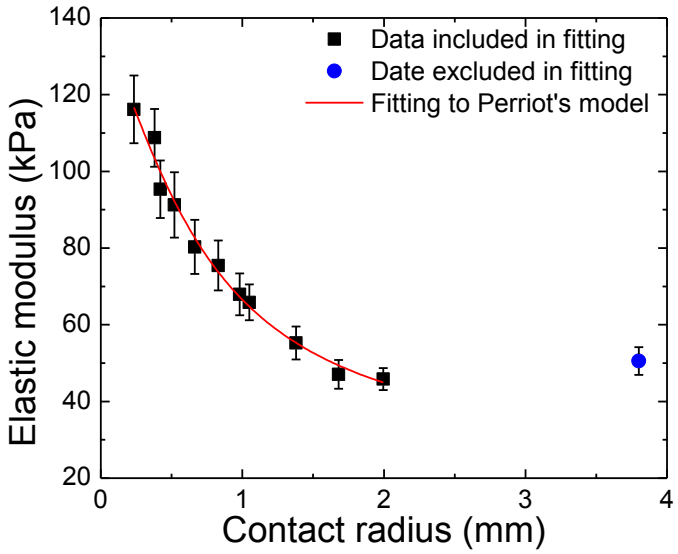

Figure 6.11 Elastic modulus of normal skin measured by PEFs of different contact sizes. The data was fit to Perriot's model to deduce the elastic modulus and thickness of dermis.

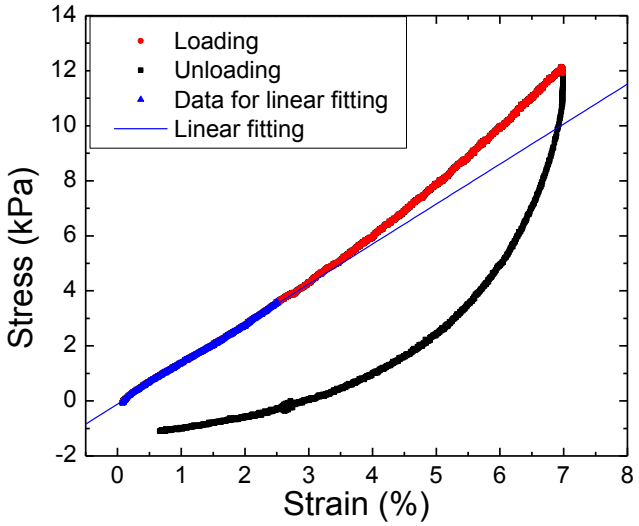

Figure 6.12 The stress versus strain curve of the dermis of porcine skin from a compression test performed by Bose ElectroForce® 3100. The slope of the linear fitting curve is the elastic modulus of the dermis, 145.4 kPa.

The 2-spring model was applied to the effective elastic modulus measured by PEFs on tumor regions to deduce the depth profile of model skin tumors as plotted in a color-coded map in Figure 6.13. The navy color stands for 0 mm for the tumor thickness, meaning that no tumors were found in the region. The green color shows where the tumor thickness is about 1.5 mm. And the red color represents the increased tumor thickness, 3-3.5 mm. The averaged thickness of tumor 1 and 2 were 1.75±0.27 and 3.57±0.54 mm, respectively. They showed good agreement with the actual thickness of tumor 1 and 2 which was 1.51±0.32 and 3.19±0.47, respectively. The discrepancy between the tumor thickness measured by PEF and by caliper was only 0.24 and 0.38 mm, indicating that the PEF is capable of determining depth profile of skin tumors very accurately. Besides, since the thickness of dermis in normal region of the porcine skin was determined to be 2.59±0.26 mm, we can easily

find that the model tumor 1 was within the dermis layer while the tumor 2 had invaded into the hypodermis layer.

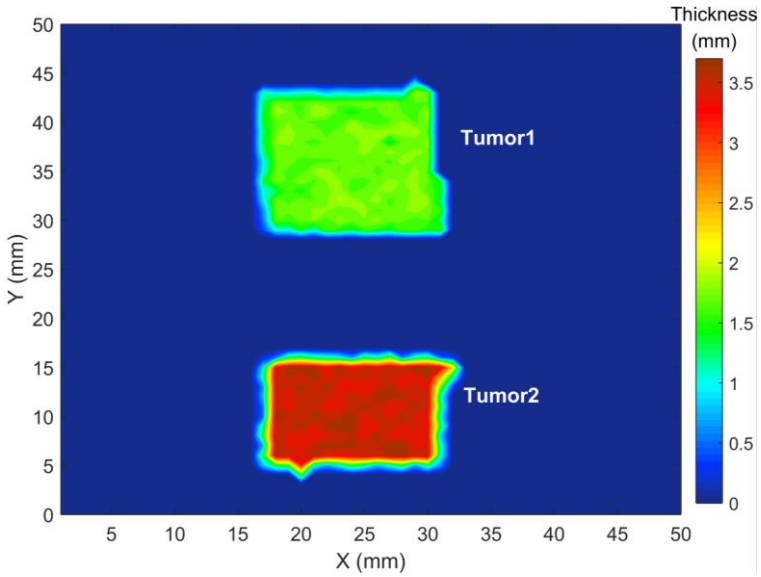

Figure 6.13 The thickness of the model skin tumors deduced from PEF measurements using spring model. The actual thickness of tumor 1 and 2 were 1.51±0.32 and 3.19±0.47, respectively

6.4 Conclusions

In this chapter, PEFs with different contact sizes were used to measure the elastic modulus of skin and skin tumors in phantoms. The PEF with a contact radius of 0.23±0.01 mm was first used to scan the entire phantom. Since the depth sensitivity of the PEF was only about 0.4 mm, smaller than the dermis thickness, the modulus change on the skin surface could be easily captured. A 2D color-coded elastic modulus map was created based on the modulus results and the location of the skin tumor could be directly determined. Then the elastic modulus at certain x

distance was plotted versus y distance and fitted to Gaussian function. The size of the tumor at that x was determined by half peak width of the bell shaped curve. The size of the tumor in y direction was estimated with a similar way. Skin tumor phantoms were built to mimic the basal cell carcinoma with a size ranging from 4×4 to 12×12 mm^2. Lateral extend of the tumors were obtained from the PEF measurements with a contact radius of 0.23±0.01 mm and showed good agreement with the actual values measured by caliper with a difference smaller than 1 mm in both x and y directions.

The depth profile of skin tumors was deduced from stiffness measurements with PEFs of different contact sizes (0.23-3.80 mm) using a modified spring model taking into account of the two-layer nature of skin. The estimated model tumor thickness ranging from 0.5 to 4 mm in phantoms were consistent with the actual values measured by caliper, with a difference smaller than 0.4 mm. Coupled with the thickness of dermis deduced from PEF measurements on normal skin regions, whether the skin tumor has grown into the hypodermis layer could be know.

Modeling clays were embedded in porcine skins to simulate skin tumors. The lateral sizes of model skin cancers determined by PEF were within an error of 1 mm and the estimated depth profiles showed good agreement with the actual thickness with <0.4 mm discrepancy.

In conclusion, PEF is able to detect skin cancers by tissue stiffness contrasting and provide the locations and lateral extend of the tumor from a 2D color-coded map. In addition, using a set of PEFs of different contact areas coupled with simple spring-model calculations the depth profile of skin cancer can be accurately determined.

7. CONCLUSIONS AND FUTURE WORK

7.1 Conclusions

In this study, Piezoelectric Fingers (PEFs), a tissue stiffness sensor that can measure the elastic modulus of tissues have been developed into a hand-held probe to detect breast cancer in patients (AIM 1). It has also been investigated to not only image the breast cancers in 2D but also determine their depth profiles using up to four PEFs of different contact areas, enabling 3D imaging of breast cancers (AIM 2). In parallel, by measuring the effective skin stiffness up to various depths using 12 PEFs of different contact radiuses 0.23-3.8 mm, we were able to determine both the elastic modulus and thickness of skin accurately (AIM 3). With this normal skin information, we then can not only detect skin cancer in 2D but also accurately determine the depth of the skin cancer, which is essential in skin cancer staging (AIM 4). The accomplishments in each of the aims are summarized as follows:

i. AIM 1: *in vivo* breast tumor detection

- A hand-held probe with an array of four PEFs of the same contact area along the methodology was developed, tested, and validated using model breast tumors as well as on patients.
- *In vivo* testing on 40 patients detected 46 of the 48 lesions, including 100% of palpable and 67% non-palpable malignant tumors, indicating PEF was capable of detecting both palpable and non-palpable lesions.

- For the 28 patients with mammography reports, PEF detected 92% malignant tumors while mammography only detected 80%, indicating that PEF could detect malignant tumors not detectable by mammography. Furthermore, PEF detection sensitivity was unaffected by breast density, an advantage for detecting breast cancer in young women and women with dense breasts for whom mammography is not effective.
- The detection results of PEF were unaffected by the depression depths (2-6 mm) of the housing of the probe.

ii. **AIM 2: Breast tumor positioning and sizing in 3D**

- The depth profile of breast cancer was determined by measuring the effective stiffness of breast up to various depths using four PEFS of different contact sizes 4.1-9.8 mm coupled with spring models. In a direct comparison, we showed the depths of bottom-supported tumors were determined within 1.1 mm of the actual depths, similar to those by inversion simulations using FEA that requires massive computation efforts, clearly an advantage of PEFs.
- For suspended tumors, we showed that the tumor depth profiles could be determined within 2.1 mm of the actual values using stiffness measurements by four PEFS of different contact sizes 4.1-9.8 mm coupled with a 3-spring model, clearly illustrating the potential of using a set of

PEFs of different contact areas coupled with spring models to determine tumor depth profiles.

iii. Simultaneous skin elastic modulus and thickness quantification

- The elastic modulus and thickness of dermis were determined simultaneously and accurately--within <10% of the actual values in skin phantoms and porcine skins--by measuring the effective skin elastic modulus up to various depths using a set of PEFs of contact radiuses 0.23-3.8 mm coupled with an empirical formula for a two-layer structure derived from Green's-function calculations.

iv. Lateral skin cancer imaging and depth profiling

- The skin cancer in phantoms was successfully detected by the PEF with a contact radius of 0.23±0.01 mm by contrasting the lower elastic modulus regions with surrounding tissues. The lateral extend of skin cancer was determined within 1 mm error in both x and y directions.

- A modified spring model taking into account of the two-layer nature of skin was applied to determine the depth profile of skin tumors using stiffness measurements with PEFs of various contact sizes of <3 mm. The estimated model tumor thickness ranging from 0.5 to 4 mm in phantoms were consistent with the actual values measured by caliper, with a difference smaller than 0.4 mm.

- The lateral sizes of model skin cancers embedded in porcine skin were determined by PEF with an error of <1 mm and the estimated depth profiles showed good agreement with the actual thickness with <0.4 mm discrepancy. Coupled with the thickness of dermis by PEF on normal regions, whether the skin cancer has grown into the hypodermis layer was determined, making the PEF a helpful tool for skin cancer characterization.

In conclusion, PEF is capable of detecting breast cancer with sensitivity better than mammography and independent of breast density. In addition, using a set of PEFs of different contact areas coupled with simple spring-model calculations the depth profiles of both breast cancer and skin cancer can be accurately determined to facilitate 3D breast cancer/skin cancer imaging.

7.2 Future Work

Although PEF has been proved to be able to not only detect breast tumors and skin cancers but also determine the 3D profile of the cancers, there is still work that should be done to bring the PEF to the ultimate goal of being used as a diagnostic tool in clinics or hospitals:

a. Mitigate the interference of neighboring PEFs in the array and carry out simultaneous measurements to speed up the *in vivo* measurements for cancer detection.

b. Apply the PEFs of different contact sizes coupled with spring model theory to determine the 3D profile of breast cancers *in vivo*.

c. Use the PEFs of different contact radiuses for *in vivo* skin elastic modulus and thickness characterization.

d. Use the PEF with a contact radius of 0.23±0.01 mm for *in vivo* skin cancer detection and lateral size determination.

e. Apply the PEFs of different contact radiuses coupled with the modified spring model to determine the depth profile of skin cancers *in vivo*.

LIST OF REFERENCES

[1] D. B. Kopans and D. Kopans, *Breast imaging* vol. 1: Lippincott Williams & Wilkins Philadelphia, PA, 2007.

[2] G. P. M. Allen Gabriel, Pankaj Tiwari. (2013). *Breast Anatomy*. Available: http://reference.medscape.com/article/1273133-overview

[3] D. Kopans, "Breast anatomy and basic histology, physiology, and pathology," *Kopans DB. Breast Imaging, 3rd Edition. Philadelphia: Lippincott Williams and Williams*, pp. 7-43, 2007.

[4] J. J. Albertini, G. H. Lyman, C. Cox, T. Yeatman, L. Balducci, N. Ku, *et al.*, "Lymphatic mapping and sentinel node biopsy in the patient with breast cancer," *Jama*, vol. 276, pp. 1818-1822, 1996.

[5] A. C. Society. (2016). *Cancer Facts & Figures 2016*. Available: http://www.cancer.org/acs/groups/content/@editorial/documents/document/acspc-044552.pdf

[6] Breastcancer.org, "U.S. Breast Cancer Statistics," ed, 2014.

[7] W. H. Organization. (2011). *Breast cancer: prevention and control*. Available: http://www.who.int/cancer/detection/breastcancer/en/index.html

[8] J. Wang, J. P. Costantino, E. Tan-Chiu, D. L. Wickerham, S. Paik, and N. Wolmark, "Lower-category benign breast disease and the risk of invasive breast cancer," *Journal of the national cancer institute*, vol. 96, pp. 616-620, 2004.

[9] L. C. Hartmann, T. A. Sellers, M. H. Frost, W. L. Lingle, A. C. Degnim, K. Ghosh, *et al.*, "Benign breast disease and the risk of breast cancer," *New England Journal of Medicine*, vol. 353, pp. 229-237, 2005.

[10] J. A. Tice, E. S. O'Meara, D. L. Weaver, C. Vachon, R. Ballard-Barbash, and K. Kerlikowske, "Benign breast disease, mammographic breast density, and the risk of breast cancer," *Journal of the National Cancer Institute*, p. djt124, 2013.

[11] W. L. Donegan and J. S. Spratt, *Cancer of the Breast*: Saunders, 2003.

[12] S. S. Coughlin and D. U. Ekwueme, "Breast cancer as a global health concern," *Cancer epidemiology*, vol. 33, pp. 315-318, 2009.

[13] A. C. Society. (2014). *Breast Cancer Prevention and Early Detection*. Available: http://www.cancer.org/acs/groups/cid/documents/webcontent/003165-pdf.pdf

[14] L. Winters, "Breast self-examination," *Canadian Medical Association Journal*, vol. 166, pp. 164-165, 2002.

[15] D. B. Thomas, D. L. Gao, R. M. Ray, W. W. Wang, C. J. Allison, F. L. Chen, *et al.*, "Randomized trial of breast self-examination in Shanghai: final results," *Journal of the National Cancer Institute*, vol. 94, pp. 1445-1457, 2002.

[16] U. P. S. T. Force, "Screening for breast cancer: US Preventive Services Task Force recommendation statement," *Annals of internal medicine*, vol. 151, p. 716, 2009.

[17] J. P. Kösters and P. C. Gøtzsche, "Regular self‐examination or clinical examination for early detection of breast cancer," *The Cochrane Library*, 2003.

[18] U. S. P. S. T. Force. (2014). *Breast Cancer: Screening*. Available: http://www.uspreventiveservicestaskforce.org/Page/Topic/recommendation-summary/breast-cancer-screening

[19] U. S. D. o. H. a. H. Services. (2014). *Breast Cancer Screening*. Available: http://www.hrsa.gov/quality/toolbox/measures/breastcancer/index.html

[20] L. Dummin, M. Cox, and L. Plant, "Prediction of breast tumor size by mammography and sonography—a breast screen experience," *The Breast*, vol. 16, pp. 38-46, 2007.

[21] L. E. McCahill, R. M. Single, E. J. A. Bowles, H. S. Feigelson, T. A. James, T. Barney, *et al.*, "Variability in reexcision following breast conservation surgery," *Jama*, vol. 307, pp. 467-475, 2012.

[22] J. Sainsbury, T. Anderson, and D. Morgan, "ABC of breast diseases: breast cancer," *BMJ: British Medical Journal*, vol. 321, p. 745, 2000.

[23] M. B. Barton, R. Harris, and S. W. Fletcher, "Does This Patient Have Breast Cancer?: The Screening Clinical Breast Examination: Should It Be Done? How?," *Jama*, vol. 282, pp. 1270-1280, 1999.

[24] I. Ma, A. Dueck, R. Gray, N. Wasif, M. Giurescu, R. Lorans, *et al.*, "Clinical and self breast examination remain important in the era of modern screening," *Annals of surgical oncology*, vol. 19, pp. 1484-1490, 2012.

[25] W. H. Goodson, N. A. Grissom, D. H. Moore, and F. M. Dirbas, "Streamlining clinical breast examination," *Journal of the National Cancer Institute*, vol. 97, pp. 1476-1477, 2005.

[26] P. Weatherall, G. F. Evans, G. J. Metzger, M. H. Saborrian, and A. M. Leitch, "MRI vs. histologic measurement of breast cancer following chemotherapy: Comparison with x‐ray mammography and palpation," *Journal of Magnetic Resonance Imaging*, vol. 13, pp. 868-875, 2001.

[27] R. Sankaranarayanan, K. Ramadas, S. Thara, R. Muwonge, J. Prabhakar, P. Augustine, *et al.*, "Clinical breast examination: preliminary results from a cluster randomized controlled trial in India," *Journal of the National Cancer Institute*, 2011.

[28] I. Mittra, M. Baum, H. Thornton, and J. Houghton, "Is clinical breast examination an acceptable alternative to mammographic screening?," *Bmj*, vol. 321, pp. 1071-1073, 2000.

[29] J. Lo, "The Clinical Breast Examination: A Useful Screening Tool?," *Journal of Patient-Centered Research and Reviews*, vol. 2, pp. 34-37, 2015.

[30] U. Connection. (2015). *Breast ultrasound*. Available: http://ultrasoundconnection.com/breast-cancer-patients-need-lymph-nodes-removed-ultrasound-narrows-study-finds/

[31] K. S. Choo, H. S. Kwak, Y. T. Bae, J.-Y. Lee, S. J. Lee, H. I. Seo, *et al.*, "The value of a combination of wire localization and ultrasound-guided vacuum-assisted breast biopsy for clustered microcalcifications," *The Breast*, vol. 17, pp. 611-616, 2008.

[32] W. K. Moon, J.-G. Im, Y. H. Koh, D.-Y. Noh, and I. A. Park, "US of Mammographically Detected Clustered Microcalcifications 1," *Radiology*, vol. 217, pp. 849-854, 2000.

[33] C. M. Sehgal, S. P. Weinstein, P. H. Arger, and E. F. Conant, "A review of breast ultrasound," *Journal of mammary gland biology and neoplasia*, vol. 11, pp. 113-123, 2006.

[34] B. Pritt, T. Ashikaga, R. G. Oppenheimer, and D. L. Weaver, "Influence of breast cancer histology on the relationship between ultrasound and pathology tumor size measurements," *Modern pathology*, vol. 17, pp. 905-910, 2004.

[35] A. M. Bosch, A. G. Kessels, G. L. Beets, J. D. Rupa, D. Koster, J. van Engelshoven, *et al.*, "Preoperative estimation of the pathological breast tumour size by physical examination, mammography and ultrasound: a

prospective study on 105 invasive tumours," *European journal of radiology,* vol. 48, pp. 285-292, 2003.

[36] S. Allen, W. Cunliffe, J. Gray, J. Liston, L. Lunt, L. Webb, *et al.*, "Pre-operative estimation of primary breast cancer size: a comparison of clinical assessment, mammography and ultrasound," *The Breast,* vol. 10, pp. 299-305, 2001.

[37] L. Leong, L. Sim, Y. Lee, F. Ng, C. Wan, S. Fook-Chong, *et al.*, "A prospective study to compare the diagnostic performance of breast elastography versus conventional breast ultrasound," *Clinical radiology,* vol. 65, pp. 887-894, 2010.

[38] W. A. Berg, J. D. Blume, J. B. Cormack, and E. B. Mendelson, "Operator Dependence of Physician-performed Whole-Breast US: Lesion Detection and Characterization 1," *Radiology,* vol. 241, pp. 355-365, 2006.

[39] H. Cheng, J. Shan, W. Ju, Y. Guo, and L. Zhang, "Automated breast cancer detection and classification using ultrasound images: A survey," *Pattern Recognition,* vol. 43, pp. 299-317, 2010.

[40] B. Friedenson, "Is mammography indicated for women with defective BRCA genes? Implications of recent scientific advances for the diagnosis, treatment, and prevention of hereditary breast cancer," *MedGenMed: Medscape general medicine,* vol. 2, pp. E9-E9, 2000.

[41] P. C. Gøtzsche and M. Nielsen, "Screening for breast cancer with mammography," *The cochrane library,* 2009.

[42] N. T. Brewer, T. Salz, and S. E. Lillie, "Systematic review: the long-term effects of false-positive mammograms," *Annals of internal medicine,* vol. 146, pp. 502-510, 2007.

[43] C. L. Christiansen, F. Wang, M. B. Barton, W. Kreuter, J. G. Elmore, A. E. Gelfand, *et al.*, "Predicting the cumulative risk of false-positive mammograms," *Journal of the National Cancer Institute,* vol. 92, pp. 1657-1666, 2000.

[44] R. A. Hubbard, K. Kerlikowske, C. I. Flowers, B. C. Yankaskas, W. Zhu, and D. L. Miglioretti, "Cumulative probability of false-positive recall or biopsy recommendation after 10 years of screening mammography: a cohort study," *Annals of internal medicine,* vol. 155, pp. 481-492, 2011.

[45] K. M. Kelly, J. Dean, W. S. Comulada, and S.-J. Lee, "Breast cancer detection using automated whole breast ultrasound and mammography in

radiographically dense breasts," *European radiology*, vol. 20, pp. 734-742, 2010.

[46] P. Crystal, S. D. Strano, S. Shcharynski, and M. J. Koretz, "Using sonography to screen women with mammographically dense breasts," *American Journal of Roentgenology*, vol. 181, pp. 177-182, 2003.

[47] N. F. Boyd, H. Guo, L. J. Martin, L. Sun, J. Stone, E. Fishell, *et al.*, "Mammographic density and the risk and detection of breast cancer," *New England Journal of Medicine*, vol. 356, pp. 227-236, 2007.

[48] V. Corsetti, N. Houssami, A. Ferrari, M. Ghirardi, S. Bellarosa, O. Angelini, *et al.*, "Breast screening with ultrasound in women with mammography-negative dense breasts: evidence on incremental cancer detection and false positives, and associated cost," *European journal of cancer*, vol. 44, pp. 539-544, 2008.

[49] P. A. Carney, D. L. Miglioretti, B. C. Yankaskas, K. Kerlikowske, R. Rosenberg, C. M. Rutter, *et al.*, "Individual and combined effects of age, breast density, and hormone replacement therapy use on the accuracy of screening mammography," *Annals of internal medicine*, vol. 138, pp. 168-175, 2003.

[50] M. Clinic. (2014). *Breast density — The four levels*. Available: http://www.mayoclinic.org/tests-procedures/mammogram/multimedia/breast-density-mdash-the-four-levels/img-20008862

[51] D. Förnvik, S. Zackrisson, O. Ljungberg, T. Svahn, P. Timberg, A. Tingberg, *et al.*, "Breast tomosynthesis: Accuracy of tumor measurement compared with digital mammography and ultrasonography," *Acta Radiologica*, vol. 51, pp. 240-247, 2010.

[52] R. M. Mann, C. K. Kuhl, K. Kinkel, and C. Boetes, "Breast MRI: guidelines from the European society of breast imaging," *European radiology*, vol. 18, pp. 1307-1318, 2008.

[53] E. A. Morris, L. Liberman, D. J. Ballon, M. Robson, A. F. Abramson, A. Heerdt, *et al.*, "MRI of occult breast carcinoma in a high-risk population," *American Journal of Roentgenology*, vol. 181, pp. 619-626, 2003.

[54] R. Eiada, J. Chong, S. Kulkarni, F. Goldberg, and D. Muradali, "Papillary lesions of the breast: MRI, ultrasound, and mammographic appearances," *American Journal of Roentgenology*, vol. 198, pp. 264-271, 2012.

[55] J. H. Menell, E. A. Morris, D. D. Dershaw, A. F. Abramson, E. Brogi, and L. Liberman, "Determination of the presence and extent of pure ductal carcinoma

in situ by mammography and magnetic resonance imaging," *The breast journal,* vol. 11, pp. 382-390, 2005.

[56] L. H. Vanderwalde, C. M. Dang, C. Bresee, and E. H. Phillips, "Discordance between pathologic and radiologic tumor size on breast MRI may contribute to increased re-excision rates," *The American surgeon,* vol. 77, pp. 1361-1363, 2011.

[57] B. S. Garra, E. I. Cespedes, J. Ophir, S. R. Spratt, R. A. Zuurbier, C. M. Magnant, *et al.*, "Elastography of breast lesions: initial clinical results," *Radiology,* vol. 202, pp. 79-86, 1997.

[58] A. L. McKnight, J. L. Kugel, P. J. Rossman, A. Manduca, L. C. Hartmann, and R. L. Ehman, "MR elastography of breast cancer: preliminary results," *American Journal of Roentgenology,* vol. 178, pp. 1411-1417, 2002.

[59] D. M. Regner, G. K. Hesley, N. J. Hangiandreou, M. J. Morton, M. R. Nordland, D. D. Meixner, *et al.*, "Breast Lesions: Evaluation with US Strain Imaging–Clinical Experience of Multiple Observers 1," *Radiology,* vol. 238, pp. 425-437, 2006.

[60] K. M. Hiltawsky, M. Krüger, C. Starke, L. Heuser, H. Ermert, and A. Jensen, "Freehand ultrasound elastography of breast lesions: clinical results," *Ultrasound in medicine & biology,* vol. 27, pp. 1461-1469, 2001.

[61] W. A. Berg, D. O. Cosgrove, C. J. Doré, F. K. Schäfer, W. E. Svensson, R. J. Hooley, *et al.*, "Shear-wave elastography improves the specificity of breast US: the BE1 multinational study of 939 masses," *Radiology,* vol. 262, pp. 435-449, 2012.

[62] F. Schaefer, I. Heer, P. Schaefer, C. Mundhenke, S. Osterholz, B. Order, *et al.*, "Breast ultrasound elastography—results of 193 breast lesions in a prospective study with histopathologic correlation," *European journal of radiology,* vol. 77, pp. 450-456, 2011.

[63] R. Sinkus, M. Tanter, T. Xydeas, S. Catheline, J. Bercoff, and M. Fink, "Viscoelastic shear properties of in vivo breast lesions measured by MR elastography," *Magnetic resonance imaging,* vol. 23, pp. 159-165, 2005.

[64] D. B. Plewes, J. Bishop, A. Samani, and J. Sciarretta, "Visualization and quantification of breast cancer biomechanical properties with magnetic resonance elastography," *Physics in medicine and biology,* vol. 45, p. 1591, 2000.

[65] R. Sinkus, K. Siegmann, T. Xydeas, M. Tanter, C. Claussen, and M. Fink, "MR elastography of breast lesions: understanding the solid/liquid duality can

improve the specificity of contrast‐enhanced MR mammography," *Magnetic Resonance in Medicine,* vol. 58, pp. 1135-1144, 2007.

[66] S. H. Heywang-Koebrunner and I. Schreer, *Diagnostic breast imaging: mammography, sonography, magnetic resonance imaging, and interventional procedures*: Thieme, 2014.

[67] H. FENG, J.-l. LI, Y. HUANG, X.-q. SHI, W.-b. WAN, and J. TANG, "Value of the Shear Wave Elastography Combined with BI-RADS in Quantitative Differential Diagnosis of Breast Tumors [J]," *Medical & Pharmaceutical Journal of Chinese People's Liberation Army,* vol. 5, p. 026, 2013.

[68] A. Sarvazyan, "Mechanical imaging: a new technology for medical diagnostics," *International journal of medical informatics,* vol. 49, p. 195, 1998.

[69] V. Egorov and A. P. Sarvazyan, "Mechanical imaging of the breast," *Medical Imaging, IEEE Transactions on,* vol. 27, pp. 1275-1287, 2008.

[70] V. Egorov, T. Kearney, S. B. Pollak, C. Rohatgi, N. Sarvazyan, S. Airapetian, *et al.*, "Differentiation of benign and malignant breast lesions by mechanical imaging," *Breast cancer research and treatment,* vol. 118, pp. 67-80, 2009.

[71] C. S. Kaufman, L. Jacobson, B. A. Bachman, and L. B. Kaufman, "Digital documentation of the physical examination: moving the clinical breast exam to the electronic medical record," *The American journal of surgery,* vol. 192, pp. 444-449, 2006.

[72] P. L. Yen, D. R. Chen, K. T. Yeh, and P. Y. Chu, "Lateral exploration strategy for differentiating the stiffness ratio of an inclusion in soft tissue," *Medical engineering & physics,* vol. 30, pp. 1013-1019, 2008.

[73] P.-L. Yen, D.-R. Chen, K.-T. Yeh, and P.-Y. Chu, "Development of a stiffness measurement accessory for ultrasound in breast cancer diagnosis," *Medical engineering & physics,* vol. 33, pp. 1108-1119, 2011.

[74] J. Lee and C. Won, "High resolution tactile imaging sensor using total internal reflection and non-rigid pattern matching algorithm," *Sensors Journal, IEEE,* pp. 1-1, 2011.

[75] J. H. Lee and C. H. Won, "Inclusion mechanical property estimation using tactile images, finite element method, and artificial neural network," in *Annual International Conference of the IEEE*, 2011, pp. 14-17.

[76] J.-H. Lee and C.-H. Won, "The tactile sensation imaging system for embedded lesion characterization," *IEEE journal of biomedical and health informatics*, vol. 17, pp. 452-458, 2013.

[77] D. O. Uribe, R. Stroop, T. Hemsel, and J. Wallaschek, "Development of a biomedical tissue differentiation system using piezoelectric actuators," in *Frequency Control Symposium*, 2008, pp. 91-94.

[78] D. O. Uribe, R. Stroop, and J. Wallaschek, "Piezoelectric self-sensing system for tactile intraoperative brain tumor delineation in neurosurgery," in *31 st Annual International Conference of the IEEE EMBS*, Minneapolis, Minnesota, USA, 2009, pp. 737-740.

[79] R. Stroop, D. O. Uribe, M. O. Martinez, M. Brökelmann, T. Hemsel, and J. Wallaschek, "Tactile tissue characterisation by piezoelectric systems," *Journal of Electroceramics*, vol. 20, pp. 237-241, 2008.

[80] J. C. Gwilliam, Z. Pezzementi, E. Jantho, A. M. Okamura, and S. Hsiao, "Human vs. robotic tactile sensing: detecting lumps in soft tissue," in *Haptic Symposium*, 2010, pp. 21-28.

[81] A. Samani, J. Zubovits, and D. Plewes, "Elastic moduli of normal and pathological human breast tissues: an inversion-technique-based investigation of 169 samples," *Physics in medicine and biology*, vol. 52, p. 1565, 2007.

[82] P. Wellman, R. D. Howe, E. Dalton, and K. A. Kern, "Breast tissue stiffness in compression is correlated to histological diagnosis," *Harvard BioRobotics Laboratory Technical Report*, 1999.

[83] T. A. Krouskop, T. M. Wheeler, F. Kallel, B. S. Garra, and T. Hall, "Elastic moduli of breast and prostate tissues under compression," *Ultrasonic imaging*, vol. 20, pp. 260-274, 1998.

[84] P. Wellman, R. D. Howe, E. Dalton, and K. A. Kern, "Breast tissue stiffness in compression is correlated to histological diagnosis," *submitted to Journal of Biomechanics*, 1999.

[85] E. Pickwell, B. Cole, A. Fitzgerald, M. Pepper, and V. Wallace, "In vivo study of human skin using pulsed terahertz radiation," *Physics in Medicine and Biology*, vol. 49, p. 1595, 2004.

[86] WebMD. (2013). *Skin Problems & Treatments Health Center*. Available: http://www.webmd.com/skin-problems-and-treatments/picture-of-the-skin

[87] D. Yudovsky and L. Pilon, "Rapid and accurate estimation of blood saturation, melanin content, and epidermis thickness from spectral diffuse reflectance," *Applied optics,* vol. 49, pp. 1707-1719, 2010.

[88] T. Gambichler, J. Huyn, N. S. Tomi, G. Moussa, C. Moll, A. Sommer, *et al.*, "A Comparative Pilot Study on Ultraviolet‐induced Skin Changes Assessed by Noninvasive Imaging Techniques in Vivo," *Photochemistry and photobiology,* vol. 82, pp. 1103-1107, 2006.

[89] S. Cotton, E. Claridge, and P. Hall, "Noninvasive skin imaging," in *Information Processing in Medical Imaging*, 1997, pp. 501-506.

[90] D. A. Wrone and N. J. Kwon, "Andrews' Diseases of the Skin: Clinical Dermatology," *Archives of Dermatology,* vol. 137, pp. 518-518, 2001.

[91] (2013). *Human Skin Diagram*. Available: http://www.rudyard.org/human-skin-diagram/

[92] D. L. Miller and M. A. Weinstock, "Nonmelanoma skin cancer in the United States: incidence," *Journal of the American Academy of Dermatology,* vol. 30, pp. 774-778, 1994.

[93] N. C. Institute. (2014). *SEER Stat Fact Sheets: Melanoma of the Skin*. Available: http://seer.cancer.gov/statfacts/html/melan.html

[94] A. C. Society. (2015). *Melanoma Skin Cancer*. Available: http://www.cancer.org/cancer/skincancer-melanoma/detailedguide/melanoma-skin-cancer-key-statistics

[95] H. W. Rogers, M. A. Weinstock, A. R. Harris, M. R. Hinckley, S. R. Feldman, A. B. Fleischer, *et al.*, "Incidence estimate of nonmelanoma skin cancer in the United States, 2006," *Archives of dermatology,* vol. 146, pp. 283-287, 2010.

[96] A. B. Mariotto, K. R. Yabroff, Y. Shao, E. J. Feuer, and M. L. Brown, "Projections of the cost of cancer care in the United States: 2010–2020," *Journal of the National Cancer Institute,* 2011.

[97] A. C. Society. (2015). *Skin Cancer: Basal and Squamous Cell*. Available: http://www.cancer.org/cancer/skincancer-basalandsquamouscell/detailedguide/skin-cancer-basal-and-squamous-cell-key-statistics

[98] S. C. Foundation. (2013). *Basal Cell Carcinoma (BCC)*. Available: http://www.skincancer.org/skin-cancer-information/basal-cell-carcinoma

[99] S. C. Foundation. (2013). *Squamous Cell Carcinoma (SCC).* Available: http://www.skincancer.org/skin-cancer-information/squamous-cell-carcinoma

[100] C. G. Clemente, M. C. Mihm, R. Bufalino, S. Zurrida, P. Collini, and N. Cascinelli, "Prognostic value of tumor infiltrating lymphocytes in the vertical growth phase of primary cutaneous melanoma," *Cancer,* vol. 77, pp. 1303-1310, 1996.

[101] A. Breslow, "Thickness, cross-sectional areas and depth of invasion in the prognosis of cutaneous melanoma," *Annals of surgery,* vol. 172, p. 902, 1970.

[102] A. C. Buzaid, M. I. Ross, C. M. Balch, S.-j. Soong, W. H. McCarthy, L. Tinoco, *et al.*, "Critical analysis of the current American Joint Committee on Cancer staging system for cutaneous melanoma and proposal of a new staging system," *Journal of clinical oncology,* vol. 15, pp. 1039-1051, 1997.

[103] C. M. Balch, S.-J. Soong, J. E. Gershenwald, J. F. Thompson, D. S. Reintgen, N. Cascinelli, *et al.*, "Prognostic factors analysis of 17,600 melanoma patients: validation of the American Joint Committee on Cancer melanoma staging system," *Journal of Clinical Oncology,* vol. 19, pp. 3622-3634, 2001.

[104] C. R. UK. (2010). *Stages of melanoma*.

[105] I. Zalaudek, G. Ferrara, G. Argenziano, V. Ruocco, and H. P. Soyer, "Diagnosis and treatment of cutaneous melanoma: a practical guide," *SKINmed: Dermatology for the Clinician,* vol. 2, pp. 20-33, 2003.

[106] D. S. Rigel, R. J. Friedman, A. W. Kopf, and D. Polsky, "ABCDE—an evolving concept in the early detection of melanoma," *Archives of dermatology,* vol. 141, pp. 1032-1034, 2005.

[107] E. Doctors. (2015). *How we diagnose skin cancers?* Available: http://www.eastmed.co.nz/how-we-diagnose-skin-cancer.php

[108] I. Leibovitch, S. C. Huilgol, D. Selva, S. Richards, and R. Paver, "Basal cell carcinoma treated with Mohs surgery in Australia II. Outcome at 5-year follow-up," *Journal of the American Academy of Dermatology,* vol. 53, pp. 452-457, 2005.

[109] N. W. Smeets, G. A. Krekels, J. U. Ostertag, B. A. Essers, C. D. Dirksen, F. H. Nieman, *et al.*, "Surgical excision vs Mohs' micrographic surgery for basal-cell carcinoma of the face: randomised controlled trial," *The Lancet,* vol. 364, pp. 1766-1772, 2004.

[110] L. Brancaleon, A. J. Durkin, J. H. Tu, G. Menaker, J. D. Fallon, and N. Kollias, "In vivo Fluorescence Spectroscopy of Nonmelanoma Skin Cancer¶," *Photochemistry and Photobiology,* vol. 73, pp. 178-183, 2001.

[111] M. Panjehpour, C. E. Julius, M. N. Phan, T. Vo‐Dinh, and S. Overholt, "Laser‐induced fluorescence spectroscopy for in vivo diagnosis of non‐melanoma skin cancers," *Lasers in surgery and medicine,* vol. 31, pp. 367-373, 2002.

[112] J. Paoli, M. Smedh, A.-M. Wennberg, and M. B. Ericson, "Multiphoton laser scanning microscopy on non-melanoma skin cancer: morphologic features for future non-invasive diagnostics," *Journal of Investigative Dermatology,* vol. 128, pp. 1248-1255, 2008.

[113] E. Drakaki, C. Dessinioti, A. J. Stratigos, C. Salavastru, and C. Antoniou, "Laser-induced fluorescence made simple: implications for the diagnosis and follow-up monitoring of basal cell carcinoma," *Journal of biomedical optics,* vol. 19, pp. 030901-030901, 2014.

[114] L. Machet, V. Belot, M. Naouri, M. Boka, Y. Mourtada, B. Giraudeau, *et al.*, "Preoperative measurement of thickness of cutaneous melanoma using high-resolution 20 MHz ultrasound imaging: a monocenter prospective study and systematic review of the literature," *Ultrasound in medicine & biology,* vol. 35, pp. 1411-1420, 2009.

[115] R. Vilana, S. Puig, M. Sanchez, M. Squarcia, A. Lopez, T. Castel, *et al.*, "Preoperative assessment of cutaneous melanoma thickness using 10-MHz sonography," *American Journal of Roentgenology,* vol. 193, pp. 639-643, 2009.

[116] T. Gambichler, G. Moussa, K. Bahrenberg, M. Vogt, H. Ermert, D. Weyhe, *et al.*, "Preoperative Ultrasonic Assessment of Thin Melanocytic Skin Lesions Using a 100‐MHz Ultrasound Transducer: A Comparative Study," *Dermatologic surgery,* vol. 33, pp. 818-824, 2007.

[117] G. Pennasilico, A. Santini, R. Bono, M. Cacciaguerra, P. Puddu, and P. Falappa, "Preoperative ultrasonographic measurement of melanoma thickness with 20 MHz probe]," *La Radiologia medica,* vol. 88, p. 388, 1994.

[118] K. Hoffmann, J. Jung, S. El Gammal, and P. Altmeyer, "Malignant melanoma in 20-MHz B scan sonography," *Dermatology,* vol. 185, pp. 49-55, 2009.

[119] C. Harland, J. Bamber, B. Gusterson, and P. Mortimer, "High frequency, high resolution B‐scan ultrasound in the assessment of skin tumours," *British Journal of Dermatology,* vol. 128, pp. 525-532, 1993.

[120] T. Cammarota, F. Pinto, A. Magliaro, and A. Sarno, "Current uses of diagnostic high-frequency US in dermatology," *European journal of radiology*, vol. 27, pp. S215-S223, 1998.

[121] A. Mandava, P. R. Ravuri, and R. Konathan, "High-resolution ultrasound imaging of cutaneous lesions," *The Indian journal of radiology & imaging*, vol. 23, p. 269, 2013.

[122] T. Hinz, L.-K. Ehler, H. Voth, I. Fortmeier, T. Hoeller, T. Hornung, *et al.*, "Assessment of tumor thickness in melanocytic skin lesions: comparison of optical coherence tomography, 20-MHz ultrasound and histopathology," *Dermatology*, vol. 223, pp. 161-168, 2011.

[123] D. Huang, E. A. Swanson, C. P. Lin, J. S. Schuman, W. G. Stinson, W. Chang, *et al.*, "Optical coherence tomography," *Science*, vol. 254, pp. 1178-1181, 1991.

[124] J. Welzel, "Optical coherence tomography in dermatology: a review," *Skin Research and Technology*, vol. 7, pp. 1-9, 2001.

[125] J. Welzel, C. Reinhardt, E. Lankenau, C. Winter, and H. Wolff, "Changes in function and morphology of normal human skin: evaluation using optical coherence tomography," *British Journal of Dermatology*, vol. 150, pp. 220-225, 2004.

[126] M. Mogensen, H. A. Morsy, L. Thrane, and G. B. Jemec, "Morphology and epidermal thickness of normal skin imaged by optical coherence tomography," *Dermatology*, vol. 217, pp. 14-20, 2008.

[127] D. Huang, E. A. Swanson, C. P. Lin, J. S. Schuman, W. G. Stinson, W. Chang, *et al.*, "Optical Coherence Tomography," *Science*, vol. 254, pp. 1178-1181, Nov 22 1991.

[128] T. Wang, S. Mallidi, J. Qiu, L. L. Ma, A. S. Paranjape, J. Sun, *et al.*, "Comparison of pulsed photothermal radiometry, optical coherence tomography and ultrasound for melanoma thickness measurement in PDMS tissue phantoms," *Journal of biophotonics*, vol. 4, pp. 335-344, 2011.

[129] J. Welzel, E. Lankenau, R. Birngruber, and R. Engelhardt, "Optical coherence tomography of the human skin," *Journal of the American Academy of Dermatology*, vol. 37, pp. 958-963, 1997.

[130] M. Mogensen, T. JOERGENSEN, B. M. Nürnberg, H. A. Morsy, J. B. THOMSEN, L. Thrane, *et al.*, "Assessment of Optical Coherence Tomography Imaging in the Diagnosis of Non - Melanoma Skin Cancer and

Benign Lesions Versus Normal Skin: Observer‐Blinded Evaluation by Dermatologists and Pathologists," *Dermatologic Surgery,* vol. 35, pp. 965-972, 2009.

[131] M. Ulrich, E. Stockfleth, J. Roewert‐Huber, and S. Astner, "Noninvasive diagnostic tools for nonmelanoma skin cancer," *British Journal of Dermatology,* vol. 157, pp. 56-58, 2007.

[132] M. Ulrich, J. Roewert‐Huber, S. González, F. Rius‐Diaz, E. Stockfleth, and J. Kanitakis, "Peritumoral clefting in basal cell carcinoma: correlation of in vivo reflectance confocal microscopy and routine histology," *Journal of cutaneous pathology,* vol. 38, pp. 190-195, 2011.

[133] C. Curiel-Lewandrowski, C. M. Williams, K. J. Swindells, S. R. Tahan, S. Astner, R. A. Frankenthaler, *et al.*, "Use of in vivo confocal microscopy in malignant melanoma: an aid in diagnosis and assessment of surgical and nonsurgical therapeutic approaches," *Archives of dermatology,* vol. 140, p. 1127, 2004.

[134] F. Hendriks, D. Brokken, C. Oomens, D. Bader, and F. Baaijens, "The relative contributions of different skin layers to the mechanical behavior of human skin in vivo using suction experiments," *Medical engineering & physics,* vol. 28, pp. 259-266, 2006.

[135] P. Agache, C. Monneur, J. Leveque, and J. De Rigal, "Mechanical properties and Young's modulus of human skin in vivo," *Archives of dermatological research,* vol. 269, pp. 221-232, 1980.

[136] Y. Fung, "Elasticity of soft tissues in simple elongation," *American Journal of Physiology--Legacy Content,* vol. 213, pp. 1532-1544, 1967.

[137] S. Diridollou, F. Patat, F. Gens, L. Vaillant, D. Black, J. Lagarde, *et al.*, "In vivo model of the mechanical properties of the human skin under suction," *Skin Research and technology,* vol. 6, pp. 214-221, 2000.

[138] M. Geerligs, L. Van Breemen, G. Peters, P. Ackermans, F. Baaijens, and C. Oomens, "In vitro indentation to determine the mechanical properties of epidermis," *Journal of biomechanics,* vol. 44, pp. 1176-1181, 2011.

[139] T. Raveh Tilleman, M. Tilleman, and H. Neumann, "The elastic properties of cancerous skin: Poisson's ratio and Young's modulus," *Optimization of Incisions in Cutaneous Surgery including Mohs' Micrographic Surgery.,* p. 105, 2004.

[140] S. J. Kirkpatrick, R. K. Wang, D. D. Duncan, M. Kulesz-Martin, and K. Lee, "Imaging the mechanical stiffness of skin lesions by in vivo acousto-optical elastography," *Optics express,* vol. 14, pp. 9770-9779, 2006.

[141] A. Markidou, W. Y. Shih, and W. H. Shih, "Soft-materials elastic and shear moduli measurement using piezoelectric cantilevers," *Review of scientific instruments,* vol. 76, p. 064302, 2005.

[142] S. T. Szewczyk, W. Y. Shih, and W. H. Shih, "Palpationlike soft-material elastic modulus measurement using piezoelectric cantilevers," *Review of scientific instruments,* vol. 77, p. 044302, 2006.

[143] S. T. Szewczyk and W.-H. Shih, "Exploring all-electrical soft-tissue stiffness measurement using piezoelectric unimorph cantilevers," in *Bioengineering Conference, 2003 IEEE 29th Annual, Proceedings of,* 2003, pp. 146-147.

[144] H. O. Yegingil, W. Y. Shih, W. Anjum, A. D. Brooks, and W. H. Shih, "Soft tissue elastic modulus measurement and tumor detection using piezoelectric fingers," in *MRS Fall Meeting,* 2005.

[145] H. Yegingil, W. Y. Shih, and W. H. Shih, "All-electrical indentation shear modulus and elastic modulus measurement using a piezoelectric cantilever with a tip," *Journal of Applied Physics,* vol. 101, p. 054510, 2007.

[146] H. Yegingil, W. Y. Shih, and W. H. Shih, "Probing elastic modulus and depth of bottom-supported inclusions in model tissues using piezoelectric cantilevers," *Review of scientific instruments,* vol. 78, p. 115101, 2007.

[147] J. Ophir, I. Cespedes, H. Ponnekanti, Y. Yazdi, and X. Li, "Elastography: a quantitative method for imaging the elasticity of biological tissues," *Ultrasonic imaging,* vol. 13, pp. 111-134, 1991.

[148] J. Ophir, I. Cespedes, B. Garra, H. Ponnekanti, Y. Huang, and N. Maklad, "Elastography: ultrasonic imaging of tissue strain and elastic modulus in vivo," *European journal of ultrasound,* vol. 3, pp. 49-70, 1996.

[149] K. M. Hiltawsky, M. Krüger, C. Starke, L. Heuser, H. Ermert, and A. Jensen, "Freehand ultrasound elastography of breast lesions: clinical results," *Ultrasound in medicine & biology,* vol. 27, p. 1461, 2001.

[150] A. Thomas, T. Fischer, H. Frey, R. Ohlinger, S. Grunwald, J. U. Blohmer, *et al.*, "Real‐time elastography—an advanced method of ultrasound: first results in 108 patients with breast lesions," *Ultrasound in obstetrics & gynecology,* vol. 28, pp. 335-340, 2006.

[151] H. O. Yegingil, "Breast cancer detection and differentiation using piezoelectric fingers," Drexel University, 2009.

[152] M. S. Richards, P. E. Barbone, and A. A. Oberai, "Quantitative three-dimensional elasticity imaging from quasi-static deformation: a phantom study," *Physics in medicine and biology,* vol. 54, p. 757, 2009.

[153] T. J. Hall, M. Bilgen, M. F. Insana, and T. A. Krouskop, "Phantom materials for elastography," *Ultrasonics, Ferroelectrics and Frequency Control, IEEE Transactions on,* vol. 44, pp. 1355-1365, 1997.

[154] S. Kalyanam, R. D. Yapp, and M. F. Insana, "Poro-viscoelastic behavior of gelatin hydrogels under compression-implications for bioelasticity imaging," *Journal of biomechanical engineering,* vol. 131, p. 081005, 2009.

[155] A. Samani and D. Plewes, "An inverse problem solution for measuring the elastic modulus of intact ex vivo breast tissue tumours," *Physics in medicine and biology,* vol. 52, p. 1247, 2007.

[156] H. Mehrabian, G. Campbell, and A. Samani, "A constrained reconstruction technique of hyperelasticity parameters for breast cancer assessment," *Physics in medicine and biology,* vol. 55, p. 7489, 2010.

[157] J. J. O'Hagan and A. Samani, "Measurement of the hyperelastic properties of 44 pathological ex vivo breast tissue samples," *Physics in medicine and biology,* vol. 54, p. 2557, 2009.

[158] J. J. O'Hagan and A. Samani, "Measurement of the hyperelastic properties of tissue slices with tumour inclusion," *Physics in medicine and biology,* vol. 53, p. 7087, 2008.

[159] X. Xu, C. Gifford-Hollingsworth, R. Sensenig, W.-H. Shih, W. Y. Shih, and A. D. Brooks, "Breast Tumor Detection using Piezoelectric Fingers: First Clinical Report," *Journal of the American College of Surgeons,* vol. in press, 2013.

[160] J. Kavanagh, T. Menand, and K. A. Daniels, "Gelatine as a crustal analogue: Determining elastic properties for modelling magmatic intrusions," *Tectonophysics,* vol. 582, pp. 101-111, 2013.

[161] S. Crandall, L. Kurzweil, and A. Nigam, "On the measurement of Poisson's ratio for modeling clay," *Experimental Mechanics,* vol. 11, pp. 402-413, 1971.

[162] W. Hayes, L. Keer, G. Herrmann, and L. Mockros, "A mathematical analysis for indentation tests of articular cartilage," *Journal of biomechanics,* vol. 5, pp. 541-551, 1972.

[163] J.-L. Gennisson, T. Baldeweck, M. Tanter, S. Catheline, M. Fink, L. Sandrin, *et al.*, "Assessment of elastic parameters of human skin using dynamic elastography," *IEEE transactions on ultrasonics, ferroelectrics, and frequency control,* vol. 51, pp. 980-989, 2004.

[164] X. Liang and S. A. Boppart, "Biomechanical properties of in vivo human skin from dynamic optical coherence elastography," *IEEE Transactions on Biomedical Engineering,* vol. 57, pp. 953-959, 2010.

[165] A. L'Etang and Z. Huang, "FE simulation of laser generated surface acoustic wave propagation in skin," *Ultrasonics,* vol. 44, pp. e1243-e1247, 2006.

[166] C. Li, G. Guan, R. Reif, Z. Huang, and R. K. Wang, "Determining elastic properties of skin by measuring surface waves from an impulse mechanical stimulus using phase-sensitive optical coherence tomography," *Journal of The Royal Society Interface,* vol. 9, pp. 831-841, 2012.

[167] M. Geerligs, "A literature review of the mechanical behavior of the stratum corneum, the living epidermis and the subcutaneous fat tissue," Philips Research2006.

[168] M. Matthew Hoffman. (2014). *Picture of the Skin*. Available: http://www.webmd.com/skin-problems-and-treatments/picture-of-the-skin#1

[169] M. F. Doerner and W. D. Nix, "A method for interpreting the data from depth-sensing indentation instruments," *Journal of Materials research,* vol. 1, pp. 601-609, 1986.

[170] R. King, "Elastic analysis of some punch problems for a layered medium," *International Journal of Solids and Structures,* vol. 23, pp. 1657-1664, 1987.

[171] A. Bhattacharya and W. Nix, "Analysis of elastic and plastic deformation associated with indentation testing of thin films on substrates," *International Journal of Solids and Structures,* vol. 24, pp. 1287-1298, 1988.

[172] R. Saha and W. D. Nix, "Effects of the substrate on the determination of thin film mechanical properties by nanoindentation," *Acta Materialia,* vol. 50, pp. 23-38, 2002.

[173] S. Bec and A. Tonck, "Nanometer scale mechanical properties of tribochemical films," *Tribology Series,* vol. 31, pp. 173-184, 1996.

[174] S. Bec, A. Tonck, J.-M. Georges, E. Georges, and J.-L. Loubet, "Improvements in the indentation method with a surface force apparatus," *Philosophical Magazine A,* vol. 74, pp. 1061-1072, 1996.

[175] G. Huajian, C. Cheng-Hsin, and L. Jin, "Elastic contact versus indentation modeling of multi-layered materials," *International Journal of Solids and Structures,* vol. 29, pp. 2471-2492, 1992.

[176] A. Rar, H. Song, and G. Pharr, "Assessment of new relation for the elastic compliance of a film-substrate system," in *MRS Proceedings,* 2001, p. L10. 10.1.

[177] A. Perriot and E. Barthel, "Elastic contact to a coated half-space: Effective elastic modulus and real penetration," *Journal of Materials Research,* vol. 19, pp. 600-608, 2004.

[178] S. Bec, A. Tonck, and J.-L. Loubet, "A simple guide to determine elastic properties of films on substrate from nanoindentation experiments," *Philosophical Magazine,* vol. 86, pp. 5347-5358, 2006.

[179] R. M. Lavker, G. Dong, P. Zheng, and G. F. Murphy, "Hairless micropig skin. A novel model for studies of cutaneous biology," *The American journal of pathology,* vol. 138, p. 687, 1991.

[180] A. M. Barbero and H. F. Frasch, "Pig and guinea pig skin as surrogates for human in vitro penetration studies: a quantitative review," *Toxicology in vitro,* vol. 23, pp. 1-13, 2009.

[181] F. P. Schmook, J. G. Meingassner, and A. Billich, "Comparison of human skin or epidermis models with human and animal skin in in-vitro percutaneous absorption," *International journal of pharmaceutics,* vol. 215, pp. 51-56, 2001.

[182] S. Avon and R. Wood, "PORCINE SKIN AS AN PORCINE SKIN AS AN IN-VIVO MODEL FOR MODEL FOR AGEING OF HUMAN BITE MARKS," *J Forensic Odontostomatol,* vol. 23, pp. 30-9, 2005.

[183] G. Morris and J. Hopewell, "Epidermal cell kinetics of the pig: a review," *Cell Proliferation,* vol. 23, pp. 271-282, 1990.

[184] W. Meyer, R. Schwarz, and K. Neurand, "The Skin of Domestic Mammals as a Model for the Human Skin, with Special Reference to the Domestic Pig1," in *Skin-Drug Application and Evaluation of Environmental Hazards*, ed: Karger Publishers, 1978, pp. 39-52.

[185] W. Heinrich, P. Lange, T. Stirtz, C. Iancu, and E. Heidemann, "Isolation and characterization of the large cyanogen bromide peptides from the α1-and α2-chains of pig skin collagen," *FEBS letters,* vol. 16, pp. 63-67, 1971.

[186] T. Jee and K. Komvopoulos, "< i> In vitro</i> measurement of the mechanical properties of skin by nano/microindentation methods," *Journal of Biomechanics*, 2013.

[187] Z. Fong and K. Tanabe, "Comparison of melanoma guidelines in the USA, Canada, Europe, Australia and New Zealand: a critical appraisal and comprehensive review," *British Journal of Dermatology*, vol. 170, pp. 20-30, 2014.

[188] J. F. Thompson, R. A. Scolyer, and R. F. Kefford, "Melanoma: A management guide for GPs," *Australian family physician*, vol. 41, p. 470, 2012.

VITA

XIN XU

Education

- 2009-2016 Ph.D. in Biomedical Engineering
  Drexel University, Philadelphia, PA
- 2009-2016 M.S. in Biomedical Engineering
  Drexel University, Philadelphia, PA
- 2005-2009 B.S.in Biomedical Engineering
  Shanghai Jiao Tong University, Shanghai, China

Publications

- Xu, X, Shih, W. H., & Shih, W. Y. (2016). Development of Array Piezoelectric Fingers towards In Vivo Breast Tumor Detection. *Review of Scientific Instrument*, submitted
- Beringer, L. T., Xu, X., Shih, W., Shih, W. H., Habas, R., & Schauer, C. L. (2015). An electrospun PVDF-TrFe fiber sensor platform for biological applications. *Sensors and Actuators A: Physical, 222*, 293-300.
- Xu, X., Gifford-Hollingsworth, C., Sensenig, R., Shih, W. H., Shih, W. Y., & Brooks, A. D. (2013). Breast tumor detection using piezoelectric fingers: first clinical report *Journal of the American College of Surgeons, 216*(6), 1168-1173.
- Wang, H., Xu, X., Li, X., Xi, P., & Ren, Q. (2011). Systematic design of a cross-polarized dermoscope for visual inspection and digital imaging. *IEEE Instrumentation & Measurement Magazine, 14*(6), 26-31.

Patents

- Wan Y. Shih, Wei-Heng Shih, and Xin Xu. "Depth measurement in tissue using piezoelectric sensors having different probe sizes." International Patent Pending # PCT/US2015/010412, Jan 2015
- Wan Y. Shih, Wei-Heng Shih, Xin Xu, and Christopher Emery. "Rapid Antimicrobial Susceptibility Testing Using Piezoelectric Sensor." Filed in Dec 2015